

Probing the Complexities of ‘Simple’ Stellar
Populations in Compact Stellar Systems

James T Banister

A THESIS SUBMITTED IN PARTIAL FULFILMENT
OF THE REQUIREMENTS FOR THE DEGREE OF
DOCTOR OF PHILOSOPHY

Jeremiah Horrocks Institute for Mathematics, Physics and Astronomy
University of Central Lancashire

October 2024

Declaration

Type of Award: Doctor of Philosophy

School: Engineering and Computing

I declare that while registered as a candidate for the research degree, I have not been a registered candidate or enrolled student for another award of the University or other academic or professional institution.

I declare that no material contained in the thesis has been used in any other submission for an academic award and is solely my own work.

No proof-reading service was used in the compilation of this thesis.

A handwritten signature in black ink, appearing to read 'James T Banister', written over a horizontal line.

James T Banister

October 2024

Abstract

In this Thesis, we present an unprecedentedly large sample of compact stellar system integrated light spectra and spectral line measurements, much of which has been obtained for this thesis through new observations or reduced for the first time with custom reduction pipelines. We present the results of the analysis of the stellar populations of several hundred compact stellar systems ranging in size from globular clusters to massive compact ellipticals and beyond. We adopt previously used analysis techniques as well as developing our own with the aim to recover “simple” parameters such as age, metallicity and alpha abundance. Based on comparison with resolved star studies of Milky Way globular clusters, we find that age is poorly constrained while metallicity is returned accurately and $[\alpha/\text{Fe}]$ is returned reliably under specific conditions.

Problems with age measurements are a common problem in integrated light studies of compact stellar systems, usually manifested in globular clusters as an underestimation in age. We suggest this is due to populations of hot blue horizontal branch stars at low metallicity ($[\text{Fe}/\text{H}] \leq -1.0$) and blue straggler stars (for higher metallicities of $[\text{Fe}/\text{H}] \geq -1.0$) which are unaccounted for in standard simple stellar population models. In order to better constrain the ages of the predominately metal-rich, massive, compact stellar system population, we therefore create a new set of models using a simple algorithm to add a fraction of younger star light to sMILES models to account for blue straggler stars. We find that these models produce better age estimations for Milky Way globular clusters and increase age

measurements in general for all objects in our sample, while having minimal effect on metallicity or alpha measurements. Under the assumption that all compact stellar systems host populations of blue stragglers we therefore suggest the common usage of such models when studying at least compact stellar populations, if not galaxies in general

We explore other parameters of compact stellar systems including relations between their mass and metallicity and dive into specific chemical abundances in the form of nitrogen enhancements. We suggest possible formation scenarios for many objects based on their derived star formation histories, metallicity spreads, measured ages and metallicities. We find nitrogen enhancement in many objects from globular clusters to the most massive galaxies hinting at a possible nitrogen - density correlation. We also identify another UCD which, based on its position in the mass-size plane, high metallicity, and high integrated velocity dispersion, is highly likely to host a supermassive black hole. Finally we identify potential signatures of star formation in a red and dead red nugget galaxy and signatures of potentially the first active galactic nucleus in a compact elliptical galaxy.

Contents

Declaration	ii
Abstract	iii
Acknowledgements	xviii
1 Background and Theory	1
1.1 Introduction	1
1.2 GCs	4
1.2.1 The Early History of GC Studies	5
1.2.2 Milky Way Globular Clusters	6
1.2.3 Magellanic Clouds	7
1.2.4 M31 and Extragalactic Globular Clusters	8
1.3 Multiple ‘Populations’ in Globular Cluster	9
1.3.1 Specific Chemical Abundance Anomalies	10
1.3.2 Genuine Secondary Populations	12
1.4 Ultra-Compact Dwarf Galaxies	12
1.5 Nuclear Star Clusters	14
1.6 Compact Elliptical Galaxies	15
1.7 Photometry	16
1.8 Spectroscopy	18

1.8.1	Spectrographs	18
1.8.2	Integrated Light Spectra	21
1.8.3	Integrated Light Spectroscopy Types	21
1.9	Summary	23
2	Data & Data Reduction	25
2.1	Introduction	25
2.2	WiFeS Atlas of Galactic Globular Cluster Survey	26
2.2.1	Instrumentation	26
2.2.2	Cluster Selection	27
2.2.3	Observations	30
2.2.4	WAGGS Data Reduction	35
2.3	Pre-Reduced Data	39
2.3.1	Schiavon MW & M31	39
2.3.2	M87 GCs and UCDs	40
2.3.3	Sloan Digital Sky Survey (SDSS) Spectra of Galaxies	41
2.4	X-Shooter	42
2.4.1	X-Shooter Reduction	43
2.5	MODS	46
2.5.1	Data Selection	47
2.5.2	MODS Reduction	47
2.6	New Observations with SOAR	54
2.6.1	SOAR	54
2.6.2	Goodman High-Throughput Spectrograph	55
2.6.3	GHTS Data	57
2.6.4	GHTS Reduction	58
2.7	Summary of Available Data	59

2.8	Single Stellar Population Models	59
2.8.1	MILES	60
2.8.2	sMILES	60
2.8.3	Conroy Models	61
2.8.4	TMJ SSPs	62
2.8.5	Model parameter interpolation	62
3	Initial Integrated Light Analysis	65
3.1	Introduction	65
3.2	LICK/IDS Index System	65
3.3	The Modern Line Index System	67
3.4	Methods for Integrated Light Spectral Analysis	69
3.4.1	Smoothing the Data	69
3.4.2	Basic Penalised Pixel Fitting (BpPXF)	71
3.4.3	Single SSP Penalised Pixel Fitting (SpPXF)	76
3.4.4	LICK Indices Minimal χ^2 Method (LISm χ)	78
3.5	Error analysis	79
3.6	BpPXF	80
3.6.1	Sample Slection	81
3.6.2	Wavelength Ranges	85
3.6.3	Running pPXF	88
3.6.4	Results	92
3.6.5	Uncertainty Calculations	100
3.7	SpPXF	101
3.7.1	Using sMILES with $[\alpha/\text{Fe}] = 0.3$	101
3.7.2	Using sMILES with all $[\alpha/\text{Fe}]$ Values	106
3.7.3	Uncertainty calculations	111
3.8	LISm χ	112

3.8.1	LICK Indices	113
3.8.2	Sample Selection	114
3.8.3	Results	116
3.8.4	Uncertainty Analysis	123
3.9	Conclusion	126
4	Simple SSP Models with Blue Straggler Stars	130
4.1	Introduction	130
4.2	Sources of Age uncertainties	131
4.2.1	Blue Horizontal Branch Stars	133
4.2.2	Blue Stragglers	136
4.3	Making BSSMILES Models	140
4.3.1	Blue-Star Sample	141
4.3.2	Blue-Star Selection	145
4.3.3	BSS SSP Combination	149
4.4	LISm χ	153
4.4.1	Age	153
4.4.2	Metallicity	158
4.5	BpPXF	163
4.6	Conclusion	169
5	Further Analysis of Compact Stellar Systems	173
5.1	Introduction	173
5.2	Initial CSS Sample Analysis	173
5.3	Age & Metallicity Measurements	177
5.3.1	BpPXF	178
5.3.2	LISM χ	179
5.4	Age and Metallicity Results	181

5.4.1	M31 Residuals	182
5.4.2	Other CSS Residuals	188
5.5	Age and Metallicity Evidence of CSS Stripping	196
5.5.1	Confirming Age & Metallicity Spreads in 2 GCs	199
5.5.2	An Anomalous Metal-Rich UCD	202
5.6	NSC Formation Classification	208
5.6.1	NGC 628 - NSC	209
5.6.2	NGC 2344-NSC	209
5.6.3	UGC 12732-NSC	210
5.6.4	EVCC1320	211
5.6.5	NSC Summary	211
5.7	CN Abundance as a Signature of Formation	212
5.7.1	NSC CN Enhancement	215
5.7.2	UCD CN Abundance	217
5.7.3	cE CN Abundances	219
5.7.4	A Possible CN - Density relation	221
5.8	OIII Emission in Two Red & Dead Galaxies	224
5.8.1	MRK1216 Red & Dead, Redemption?	225
5.8.2	AHcE0 AGN Candidate	227
5.9	Conclusion	228
6	Thesis Overview and Discussion	232
6.1	Methods of CSS Spectral Analysis	233
6.1.1	BpPXF	234
6.1.2	SpPXF	235
6.1.3	LISm χ	236
6.2	BSsMILES	237
6.3	CN Overabundance in CSSs	240

6.4	Anomalous Objects	241
6.5	Final Conclusions	243
A	Compact Stellar systems Information	259
A.1	Local Globular Clusters	259
A.2	Other Compact Stellar systems	265
B	CSS Analysis Method Results	268
B.1	Local Globular Cluster Results	268
B.1.1	Local GC Results with BSsMILES Models	278
B.2	Results for the Other CSSs	281
C	Results Analysis Plots	284
C.1	Age and Metallicity Residual Comparison.	285
C.2	BpPXF NSCs	285
C.3	CN enhancements	287
D	Further Information	289

List of Tables

2.1	The resolution and wavelength ranges of the WiFeS gratings.	27
2.2	Signal to noise ratios of the WAGGS data.	35
3.1	LICK/IDS FWHM Resolution	68
3.2	BpPXF age and metallicity mean offsets for just Milky Way GCs . . .	97
3.3	SpPXF age and metallicity mean offsets	102
3.4	SpPXF age and metallicity mean offsets for sMILES SSPs with all alpha values	106
3.5	SpPXF α offsets for sMILES SSPs allowed to fit to all alpha values. .	110
3.6	mean offsets of age and metallicity for LISm χ using sMILES models with alpha enhanced to 0.3	117
3.7	mean offsets of age and metallicity for LISm χ using sMILES models with all alpha values	121
5.1	Table of LICK/IDS indices used for the LISm χ analysis.	181
A.1	Part 1 of the table of WAGGS globular cluster data used in this project.	259
A.2	Part 2 of the table of WAGGS globular cluster data used in this project.	262
A.3	The CSSs from MODS, GHTS, XShooter and Keck used in this thesis.	265
B.1	BpPXF Outputs for WAGGS GCs	268
B.2	SpPXF outputs using $[\alpha/Fe] = 0.3$ and all $[\alpha/Fe]$ value models. . . .	272
B.3	LISm χ outputs using $[\alpha/Fe] = 0.3$ and all $[\alpha/Fe]$ value models. . . .	276

B.4	LIS χ Outputs with BSsMILES models	278
B.5	CSS BpPXF & LIS χ Outputs with sMILES & BSsMILES models .	282
D.1	Table of LICK/IDS Indices.	289
D.2	Table 1 of LICK/IDS - LIS Index conversion values for Equation 3.3 .	291
D.3	Table 2 of LICK/IDS - LIS Index conversion values for Equation 3.3 .	292

List of Figures

1.1	CSS mass against radius defining different CSS types From the AIMSS project	3
1.2	The CMD of NGC 6352 showing evidence of MPs in the UV light . .	17
1.3	Line diagram of a single slit spectrograph	19
1.4	X-Shooter Arc Spectrum	20
2.1	WAGGS Age against metallicity	28
2.2	WAGGS Globular Clusters in the Small Magellanic Cloud	30
2.3	Field-of-view of the WAGGS observations for 3 GCs	32
2.4	The fraction of the V-band luminosity in the WiFeS field-of-view compared to the full V-band luminosity of the GC	33
2.5	The CMD of NGC 2808 showing cluster stars and stars obtained in the integral field	34
2.6	The grating combination process used for WAGGS spectra	38
2.7	Voronoi plot of the binned SDSS galaxies	42
2.8	PypeIt output wavelength calibration image	45
2.9	Raw MODS2 Image	48
2.10	Biased and Flat Fielded MODS2 Image	49
2.11	RASCAL wavelength calibration	50
2.12	The effects of wavelength calibration	51
2.13	Increased SNR in the combined MODS spectra	53

2.14	SOAR Telescope Diagrams	55
2.15	GHTS 3D diagram	57
2.16	sMILES models interpolated in metallicity	64
3.1	Example of indices, CN_1 and CN_2 over the spectra of NGC 2808 . . .	67
3.2	pPXF Best Fit for NGC6352	74
3.3	pPXF: single SSP model at a time	77
3.4	Monte Carlo of LISm χ for NGC6864	81
3.5	OIII absorption in SMC GCs	83
3.6	Different wavelength ranges used for BpPXF and SpPXF	87
3.7	Regularisation factor against signal-to-noise for the WAGGS GCs using BpPXF	91
3.8	BpPXF Age and metallicity fits of the full spectral range	94
3.9	BpPXF Age and metallicity fits of the full spectral range with regions omitted from the fit	95
3.10	BpPXF Age and metallicity fits of the narrower spectral range	96
3.11	BpPXF metallicity residual for all WAGGS GCs	98
3.12	BpPXF metallicity residual for Milky Way WAGGS GCs	99
3.13	SpPXF Age residual against literature age using sMILES SSP models with α values of 0.3	103
3.14	SpPXF metallicity against literature metallicity using sMILES SSP models with α values of 0.3	105
3.15	SpPXF Age residual against literature age using sMILES SSP models with all α values	107
3.16	SpPXF metallicity against literature metallicity using sMILES SSP models with all α values	108
3.17	SpPXF metallicity for sMILES models with alpha values of 0.3 and a finer binned metallicity	110

3.18	The output alpha values from SpPXF	111
3.19	The “narrow” wavelength region used in BpPXF and SpPXF with the LICK indices used in LISm χ highlighted.	115
3.20	LISm χ results plots for sMILES SSP models using α values of 0.3 . .	118
3.21	LISm χ metallicity against literature metallicity for sMILES SSP models using α values of 0.3	119
3.22	LISm χ results plots for sMILES SSP models using all α values	120
3.23	LISm χ metallicity against literature metallicity for sMILES SSP models using all α values	121
3.24	LISm χ alpha values against literature values using sMILES SSPs . . .	123
3.25	The Monte Carlo runs of NGC 5904 & NGC 7099	125
3.26	Mean χ residual value for the indices used with LISm χ	128
4.1	LISm χ contour plot of NGC 6838 showing the best fitting SSP and the normalised reduced χ^2 value of each SSP model.	132
4.2	Hertzsprung-Russell diagram of 14 GCs combined together using GAIA photometry	136
4.3	The Stellar library used for the construction of BSsMILES models . .	143
4.4	BaSti Isochrones at different ages	146
4.5	The Teff against metallicity plot showing the stellar sample and the effective temperatures of the MSTO (between 4 and 14 Gyr every 100 Myr) and the most massive BSS of SSP models at different ages. . . .	148
4.6	The creation of BSsMILES	151
4.7	H β / metallicity plot showing sMILES and BsSmiles models at different ages.	152
4.8	LISm χ output values using sMILES models with 0% BSS addition. .	155
4.9	LISm χ output values using BSsMILES models with 1% BSS addition.	156
4.10	LISm χ output values using BSsMILES models with 5% BSS addition.	157

4.11	LISm χ output values using BSsMILES models with 10% BSS addition.	158
4.12	LISm χ output metallicity against the literature using sMILES models with 0% BSS addition.	160
4.13	LISm χ output metallicity against the literature using BSsMILES models with 1% BSS addition.	161
4.14	LISm χ output metallicity against the literature using BSsMILES models with 5% BSS addition.	162
4.15	LISm χ output metallicity against the literature using BSsMILES models with 10% BSS addition.	163
4.16	BpPXF output for NGC 104 using BSsMILES models at different percentages	167
4.17	BpPXF output for NGC 6356 using BSsMILES models at different percentages	168
4.18	BpPXF output for NGC 5927 using BSsMILES models at different percentages	169
5.1	Radius Vs Mass plot of the CSS sample for this project	176
5.2	Output results from BpPXF and LISm χ for CSSs using both sMILES and BSsMILES models	182
5.3	M31 GC residuals between the literature	185
5.4	M31 GC residuals between measured age and literature age	186
5.5	M31 GC residuals between measured metallicity and literature metallicity	187
5.6	BpPXF and LISm χ metallicity against Literature metallicity for CSSs	190
5.7	Residual metallicity against literature alpha abundance for CSSs . . .	191
5.8	BpPXF and LISm χ metallicity against Literature metallicity for CSSs	194
5.9	Residual age against literature metallicity for CSSs	195
5.10	Mass against radius plot for the CSS sample with measured metallicity on the colourbar	197

5.11	Mass against metallicity for the cEs in the CSS sample separated by their isolated status	198
5.12	BpPXF mass fraction plots of Ω Cen and B023-G078	201
5.13	BpPXF mass fraction plot of NGC4546-UCD1	202
5.14	Mass fraction age vs metallicity plot and spectral fit from BpPXF for UCD-FORS 45	204
5.15	Mass against velocity dispersion plot for UCDs	207
5.16	BpPXF fit over the CN enhanced region for NGC6864	213
5.17	CN vs metallicity SSP models comparison using WAGGS GCs	213
5.18	CN vs metallicity of NSCs	216
5.19	CN vs metallicity of UCDs	218
5.20	CN vs metallicity of cEs	220
5.21	CN vs metallicity plots of the cEs showing their mass and their stellar density	221
5.22	CN vs metallicity plot for the larger CSS sample showing stellar density	222
5.23	CN vs metallicity plot for all the previous CSSs and SDSS galaxies .	223
5.24	H β and OIII emission in MRK1216 at different radii	226
5.25	H β and OIII emission in AHcE0	228
C.1	Residual age against residual metallicity for CSSs	285
C.2	BpPXF mass fraction plots of NGC 628-NSC	286
C.3	BpPXF mass fraction plots of NGC 2344-NSC	286
C.4	BpPXF mass fraction plots of UGC12732-NSC	287
C.5	BpPXF mass fraction plots of EVCC1320	287
C.6	Comparison plot showing the residuals for the Conroy C and N enhanced spectra to a Solar abundance spectrum	288

Acknowledgements

I have far too many people to thank for such a short portion of text, but I better start at the beginning. It is a pleasure to thank Dr Mark Norris for his supervision and for being the most knowledgeable mentor. His constant advice and support have been wholly invaluable. I would also like to thank Dr Victor Debattista, my second supervisor for useful insight and Dr Anne Sansom for indispensable advice as my “third” supervisor whose title does very little justice for the amount of support she has offered me at every stage of this project. I would like to thank all of the staff and my fellow postgraduate students at the Jeremiah Horrocks Institute, for their support and particularly the Thursday pub quiz crew and Friday pub regulars for much-needed relief from the postgraduate office. I would like to thank my parents and family for their constant support throughout the whole of my university experience. Grateful acknowledgements to Prof Derek Ward-Thompson and the Jeremiah Horrocks Institute for supporting me with a studentship. Thanks go to the Astrophysics department of the University of North Carolina at Chapel Hill for providing four observation runs on the SOAR telescope. Finally, I am incredibly grateful to Liv, without whom I would have at the least undoubtedly starved during the final few months of the write-up, her constant support has been inspiring and I could never thank her enough.

Chapter 1

Background and Theory

1.1 Introduction

The term Compact Stellar Systems (CSSs) is used as a catch-all term to describe a range of relatively small, incredibly stellar dense objects which have a wide range of names in the literature e.g. Globular Clusters (GCs), Ultra Compact Dwarfs (UCDs), Compact Ellipticals (cEs) etc. They range in size from the smallest GCs with effective radii of $r_e \approx 1.5$ pc (Harris, 1996) to massive Compact Elliptical galaxies ($r_e \lesssim 600$ pc, Du et al. 2019) with a host of other types of dense stellar environments in between. They have many formation scenarios (Naab, Johansson & Ostriker, 2009; Forbes et al., 2018; Du et al., 2019; Davison et al., 2021b), can have extreme local stellar environments (being the most stellar dense objects in the universe, Fahrion et al. 2021) with high stellar collision and binary interaction rates (Hills & Day, 1976; Sills et al., 1997; Chatterjee et al., 2013; Kremer et al., 2020; Kravtsov et al., 2022; Dib et al., 2022) and many are thought to host to intermediate mass black holes (IMBH) and even super massive black holes (SMBHs) (Merritt, Schnittman & Komossa, 2009; Seth et al., 2014; Ahn et al., 2017). Their chemistries are complex, with even the smallest having multiple chemically distinct stellar populations (MPs, Bastian & Lardo 2018). Yet we often only use the simplest

CHAPTER 1

of stellar population synthesis models to infer their properties. Compact stellar systems are small but powerful, and as we shall see, they are far from simple.

In this thesis, the complexities of these objects are explored and probes are made into how effectively their properties and formation mechanisms can be measured using modern ‘simple’ Single Stellar Population (SSP) models. Also, in recent years, the intermediate mass range of stellar systems has become increasingly more populated, with the gap between star clusters and galaxies being filled by CSSs such as Ultra-Compact Dwarf Galaxies and Compact Elliptical Galaxies (Norris et al., 2014; Janz et al., 2016). There is still a significant overlap between CSS type in mass, size and formation mechanisms. This thesis will probe the definitions of these objects, it will identify signatures within the integrated light of CSSs which could potentially be used to further differentiate CSS type (e.g. to separate UCDs formed as massive GCs from those formed by the tidal stripping of a nucleated galaxy), or be used to highlight common trends between all compact stellar systems.

There is a suite of methods available for the observation and measurement of CSSs, ranging from individual resolved star analysis for the closest stellar systems, to integrated light analysis for the furthest objects and near objects alike. Below, the different classes of CSS are introduced, different observation and analysis techniques are discussed and the benefits of each method are debated.

There are many objects which are defined under the envelope of a “Compact Stellar System” (shown in Figure 1.1, along with many larger objects used to demonstrate the relative sizes and masses of CSSs), in order to understand these objects, one must understand how they are defined, the processes thought to form them and how they evolve chemically and structurally. Here, we start with GCs, the “simplest” compact stellar systems.

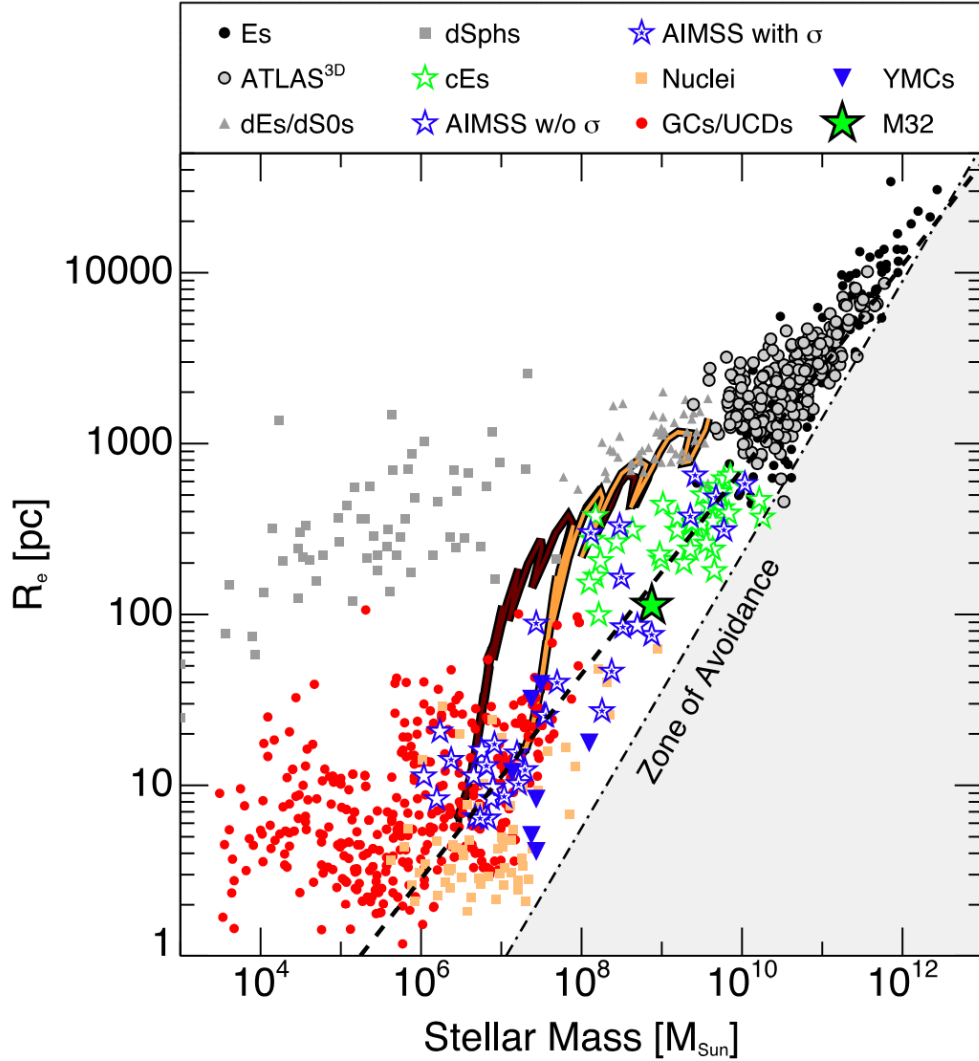


Figure 1.1: The mass vs radius plot (taken from Norris et al. 2014) for all of the objects in the Archive of Intermediate Mass Stellar Systems (AIMSS) sample (Norris et al., 2014; Forbes et al., 2014; Janz et al., 2016), separated by object type. Any object in black and grey is not considered a CSS in this project. The brown and orange lines represent the mass-radius path of a simulation of two nucleated dEs as they are tidally stripped from Pfeffer & Baumgardt (2013) (specifically simulations 3 and 17). AIMSS and ATLAS3D are surveys of CSSs and early-type galaxies respectively. The acronyms introduced in this figure are discussed below. Es, dSphs, YMCs and dEs/dS0s are for Elliptical galaxies, dwarf Spheroidal galaxies, Young Massive Clusters and dwarf Elliptical galaxies / dwarf spiral galaxies respectively.

1.2 GCs

Globular clusters are the least massive class of CSS explored in this thesis. They are densely packed stellar systems that can contain 10's of thousands to millions of stars in a roughly spherical volume often as small as a few parsecs across. Most GCs are thought to be formed in a single burst of star formation during a collapse of a giant gas cloud in the early stages of the universe around the epoch of reionisation (Peebles & Dicke, 1968) and as such are key probes to the early universe. It is thought that during cloud collapse, stars in the GC are formed consistently over only a few million years until the most massive star in the system goes supernova. This event unbinds the remaining gas and blows it out of the system as the gravity of the system is not adequate to prevent gas ejection, effectively quenching star formation (Lin & Murray, 1991; de Grijs, 2001). These stars were formed in the very early stages of the universe (though importantly after the very first metal-free populations III stars) and as such are known as population II stars and are very metal-poor but subsequent younger GCs (such as those of the Magellanic Clouds, Mucciarelli et al. 2023b) can be relatively metal rich. GCs relative isolation (minimal interaction with other star systems or gas clouds due to their location in galaxy halos) since formation means these objects are relics from the very beginning of the universe and are key probes into stellar evolution showing what a “single stellar population” looks like after billions of years of isolated evolution.

Almost all globular clusters are incredibly old (≥ 10 Gyr for Milky-Way GCs, while most GCs are very old, there are some GCs which continue to be formed in major periods of star formation up to this day. e.g. NGC 7251-W3, Fellhauer & Kroupa 2005) and, when left in isolation with no pollution from merging events, metal-poor (Forbes et al., 2018). The Milky Way (MW) GCs can be split into two populations* one metal-poor population usually located outside of the plane of the

*both extremely old

CHAPTER 1

galaxy and a more metal-rich population located in the plane of the galaxy closer to the bulge often known as thick disc GCs (Forbes et al., 2018). The origin of the GCs in the MW is thought to be a mix of ex-situ accreted GC from other dwarf galaxies such as Sagittarius and Canis Major and in-situ GC formation (Forbes & Bridges, 2010; Massari, Koppelman & Helmi, 2019; Shirazi, Khalaj & Haghi, 2023).

The MWs companion dwarf galaxies, the Small and Large Magellanic Clouds (SMC & LMC respectively), are host to populations of GCs of a range of ages, with some being as young as 30 Myr (Sirianni et al., 2002). There is however a “gap” in the ages of GCs in the LMC which is explored in Section 1.2.3.

1.2.1 The Early History of GC Studies

The first observations of a GC were made in 1665 by German astronomer, Abraham Ihle and published 16 years later in Kirch (1681). The observed GC M22[†] (NGC 6656) would not be identified as a globular cluster for another 124 years, in William Herschel’s paper “Catalogue of Second Thousand New Nebulae and Clusters of Stars” (Herschel, 1789), as the term had not yet been coined.

Historically, GCs have been used in many studies, looking at the formation and structure of our galaxy. But, probably most famously is the discovery made in 1918 by Shapley (1918). Using parallax and variable stars to measure the distance to 30 galactic GCs, Shapley (1918) discovered that the solar system is not in the centre of our Galaxy and is, in fact, far from the centre. He was the first to discover that unlike other stellar systems and against predictions, globular clusters did not lie in the plane of the galaxy but were in fact in a ‘halo’ around the Galaxy. It was from the dimensions of the halo that he concluded that the sun was not the centre of the Galaxy. Shapley (1918) states that the “galactic centre lies in Sagittarius” which is

[†]Although it would not be named as such until Charles Messier published his library of nebulae and star clusters in Messier (1771)

CHAPTER 1

where the true centre of our Galaxy is. This was the first of many cases of using globular clusters to probe the formation and structure of galaxies.

1.2.2 Milky Way Globular Clusters

The current number of globular clusters observed in the MW is around 164 according to the database of Milky Way GCs published in Kronberg & Frommert (2019), although more MW GCs continue to be discovered, particularly behind the dust of the galactic plane and centre (e.g. Garro et al. 2020 which used deep near-infrared (IR) images and photometry to see through the dust of the galactic plane and discovered a potential GC with age and metallicity 11.0 ± 1.0 Gyr and $[\text{Fe}/\text{H}] = -0.70 \pm 0.2$ dex). Surdin (1994) states that low luminosity and galactic dust could be “hiding” many GCs and they estimate that 170 ± 8 GCs are actually associated with the MW.

As mentioned before the origin of MW GCs is complex, according to the Λ CDM theory of the universe, a large fraction of the material in the halos of large spiral MW-like galaxies is thought to comprise of accreted material from orbiting dwarf galaxies (Abadi, Navarro & Steinmetz, 2006). For the MW, it is known that accretion from the dwarf galaxies can account for a significant proportion of the GC population (Forbes & Bridges, 2010; Massari, Koppelman & Helmi, 2019; Shirazi, Khalaj & Haghi, 2023). While small galaxies, which are held together by dark matter, will be completely tidally disrupted by these tidal stripping matter accretion events, GCs are self-gravitating without dark matter and survive such events intact. GCs will instead stay gravitationally bound together orbiting its new host galaxy (Forbes & Bridges, 2010). Massari, Koppelman & Helmi (2019) state that only around 40% of MW GCs formed in-situ, 35% were classed as ex-situ with the remaining having a more “heterogeneous” origin. While Shirazi, Khalaj & Haghi (2023) find that of the 154 GCs they studied, only 41 could have come from MW

CHAPTER 1

dwarf galaxy accretion, this value is in agreement with Forbes & Bridges (2010) which state only a quarter of MW GCs could have been accreted from 6-8 dwarf galaxies to create the MW GC system seen today.

1.2.3 Magellanic Clouds

The MW has multiple satellites, prominent among these are the Small and Large Magellanic Clouds (SMC and LMC respectively). These dwarf galaxies are host to many GCs (shown in Figure 2.2 for the WAGGS sample of the SMC GCs). The Magellanic Clouds are located in the southern galactic hemisphere and are the most massive dwarf galaxies in the orbit of the MW (Bekki & Stanimirović, 2009; Graczyk et al., 2013; Pietrzyński et al., 2019; Shipp et al., 2021).

Unlike the MW, the SMC and LMC contain populations of young GCs with ages less than 100 Myr (the youngest being NGC 330 at 30 Myr, Sirianni et al. 2002). However, while the SMC has GCs of all ages from the young (age ≤ 3 Gyr) to intermediate ($3 \text{ Gyr} \leq \text{age} \leq 9 \text{ Gyr}$) to old (age $\geq 9 \text{ Gyr}$), The LMC has very few intermediate-age GCs in what is an apparent age gap (Mackey, 2009).

There is currently no certain cause for the age gap. The star formation rate of the LMC during this time is known to be non-zero (Smecker-Hane et al., 2002; Carrera et al., 2008) indicating that at least some GC formation may have occurred during this time. There have been suggestions that, via tidal interactions beginning 4 Gyr ago, the SMC may have accreted several GCs from the LMC including the intermediate age GCs (Bekki et al., 2004). More recently there has been discovery of some intermediate-age GCs in the LMC (Piatti, 2022) but there is still a lack in their number relative to those of the SMC.

1.2.4 M31 and Extragalactic Globular Clusters

GCs are common in all galaxy types from the smallest of dwarf galaxies to the most massive early-type galaxies. GCs are also present in our neighbour M31. The GC population of M31 hosts GCs of similar ages and metallicities to the MW, however, with a proportion of very young (age ≤ 150 Myr) GCs (Caldwell et al., 2011; Cezario et al., 2013). The MW has bimodality in its metallicity with a metal-poor population in the halo and a more metal-rich in the plane of the disc located more centrally near the bulge. This is due to differences in accreted GCs and GCs formed in-situ (e.g. Muratov & Gnedin 2010; Tonini 2013; Renaud, Agertz & Gieles 2017). M31, however, possesses metallicity ‘tri-modality’, i.e. three peaks in GC metallicity within the same range as the metallicity of MW GCs (Caldwell et al., 2011; Cezario et al., 2013; Caldwell & Romanowsky, 2016). These papers suggest that M31 has a more metal-rich halo than the MW (which is perhaps to be expected given M31’s larger mass). M31’s halo possesses substructures and a metallicity spread which suggest an extended accretion history. M31, generally, has a metal-poor halo much like the MW but accretion events have created a central metal-rich population in the halo (Gilbert et al., 2012, 2014, 2018). Caldwell & Romanowsky (2016) estimate that the number of M31 GCs is 441. This is significantly more than the MW possesses, and is a key reason why M31 is an excellent target for GC studies due to its proximity and richer GC population.

There are similarities in the metallicity distribution of the MW and M31, with the same lower metallicity regions in the halo with higher metallicity in the galaxy plane. As well as this, M31 and MW GCs are generally enhanced in alpha elements (relative to solar abundance, Colucci et al. 2009). This is important as it indicates they underwent similar formation and evolutionary paths and means that there can be a reliable comparison of the measurements of MW GCs from this work (where literature values were measured with resolved star analysis, i.e. Dotter et al. 2010)

CHAPTER 1

to M31 GCs (where literature values were measured using integrated light analysis, i.e. Caldwell et al. 2011).

There are GCs found around all galaxies and are particularly common around early-type galaxies (Harris & van den Bergh, 1981; Harris, 1991; Miller et al., 1998; Côté et al., 2004; Faifer et al., 2011). However, due to their size, observing these objects in detail remains very difficult with modern telescopes (but not impossible). Where in the MW and its orbiting dwarf galaxies individual constituent stars can be observed, in local galaxies like M31, only high-resolution Hubble imagery can detect the brightest constituent stars on the less stellar dense outskirts of these GCs (e.g. Peacock et al. 2018). For GCs even further away, they appear as nothing more than increasingly dim point sources. Nonetheless, with modern technology, we are able to observe these objects and still obtain moderate signal-to-noise ratio (SNR) intermediate-resolution spectra. In this thesis, the spectra of extra-galactic GCs from the GC systems of M31, Centaurus A, M87, and NGC 7252 have been obtained. However for objects at these distances (0.74, 4.04, 15.80, & 57.2 Mpc, Vilardell et al. 2010; Crnojević et al. 2016; Oldham & Auger 2016; Theureau et al. 2007 respectively), the mass of the object needed to make it luminous enough for observation is very large, (Maraston et al., 2004) and overlaps with the masses of more massive objects such as UCDs adding an extra complication in the identification of extra-galactic CSS type.

1.3 Multiple ‘Populations’ in Globular Cluster

Globular Clusters were thought to be examples of single stellar populations due to their simple single-burst formation scenario mentioned earlier. However, observational evidence now suggests that almost all globular clusters contain multiple stellar populations (Bastian & Lardo, 2018). ‘Multiple Populations’ (MPs) are the presence of apparent secondary populations of stars which have different chemical abundances

CHAPTER 1

to the “first” generation of stars. This difference in chemical abundances often presents itself as a population of stars that appear younger (King et al., 2012; Milone et al., 2018; Bastian & Lardo, 2018) (hence ‘secondary’ or ‘multiple’ populations). However, there is no evidence in the vast majority of GCs for later rounds of star formation after the initial burst so this “younger” population are of the same age as the first population.

There are many theories as to the origin of MPs, such as the low-velocity winds coming off diffuse outer layers of massive stars (Kim & Lee, 2018) or ISM pollution coming from black hole accretion disc nucleosynthesis in the cores of these GCs (Breen, 2018) and many others (e.g. Gratton, Sneden & Carretta 2004; Hu & Peng 2008; D’Ercole et al. 2008; de Mink et al. 2009; D’Ercole, D’Antona & Vesperini 2016; Bekki 2017; Milone et al. 2018; Wei et al. 2020). Unfortunately, none currently fully satisfy the exact chemical abundances seen in MPs (as discussed in Bastian & Lardo 2018, Banister 2020, & Milone & Marino 2022). Bastian & Lardo (2018) states that “The evidence that each GC has its own specific pattern of MPs calls for a high degree of variety (or stochasticity) that must be taken into account when proposing MP formation mechanisms”. It is possible that each GC system, which exhibits MPs, relies on the mechanisms cited here in different proportions and the resulting populations of stars are the result of a combination of many complex mechanisms. Due to the difference in cluster-to-cluster chemical abundances (Bastian & Lardo, 2018), the proportion of each mechanism may be directly related to the properties of the original gas cloud and initial mass function (IMF) for each GC individually.

1.3.1 Specific Chemical Abundance Anomalies

It has been mentioned that MPs exist and that their source is still uncertain. In this section, we will delve into the specific chemical abundance anomalies present in MPs. There are several key relations and anti-correlations between individual

CHAPTER 1

elements which are the specific signatures of a secondary population.

Galactic halo GCs have long been known to be alpha (O, Ne, Mg, Si, S, and Ca) enhanced (e.g. Salaris, Chieffi & Straniero (1993) found that fitting alpha-enhanced isochrones to colour-magnitude diagrams (CMD) provided better fits indicating that the GCs are enhanced in alpha elements). However, this is not a sign of multiple populations. Alpha element abundances are almost universal amongst the stars within a GC and do not show populations with anomalous abundances.

The main MP abundance anomalies are in He, N, C, Na, & O with there being strong anti-correlations between nitrogen and carbon[‡] and between sodium and oxygen with a positive correlation between nitrogen and sodium (Bastian & Lardo, 2018; Milone & Marino, 2022). There is also an anti-correlation between Mg and Al (Bastian & Lardo, 2018; Milone & Marino, 2022). However, Al overabundance is not common in every GC with MPs, and therefore cannot be used as a universal indicator for the presence of MPs. Similarly to Al and Mg, there are also occasional abundance variations in Si, and K and, in fact, in most light elements (Carretta, 2021; Milone & Marino, 2022).

These abundance anomalies are less obvious at lower metallicities due to there simply being less of that element to influence the light. However, Mészáros et al. (2015) states that as metallicity decreases, the spread in Al abundances in the populations of GCs increases. Which makes Al a useful candidate for the observation of MPs at low metallicities. However, there are no strong Al features available in low and intermediate resolution integrated light spectra, so Al is of limited use except for high resolution star-by-star studies. In Banister (2020) it was found that even at intermediate-low metallicities ($[\text{Fe}/\text{H}] \sim -1.5$) the presence of enriched nitrogen can still be observed in the integrated light spectra via index measurement and full spectral fitting, hence N abundance may provide an interesting probe of abundance

[‡]meaning as nitrogen is enriched, carbon is depleted

CHAPTER 1

anomalies in integrated light spectroscopy.

1.3.2 Genuine Secondary Populations

A handful of GCs have even been found to show spreads in the abundances of heavy elements such as Fe (Bastian & Lardo, 2018; Milone & Marino, 2022). Ω Cen (NGC 5139) is a good example of this, where there are genuine secondary populations of stars in the cluster (Villanova et al., 2014). This is due to the fact that it is believed to be formed by the tidal stripping of a nucleus from a dwarf galaxy (Fellhauer, 2004). Later in this thesis, Section 5.5.1 will examine whether evidence for this metallicity spread can be found using analysis of the integrated light spectrum.

MPs are thought to only exist in GCs of ages $\gtrsim 2$ Gyr (Bastian & Lardo, 2018). While this is generally the case, Mackey & Broby Nielsen (2007) found the presence of a double main sequence turn-off (MSTO) in the 1.7 Gyr (Goudfrooij et al., 2014) GC NGC 1846. The double MSTO is indicative of MPs in older GCs. Goudfrooij et al. (2014) found that an extended MSTO that is wider than can be accounted for by simple stellar population models is also present in all their sample of 18 intermediate-young (1-2 Gyr) GCs. The extended MSTOs had spreads in the range of 200-550 Myr which for young GCs, is a significant proportion of their lives. This is misleading however as the extended MSTO is likely caused by an extended period of star formation, indicating actual secondary populations of stars not star-to-star chemical variations imitating a secondary population.

1.4 Ultra-Compact Dwarf Galaxies

At the dawn of the millennium, a new class of stellar system was discovered which covered the previously empty region between GCs and dwarf galaxies in the mass-radius domain (Figure 1.1). The low mass ($M_* \geq 10^6 - 10^8 M_\odot$, Janz et al. 2016) end of

CHAPTER 1

the discovered new objects were the Ultra-Compact Dwarf galaxies (Hilker et al., 1999; Drinkwater et al., 2000, 2003).

UCDs can have radii equivalent to many GCs at $r_e \sim 5$ pc but can also be much larger with an upper limit of $r_e \sim 100$ pc (Norris et al., 2014). Their masses are in general, however, much larger than GCs and this can lead to substantial stellar densities (Fellhauer & Kroupa, 2002; Norris et al., 2014; Goodman & Bekki, 2018).

There are many formation scenarios currently debated, but a consensus has been reached that they are a composite population formed in at least two ways. One way is that they are the result of the tidal stripping of dwarf galaxies and all that remains is the stellar dense, central nucleus (e.g. Oh, Lin & Aarseth 1995; Bekki, Couch & Drinkwater 2001; Bekki et al. 2003; Drinkwater et al. 2003; Goerdts et al. 2008; Pfeffer & Baumgardt 2013; Mayes 2019; Mayes et al. 2021). Another formation path is that they are simply the result of the high mass end of globular cluster formation (e.g. Mieske, Hilker & Infante 2002; Forbes et al. 2008; Murray 2009; Dabringhausen, Kroupa & Baumgardt 2009; Chiboucas et al. 2011; Mieske, Hilker & Misgeld 2012; Renaud, Bournaud & Duc 2015; Goodman & Bekki 2018). These two leading theories are both likely and would predict a split in some of the properties of these UCDs, potentially making it possible to isolate their formation scenario. The recent discovery of SMBHs in the cores of some of these UCDs (Seth et al., 2014; Ahn et al., 2017) indicates that these UCDs formed via tidal stripping and identifying differing signatures between known high mass GC type UCDs and UCDs formed via tidal stripping via spectra would be a logical next step to further classifying these objects. This can be achieved by the detection of a SMBH, or an extended star formation history indicating a more massive history for that object. It may be possible to detect the chemical signatures of the MPs of GCs in UCDs formed via the high mass end of GC formation, and detection of metallicity spreads similar to Ω Cen may also indicate a stripped nuclei formation history. These are

the formation signatures that will be explored in this thesis.

1.5 Nuclear Star Clusters

Nuclear Star Clusters (NSCs) are the most stellar dense objects in the universe (Schödel, Merritt & Eckart, 2009). Located near the centre of their host galaxies, they can range in sizes equivalent to GCs ($0.4 \text{ pc} \leq r_e \leq 40 \text{ pc}$, Norris et al. 2014; Neumayer, Seth & Böker 2020, with Norris et al. (2014) stating that most NSC are smaller than $R_e \sim 10 \text{ pc}$) all the way to massive UCDs with masses in the range $M_* \geq 10^4 - 10^8 M_\odot$ (Norris et al., 2014; Fahrion et al., 2022).

NSCs were, likewise to UCDs, first identified at the turn of the millennium to the mid-2000s (Phillips et al., 1996; Carollo, Stiavelli & Mack, 1998; Matthews et al., 1999; Côté et al., 2006). Their formation scenarios are also not fully clear, however, there are a few leading theories. Fahrion et al. (2022) states that most low-mass NSC are the result of GCs which have inspiralled into the stellar dense cores of large galaxies via dynamical friction (i.e the origin of metal-rich GCs in the plane of the galaxy mentioned previously) which have then merged together in collision events (e.g. Tremaine, Ostriker & Spitzer 1975; Capuzzo-Dolcetta 1993; Capuzzo-Dolcetta & Miocchi 2008; Agarwal & Milosavljević 2011; Portaluri et al. 2013; Antonini 2013; Arca-Sedda & Capuzzo-Dolcetta 2014; Gnedin, Ostriker & Tremaine 2014). This can explain metal-poor NSCs as GCs which have fallen into the central regions of their galaxies are usually much more metal-poor than the surrounding environment they find themselves in (if still more metal-rich than their halo counterparts). The other commonly accepted formation scenario for NSCs is that NSC form via in-situ star formation from gas in the cores of their host galaxy (e.g. Loose, Kruegel & Tutukov 1982; Milosavljević 2004; Bekki, Couch & Shioya 2006; Bekki 2007; Antonini, Barausse & Silk 2015). This formation scenario fits better for the younger and more metal-rich NSCs.

1.6 Compact Elliptical Galaxies

As stated earlier, at the turn of the century, the mass and size gap between star clusters and dwarf galaxies was bridged by the discovery of intermediate-mass compact stellar systems. They were the compact elliptical galaxies (cEs) which were thought to be rare, but which have now been found in increasing numbers (e.g. Mieske et al. 2005; Chilingarian et al. 2007, 2009; Smith Castelli et al. 2008; Price et al. 2009; Norris et al. 2014; Chilingarian & Zolotukhin 2015). cEs typically have masses in the range $M_* \geq 10^8 M_\odot$ and effective radii in the range of $\sim 100 \text{ pc} \leq r_e \leq 600 \text{ pc}$ (Norris et al., 2014; Janz et al., 2016). They are generally intermediate - old and possess a high metallicity (Norris et al., 2014).

The formation process of such objects is still a long-standing problem with multiple possible mechanisms also under consideration for these objects. Papers like Huxor et al. (2011b); Paudel et al. (2013); Janz et al. (2016) state that some are the result of the tidal stripping of galaxies with the bulges of these galaxies being all that remains after the stripping. The reasoning for this is the observed presence of cEs in tidal streams accreting onto galaxies (Huxor et al., 2011a; Deeley et al., 2023). This is the same (higher mass) formation mechanism as the stripped formation UCDs where UCDs were nuclear star clusters and cEs are the more massive galactic bulges stripped of their host galaxies.

Another formation avenue is presented in Du et al. (2019). Here they state that cEs are the result of a low-mass gas-rich galaxy on a highly radial orbit of a much more massive galaxy passing through the corona of the host galaxy. As the cE candidate passes through the gaseous corona (Chevalier & Oegerle, 1979), the gas on the outskirts of the cE candidate gets stripped away. However, due to a burst of star formation, the compactness of the smaller galaxy increases rapidly. The gas produced by stellar winds and supernovae is confined (by the ram pressure of the interaction between the proto-cE and the inter-galactic medium) to the centre of the

CHAPTER 1

smaller galaxy causing subsequent bursts of metal-rich star formation resulting in the formation of a stellar dense compact elliptical galaxy. It has also been suggested that cEs are the low-mass local descendants of so-called ‘red nuggets’ (van der Wel et al., 2014; Zolotov et al., 2015; Janz et al., 2016; Kang & Lee, 2021; Costantin, 2022) providing yet another formation scenario for these complex CSSs.

Modern studies have found overlap between the most massive UCDs and least massive cEs (Norris et al., 2014; Janz et al., 2016). This is likely due to their formation being opposite mass ends of the same formation mechanism. The difference in spectroscopic abundances between UCDs (those formed as stripped nuclei of larger galaxies) and cEs (potentially formed as stripped bulges) may be key in further providing a more physically motivated classification for the two compact stellar systems.

This section has looked at many types of CSS, now we will explore the different methods utilised to observe these objects.

1.7 Photometry

One form of CSS analysis is individual resolved star photometry. Simply put, photometry is the observation and magnitude measurement of an object in a specific wavelength range using a specific passband filter. For CSSs observation of the individual constituent stars is useful for the creation of CMD diagrams, e.g. Figure 1.2. For example, the MSTO has long been used to determine age of a stellar population such as globular clusters where the stars all formed at the same time and therefore should represent an initial mass function (IMF) evolved along an isochrone matching the clusters’ age. What can be seen in Figure 1.2 is another use for the photometric study of GCs, UV CMDs can be used to identify the presence of multiple populations. Here, this is identified by splits in the main sequence, the sub giant branch (SGB) and red giant branch (RGB).

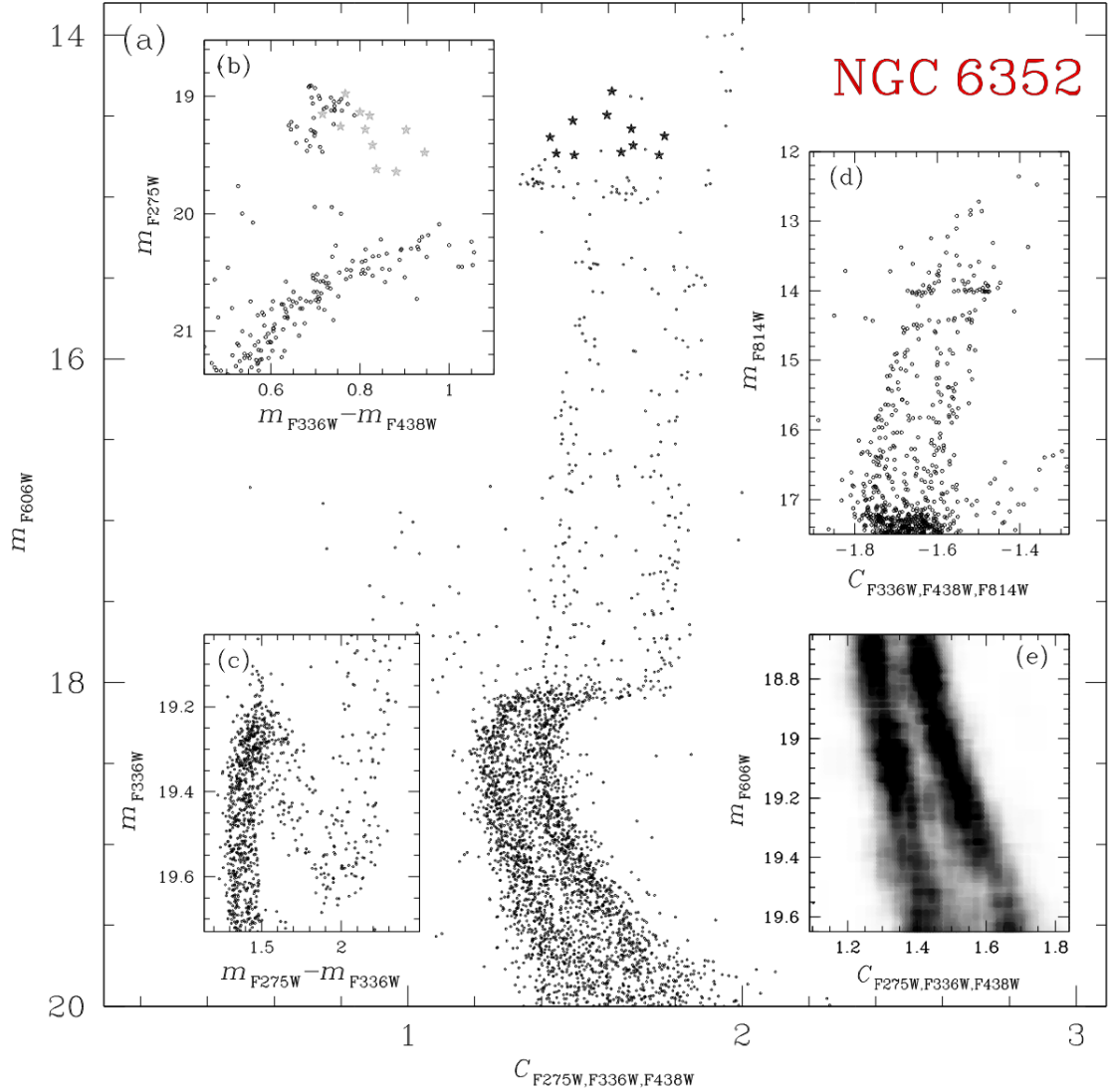


Figure 1.2: Figure 2 of Nardiello et al. (2015). This figure shows the CMD of NGC 6352. Shown in each sub figure are the differences seen in the separate populations. (a) shows the full CMD of m_{F606W} versus $C_{F275W, F336W, F438W}$, (b) shows the horizontal branch, (c) shows the population split in the sub giant branch, (d) shows a split in the red giant branch and (e) shows a Hess diagram of the main sequence of (a) highlighting the double main sequence.

Photometry is a powerful tool, however, it is unable to look at chemical abundances in as much detail as spectroscopy (Section 1.8). In addition, for distant objects where

CHAPTER 1

individual stars cannot be resolved, integrated light observations must be used. For this purpose, modern spectroscopy can offer high resolution, high SNR spectra of GCs where analysis of this data can potentially identify the presence of MPs in the integrated light of the cluster (Banister, 2020).

1.8 Spectroscopy

Spectroscopy is the splitting of light to separate its different wavelengths resulting in a spectrum intensity as a function of wavelength. In a sense photometry is simply the low spectral resolution limit of spectroscopy. It is an incredibly powerful tool for astronomical observations and can be used on any object from individual stars to full galaxies in the form of integrated light spectra.

1.8.1 Spectrographs

There are a few types of spectrograph, shown in Figure 1.3 is a spectrograph which uses a surface relief grating. This type of grating uses microscopic grooves in a reflective surface to reflect the different wavelengths of incident light to different diffraction angles based on the equation:

$$d(\sin\alpha + \sin\beta) = n\lambda \tag{1.1}$$

Where d is the grating spacing, α is the incident angle, β is the diffraction angle, λ is the wavelength and n is the diffraction order. $n = 1$ is the first order diffraction, $n = 2$ is second order and so on.

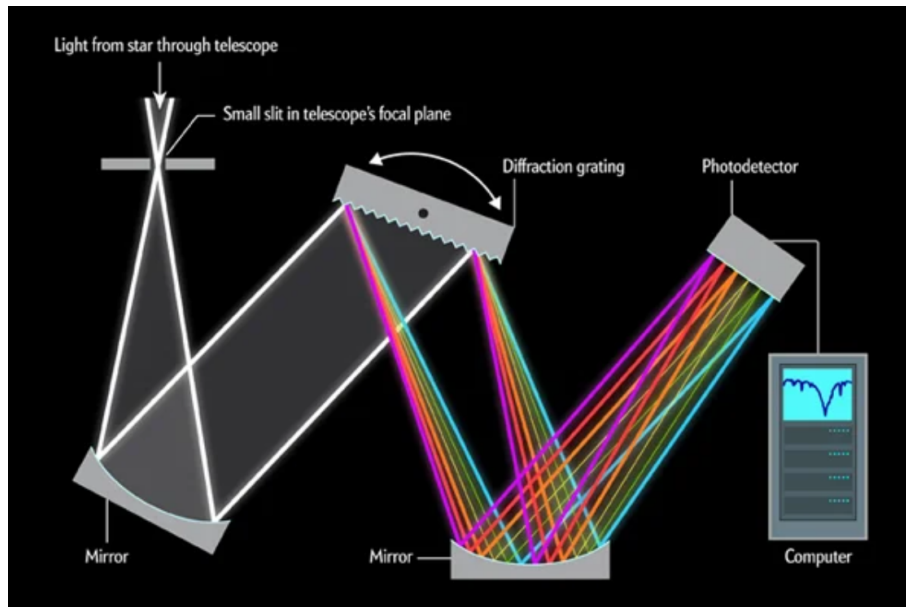


Figure 1.3: A simple diagram of a surface relief grating in a spectrograph splitting incoming light into its spectrum. Taken online from: Retseck (2012).

Other types of grating are transmission gratings, these work in a very similar way to reflective gratings (following the same diffraction equation as Equation [1.1]) but the angle of diffraction is on the other side of the plane as the light passes through the grating. Volume Phase Holographic Gratings (VPH Gratings) use a near sinusoidal change in refractive index in the transmissive medium (typically gelatin) which is then encased within a substrate material. They are almost exclusively used in astronomy for moderate-resolution spectroscopy due to higher diffraction efficiencies, they can have typical line densities in the order of 300-6000 lines/mm (where ruled gratings typically have line limits of 1200 lines/mm) resulting in higher resolution spectra (Barden et al., 2000; Baldry, Bland-Hawthorn & Robertson, 2004; Barkhouser, Arns & Gunn, 2014)

For higher resolution spectra over a broad range, astronomers may turn to Echelle spectrographs such as X-Shooter (Vernet et al., 2011). Echelle spectrographs use high orders of refraction (in the range of $n = 50 - 150$) which reflect light at high

CHAPTER 1

angles. They often use reflection diffraction gratings and due to the high diffraction orders, they use the ‘short’ side of the grating leading to higher diffraction angles. When using multiple, high, diffraction orders there will be overlapping wavelengths. For example, the wavelength 8000 \AA in n order 71 may fall on top of 4000 \AA light in diffraction order $n = 100$. Echelle spectrographs use two diffraction gratings to disperse light into two orthogonal angles which separate the different diffraction orders (Figure 1.4) separating the wavelength overlap into a 2-dimensional ladder ‘echelle’ (in French) structure and so, allowing high-resolution spectra within wide bandpasses.

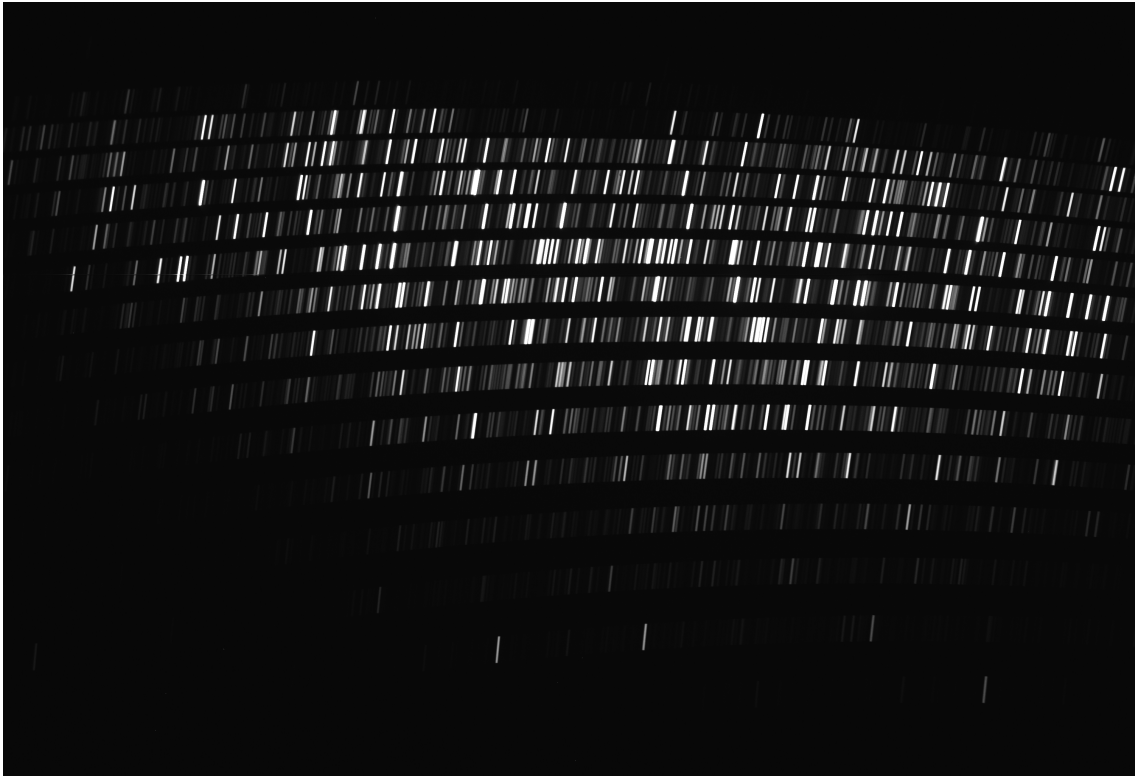


Figure 1.4: An Arc spectrum from the X-Shooter Spectrograph, From Puzia (2011) survey available on the ESO archive

1.8.2 Integrated Light Spectra

Integrated light spectroscopy is the combination of all of the light of an object or region of space into a single summed spectrum. It is a powerful tool for examining stellar populations which are too distant to have individually resolvable constituent stars.

Previously, it has been shown how integrated light spectra can be used to detect the presence of multiple chemically distinct stellar populations in GCs (e.g. Banister 2020) even where the individual stars are unresolved. This was done by comparing the GC spectra to libraries of single stellar population models and where discrepancies between the two spectra existed, the presence of chemical complexity[§] could be inferred. Later in this thesis, it is investigated if the abundance variations seen in GCs can be identified more widely in other stellar populations and if they be can used as signatures of GC-like formation.

Modern spectrographs, such as MODS (Pogge et al., 2010), X-Shooter (Vernet et al., 2011), MUSE (Bacon et al., 2010) and WiFeS are producing large samples of high signal to noise and high-resolution spectra of compact stellar systems for the first time, allowing investigation of the stellar populations and chemical enrichment histories in a greater detail than ever before.

1.8.3 Integrated Light Spectroscopy Types

There are a few different methods of integrated light spectroscopy which can be used and offer different benefits over each other.

Long Slit Spectroscopy

This is a simple form of spectroscopy. It involves aligning the slit of the spectroscope over the object and allowing the slit of light to intercept the grating. The result is

[§]relative to the SSP models

CHAPTER 1

a two-dimensional spectrum with wavelength along one axis with the other being a spatial axis.

While long-slit spectroscopy is a very useful tool, it can only look at a region of space within the width and length of the slit used. In order to look at a wider region of space, other methods need to be employed.

Drift Scanning Spectroscopy

This method is similar to the single long-slit method of spectroscopy in that it uses just a single slit. However, by turning off tracking or deliberately moving the slit relative to the sidereal motion, this method allows the object to “drift” across the aperture. The main reason why this is advantageous is that one does not need a specialist wide-field spectrograph to see spatially larger objects and can be done with any spectrograph attached to a suitable telescope.

Drift scanning is a versatile technique that can be used on both distant and near objects. It does, however, have drawbacks. Light from other objects and field stars may pollute the spectrum. Surveys which use drift scanning (such as Kim et al. 2016) will often look at just the cores of compact objects and repeat observations at an orthogonal angle to reduce the number of field stars contaminating the light. This comes with its own problems where only observing the cores of GCs can introduce visible spectral effects from poor sampling of the cluster due to the stochastic distribution of stars within GCs. There is a balance between poor sampling of the stellar environment of an object and the percentage of field star contamination in the spectrum which has been a constant problem in the observation of compact stellar systems.

Integral-Field Spectroscopy

Integral-field Unit (IFU) spectroscopy is the simultaneous observation of a wide field of the sky. They can analyse a 2-dimensional region of the sky at a single time. IFU spectrographs are very versatile. They can cover a large area of the sky (depending on design) and can be used to create integrated light spectra of a single object, multiple independent regions of an object simultaneously, or used to look at multiple objects in the same field.

Two types of IFUs are the image slicer and the fibre bundle types. Image slicers use multiple slits with a long spatial axis allowing multiple objects per slit and allowing for observation in the spatial axis perpendicular to the slit direction. This allows the spectrograph to observe the full field of view with a single spectrum coming from each slit (i.e. WAGGS Usher et al. 2017).

Another type of IFU is the fibre bundle IFU. This type often uses an array of “microlenses” (e.g. VIMOS, Le Fèvre et al. 2003) which cover a large FoV on the sky to direct light from different regions into a fibre bundle where each fibre corresponds to a spatial position. The light from each fibre is then passed through a spectrograph.

The local GC data obtained for this project comes from the image slicer IFU spectrograph WAGGS (Usher et al., 2017) which provided very high SNR, optical spectra at intermediate resolution.

1.9 Summary

The study of compact stellar systems is a complex field of astronomy where CSSs’ formation and chemical behaviour are still not fully understood. One aim of this project is to assess how well current techniques can obtain apparently basic information such as age, metallicity and alpha abundance of these supposedly simple objects via

CHAPTER 1

their integrated light spectra. The integrated light spectra is used because only the closest CSSs have resolvable constituent stars, however, these nearby objects whose basic parameters are known (from photometric studies) make ideal candidates for the testing of the analysis methods adopted and developed for this project. As well as this, later, this thesis will probe the chemical abundances and specific properties of CSSs which may make them, as a class, poorly suited to comparison with simple population models.

This Chapter has introduced the CSSs that will be analysed in this project and the techniques that are available for their observation. The next Chapter, will look at what data is available and dive into the SSP models available for the analysis of these objects.

Chapter 2

Data & Data Reduction

2.1 Introduction

This thesis assembles an unprecedented catalogue of spectroscopy of compact stellar systems which will be made available to the wider community. This Chapter will outline each source of data, the objects provided, their parameters (resolution wavelength range etc) and what data reductions need to be taken to prepare the data for analysis.

There exists, already, many published surveys of compact stellar systems. Here are listed the sources of the CSS data that was available for use in this project. There is data in the sample which is not used in this project as they do not provide spectra (only indices) and only contribute a handful of objects. However, this data is made available for further research with the goal of repeating the analysis presented here on larger and larger samples as the database increases in size.

2.2 WiFeS Atlas of Galactic Globular Cluster Survey

Globular clusters are the oldest stellar systems in the universe with many in the local galactic systems having survived since the earliest period of galaxy formation. The WiFeS Atlas of Galactic Globular Cluster Survey (WAGGS) aimed to provide high-resolution high signal-to-noise integrated light spectra of a large set of local GCs (Usher et al., 2017). This data is prominently used in this project and as such, further detail on this source of data than other sources is given.

2.2.1 Instrumentation

Usher et al. (2017) used the WiFeS Integral Field Spectrograph (WiFeS from here) on the Australian National University Telescope (ANU 2.3m) at Siding Spring Observatory. WiFeS covers an area of sky 38×25 arcsec in size. The spectrograph consists of 25 slitlets that are 1 arcsecond wide and 38 arcseconds long covering the wavelength range 3300-9000 Å.

The WiFeS Spectrograph is designed to simultaneously observe 25 spectra at the same time from each slit which will then be combined to an integral field value in the reduction pipeline (PyWiFeS Childress et al. (2014)). The spectrograph's design is similar to its predecessor the Duel-Beam Spectrograph (DBS) Rodgers, Conroy & Bloxham (1988) but is capable of a much higher resolution. WiFeS is split into 6 different gratings U7000, B7000, R7000, I7000, B3000 and R3000. The resolutions and wavelength ranges of these gratings are listed in Table 2.1. The gratings used for the WAGGS survey were the R = 7000 gratings (U,B,R,I), however, the actual resolution of the data published by Usher was closer to R = 6800. Since there was no individual resolution data for each GC and sky spectra where emission lines can be measured to confirm the published value, the R-value of 6800 was used as the instrumental resolution of all of the WAGGS data.

CHAPTER 2

Table 2.1: The resolution and wavelength ranges of the WiFeS gratings.

Grating	Resolution	Wavelength minimum (\AA)	Wavelength maximum (\AA)
U7000	7000	3290	4380
B7000	7000	4180	5580
R7000	7000	5290	7060
I7000	7000	6830	9100
B3000	3000	3200	5900
R3000	3000	5300	9800

There is significant overlap between the gratings used in the survey allowing for a continuous spectrum from $\min\lambda$ to $\max\lambda$ with reduced noise in the overlapping regions due to the grating combination method described Section 2.2.4.

2.2.2 Cluster Selection

The data set consists of 86 GCs from the Milky Way the Small and Large Magellanic Clouds and the Fornax dwarf galaxy. Figure 2.1 shows the age-metallicity distribution of the selected globular clusters.

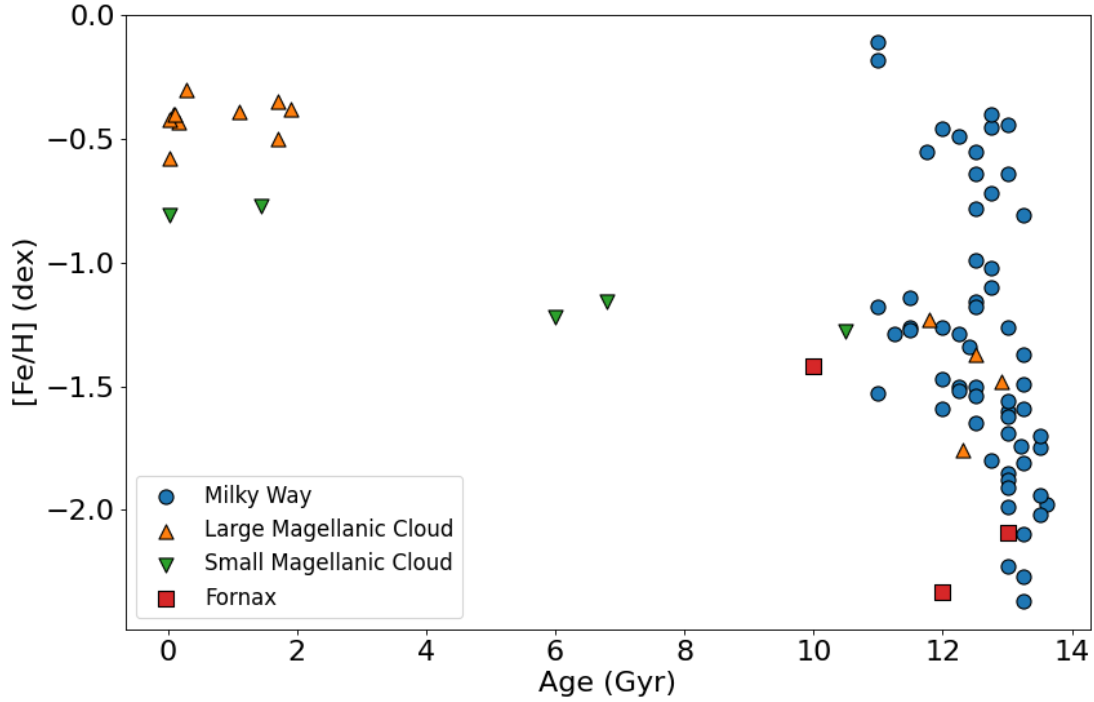


Figure 2.1: Age against $[\text{Fe}/\text{H}]$ for the GCs in the WAGGS sample (Usher et al., 2017, 2019a).

The full table of WAGGS GCs can be found in Tables A.1 & A.2. The survey consists of 64 Milky Way GCs, 5 & 14 GCs from the Small and Large Magellanic Clouds respectively and 3 GCs from Fornax. They range in age from GCs such as NGC 330 (SMC) and NGC 2136 (LMC) which have ages of 30 and 100 Myr, respectively (Sirianni et al., 2002; Niederhofer et al., 2015) to GCs like NGC 5694 at ~ 13.6 Gyr old (De Angeli et al., 2005).

What defines a GC and where they transition to more massive types of CSS is still up for debate (Chilingarian, Cayatte & Bergond, 2008; Hilker, 2009; Gratton et al., 2019). Therefore Usher et al. (2017) chose a sample with ages, metallicities, sizes and masses representative of the range of GCs in the local galactic environment. Milky Way globular clusters are all old and mostly metal-poor (with the exception of a few GCs in the bulge). As stated before, the sample of Milky Way GCs was

CHAPTER 2

supplemented by a number of GCs from the Milky Way’s satellite galaxies. This was in order to increase the age and metallicity range of the sample so that young and intermediate metal-rich globular clusters could also be sampled. Usher et al. (2017) chose 3 old GCs from the Fornax dwarf galaxy. From the SMC (Figure 2.2) they chose 1 old, 2 young GCs (age < 2 Gyr) and 2 GCs of intermediate age (2 Gyr < Age < 10 Gyr). From the LMC they chose 4 old GCs and 10 young GCs. As Figure 2.1 demonstrates, there are significant gaps in the age coverage of the sample. There are only two intermediate age GCs meaning there is effectively a gap of over 9 Gyr in the sample. Why there is a gap in the ages (specifically in the LMC) is discussed in Section 1.2.3.

It should be stated that WAGGS “favoured GCs with a higher central surface brightness in order to maximise observation time” (Usher et al., 2017). They could get a larger sample if they chose the brighter objects, as this would reduce the observation time needed to obtain a satisfactory SNR for each object. This is a common issue in observational projects but the result of this is that the sample is biased towards the more massive GCs with lower mass GCs having less representation.

Dynamical masses were not available for all GCs in the sample. Therefore WAGGS calculated the mass of the globular clusters based on their extinction-corrected V-band absolute magnitudes by using a constant $M/L_V = 2$ for the GCs that were older than 10 Gyr. For the younger GCs, they used the mass-to-light ratios described in McLaughlin & van der Marel (2005) and Bruzual & Charlot (2003). Having only higher mass GCs does, however, help to ameliorate the problem of stochastic sampling of the IMF, which is an issue in lower mass stellar clusters (da Silva, Fumagalli & Krumholz, 2012; Hannon et al., 2019; Stanway & Eldridge, 2023).

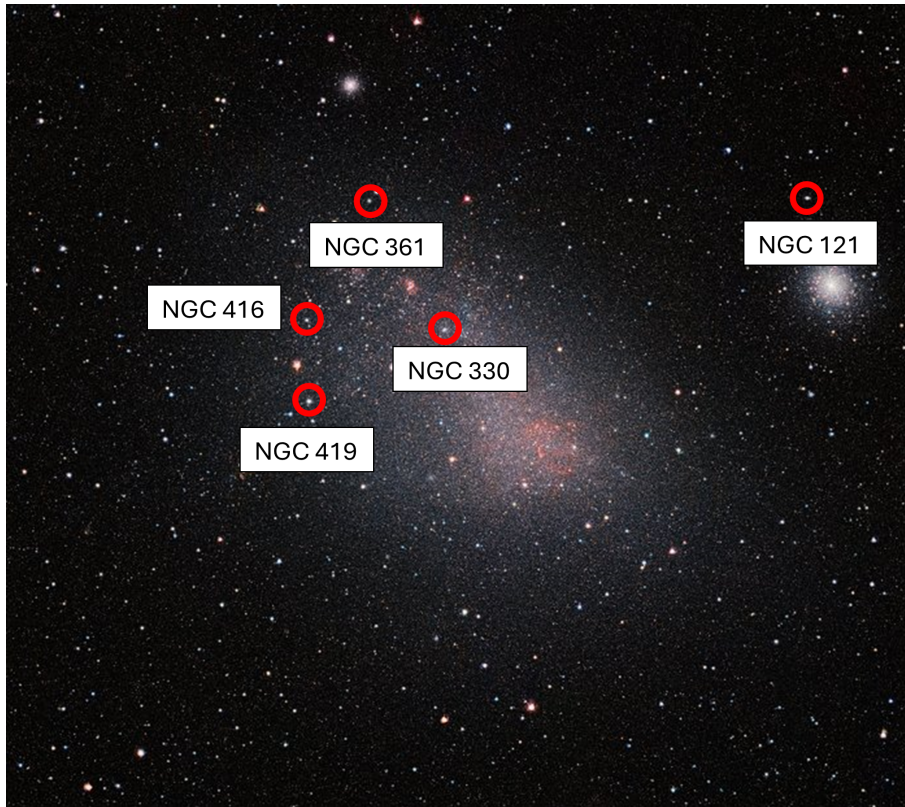


Figure 2.2: The selected WAGGS GCs from the SMC highlighted on an image taken using ESO's VISTA (Visible and Infrared Survey Telescope for Astronomy) telescope (ESO/VISTA, 2017).

2.2.3 Observations

The spectra were obtained by observing a single central pointing for each globular cluster using the 38×25 arcsecond field to cover as much of the GC as possible (Figure 2.3). Because of the variable distances and physical extent of the GCs, the amount of light captured by the single WiFES pointing varied from cluster to cluster. This is shown in Figure 2.3 where three globular clusters are shown with varying distances. The plot shows how the vast majority of the stars in Fornax 3, lie within the WiFES field. For GCs with large effective radii that are relatively close such as NGC 6121 with a heliocentric distance of 2.2 kpc (as opposed to Fornax 3s

CHAPTER 2

heliocentric distance of 137 kpc), Figure 2.3 shows how only the very centre of the GCs core is in the field. Poor luminosity fraction observation is demonstrated in Figure 2.4 where the observed luminosity fraction within the WiFeS field ranges from 0.005 for NGC 5139 up to 0.81 for the GC Fornax 4, with a median V-band light fraction of 0.19 for all WAGGS objects and just 0.12 for the Milky Way globular clusters alone. Figure 2.4 also shows the ratios of the core radius and half-light radius to the equivalent radius of the WiFeS field of view (17.4 arcsec) showing that most WAGGS observations of MW GCs fail to cover even the full core region.

There can be considerable effects on the spectra due to small field-of-views when taking integrated light exposures. The smaller observed light fraction may not be large enough to reduce the stochastic sampling of bright stars within the cluster to an acceptable level. This could mean the observed integrated light spectrum of a GC may not fairly sample the whole stellar population of the cluster.

CHAPTER 2

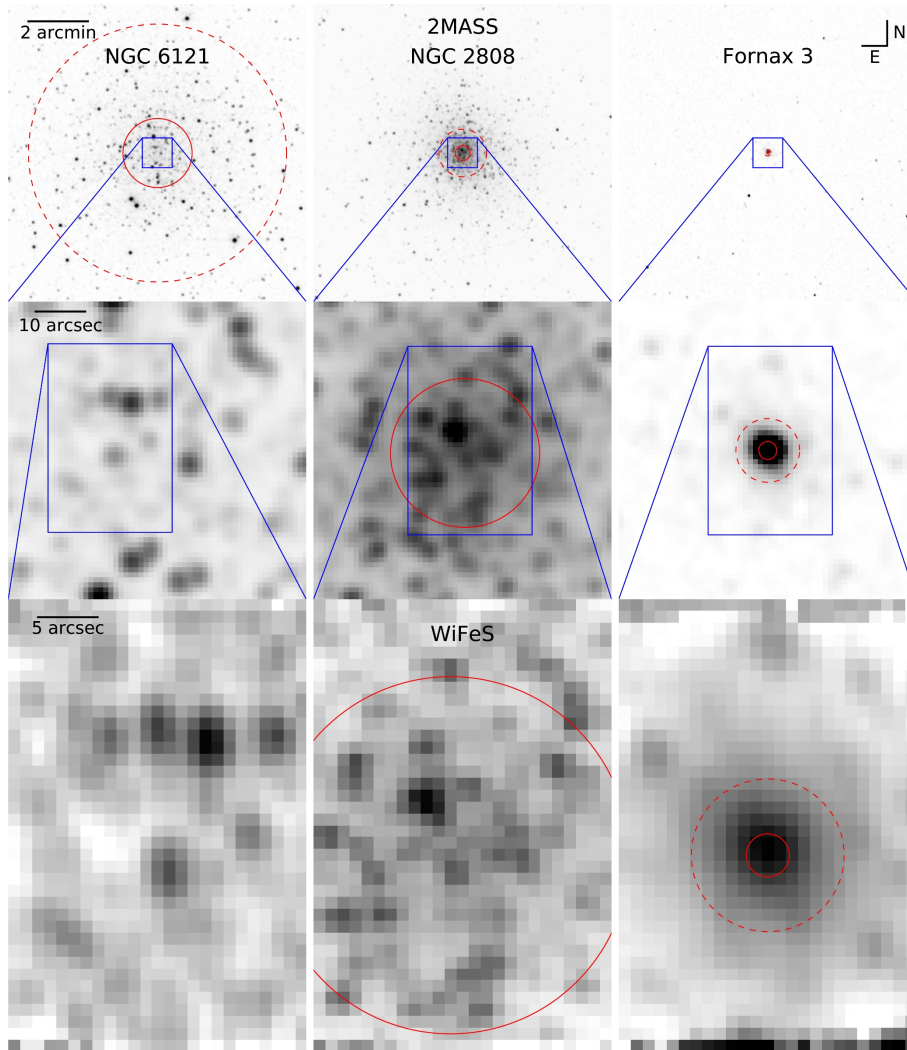


Figure 2.3: Field-of-view of the WAGGS observations for 3 GCs. Fornax 3 (right), NGC 2808 (middle) and NGC 6121 (left). This plot is Figure 2 from the first WAGGS paper (Usher et al., 2017) and shows the field-of-view of the WiFeS spectrograph in the bottom row of images. The dashed red line shows the half-light radius while the solid red line shows the core radius of the GC. The blue lines are the footprints of the preceding image.

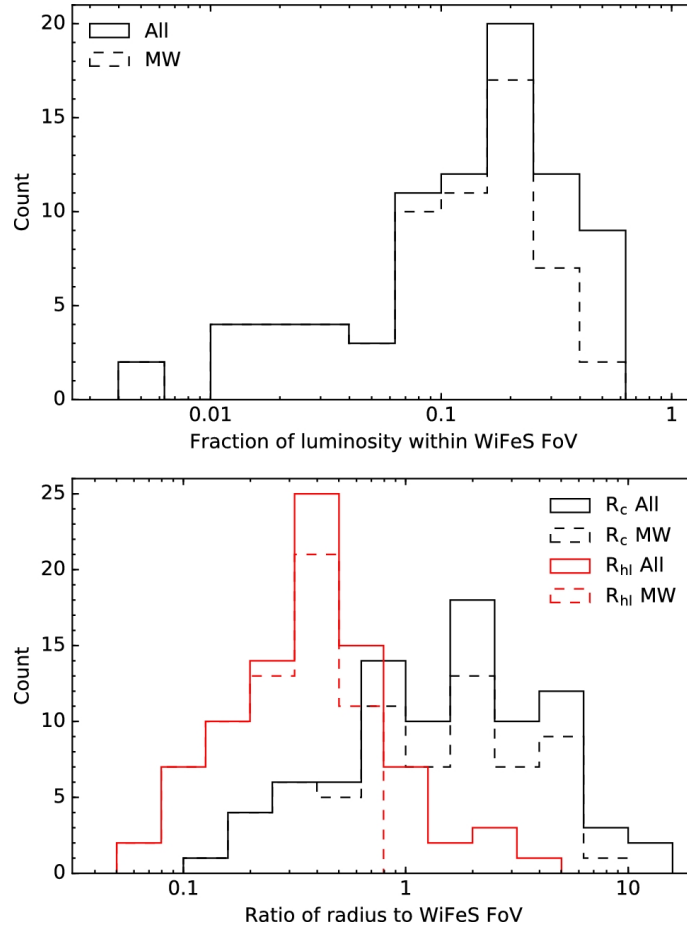


Figure 2.4: The upper plot shows the fraction of the V-band luminosity in the WiFeS field-of-view compared to the full V-band luminosity of the GC. The dashed line represents Milky Way GCs while the solid line represents the full sample of GCs. The lower plot shows the ratio of the core radius (black) and half light radius (red) of the GC inside the WiFeS FoV. These plots are Figure 3 from Usher et al. (2017).

GCs are affected by mass segregation (Fregeau et al., 2002; Baumgardt, De Marchi & Kroupa, 2008; Baumgardt et al., 2022), meaning the most massive stars have “sunk” to the core of the cluster and now dominate the light from that region. As well as this, the distribution of secondary population (MP) stars can vary with radius (Larsen et al., 2015) leading to radial gradients of chemical abundances in the GCs which may not be fully sampled by just core observation. However, an upside

CHAPTER 2

to studying closer objects is that there is a lower proportion of non-population stars (i.e. interloping fore or background stars from the host galaxy) within the field. It should also be said that previous integrated light studies of globular clusters have been limited to cores of GCs (e.g. Puzia et al. 2002; Schiavon et al. 2005; Colucci, Bernstein & McWilliam 2017) so this is not unusual.

Usher et al. (2017) discuss the stellar sampling of the GCs in the survey. They state that while some nearby GCs show poor stellar sampling, most globular clusters showed good sampling with the paper using NGC 2808 as an example GC. NGC 2808 has a distance close to the median value of the WAGGS objects and was fairly well sampled as is shown in Figure 2.5. Meaning that while the closest GCs may not be well sampled and will not represent the full cluster population, most of the GCs in the sample are well sampled enough to accurately represent the stellar population of the GC. To maintain as large a sample as possible, in this project the effects due to stochastic distribution and small fields-of-view have been assumed to be minimal.

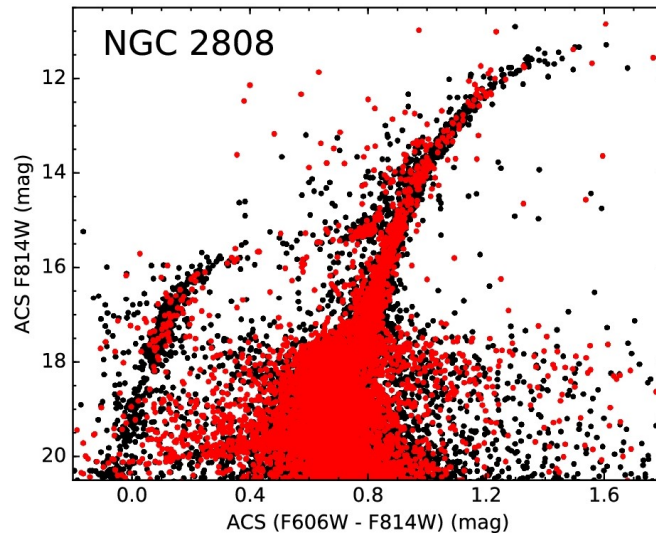


Figure 2.5: Figure from Usher et al. (2017): showing the CMD of NGC 2808 using ACS Globular Cluster Treasury Survey (Anderson et al., 2008) data. The black points show the stars of the GC while the red points show the stars in the WAGGS sample.

CHAPTER 2

The total stellar mass in each cluster and the mass in the WiFeS field-of-view are available in Table A.2 with the literature values for mass coming from a variety of sources in the supplementary files of Usher et al. (2019a) (listed with Table A.2). Usher et al. (2017) state that the mass in the field is calculated from the surface brightness profile (as mentioned earlier) and the luminosity in the WiFeS field-of-view is calculated by integrating the surface brightness profiles which were calculated from the structural parameters given in Table 1 of that paper.

Integral-field (IFU) spectroscopy is preferable, however, to methods such as drift scanning as wide-field IFUs tend to have increased signal-to-noise values for the same exposure time. The signal-to-noise values of the WAGGS data (Table 2.2) show how for high-resolution spectra, the WAGGS survey has achieved high signal-to-noise for much of their sample allowing for detailed chemical abundance measurements.

Table 2.2: Signal to noise ratios of the WAGGS data.

Grating ⁽¹⁾	λ_{min} ⁽²⁾	λ_{max} ⁽³⁾	SNR_{min} ⁽⁴⁾	SNR_{mid} ⁽⁵⁾	SNR_{max} ⁽⁶⁾
	Å	Å	Å ⁻¹	Å ⁻¹	Å ⁻¹
U7000	4000	4050	0.3	29	264
B7000	4800	4850	4.4	77	689
R7000	6400	6450	1.2	161	1145
I7000	8400	8450	7.9	157	911

(1): Grating. (2): Minimum wavelength for SNR calculation. (3): Maximum wavelength for SNR calculation. (4): Minimum SNR per Å. (5): Median SNR per Å. (6): Maximum

SNR per Å. This table is from Usher et al. (2017) Table 3.

2.2.4 WAGGS Data Reduction

Usher et al. (2017) used the “PyWiFeS” pipeline to produce flux and wavelength calibrated, normalised spectra as well as a 1σ error spectrum for each object.

CHAPTER 2

Therefore no data reduction was actually needed. The only data processing required was the combination of the different gratings (U7000 & B7000 etc.). In addition, the object’s redshift was also accounted for in the combination process to save time in later analysis steps (i.e. Chapters 3, & 4).

Usher et al. (2019a) provided supplementary data which contained literature values of the observed GCs. The published recessional velocities were used for each GC to calculate redshift. The wavelength range for each grating was then “de-redshifted” to the laboratory rest frame.

With the wavelength ranges “de-redshifted” the gratings were then combined together. Each grating had its own pixel spacing ($\delta\lambda$). If the overlapping regions were to be combined they had to have the same $\delta\lambda$, so each grating was re-gridded to a common pixel spacing of $0.4 \text{ \AA}/\text{pix}$. This was a good solution for U7000 and B7000 but for the R7000 and I7000 gratings, it resulted in the pixel spacing being reduced. 0.4 was chosen to ensure adequate (i.e. Nyquist) sampling of the spectra from the highest resolution U7000 grating. During interpolation, the flux of each grating is conserved meaning the total flux of the input spectrum is equal to the total flux of the new spectrum. This resulted in different continuum levels between the gratings so an adequate combination could not be undertaken. Therefore each grating was normalised so that the median value of the overlapping region matched that of the subsequent grating, ensuring that the continuum of each grating aligned with the subsequent grating.

The full grating combination process was completed in Python. Figure 2.6 shows the step-by-step combination process for the compact object NGC 104 (47 Tuc). It shows how the regions of each grating which overlap have been separated from their original grating then combined together before all 7 sections of the spectrum are combined together. This process was done for all of the objects in the WAGGS catalogue

CHAPTER 2

The error spectrum for each grating was combined in a similar way. For every process done to the object's spectrum, the same process had to be done to the error spectrum. Therefore each error spectrum was de-redshifted and combined in the exact same way, normalised so that the SNR between the data and uncertainty remained the same before and after combination (except for the overlapping regions where the combination process increased the signal to noise). At wavelengths lower than $\sim 4000 \text{ \AA}$ the uncertainty starts to rapidly increase as wavelength reduces for most objects in the data set. This rapid drop in SNR at shorter wavelengths had to be taken into consideration when further analysis was undertaken.

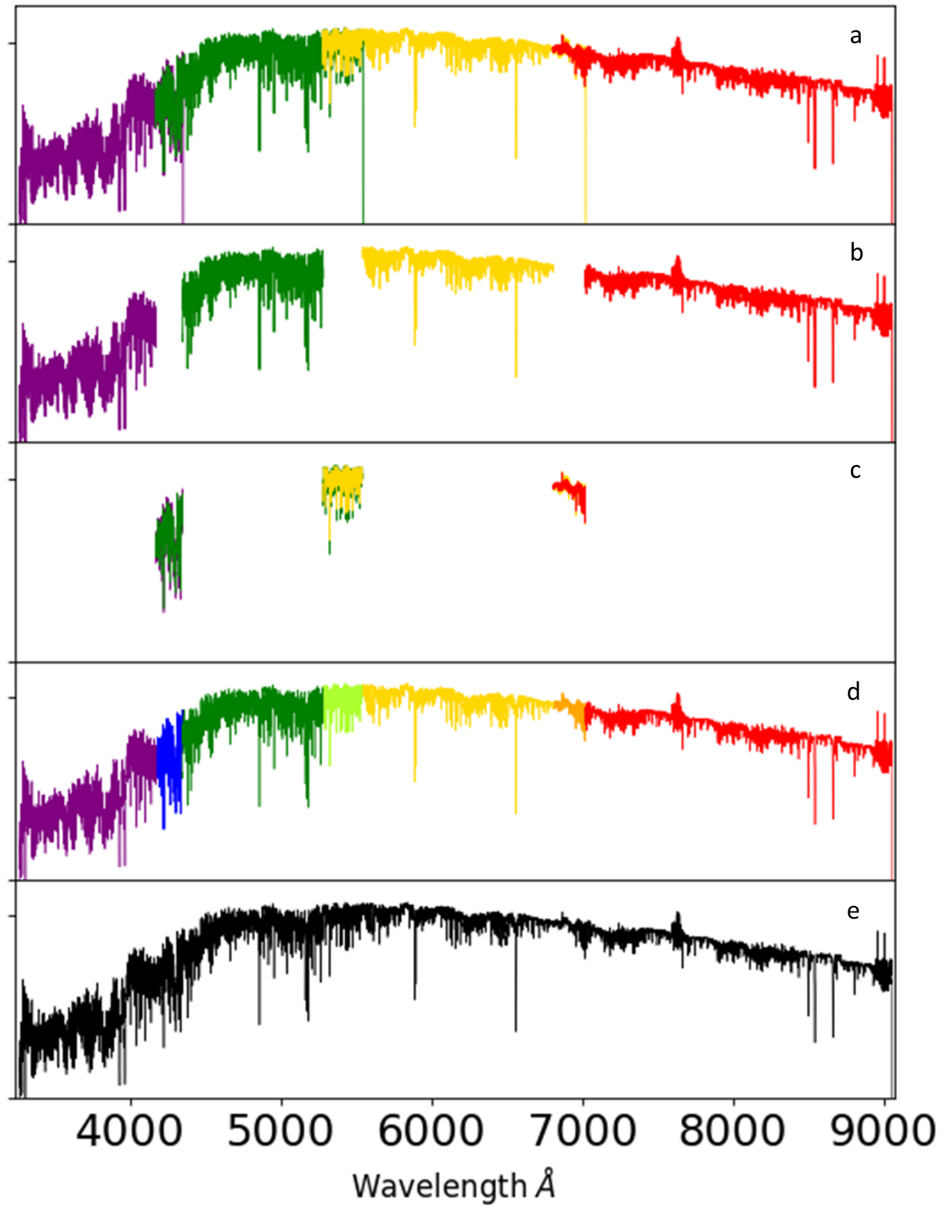


Figure 2.6: The stages of the combination of the WAGGS gratings for the GC NGC 104. (a) First, there is the flux conserved redshifted and re-gridded spectra for each grating. (b+c) The overlapping regions are then isolated from each grating. (d) The isolated overlapping regions are then median combined. (e) All 7 sections of the spectrum are combined.

CHAPTER 2

There were some issues with this data, for a few of the objects there were absorption lines at wavelengths of 4959Å and 5007Å which are typically [OIII] emission lines. Discussed further in Section 3.6.1 & 3.8.2, this is probably due to the sky region used for sky subtraction being contaminated by [OIII] emission from the host galaxy. However, this would also therefore have an effect on the Hydrogen Balmer lines which are used typically as key age indicators. This would make the object appear younger than it actually is. However, the OIII emission (and absorption lines) are only apparent in a few of the objects and as stated later these objects have been removed from the sample. Supporting evidence for poor sky subtraction is that some GCs also have absorption lines at 5577Å in the raw spectrum, before redshifting, which is a major sky emission line which is typically removed during sky subtraction but can leave a region of larger uncertainty. A large absorption line here indicates that the flux value of the sky was too large for the measured spectrum. Again, any object showing these signs of poor sky subtraction was omitted from the sample (for the WAGGS sample this was the GCs NGC 330 and NGC 416 and this is discussed further in Section 3.6.1).

2.3 Pre-Reduced Data

While a lot of data for the catalogue was obtained as raw, or partly reduced data, there were some sources of data which provided reduced, flux and wavelength calibrated spectra and absorption line index measurements. Below, this data is discussed.

2.3.1 Schiavon MW & M31

Line indices for 41 galactic and 313 M31 GCs were obtained from Schiavon et al. (2012). The data (“S12” from here) came as indices measured on the LICK/IDS

CHAPTER 2

system (a system for measuring the strength of absorption lines in a spectrum, for more information see Section 3.2) and had to be converted to the more modern LIS (Line Index System, Section 3.3) system for this project with a resolution of 5 \AA (FWHM). S12 had a relatively high median SNR of $\sim 75 \text{ pix}^{-1}$ which was equivalent to most WAGGS GCs. The data were obtained with the Hectospec spectrograph attached to the 6.5m Multiple Mirror Telescope at Mount Hopkins, Arizona (Fabricant et al., 2005).

Of the 41 galactic GCs, 37 are in common with WAGGS. Due to the limited addition to the total CSS sample, the different resolution to the other galactic GCs and the fact that the data only came as indices, the galactic GCs are not analysed in this project. Of the 313 GCs from M31, only 2 are in common with the other data obtained in this project. The 2 GCs in common with S12 come from MODS (Section 2.5), which is covered below. Analysis of all 313 M31 GCs is included in this thesis.

2.3.2 M87 GCs and UCDS

Using the Keck Cosmic Web Imager (Morrissey et al., 2018), Forbes et al. (2020) observed several GCs and UCDS in the field of the elliptical galaxy M87. These objects (Table A.3) consist of 3 GCs and 3 UCDS. The data were provided as full spectra with a wavelength range $\lambda = 3600 - 5700 \text{ \AA}$ and a resolution of $R \sim 900$ (5.06 \AA per pix at the central wavelength). The spectra were proved with wavelength calibration completed, but they needed to be de-redshifted. Unfortunately, no error spectrum was provided with this data so in order to have an estimation of the individual pixel error the pixel flux values were divided by the SNR value provided for each object in Forbes et al. (2020).

2.3.3 Sloan Digital Sky Survey (SDSS) Spectra of Galaxies

It is important to have a comparison of more massive galaxies when studying compact stellar systems to understand what pre-stripped nuclear looked like and to understand how system mass can affect other parameters of stellar systems both compact and non-compact. In preparation work for his PhD Thesis, Davison (2021) produced binned galaxy spectra of several thousand galaxies from the Sloan Digital Sky Survey SDSS. For this data (SDSS21 from here) Davison (2021) performed a linear binning on the galaxies combining galaxies based on a Voronoi diagram (Figure 2.7) of radius against mass. This also had the effect of combining galaxies which had similar velocity dispersions. This is because, in large galaxies such as these, the velocity dispersion is the dominant force driving the spectral resolution. He binned this data together in order to produce high SNR data for subsequent spectral analysis.

The SDSS data came in two main data sets. The first sample was comprised of 37,258 galaxies chosen because the SDSS fibre captured an average of 12.5% of the light of the galaxy. These galaxies were then arranged by physical size and stellar mass (see Figure 2.7) and coadded to produce 248 high signal-to-noise binned spectra across the mass-size plane. The same approach was used to produce a similar set of 506 spectra using a different galaxy sample where the SDSS fibre captured an average of 50% of the light of the galaxy. This data is of interest in this project as it covers the more densely populated cores of these galaxies with less input from the less dense outer annuli. Unfortunately, there are no pixel flux uncertainty values given for this data. SDSS spectra have a median resolution of around 2.95 \AA (FWHM) (Aguado et al., 2019), but as stated previously for galaxies of this size the spectral resolution is dictated by the velocity dispersion of the galaxy. For measurement later in the project the velocity dispersion of each individual bin is used as the base resolution for that spectrum (where it gives resolutions greater than the instrumental resolution

of the spectra) and smoothed to the relevant measurement resolutions needed from this ‘base’ resolution.

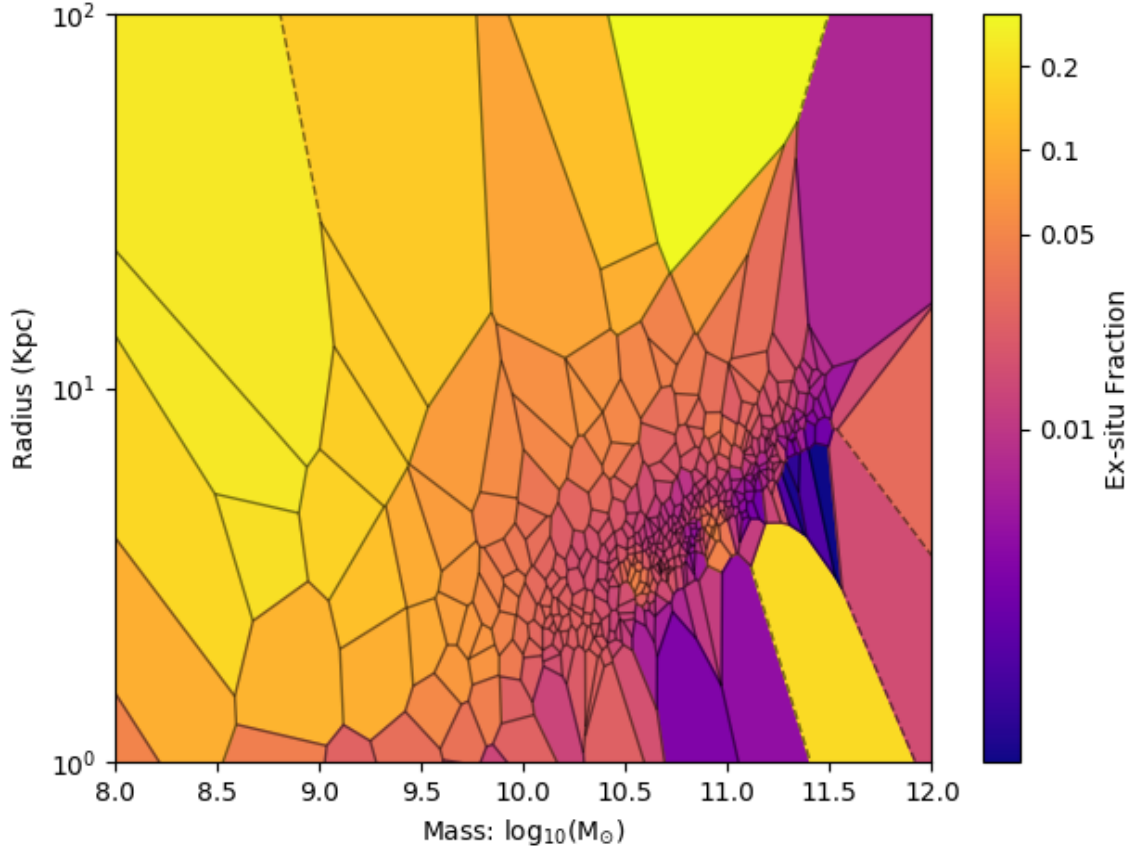


Figure 2.7: The Voronoi plot of the inner 12.5% light binned SDSS galaxy spectra showing stellar mass against galactic radius taken from Davison (2021). The colourbar represents the fraction of in-situ vs ex-situ accreted stars which was relevant for that thesis. This plot has the same axis as Figure 1.1 and as such shows how the objects in this have the mass and radii up to the most massive Elliptical galaxies.

2.4 X-Shooter

Data was also collected from the ESA Science archives for the X-Shooter spectrograph on the VLT (Vernet et al., 2011).

CHAPTER 2

The data was obtained by querying for “UCD” and “CSS” (as UCDs were the least populated CSS in the sample at the time). From various surveys spread between 2011 and 2018 spectra of 12 objects were obtained, mostly consisting of UCDs and GCs (publicly available CSS surveys with XShooter after 2018 could not be found, although a more in-depth search with different query keywords and searches for specific objects may find more data in future). The full list of objects and their respective surveys can be found in Table A.3.

X-Shooter is an echelle spectrograph (covered in Section 1.8.1) and consists of three arms: UVB, VIS, and NIR. It is based in Cerro Paranal, Chile, on the VLT. The wavelength ranges of these arms are 3000-5595 Å, 5595-10240 Å and 10240-24800 Å respectively. Near infra-red spectroscopy was not needed for this project and therefore only the UVB and VIS arms were used. Their combination is outlined in the next section. Because this is an echelle spectrograph, the resolution of the data was high with resolutions of $R = 6700$ in the UV band and $R = 8900$ in the visible band.

2.4.1 X-Shooter Reduction

The standard ESO pipeline was not used to reduce this spectra and instead, a pre-written data reduction pipeline was used which is designed to reduce data from multiple spectrographs, PypeIt (Prochaska et al., 2020a,b). PypeIt is a python package which is designed to ‘semi-automatically’ reduce astronomical spectroscopic data.

The usage steps for PypeIt are outlined in Prochaska et al. (2020b), however it follows the main steps for spectral data reduction. It first sets up the reduction process by classifying all of the raw science and calibration data using their “setup” data classification script. Once it has classified the data one must run the reduction script and the code begins to reduce the data. PypeIt both biases and flat fields the

CHAPTER 2

data and then does wavelength and flux calibration and removes the sky background, all with very little input from the user. It produces several calibration images showing each reduction phase such as wavelength calibration (Figure 2.8) as well as throughput values for each echelle arc during flux calibration.

This process was not perfect, however, and often the wavelength calibration had a slight linear shift of 1-2 Å for each object. Therefore the 5577 sky emission line of each spectrum was manually checked and the spectrum de-redshifted to the new calculated wavelength range (keeping the same pixel width and conserving flux).

To measure the resolution of the spectra one would normally measure the FWHM of the arc spectrum. However, for the data obtained, the arc spectra used a smaller slit width and so the resolution would be different. Therefore, FWHM of sky emission lines had to be measured, which were often in the low SNR overlapping wavelength region between spectral arms. However, the resolution values measured from this roughly agreed with the published resolution values for the slit widths used and therefore the published resolutions (Puzia 2011, the resolutions were updated in July 2011 when a new filter was installed) are the values used ($R = 5400$ & 6700 for the UVB arm for objects observed with slit widths of $1''$ & $0.8''$ respectively and $R = 8900$ for the VIS arm where all observations used a slit width of $0.9''$).

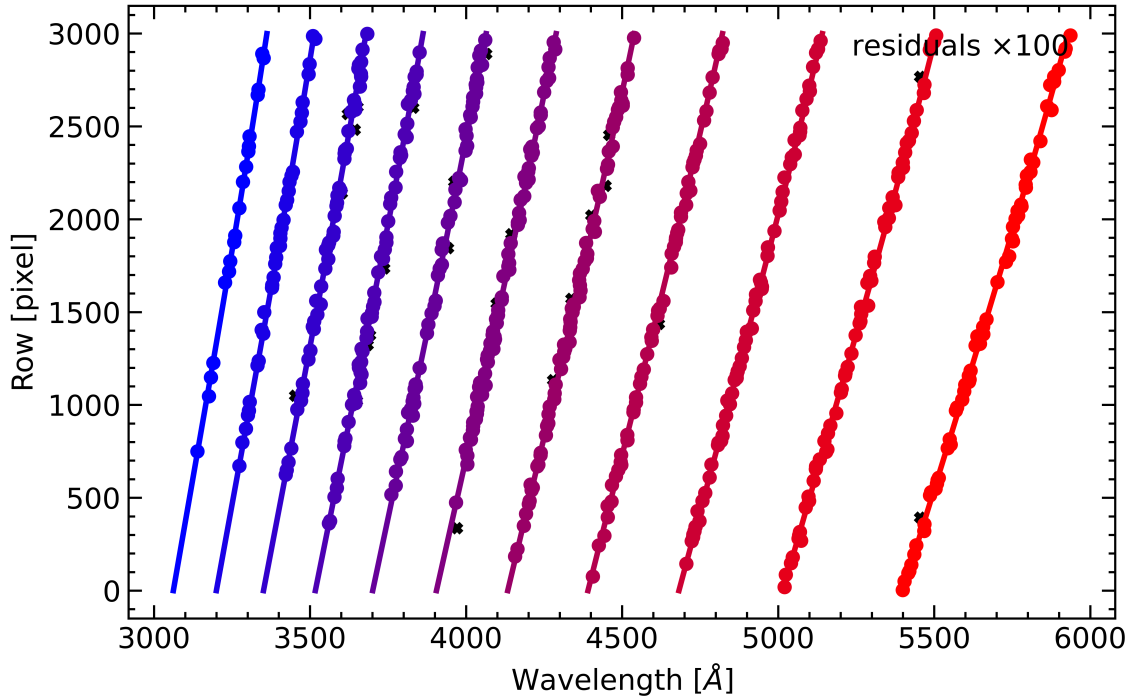


Figure 2.8: The PypeIt wavelength calibration output diagram showing each order of the echelle spectrograph and the points used to measure their wavelength values. The black crosses mark calibration peaks which have been excluded due to non-alignment. The colour simply represents the median wavelength of each order.

PypeIt could not combine the different XShooter arms, so a Python script to do this was written. The first step was to smooth the visible arm (which had the highest resolution in all of the data) to the resolution of UVB arm. Then, similarly to the WAGGS spectral combination procedure, The data was interpolated to have the same pixel spacing in the overlapping region, then used an uncertainty weighted combination of pixel flux values to get a single spectrum in the overlapping region.

The overlapping region of both UVB and VIS arms had very low SNRs and there was in some data (such as M59cO) a flux continuum difference between the arms probably due to poor flux calibration with PypeIt. Overall, PypeIt made the reduction of this data very simple, however, there were several issues with wavelength

CHAPTER 2

and flux calibration which made its use less desirable to writing a custom reduction pipeline. The data from this spectrograph, while high resolution is relatively low SNR compared to the spectra from other sources.

2.5 MODS

MODS (the Multi-Object Double Spectrographs) (Pogge et al., 2010) is a pair of spectrographs used on the Large Binocular Telescope (LBT). These spectrographs are known as MODS1 and MODS 2. MODS1 came into service in September 2011 and has been continually operated since then. It has two arms, MODS1b and MODS1r the blue and red arms covering the wavelength ranges 3200-6000 Å and 4500-10500 Å respectively. The MODS2 spectrograph was later in its commissioning with full dual use of both MODS1 & 2 not initiated until early 2016. MODS2 covered the same wavelength ranges as MODS1 in two separate arms and they both have a spectral resolution of $R \sim 1850$ and $R \sim 2300$ in the blue and red arms respectively.

To match with wavelength ranges defined later for the WAGGS dataset in Section 3.6.2, and to save on time, it was decided to only reduce the blue arm, MODS1b and MODS2b. The instrumental resolution of the data in the blue arm is around $R \sim 1850$ (~ 2.7 Å FWHM at 5000 Å) for a 0.6" slit width. The slit width used in the MODS data is 0.8" and it is found that (through Gaussian fitting of the 5577 sky line) the median instrumental resolution of this data is $R = 1637$ (~ 3.053 Å FWHM at 5000 Å). Therefore, the sky line measured value of instrumental resolution for each object is used when using the data later in this thesis.

The majority of the data taken with the LBT was taken prior to 2016 and therefore only exists as MODS1 spectra. However, where MODS1 and MODS2 data are available the SNR of this data is significantly higher, this is discussed below in Section 2.5.2.

2.5.1 Data Selection

MODS is designed to be capable of multi object spectroscopy via custom slit masks. The data in this sample, however, has used single slit spectroscopy. The data for this thesis is limited to 1-3 objects per frame, i.e. as many objects as can be placed on a single linear slit.

This thesis includes all data presented in the AIMSS papers: Norris et al. (2014); Forbes et al. (2014); Janz et al. (2016) with some additional objects added subsequently. After reduction, the spectra of 30 CSSs are available for this project. None of the AIMSS papers had access to the MODS2 data as there is no LBT data reduction pipeline that works for MODS2 either at the time, or still today. The full object list is available in Table A.3. The sample consists of 2 GCs, 4 NSCs, 6 UCDS, 16 cEs, and 1 dE. Seven of these objects have data from both MODS1 and MODS2 (Table A.3) and are combined and analysed here for the first time.

2.5.2 MODS Reduction

At the time of data reduction, there was no open-source reduction code provided by the LBT that was able to reduce both LBT/MODS 1 and MODS 2 data. MODS1 has a reduction pipeline in IDL/Python, but funding stopped before the necessary calibration files could be obtained to make the pipeline work with MODS2. Therefore a pipeline consisting of several Python scripts has been developed which can reduce and extract 1D and 2D spectra from the MODS 2 data. The pipeline also worked with MODS1 so for ease it was used on both sets of data. Having data from both MODS spectrographs increases the SNR calculable for each object by $\sim 41\%$ ($\sqrt{2}$)*, making measurements much more robust.

It was originally hoped that new python-based reduction programmes such as Pypeit (Prochaska et al., 2020a,b) could be used. As shown before, this programme

*Assuming identical exposure time and throughput for each spectrograph.

CHAPTER 2

can reduce data for spectrographs such as XShooter (Vernet et al., 2011). But for MODS2, Pypeit unfortunately did not support reduction in the UV “MODS2_blue”. Instead of waiting on updates from this package (and due to the calibration issues described previously), it was decided that writing a series of Python scripts able to reduce both the MODS1 and 2 data would be necessary.

The way this process worked is as follows:

- After the raw files (e.g. Figure 2.9 showing the raw unreduced 2d spectrum for UCD NGC4621-UCD3) were acquired they were organised using Pypeit which, while not useful for the rest of the reduction, has a functional file organisation and classification system.

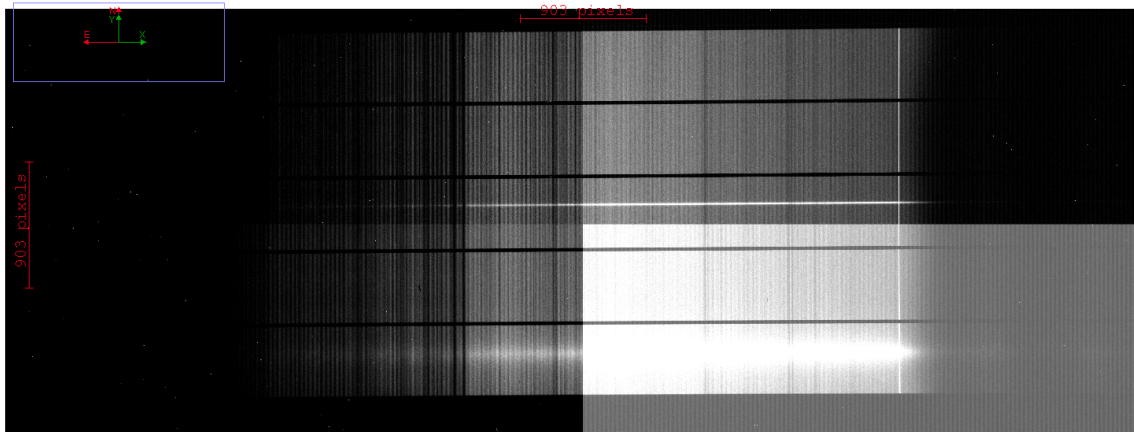


Figure 2.9: The raw MODS2 “Science” image of the UCD NGC4621-UCD3. The varying bias level due to the four separate readout nodes are obvious.

- A set of scripts has been published called modsCCDRed (Pogge, 2019) which offers a simple way of flat-fielding and de-biasing the science images. Only flat field images were needed as the software has an inbuilt version of the bias frames which through testing can reliably account for the bias when reducing spectra. The resulting image is shown in Figure 2.10 where effects such as vertical stripes of alternating high/low flux always present in MODS data and the 4 quadrants (Figure 2.9) have been removed.

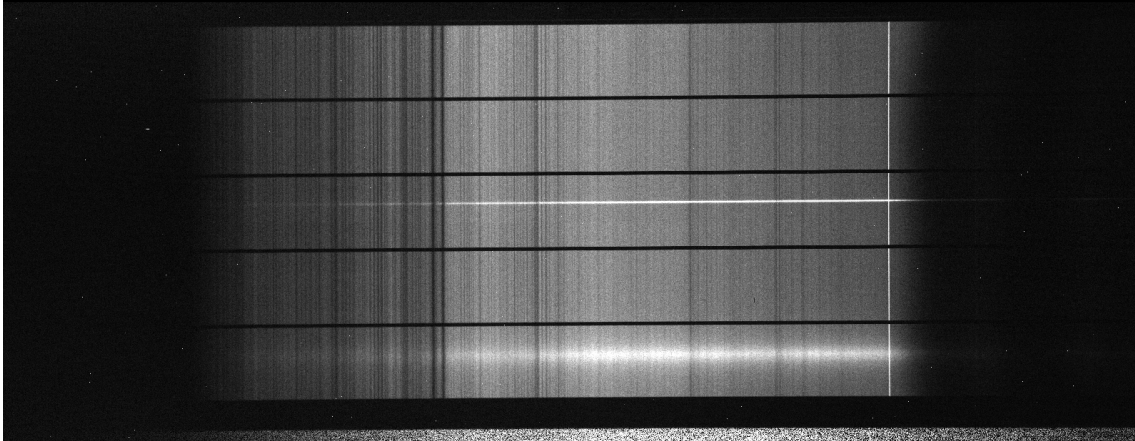


Figure 2.10: Figure 2.9 after being bias corrected and flat fielded.

- These images were then processed further by using a tool called LaCosmic (van Dokkum 2001) to remove any cosmic rays present in the image. It does this by iteratively finding non-Gaussian peaks in flux and removing them to match the level of the field surrounding the points.

Now the extraction of the spectrum can start.

- The spectrum is not perfectly linear on the sensor, there is a slight curve on the horizontal (wavelength) axis. To correct this, a short code was produced which calculated a polynomial from a trace of the spectrum. Each pixel in the full 2d image was then adjusted ‘up’ or ‘down’ by the polynomial straightening the spectrum.
- The next step was wavelength calibration, which was done via a Python package called Rascal (Veitch–Michaelis & Lam 2020). The raw data came with arc frames which were images taken with the spectrograph of lamps of certain elements with peaks at known wavelengths. These arc frames were first reduced in the same way as the science spectrum.

The peaks were identified using Rascal (Figure 2.11) and assigned to the correct wavelength. The process worked by going to each row of pixels and

CHAPTER 2

running the calibration to get the correct wavelength values for that row. The rows were then re-binned, meaning they would start on the same wavelength and each row was interpolated to have the same pixel width. The correction which happened to the arc frames was then applied to the science frames, producing a wavelength-calibrated spectrum. This also had the effect of straightening the vertical curves in the data (Figure 2.12). This Figure also shows how at the edges of the frame there is generally a lower instrumental resolution (possibly due to a focusing problem with some of the frames) and this had to be taken into account when measuring the spectra produced from frames with multiple objects in them.

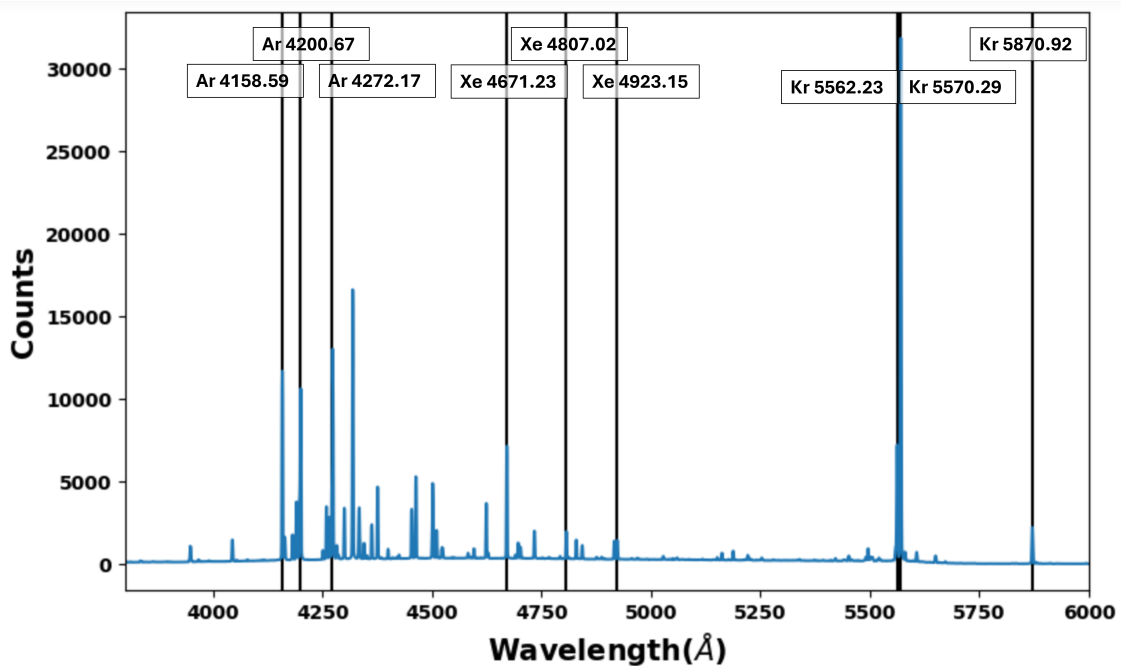


Figure 2.11: A plot showing the flux peak wavelength identification of the RASCAL calibration process. Here a combination of Xe, Kr and Ar arc frames are combined and key peaks have been identified (marked with black vertical lines, only 3 lines for each element in the frame have been shown here but the full Rascal step utilised many more of the peaks shown here).

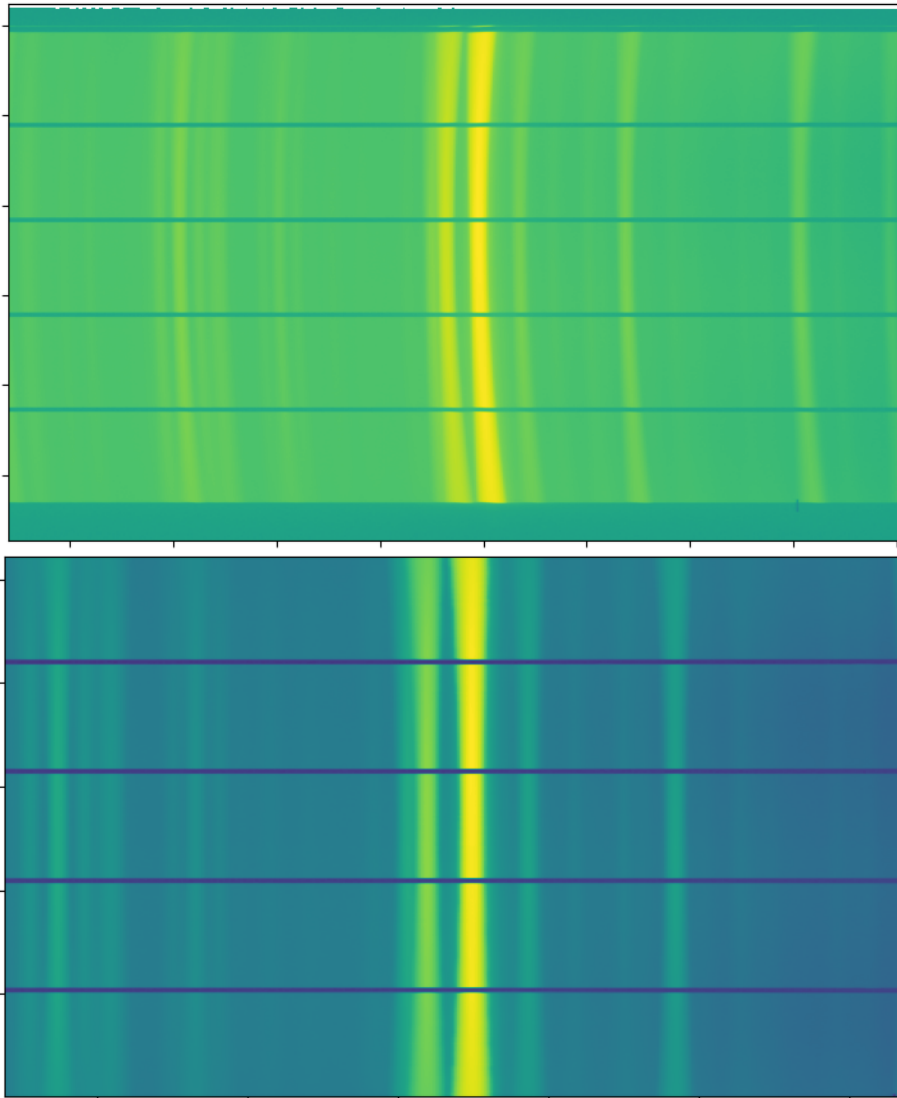


Figure 2.12: The effects of the wavelength calibration procedure. Here is the arc frame combination of Xe Kr and Na before (top) and after (bottom) their peaks were measured and the image was calibrated.

- The next step is sky subtraction. A script was produced where the user defines regions on either side of the central flux peak (per column in the wavelength domain) and the code measures the flux in those regions as the sky background. The code then fits a curve between those two regions and subtracts that polynomial from the column, this is then repeated for all columns of pixels

CHAPTER 2

in the image making the background \sim equal to zero. A polynomial was fit between the sky regions to account for the presence of varying background light in the frame. Many objects are local to larger ‘host’ galaxies and the light from these galaxies often pollutes the background of the image in a non-linear gradient (particularly NSCs) which the ‘sky’ removing programme aimed to account for.

- The final stage was extracting the 1D spectrum. A code was developed based on the optimal extraction routine outlined in Horne (1986). Optimal extraction increases SNR by $3/\sqrt{\pi}$ compared to simply adding the flux in a column (physical axis) in a $3\text{-}\sigma$ distribution about the peak. This produced an optimal flux value and a variance value for each pixel (the square root of the variance being used as the pixel uncertainty). The code did this for every column of pixels in the science image producing a single 1-dimensional spectrum, this was then done for all of the other science frames of each object (often 4-5 different images with exposure times of 600-1200 seconds) which were then median combined together into one spectrum and normalised exposure time of 1 second so flux calibration could be done.
- The combined science spectrum was then flux calibrated by doing the same reduction process on standard star spectra (also normalising flux to get an equivalent exposure time of 1 second). Using the known flux values per pixel for those standard stars and the measured values, a calibration function was created which converted the pixel value to the correct flux value in $\text{ergs}/\text{s}/\text{cm}^2/\text{\AA}$. This was then applied to the science frames. The MODS1 and MODS2 spectra were then combined using a simple uncertainty-weighted median combine. As can be seen in Figure 2.13.

CHAPTER 2

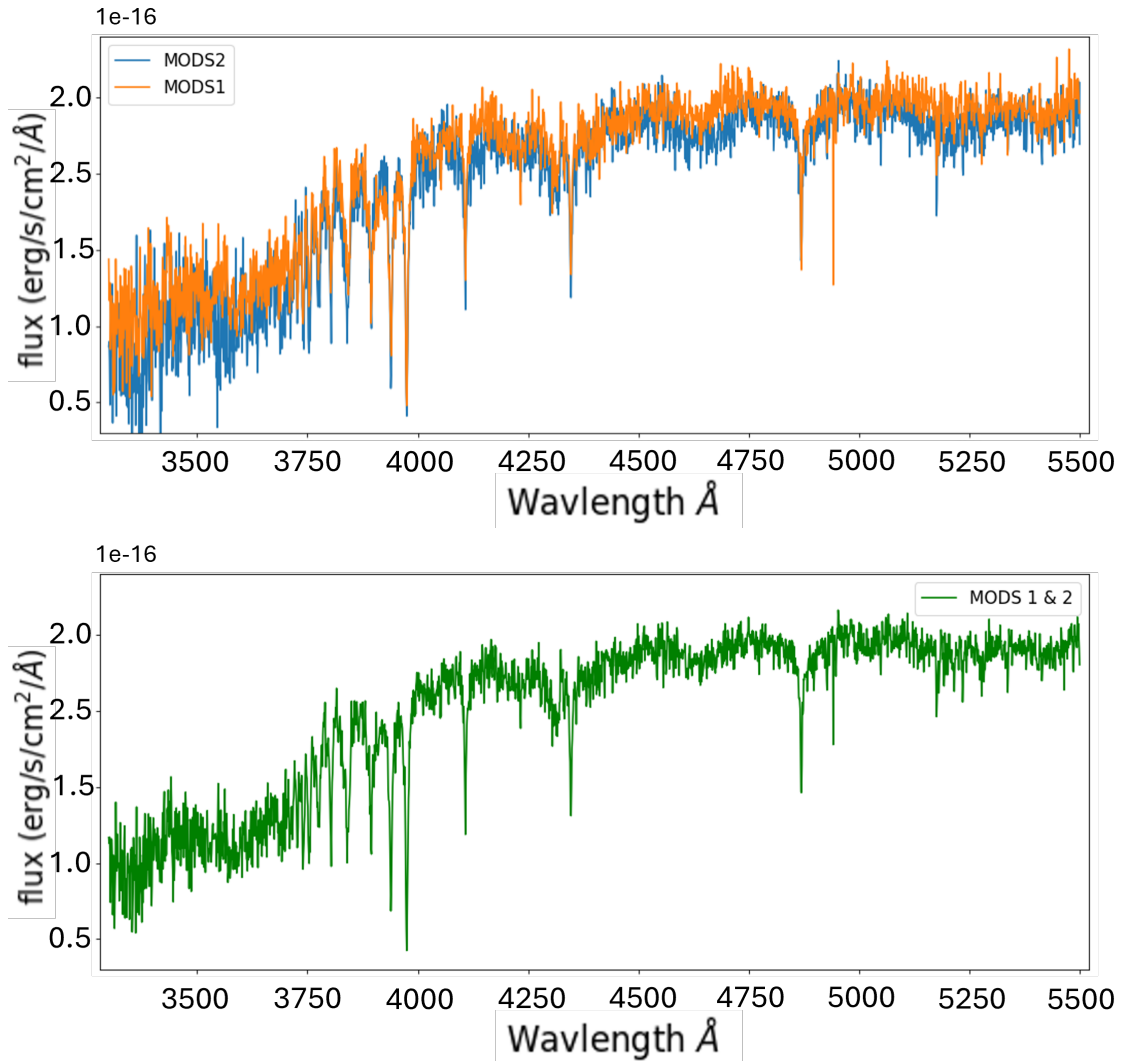


Figure 2.13: These plots show the increased SNR (to be calculated quantitatively when the error during the error spectrum calculation) of combining MODS1 and MODS2 data together. The above plot shows both the MODS1 and 2 spectrum of nuclear star cluster LEDA4573336-NSC and the bottom plot is both spectrums median combined.

2.6 New Observations with SOAR

For this project, there was opportunity, courtesy of The University of North Carolina at Chapel Hill, to observe on the 4.1m SOAR telescope based on Cerro Pachon, Chile (Section 2.6.1). Four dates were available from the 22nd of November 2022 to the 15th of July 2023. The observations were conducted in remote observer mode from The University of Central Lancashire’s Alston Observatory based east of Preston, Lancashire. From here SOAR and the Goodman spectrograph were connected to and operated remotely.

2.6.1 SOAR

The SOAR (Southern Observatory Astrophysical Research) telescope was proposed in 1987 by The University of North Carolina at Chapel Hill with the development team being finalised in 1997 and the conceptual design approved in 1998. The telescope opened in 2003 with the first scientific observations in February of 2005. SOAR is a collaborative project of the University of North Carolina at Chapel Hill (UNC); the Ministério da Ciência, Tecnologia e Inovações do Brasil (MCTI/LNA); Michigan State University (MSU); and NSF’s NOIRLab.

SOAR is a 4.1m reflector telescope based 2700 meters above sea level in Cerro Pachón (in a shared location with the Gemini-South and Vera Rubin Observatories) which observes in the UV to near IR. Shown in Figure 2.14, SOAR is a Ritchey-Chrétien (RC) design with a focal ratio of $f/16.63$ with 2 Nasmyth and 3 folded Cassegrain foci. RC telescopes are a variant of the Cassegrain telescope design using a hyperbolic primary and secondary mirror which is designed to minimise comatic aberrations.

Good natural seeing, due to its location (as low as 0.6 arcseconds on one of the observing nights), and the use of adaptive optics mean that SOAR is capable of obtaining incredibly detailed images with a record of 0.25 arcseconds FWHM at 8000 Å in a field of view of 3x3 arcminutes.

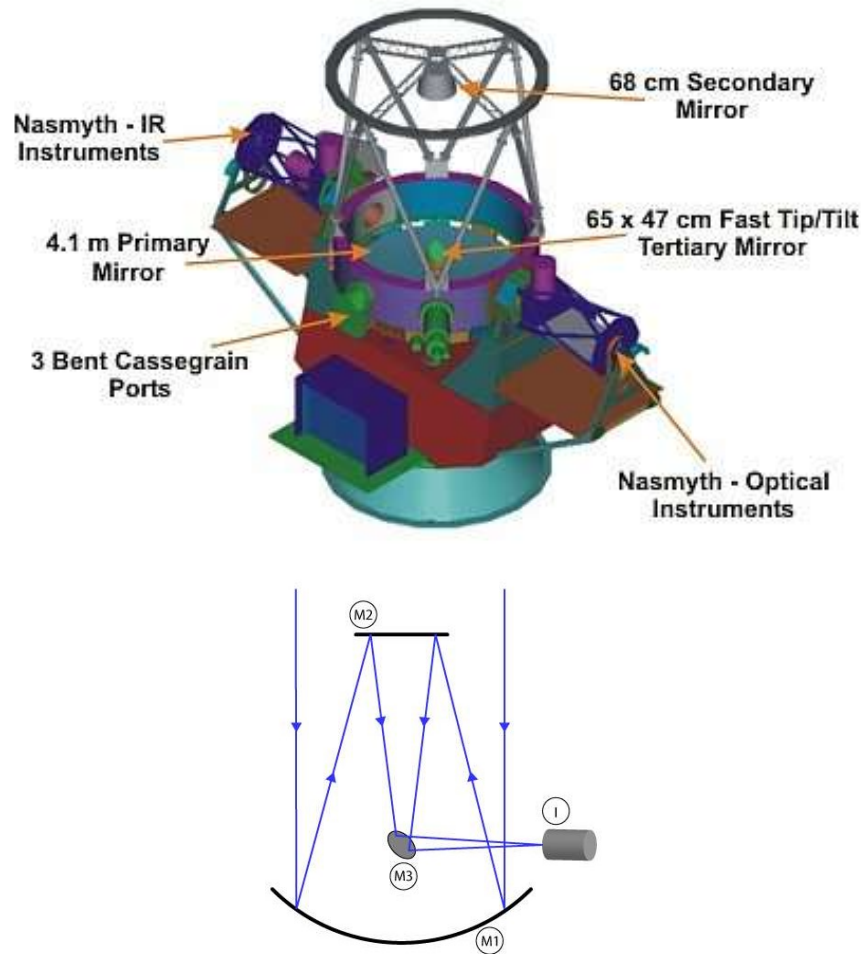


Figure 2.14: The Schematic and optical layout of SOAR as presented by NOIRLab (2015b) & NOIRLab (2015a).

For this project, SOAR was used to obtain relatively high-resolution spectra of local CSSs (listed in Table A.3 and Section 2.6.3).

2.6.2 Goodman High-Throughput Spectrograph

The spectrograph used in the observations was the Goodman High-Throughput Spectrograph (GHTS) (Clemens, Crain & Anderson, 2004) (Figure 2.15) which was built in The Goodman Laboratory at the University of North Carolina.

GHTS has a plate scale of 0.15 arcseconds per pixel and a wavelength range in

CHAPTER 2

the UV at 3200 Å to near IR at 9000 Å. GHTS has two cameras which have to be selected by the user before the observation date: the Blue Camera and the Red Camera. The Red Camera is optimised for observations in the red - IR regime and was not used in this project. In order to make use of GHTSs lower wavelength range, the Blue Camera was used. The Blue Camera is recommended for programs requiring a high throughput on the blue side of 4500 Å. Since this project makes use of particular UV-blue chemical spectral features (Chapter 5) the blue camera was chosen.

In order to maximise the wavelength range while maintaining a reasonable resolution a 1-arcsecond slit along with a grating of 930 lines/mm was chosen along with a custom grating and camera angle to give a wavelength range of 3980 Å to 5665 Å. This range was chosen so that the Fe5335 LICK index's red pseudo-continuum (at 5363.375Å) could be measured for objects at redshifts of $z = 0.05$ (the arbitrary limit set for this project to allow for apparent magnitudes which are able to obtain suitable SNRs). The resultant low end of this wavelength range was 3980 Å and was determined to be acceptable as the $H\delta$, LICK, blue pseudo-continuum (at 4041.6Å) would be observable. The maximum resolution of the 930 grating is listed in the GHTS documents as $R = 4450$ for a 0.46-arcsecond slit at 5500Å. A larger slit of 1 arcsecond was used for observations which would decrease the resolution. Measured with sky lines at 5577Å, the resolution ended up being closer to a value of $R \sim 2000$. This was confirmed by measurement of the FWHM of Ar lines in the arc spectra used for each object's wavelength calibration (Section 2.6.4).

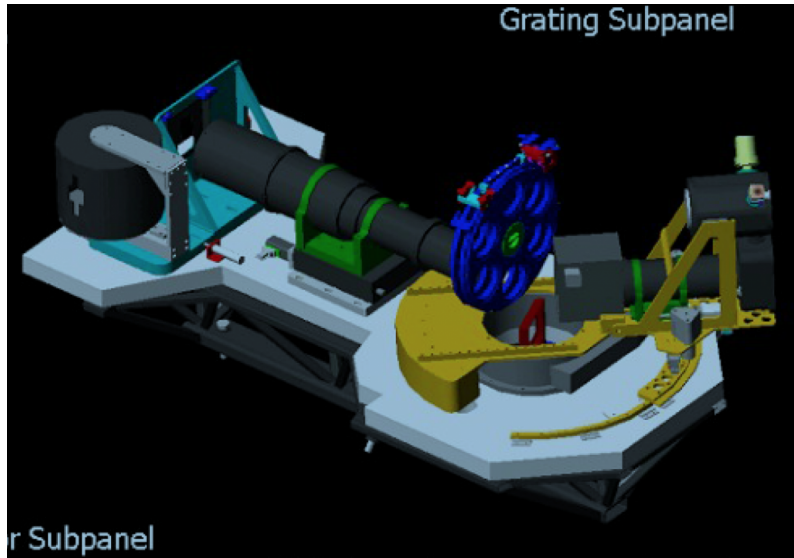


Figure 2.15: A 3 dimensional diagram of The Goodman High Throughput Spectrograph from NOIRLab (2018).

2.6.3 GHTS Data

The dates of the observations using the GHTS were the 28th of October and the 22nd of November in 2022 and then the 26th of March and 15th of June in 2023. These dates were fairly spread apart which made observations of the same object over different runs difficult. However, the dates of run 1 and run 2 were close enough together that the same objects were able to be observed increasing the signal-to-noise of those objects through combination of the data (outlined in Section 2.6.4).

Table A.3 shows the objects selected for the SOAR observations. Care was taken to choose objects which would fill gaps in the data already acquired. As such the main aim was to look for UCD candidates. However, there never were any UCDs in the field each observing night that had magnitudes bright enough to be observed with satisfactory signal-to-noise. This meant that most of the objects observed were cEs or bright globular cluster types around known galaxy clusters.

2.6.4 GHTS Reduction

For the initial data reduction steps the Goodman Data-Reduction pipeline was used. This is a pair of Python scripts which are designed to produce “one-dimensional, wavelength-calibrated, science quality spectra, in a highly automated way, with minimal user intervention” Torres-Robledo, S. (2019).

The first script in this code was “redccd”. This code is designed to perform standard initial data processing like subtracting bias, correcting by flat fielding and cleaning cosmic rays. It was found that the cosmic ray removal was inadequate, so the data was run through LaCosmic (van Dokkum, 2001). The second Python script is “redspec” and this is designed to do object detection, tracing, extraction, background estimation and subtraction, and wavelength calibration with no user input. However, it was found that this code could not be used on this data. Due to using a custom wavelength range the code would not accept having to use a wavelength range outside of the set parameters. As well as this a non-standard arc lamp setup was used when measuring an arc spectrum. This was overcome by running the part-reduced data through the previously written reduction code for MODS adapted to reduce GHTS data. In this code, in the same way with MODS, the data was wavelength-calibrated and sky subtracted, the optimal extraction technique defined in Horne (1986) was used and then flux calibrated the output 1-dimensional spectra.

The same objects were observed on multiple nights and this data was median combined as pre-flux-calibrated spectra with each wavelength pixel weighted to its uncertainty value.

2.7 Summary of Available Data

This Chapter has discussed the sources of the data for this project and the reduction processes used to process the data ready for scientific analysis. An unprecedented catalogue of spectroscopic data of CSSs has been acquired.

The catalogue consists of spectra and indices measurements of 418 GCs, these are split into 86 local (MW and dwarf satellite) GCs, 313 M31 GCs, 3 M87 GCs, 3 Cen A (NGC 5128) GCs, and 2 NGC 7252 GCs. There are also 18 UCDs, 29 cEs and 4 NSCs, in terms of CSSs. There are more, less compact objects available in the catalogue. There are 754 binned spectra of SDSS galaxies, these are split into 506 binned spectra of the inner 50% of galaxy light and 248 binned spectra of the inner 12.5% of galaxy light. There is also spectra of a dwarf Elliptical galaxy (dE) and 1 red nugget.[†] This makes for a massive catalogue of stellar systems that is used in this thesis and is also intended for future work, and I make this catalogue publicly available.

2.8 Single Stellar Population Models

To understand the CSS spectra in this project SSP models are used. SSP Models are model spectra which describe a population of stars with a single age, metallicity, and abundance pattern. They are commonly based on a combination of stellar spectral and photometric libraries, theoretical isochrones and IMFs. There are several model libraries published which apply to different stellar environments and are based on different ‘ingredients’. In this thesis, the sMILES library of SSP models is mostly used. However, other SSP model libraries are implemented for other specific uses in this project and these models are outlined below.

[†]There was also a star that was incidentally in the slit for the GHTS observations of LEDA43301 which I have decided to name “BaniStar” (if we all ignore the name given by Gaia, who gave it the sensible but boring name “Gaia DR3 6140025975813181184”)

CHAPTER 2

2.8.1 MILES

The sMILES (Knowles et al., 2023) SSP models used in this project are based on the more commonly used MILES (Medium-resolution Isaac Newton Telescope library of empirical spectra) models (Vazdekis et al., 2010). These models are a widely used library of SSP models and cover a range of IMFs and isochrones which can be selected depending on a project’s specific needs. The MILES Spectral Library SSP models are based on code presented in Vazdekis et al. (2010) and the stellar libraries presented in Sánchez-Blázquez et al. (2006), Cenarro et al. (2007) & Falcón-Barroso et al. (2011). They cover a wavelength range of 3540.5 – 7409.6 Å with a FWHM of ~ 2.5 Å. The pixel width ($\Delta\lambda$) is 0.9 Å.

The models have a metallicity range of $-2.27 \leq [Z/H] \leq 0.4$ in 12 metallicity bins and ages between 0.03 – 14.00 Gyr at increasing intervals as age increases in 53 bins. MILES models have 3 options for $[\alpha/Fe]$ abundance: “base”, +0.00 and +0.40. “Base” is the $[\alpha/Fe]$ abundance of the empirical stars used in the construction of the models, +0.00 is solar alpha elemental abundance and +0.40 is where $[\alpha/Fe]$ is enhanced by 0.40 dex. Therefore, for each alpha value, there are 636 models.

2.8.2 sMILES

The sMILES (Knowles et al., 2023) SSP models are a series of semi-empirical model spectra based on the empirical MILES library (Vazdekis et al., 2010). The models are of the same resolution and wavelength range of the MILES models and are specifically designed for use in stellar population studies. By taking theoretical stellar spectra and applying them to existing MILES stars, Knowles et al. (2021, 2023) created a library of semi-empirical MILES star spectra with different $[\alpha/Fe]$ abundances that were then used to compute semi-empirical SSP models. For this project, the models use a simple bimodal IMF (which is an IMF with 2 different gradients in the number of stars to stellar mass domain stated in Vazdekis et al.

CHAPTER 2

1996) and BaSTI isochrones (Pietrinferni et al. 2004). In future data releases, there will be the option of using different IMFs.

One of the key advantages of this system over the MILES models used previously is the range of $[\alpha/\text{Fe}]$ now goes from $[\alpha/\text{Fe}] = -0.2$ to 0.6 at a binning of every 0.2 dex, with the possibility of adding specific elemental enhancements in future library updates. The benefit of adding specific elemental enhancements to these models cannot be understated and later it is shown how Conroy et al. (2018) with different elemental abundances can indicate population abundance issues in integrated spectra.

It is important to note that the sMILES models were created within the Jeremiah Horrocks Institute at the University of Central Lancashire and as such access to the source code and the team behind the models' creation was available. Part of the initial work was to assist in the assessment of these models and it was found that they were as reliable as the MILES for stellar population analysis.

2.8.3 Conroy Models

Later in this project, models which show specific elemental enhancements are required. The Conroy et al. (2018) (“Conroy” from here) models offer this. These models cover the wavelength range $0.37 - 2.4 \mu\text{m}$ and cover the metallicities $-1.5 \leq [\text{Fe}/\text{H}] \leq 0.3$ separated into 5 bins ($[\text{Fe}/\text{H}] = -1.5, -1.0, -0.5, 0.0$ and 0.2). These models are designed for old stellar populations and as such only cover ages 1 Gyr and above, in 5 age bins (1, 3, 5, 9 and 13 Gyr). This is a much lower resolution binning compared to sMILES with a smaller metallicity range. Conroy et al. (2018) used Kroupa (2001) IMFs and isochrones from the MIST stellar evolution database (Choi et al., 2016; Dotter, 2016). They also decided to smooth the SSPs to a common dispersion of $\sigma = 100 \text{ km s}^{-1}$ which gives a resolution of $\text{FWHM} = 3.919 \text{ \AA}$ at 5000 \AA compared to the sMILES resolution of $\text{FWHM} = 2.51 \text{ \AA}$. Therefore for almost all applications

CHAPTER 2

in this thesis sMILES was chosen.

However, the Conroy et al. (2018) models offered abundance variations for 18 different elements including C, N, O, Mg, Si, Ca, Ti, and Fe. For GCs many of these elements have abundance enhancements and depletions in the MP phenomenon and it has been shown previously (Banister, 2020) how using N enhanced SSP models can account for the large measurements in the CN Lick indices measurements for GCs. Banister (2020) suggests that this N enhancement may continue to larger more complex stellar populations and this is an avenue which is explored in Chapter 5.

2.8.4 TMJ SSPs

Another set of SSP models which are able to enhance individual elemental abundances are the TMJ models Thomas, Maraston & Johansson (2011). These models came as index measurements on the LICK/IDS system and therefore had to be converted to the LIS system via Equation 3.3 and Tables D.2 & D.3. These models originally had the same resolution as the MILES models but were smoothed before measuring to match the LICK/IDS resolutions needed. The models cover the ages 0.1 - 15 Gyr in 20 age bins and cover the metallicity range of $-2.25 \leq [M/H] \leq 0.67$ in 6 different bins. The models also varied in $[\alpha/Fe]$ to -0.3, 0.0, 0.3, and 0.5 dex.

2.8.5 Model parameter interpolation

Later chapters show the attempt to measure $[\alpha/Fe]$. For this to work adequately, finer $[\alpha/Fe]$ sampling than is provided by any of the SSP models discussed here is required. The sMILES models have a large range in alpha abundance of $-0.2 \leq [\alpha/Fe] \leq 0.6$ but with a binning of every 0.2 dex. The aim here is to see if, by binning alpha to a finer resolution, accurate alpha abundances can be measured for compact stellar systems from their full spectrum.

Therefore the binning is changed to a resolution of every 0.1 dex with a simple

CHAPTER 2

linear interpolation code with an option for even finer binning if needed. The ages and metallicities of the models have also undergone linear interpolation to get finer binning at high ages and a consistent spread in metallicity values (Figure 2.16). The age and metallicity ranges have stayed the same but now there is a model at every 0.1 Gyr and $[Z/H] = 0.1$ dex. The result of this binning is a sample of 33777 SSP models covering metallicities of $-2.20 \leq [Z/H] \leq 0.40$, ages of 0.10 – 13.90 Gyr and $[\alpha/Fe]$ values of -0.2 to 0.6 .

This is a very large sample of models and as such this thesis has, in general, stayed with the original binning, using the interpolated: $[\alpha/Fe] = 0.3$ value for measuring GCs in the next chapters due to the general alpha enhancement of GCs.

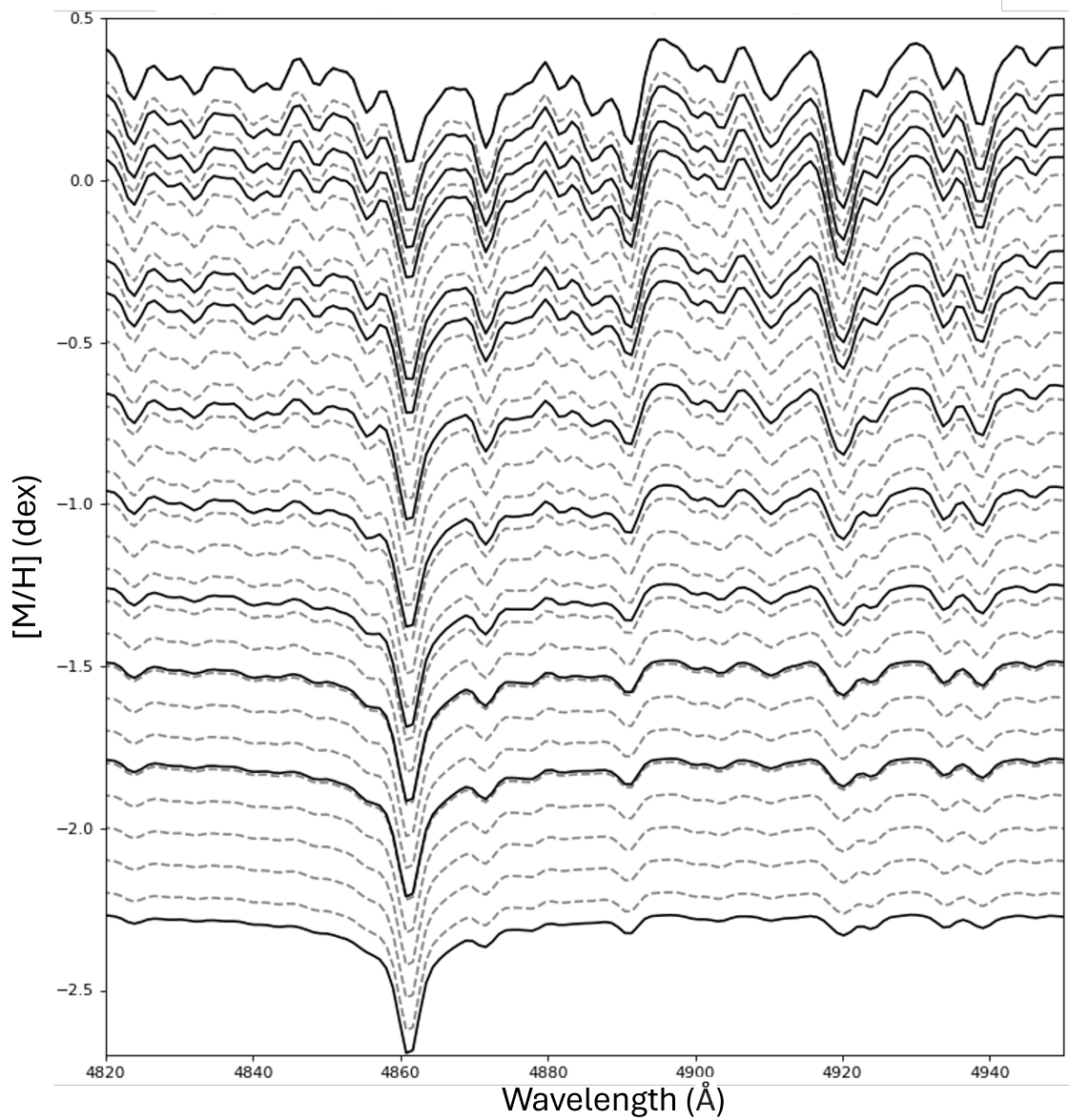


Figure 2.16: sMILES models at 12.5 Gyr and $[\alpha/\text{Fe}] = 0.3$ at a range of metallicities ($[\text{M}/\text{H}]$). Solid black lines represent the published spectra. Dashed black lines show the data interpolated to every 0.1 dex.

Chapter 3

Initial Integrated Light Analysis

3.1 Introduction

There have been multiple methods developed for the measurement of stellar population parameters from integrated light spectroscopy. This Chapter will cover the history of these methods, how they have been used in this project, and cover a new method (Section 3.4.3), comparing their abilities and addressing issues with each method.

The second half of this chapter, will look at the application of these methods to the spectra of GCs (the “simplest” objects in the full CSS sample of this project) and analyse the results. It is found that even for “simple” globular clusters current integrated light analysis techniques and models fall short of their desired abilities.

3.2 LICK/IDS Index System

In 1993 (Gorgas et al., 1993) a method was developed to quantify the the strength of absorption lines in a spectrum. While the method of measuring line strengths of absorption features is much older (Shajn, 1934), Gorgas et al. (1993) refined the method, trying to create a universal system quantifying strength of absorption lines. They created empirical fitting functions for 11 prominent molecular features in the

CHAPTER 3

spectra of G and K type stars based on the measured indices of Burstein et al. (1984). The 11 index features were then increased to a list of 21 in Worthey et al. (1994) and increased again in Trager et al. (1998) supplemented with several key Balmer hydrogen features from Worthey & Ottaviani (1997). At this point the LICK/IDS index system, as it is known, was comprised of 25 indices in a spectral wavelength range of 4000 – 6000 Å.

Shown in Figure 3.1, an index works by measuring the equivalent width (EW) or magnitude of a filter. A filter is the region of a spectrum, within a defined blue and red pseudo-continua, which corresponds to a specific chemical absorption or emission line. The equivalent width of a spectral feature is the width of a column of the same area as the absorption feature between zero flux and the measured continuum flux. Therefore, the larger the measured absorption line is the larger the index measurement will be. For very broad spectral features such as the CN region or the Mg regions (not including Mgb) magnitude is used instead of EW as the index value depends more on continuum differences caused by multiple lines in the index region, so no single equivalent width can be used to integrate the area of the region. This has no real implications as the area under the continuum is still being used to measure feature strength. Figure 3.1 shows the blue, red and central measurement regions for the LICK/IDS indices CN₁ and CN₂.

Trager et al. (1998) defines a line index as

$$EW = \int_{\lambda_{max}}^{\lambda_{min}} \left(1 - \frac{F_1(\lambda)}{F_c(\lambda)} \right) d\lambda \quad (3.1)$$

where EW is the equivalent width measurement, $F_1(\lambda)$ is the flux of the spectrum and $F_c(\lambda)$ is the flux of the pseudo-continuum, both in the central region defined by λ_{min} and λ_{max} . The blue and red pseudo-continuum fluxes are calculated by:

$$F_p = \frac{1}{\lambda_2 - \lambda_1} \int_{\lambda_1}^{\lambda_2} F_\lambda d\lambda, \quad (3.2)$$

where λ_1 and λ_2 are the wavelength limits of the pseudo-continuum, F_λ is

the individual pixel flux. The wavelength values for the spectral filters and their pseudo-continua is available in Table D.1.

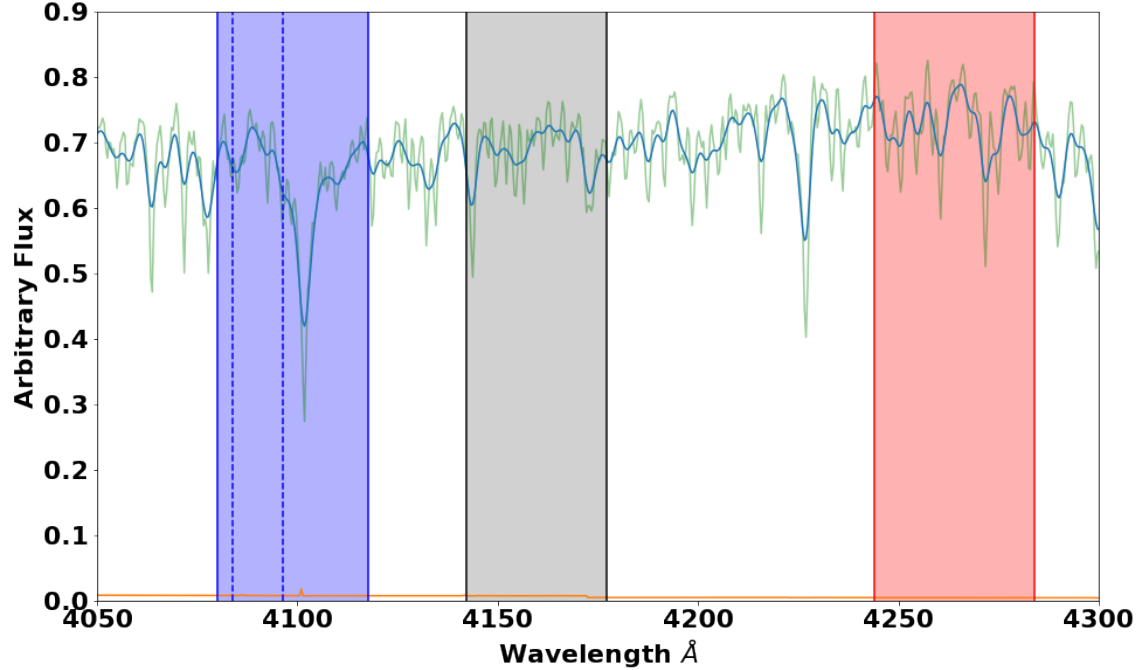


Figure 3.1: The WAGGS spectrum for NGC 2808 (green and blue, the green spectrum shows a resolution of $\lambda_{FWHM} = 0.8 \text{ \AA}$ while the blue spectrum has been smoothed to $\lambda_{FWHM} = 2.51 \text{ \AA}$) with the orange line displaying the $1\text{-}\sigma$ uncertainty from Usher et al. (2017). The vertical columns show the blue and red pseudo-continua of the CN_1 (and CN_2 shown with the dashed blue line) line index with the grey column showing the measured region of the index. CN_2 differs from CN_1 in the blue continuum which omits the $H\delta$ line (signified with dashed lines) making it potentially more useful for stellar populations with hot stars (Worthey et al., 1994).

3.3 The Modern Line Index System

The LIS (Line Index system) was proposed in 2010 by Vazdekis et al. (2010) as library of spectral indices designed to avoid the intrinsic errors associated with

CHAPTER 3

the previous system. LIS uses the same indices as the LICK/IDS system but has improved, wavelength independent, resolutions.

One of the downsides to the original LICK/IDS system was that the resolution varied with wavelength (Table 3.1), a peculiarity caused by the IDS spectrograph used to obtain the data from which the system was defined. Modern spectrographic data has a much higher resolution than the original data used for the LICK/IDS system and therefore the spectra of low velocity dispersion systems like GCs have to be smoothed considerably to match LICK/IDS resolution which potentially discards valuable information. LIS has 3 different resolutions, 5\AA , 8.4\AA and 14\AA (FWHM) which are not wavelength-specific like LICK/IDS but are selected depending on what objects you are studying and is dependant on the observed objects mass. 14\AA is appropriate for massive galaxies, 8.4\AA for low to intermediate mass galaxies while 5\AA is best for GCs and compact dwarf galaxies where the objects velocity dispersion allows for higher resolutions of integrated spectra.

Table 3.1: LICK/IDS FWHM Resolution

λ in \AA	4000	4400	4900	5400	6000
Resolution (FWHM in \AA)	11.5	9.2	8.4	8.4	9.8

In fact, modern spectrographic data of GCs can have higher resolutions for example the $\sim 0.8\text{\AA}$ (FWHM) resolution of the WAGGS survey (Usher et al., 2017) so smoothing to 5.0\AA necessary for the LIS measurements can lose a significant amount of information. As such, in this project where available, the data has only been smoothed to a minimum equivalent resolution for all the data so internal project comparisons can be made (Section 3.4.1).

Figure 3.1 shows the spectra of the object NGC 2808, it has been smoothed with a Gaussian smoothing technique described in Section 3.4.1 to match the resolution of MILES model spectra for full spectral fitting (2.51\AA FWHM, Falc3n-Barroso

CHAPTER 3

et al. 2011). Details more significant than the 1σ uncertainty values have been lost showing the need for higher-resolution models that keep up with the high resolution of modern spectrographs.

In order for the LIS system to be comparable to historical LICK/IDS data a conversion chart was also published in Vazdekis et al. (2010) which can convert LICK/IDS index values to the LIS system at the appropriate resolution for that object:

$$I_{LIS} = a_0 + a_1 \cdot I_{Lick/IDS} + a_2 \cdot (I_{Lick/IDS})^2 + a_3 \cdot (I_{Lick/IDS})^3 \quad (3.3)$$

where a_0 , a_1 , a_2 and a_3 are constants specific for each index at each LIS resolution and are given in Tables D.2 & D.3.

3.4 Methods for Integrated Light Spectral Analysis

This thesis has examined several methods for determining age, metallicity and $[\alpha/Fe]$ from integrated light spectroscopy by both refining previously used methods and developing a method that, to the author's knowledge, has not been used before. This section will discuss those methods and the data processes that needed to be done before analysis could be undertaken.

3.4.1 Smoothing the Data

For the methods used in this project, the resolution of the data and those of the comparison models needs to be the same. If they are not the same resolution it will skew the results in a way that will cause errors in the kinematic measurements (i.e. inaccurate velocity dispersions) and inaccurate comparison of absorption line strengths. Therefore for each set of data a common 'low' resolution was used so that all of the objects and the models were identical.

CHAPTER 3

“High resolution” spectra of galaxies are influenced by the velocity dispersion (σ) of the object observed, only if the instrumental resolution is smaller than the σ resolution of the galaxy. For the data used in this section (WAGGS Usher et al. 2017) there was a common instrumental resolution of $R = 6800$ ($\sim 0.8 \text{ \AA}$ FWHM at 5000 \AA) for all of the data this is equivalent to a velocity dispersion of 19 km/s . This value of σ is larger than that of galactic globular clusters which have velocity dispersions with a mean $\sigma = 5.12 \text{ km/s}^*$ with the largest value in the sample being $\sigma = 17.6 \text{ km/s}$ for NGC 5139 ($\Omega \text{ Cen}$) (Baumgardt & Hilker, 2018). Therefore the instrument resolution for these globular clusters would be used as the resolution of the spectra.

The models that these objects will be measured against are the sMILES models (Knowles et al., 2023). The model resolution is 2.51 \AA (FWHM). This is significantly larger than that of the instrument resolution of the WAGGS GCs. Therefore the GC spectra were smoothed from the instrumental resolution of 0.8 \AA (FWHM) to 2.51 \AA .

The data was smoothed in Python. Firstly an initial reference resolution was given in \AA as a FWHM value at a reference wavelength and then the data was clipped to the specific wavelength range used for the fitting procedures. Then, using the new wavelength range, the reference instrumental resolution was linearly scaled down to the central wavelength of the new range using the equation:

$$B = A \frac{(\lambda_0 + \lambda_1)}{(2\lambda_r)} \quad (3.4)$$

where A is the initial reference instrument FWHM resolution in Angstroms, B is the new instrument FWHM resolution in Angstroms, λ_0 and λ_1 are the start and end wavelength values, where λ_r is the reference wavelength.

Then the quadratic difference between instrument resolution (B) and the desired resolutions (C) was calculated (Δ_{BC}) and the standard deviation for the Gaussian

*Calculated mean from Baumgardt & Hilker (2018), the values are presented in Table A.2

CHAPTER 3

smoothing procedure (σ_{BC}) was calculated with the equation:

$$\sigma_{BC} = \frac{\Delta_{BC}}{2\sqrt{2\ln 2}} \times \frac{1}{\Delta\lambda} \quad (3.5)$$

with $\Delta\lambda$ being the pixel spacing in Angstroms.

Using the python package `scipy.ndimage`: the command “`gaussian_filter1d(spectra, σ_{BC})`” smoothed the data to the new resolution on the same wavelength grid using σ_{BC} as the standard deviation for the smoothing operation. This process was manually checked where a Gaussian shape of known FWHM was used and the process used to smooth the Gaussian to a new resolution where the FWHM was measured and confirmed to be the correct resolution.

Now that the data was at the correct resolution, the analysis methods could be used. This section will look at three different methods: BpPXF, SpPXF, and LISm χ . Below their function is described.

3.4.2 Basic Penalised Pixel Fitting (BpPXF)

BpPXF is just pPXF in its completely standard mode, the prefix B (for “Basic”) is used to separate it from another method used in this thesis which uses pPXF (SpPXF, Section 3.4.3). pPXF (Cappellari & Emsellem, 2004; Cappellari, 2017) is a very versatile tool that has been used previously in many studies for multiple uses (e.g. Göttgens et al. 2019; Boecker et al. 2020; Banister 2020; Davison et al. 2021a,b; Cappellari 2023; Grasser et al. 2023). This project uses it to fit SSP models to the integrated light spectra of CSSs, more specifically here will use it to estimate the age and metallicity of GCs. This process finds the best-fitting combination of SSP models needed to reproduce an input spectrum (Figure 3.2). This section will look into how it works and its multiple uses and limitations.

Penalised Pixel-Fitting (pPXF, and called BpPXF in this project to separate it from other methods) was first developed for IDL but has since been adapted for Python implementation. It was created by Cappellari & Emsellem (2004) but it

CHAPTER 3

has been greatly improved upon since in Cappellari (2017) and again in Cappellari (2023). It was designed to extract stellar or gas kinematics from galaxy spectra and later extended to provide stellar population information. However, it has been shown to work well extracting information from GC spectra (Koleva et al. 2008; Boecker et al. 2020). The process adopts a maximum penalised likelihood approach to the fits based on an input noise spectrum (e.g. Merritt 1997, the implementation of which is outlined in Cappellari & Emsellem 2004) and can be used to extract galaxy kinematics such as radial velocity (V) and velocity dispersion (σ)[†]. pPXF can also do basic stellar population analysis via the production of a plot in age-metallicity space of the fraction of each SSP model used in the best fit produced (bottom panel, Figure 3.2). By using SSP models with different chemical abundances, ages and metallicities one can use pPXF to analyse the integrated light of stellar populations to identify the best-fitting parameters defined in the SSP models.

However, it should be noted that due to the large number of input SSP files for each fit, the solution may not be unique. Other SSP combinations may fit the spectra to an equivalent standard as the fit produced by pPXF. Cappellari describes this as “a textbook example of [an] ill-conditioned inverse problem ... the recovery suffers from severe degeneracies and a unique solution cannot be found”. To attempt to overcome this, pPXF uses regularisation (regularised least-squares minimisation). Regularisation can be thought of as a damping effect on the high-frequency variations in the fit, it is a compromise between the quality of the fit and the noise in the solution and selects the “smoothest solution, among the many degenerate solutions that are *equally* consistent with the data” Cappellari (2017)[‡]. The ideal regularisation

[†]Plus higher order terms in the form of Gauss-Hermite polynomials (van der Marel & Franx, 1993).

[‡]In effect, it prevents a solution being too “bursty” and selecting, for example, a single SSP when it is not possible to be so precise given the available errors and similarities of adjacent SSPs in the age-metallicity space.

CHAPTER 3

parameter (regul) controls this and is set to when $\Delta\chi^2 = \sqrt{2 \cdot N_{Pix}}$ (Cappellari 2017) where $\Delta\chi^2$ is the change in the sum of the squared deviations and N_{Pix} is the number of pixels that need to be fit (after the noise vector is re-scaled with an unregularised fit).

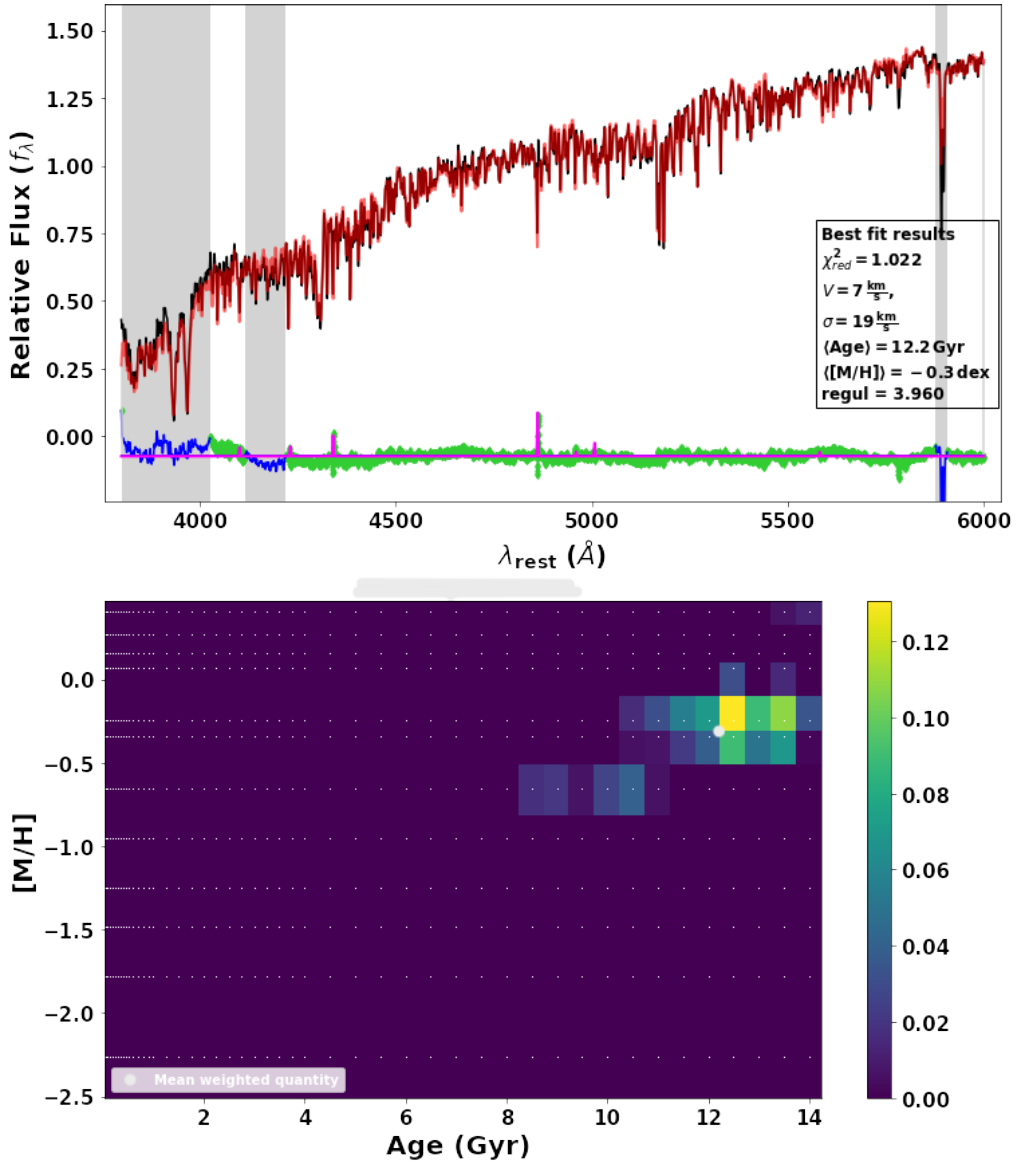


Figure 3.2: The pPXF best fit for NGC 6352 using WAGGS spectral data fitting to sMILES SSP models. Upper: The black line is the spectrum, and the red line is the best-fitting combination of SSP models with the green points being the residuals. The grey regions and blue dots mark areas excluded from the fit and the pink lines show the emission lines that have been masked. Lower: The light-weighted mass fraction of models used in the best fit on the age - metallicity grid.

A key parameter for running pPXF for population studies is “mdegree”. This is

CHAPTER 3

a multiplicative Legendre polynomial which acts to correct the continuum shape of a spectrum, correcting flux continuum issues such as imperfect flux calibration and extinction due to reddening. The value of `mdegree` denotes the number of coefficients in the polynomial and there has been much variation in its value in the literature. Liu (2020) used an `mdegree` value of 10 for the wavelength range $4800 - 5500 \text{ \AA}$, while Cappellari (2023) used a value of 2 for multiple wavelength ranges. It should be noted that the higher the value of `mdegree` the lower the residuals in the output ‘best fit’ spectrum are but this also increases the running time considerably. Therefore for this project, a value of `mdegree = 4` was used for all methods utilising pPXF. The WAGGS data is fairly well flux calibrated and most GCs lie off the galactic plane and have low extinctions. However for CSSs with higher extinctions and potentially poor flux calibrations `mdegree = 4` would be sufficient as including `mdegree` at all make the fit insensitive to reddening (Cappellari, 2023).

Another parameter of the pPXF operation is the additive polynomial labelled “degree” which can change the strength of individual absorption lines. For population studies the pPXF example code which comes with the package states that additive polynomials should be excluded (setting `degree = -1`) but for kinematic extraction `degree` should always be used. They are intended to help with template mismatch and errors during sky subtraction. For this project, `degree` has been ignored except when kinematic measurements have been done in which case the value matched that of `mdegree` at `degree = 4`.

The “`gas_component`” parameter is used to account for emission lines that may be present in the data, it uses known emission line data and flux ratios which are in the utility Python files provided in the package but allows one to add their own emission lines if one would like to exclude certain lines which are not present in their list. As is shown in Section 3.6 there were several WAGGS GCs (such as the LMC and SMC GCs which are projected against their galaxies stars and ISM) that had

CHAPTER 3

emission lines where the use of the parameter: “gas_component” was necessary.

pPXF outputs two plots, one shows the spectrum of the best-fitting combination of SSP models and the input spectrum along with the residual values (top figure in 3.2). The other output plot shows the light-weighted mass fraction of the models used to create the best-fitting model (bottom panel Figure in 3.2).

3.4.3 Single SSP Penalised Pixel Fitting (SpPXF)

SpPXF uses pPXF’s fitting procedure to fit a CSS spectrum to all of the SSP models individually instead of finding a best-fitting combination of SSP models. The best model is decided using a minimum reduced χ^2 solution. This method is not used in the literature as it is not appropriate for galaxies with extended star-forming histories but should work for SSP-like objects such as GCs. It is similar to the minimum χ^2 approach to globular cluster integrated spectra analysis described by Proctor, Forbes & Beasley (2004) and developed for this project as LISm χ (section 3.4.4). However, SpPXF uses the full spectrum instead of individual absorption line indices.

As well as age and metallicity, this process can fit freely to any available alpha abundance value of the models, which in the case of the sMILES models ranged from -0.2 to +0.6 dex with a binning of every 0.2 dex. These models were then interpolated following Section 2.8.5 so that the step in alpha values was $\Delta[\alpha/\text{Fe}] = 0.1$ dex. This had an advantage over BpPXF which could not estimate $[\alpha/\text{Fe}]$. The data could also be interpolated so that there was consistent binning in the metallicity or age values. But it was decided, to save on run time and to avoid any issues caused by non-linear differences between the models used for the linear interpolation, that the original binning would be used. Therefore the $[\alpha/\text{Fe}]$ interpolated SSP model database of 5724 sMILES models are used here.

The method works by only allowing pPXF to fit one SSP model to the object

CHAPTER 3

spectrum at a time and then uses pPXF’s in-built reduced χ^2 routine (which follows equation 3.6 with degrees of freedom being the number of pixels in the spectrum) to produce a goodness-of-fit value for each SSP model, with the lowest value of reduced χ^2 indicating the best fitting model. This has been plotted in Figure 3.3 showing a 3-dimensional plot of age against metallicity against $[\alpha/\text{Fe}]$. For Figure 3.3 the SSP models with the 100 lowest reduced χ^2 have been highlighted showing a grouping of age/metallicity/ $[\alpha/\text{Fe}]$ which mostly agree with literature values.

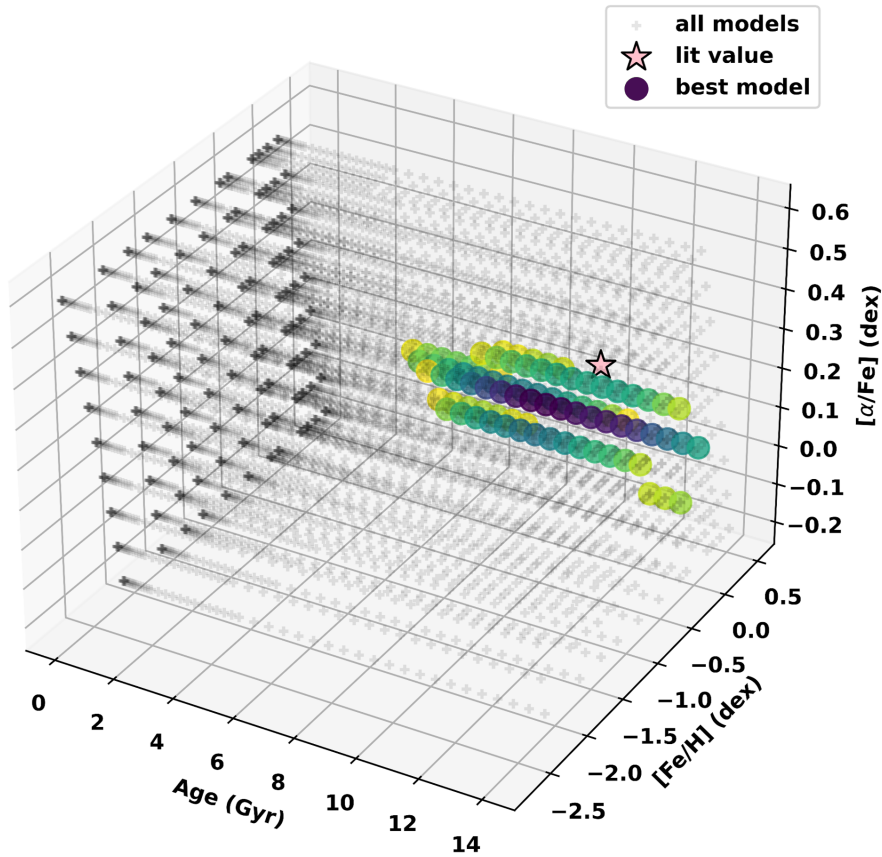


Figure 3.3: A 3d plot of the results of the SpPXF method for NGC 6528. Shown in grey is the position of every available model (5724 models) and the 100 “best” models are shown coloured to their χ^2 value (purple to yellow being the lowest to highest value of χ^2 for the selected 100, respectively), while the literature value is the pink star.

3.4.4 LICK Indices Minimal χ^2 Method (LISm χ)

Another method that has been examined for this project is LISm χ which is a system that uses the line index system and a minimum χ routine similar to that of SpPXF to find the best fitting model. It is based on Proctor, Forbes & Beasley (2004) and measures both the line indices of the CSS spectrum and the SSP models.

The line indices were measured using the Python package PYPHOT. This package uses the method described in Section 3.2 to measure the strength of individual spectral features giving results in the equivalent width or in magnitudes. The next step is to use a χ^2 minimisation technique using only certain line indices to find the most mathematically similar SSP to the GC spectrum. This is a commonly used method (Proctor, Forbes & Beasley 2004, Norris et al. 2008, Zhang et al. 2012 & Fan et al. 2016) but these previous studies use lower resolution and lower signal-to-noise data than is available for this project. Modern data offers much higher resolution spectra with particularly high signal-to-noise in studies such as WAGGS. This could translate into more accurate and precise population information being extracted from the GCs via this method than in previous studies.

The “best” SSP from this method is selected by choosing the SSP with the lowest reduced χ^2 . Reduced χ^2 is calculated via the Equation:

$$\chi_{red}^2 = \frac{\sum((\frac{\delta_{CSS} - \delta_{SSP}}{\sigma_{CSS}})^2)}{DOF} \quad (3.6)$$

where δ represents the line index value and σ the CSS index uncertainty (the SSP models are assumed to have 0 uncertainty, though of course systematic errors can be significant). DOF is the degrees of freedom and is calculated as the number of indices used (which ranges from 4 to over 40 in some of this work) minus the output parameters, which for this project is currently 3 (age, metallicity and $[\alpha/\text{Fe}]$). The uncertainty in lick index measurement is described in Section 3.8.4.

Much like SpPXF, this process can fit freely to any available $[\alpha/\text{Fe}]$ value from the input models. Initially, the same models as SpPXF were used for comparison

with the other two methods, but due to the efficient run time of the code, LISm χ was able to use a much higher level of SSP model binning to more precisely constrain CSS age, metallicity and $[\alpha/\text{Fe}]$. This method does have the same shortfall as SpPXF in that it is not appropriate for galaxies with extended star-forming histories, but as stated previously and as shown in Proctor, Forbes & Beasley (2004), Zhang et al. (2012) & Fan et al. (2016), this method can accurately extract parameters of “simple” populations such as globular clusters giving the light weighted average age metallicity and $[\alpha/\text{Fe}]$ abundance.

3.5 Error analysis

BpPXF, SpPXF, and LISm χ rely on Monte Carlo simulations to calculate uncertainty in the output parameters. Simply put, this is where one varies the input spectrum pixel by pixel by a Gaussian-distribution multiplication of the pixels $1-\sigma$ error value and run the process again, repeating the process multiple times[§]. The standard deviation of the results of the MC simulations can be used as the $1-\sigma$ uncertainty in the age, metallicity, and $[\alpha/\text{Fe}]$ values. An example of a Monte Carlo simulation is shown in Figure 3.4. The uncertainty calculations for each method are described below where each method has been implemented and it is found that only LISm χ has uncertainty calculations that can be run within a short enough length of time to make this method practical for large SSP model grids. The other two methods require significant time to run the Monte Carlo simulations. Because of this, this Chapter provides an average uncertainty value taken from a sample of objects with the same median SNR as the WAGGS GC data for BpPXF and SpPXF.

SpPXF and LISm χ rely on the assumption that CSSs observed are single-population stellar systems. This is, of course, not true even for GCs (Larsen et al. 2014, Bastian

[§]To at least 50 iterations for this project but can be higher or lower for specific applications (Ge et al., 2018).

CHAPTER 3

& Lardo 2018, Milone et al. 2020). The presence of multiple stellar populations could potentially complicate the analysis. However, this can be overcome in both cases by identifying where multiple populations affect an integrated light spectrum. For SpPXF these regions can be omitted from the pixel fitting routine. For LISm χ , line indices that cover the regions affected by multiple populations can be ignored. The only problem with this is that it is often difficult to identify spectral regions that are affected by the chemical enhancements of multiple populations of GCs in actual data. As well as this, there may be systematic errors in the SSPs. SSP models are often made using GCs as references of single simple stellar populations, so it may be the case that SSPs made in this way will not be able to detect the effects of multiple populations and it is difficult to predict how this might affect measurement methods.

The most prominent example of multiple populations affecting integrated light spectra is the extended CN region (top panel Figure 3.2) which is due to strong nitrogen enhancements in the secondary populations (Larsen et al. 2014 & Bastian & Lardo 2018). The topic of chemical abundance anomalies in compact stellar systems is covered in part in Chapter 5 and the regions masked for the methods described in this project are outlined in Section 3.6.2.

3.6 BpPXF

To understand the results of these methods, they were used on the “simplest” stellar systems in this project’s full sample of data: globular clusters. Specifically the WAGGS data set of high-resolution GC spectra, where the comparison with literature values of age, metallicity, $[\alpha/Fe]$, and other chemical abundances, obtained from individual stellar analysis, can be done. For these methods, the models used were the sMILES models with the published age and metallicity binning and $[\alpha/Fe]$ binned to every 0.1 dex between -0.2 and 0.6, (although a finer binning of age and

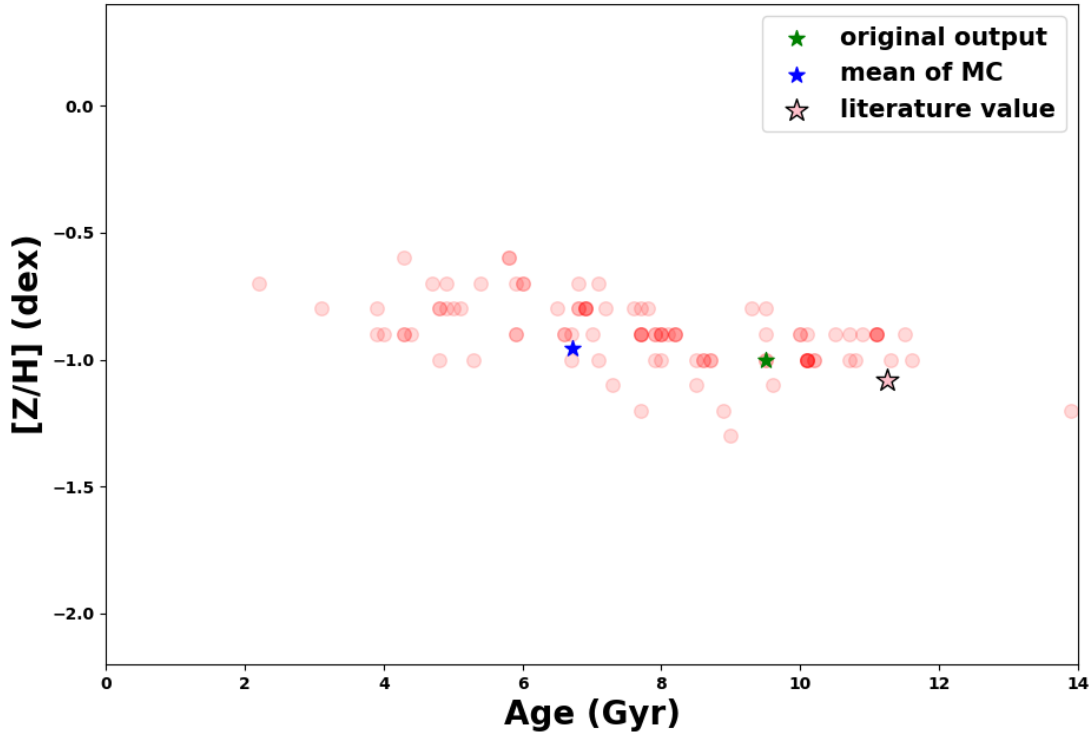


Figure 3.4: This plot shows the results of a Monte Carlo simulation of the LISm χ method (Section 3.4.4) on GC NGC6864. This Monte Carlo simulation also ran with $[\alpha/\text{Fe}]$ as a variable but is not shown in this plot. Shown in this plot is the poor precision in age estimation with this method, which is explained in the next section.

metallicity is used later in this chapter) running BpPXF on 86 globular clusters to find the best fitting combination of SSP models for each. Below the process are described and the results are presented.

3.6.1 Sample Slection

Not all of the WAGGS data was appropriate for these methods. Some globular clusters had poor signal-to-noise values or missing data entirely (NGC 2004 and Fornax 3 respectively) so these were removed from the sample.

CHAPTER 3

The BpPXF best-fitting procedure is a good tool for the visual identification of anomalous emission and absorption lines. Using BpPXF best fits it was found that the SMC GCs NGC 330 and NGC 416 both appeared to possess OIII absorption lines compared to the best-fitting model (Figure 3.5). This OIII absorption is most likely due to errors in the sky subtraction where the sky region used to subtract from the spectrum was polluted by ionised gas in the ISM of the SMC. Figure 2.2 shows the distribution of the selected SMC GCs in the WAGGS sample. Both GCs have significant field stars and ionised ISM surrounding them, which, if used in the sky image for subtraction, could be a cause of excess absorption of OIII. However, without access to the raw data, it is impossible to know what the cause of these issues are. Without knowing the exact ratios between the elements in the ionised gas polluting the sky subtraction it is not possible to know what other effects the gas may have on the rest of the spectrum. The pPXF additive polynomial “degree” would be useful for removing the effects of these absorption lines but degree should not be used in population studies (Cappellari, 2017) so these objects have been excluded from the sample.

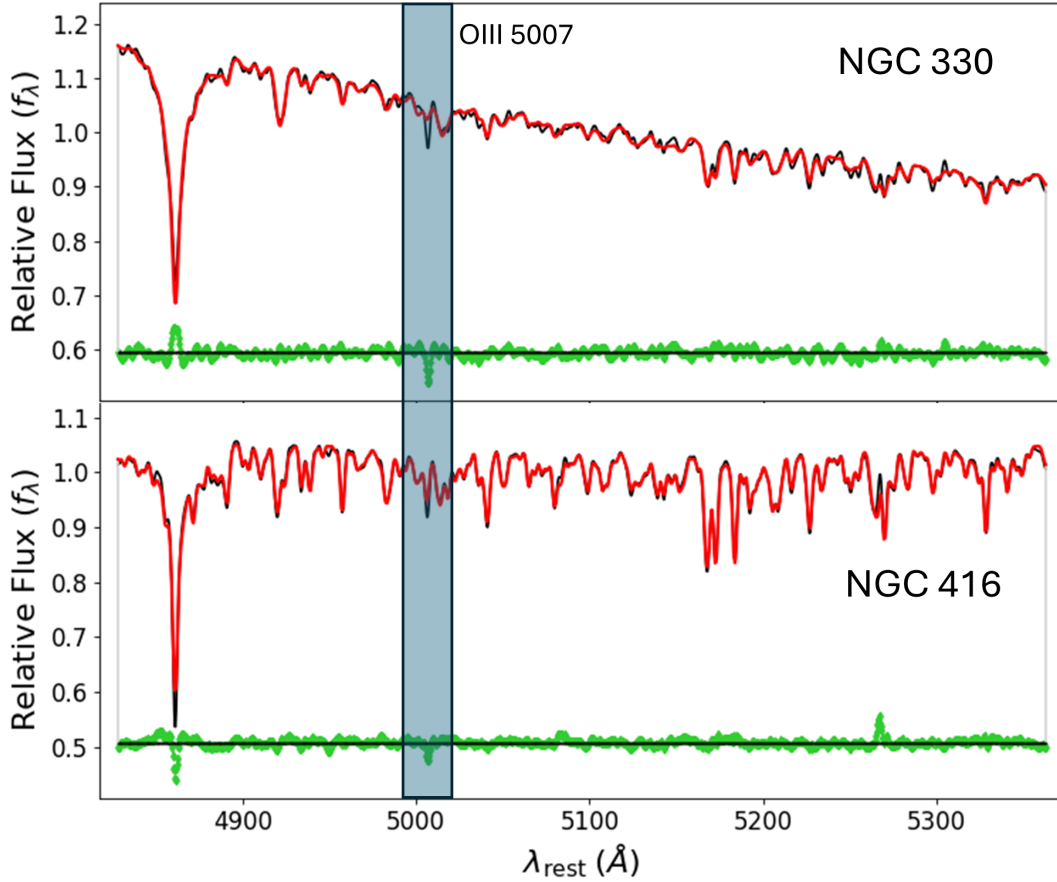


Figure 3.5: The pPXF output for the GCs NGC 330 (top) and NGC 416 (bottom) highlighting the anomalous absorption line at 5007 Å. Note how $H\beta$ is also over and under-sampled in the best-fitting model for NGC 330 and NGC 416 respectively indicating a difference in the ratio between the two. NGC 416 also has anomalous emission at ~ 5270 Å which may also be due to poor sky subtraction.

Other examples of poor sky subtraction are the GCs NGC 1898, NGC 4590, NGC 6522, NGC 6553, NGC 6752, NGC 7006 and NGC 7099 which all possess emission lines at 5577 Å which is a bright sky emission line. This indicates that not enough sky was subtracted from the GC spectrum for each object. The 5577 Å line is a line caused by the earth's atmosphere, atmospheric (telluric) lines are

CHAPTER 3

well studied and can be masked in pPXF therefore these objects are still included with known telluric regions masked. Although other regions are likely affected by under-subtraction of the sky to an unknown degree.

The SMC GC NGC 361 possesses OIII emission lines and this is possibly due to the same (but opposite) effects as NGC 330 and NGC416 where poor sky subtraction is not taking into account the spectrum of this object also possesses a very large emission line at 5577 indicating that this object has not been satisfactorily sky subtracted and is therefore removed from the sample. What is unfortunate is that the loss of NGC 361, combined with the loss of NGC 416 means that there are no longer any intermediate-age star clusters for analysis with this sample.

The WAGGS spectrum of Fornax 5, NGC 1850, NGC 2100, and NGC 6352 also possess OIII and hydrogen emission lines, while NGC 6637 just possesses Balmer hydrogen emission lines. Further study on the emission lines of these GCs is presented in Section 3.8.2. To keep the sample as large as possible, these were still included with their emission lines masked out in pPXF. In pPXF emission lines can be accounted for: for these objects, OIII and Hydrogen Balmer emission lines were “filled in” out from the fit using pPXF’s inbuilt gas emission line masking program which can exclude the emission lines at fixed ratios or freely omits emission lines of any strength. The ionised gas of a PNe (if these are the cause of the emission) has specific emission lines (Douglas et al., 2002) that pPXF can mask out. Any continuum effects (Byler et al., 2017) caused by light from ionised gas can be accounted for by the multiplicative Legendre polynomial applied to the spectrum before fitting which (as explained previously) is meant to account for any continuum effects from poor flux calibration, but also works here to cancel any anomalous continuum effects.

After the sample had been selected and the appropriate line masking had been done BpPXF was run on all remaining GCs. The sample selected for this method

CHAPTER 3

(and the appropriate line masking) was used for the other two analysis methods where applicable. The total GC count used with these methods was 82, 2 from Fornax, 3 from the Small Magellanic Cloud, 13 from the Large Magellanic Cloud, and 64 from the Milky Way.

3.6.2 Wavelength Ranges

The WAGGS spectra covered a wavelength range of 3290 - 9100 Å which covers near UV to near infrared. For this section of the project sMILES models are used. These models cover 3540.5 - 7409.6 Å which limited the selected range available for study.

It was decided that 3 different wavelength ranges would be examined (Figure 3.6), the largest of which is 3800 - 6000Å. This range was chosen so that important metal lines such as CaH&K, Mgb, Fe5270, Fe5335, and NaD could be studied as well as many Balmer hydrogen lines which are the key age indicators for visible light spectra. 3800Å was decided as the blue cut-off as a lot of the WAGGS data below this point had SNR too low to extract meaningful data. The red limit of the wavelength range was chosen as 6000 Å due to the run time of the code. Greater wavelength ranges greatly increased the runtime and enough key spectral features were included to extract meaningful data within this range.

As was shown in Banister (2020) this spectrum range includes regions affected by the presence of multiple populations. Therefore, as well as the “full” range of 3800 - 6000 Å, it was decided to study a second “omitted” wavelength range in pPXF which was still 3800 - 6000 Å, but with some key regions excluded from the fit. The extended CN region described in Banister (2020) of 4117 - 4218 Å was masked. It was noted that for many GCs the SNR below ~ 4000 Å was comparatively low to the data from the other gratings (Table 2.2). Because of this, anything lower than 4010 Å was omitted from the fit while still showing it in the fits to observe any anomalously poor fitting regions. The NaD doublet around 5890 and 5896 Å was

CHAPTER 3

also masked, although it is a key metallicity indicator it has a known problem of being affected by blending with absorption lines in the interstellar medium (Welsh, Vedder & Vallergera, 1990; Koo et al., 2022) and sodium is one of the elements showing anomalous abundance patterns in the MP phenomenon (e.g. Milone & Marino 2022).

LISm χ allows one to choose which individual spectral features can be used for a ‘best fit’. The simplest combination of LIS indices which can still provide useful information on age (primarily from H β), metallicity (Mg and Fe lines) and $[\alpha/\text{Fe}]$ (Mg, Zheng et al. 2019) used are H β , Mgb, Fe5270, and Fe5335 where the alpha insensitive $[\text{MgFe}]'$ is used as a metallicity indicator. $[\text{MgFe}]'$ is calculated from

$$[\text{MgFe}]' = \sqrt{\text{Mg}_b(0.72 \times \text{Fe5270} + 0.28 \times \text{Fe5335})} \quad (3.7)$$

(Thomas, Maraston & Bender, 2003). For comparison with this spectral range, the other analysis methods are restricted to the same spectral ranges as the four LIS indices used in LISm χ which is labelled as the “narrow” range which has a lower limit of 4828 Å (the blue end of the blue pseudo-continuum for the H β index) and an upper limit of 5363 Å (the red end of the red pseudo-continuum of the Fe5335 index). This “Narrow” wavelength range is similar to that used with the Sauron and Atlas3D projects (Bacon et al., 2001; Cappellari et al., 2011).

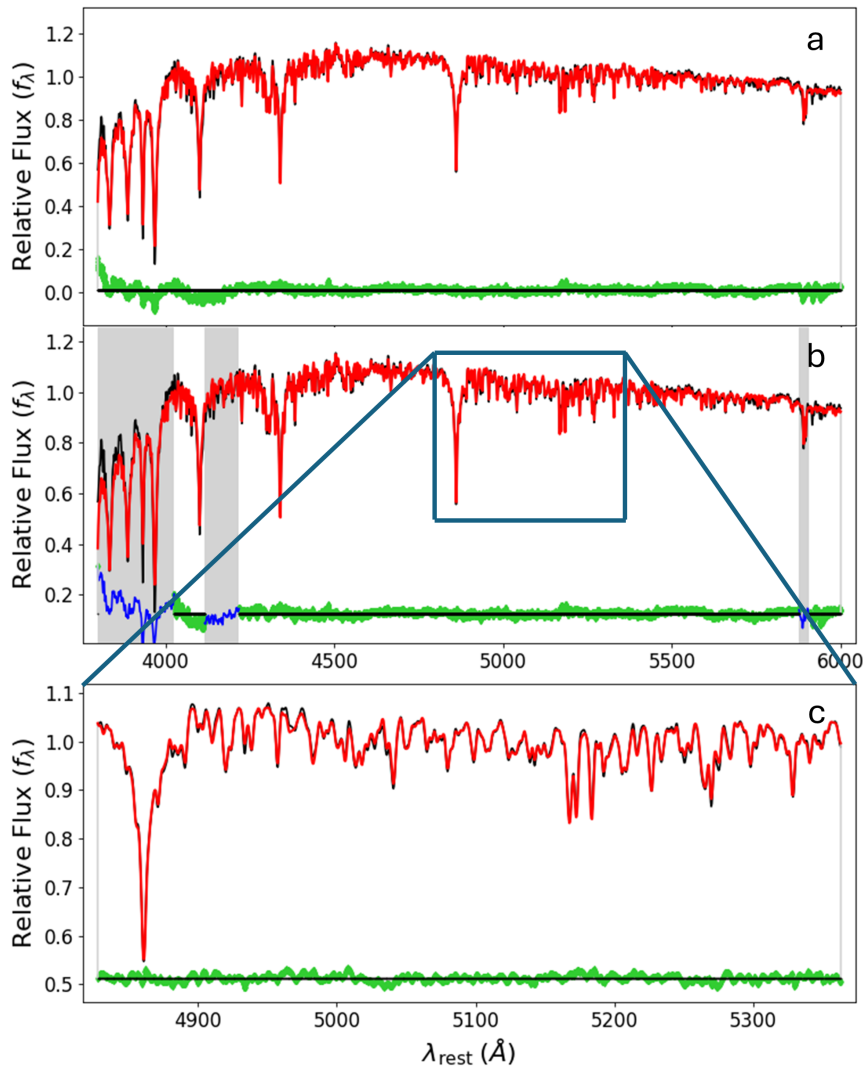


Figure 3.6: The three fitting regions used for this section a: Full, b: Omitted, and c: Narrow. Figure ranges from 3800 - 6000 \AA , b has the same range but excludes known anomalous or low SNR regions, c is a narrower wavelength range of 4828 - 5363 \AA and is representative of the LIS indices $H\beta$, Mgb Fe5270 and Fe5335. The plot shows the output from BpPXF with the black line being the input spectra, the red showing the best fitting model combination and the green showing the residual to the fit. Grey regions and blue lines show the regions omitted from the fit and the residuals in that area.

3.6.3 Running pPXF

Although publications have managed to run pPXF with age, metallicity, and $[\alpha/\text{Fe}]$ as variables (Liu, 2020; Grasser et al., 2023), this required customisation of the pPXF version used here (8.2.6). This project only ran pPXF with SSPs of one $[\alpha/\text{Fe}]$ value at a time. While the code to run pPXF with $[\alpha/\text{Fe}]$ as a third fitting parameter was written for this project it was decided that it would not be used due to the run time needed for the number of models used and that the more models used the more ill-conditioned the results become. For this project, an attempt to utilise SpPXF and LISm χ to fill the gap of $[\alpha/\text{Fe}]$ measurements is undertaken.

The selected SSP model $[\alpha/\text{Fe}]$ value was $[\alpha/\text{Fe}] = 0.3$. This was because the mean $[\alpha/\text{Fe}]$ value of MW GCs with known values is 0.27 (calculated from data in Table A.1) and $[\alpha/\text{Fe}] = 0.3$ was the closest binning in the SSP sample. To save run time, and for equivalent comparison with all GCs using the same SSP sample the same $[\alpha/\text{Fe}]$ value was used for all GCs. However, it should be noted that $[\alpha/\text{Fe}]$ values for the Magellanic cloud GCs are lower on average at ~ 0.1 for those with published values (Table A.1). There were a total of 636 sMILES SSP models used for this method at 53 ages and 12 metallicities. These were used at their base resolution of 2.51\AA (FWHM) with the GC spectra smoothed to the same resolution.

Regularisation (‘regul’) was a key parameter in the operation of BpPXF (Section 3.4.2). It had to be input to the operation so that $\Delta\chi^2 = \sqrt{2N_{pix}}$ after a first unregularised fit was done. This had to be done iteratively where BpPXF would be run with differing values of regul input each time until the desired value of $\Delta\chi^2$ was reached. Davison (2021) wrote a programme that iterated BpPXF until the ideal regul value was found. This code was written for high SNR MUSE galaxy data. Generally, it has been found in this project that the lower SNR GCs require higher regul values (e.g. Figure 3.7). So the code was rewritten to accommodate this ‘noisier’ data by allowing for larger ranges in the initial regul estimations before

CHAPTER 3

locating the ideal value and removing the cap on the regularisation value. The fitting function was also changed to accommodate larger regul values.

At very low regul values (< 2) the value of $\Delta\chi^2$ tends to increase at an exponential rate with regul but for the values of regul higher than this, $\Delta\chi^2$ behaved logarithmically. The typical regul value needed for the WAGGS GC data was ~ 35 and so a logarithmic fitting procedure was written. Based on Thomas' work, the code chose an initial "high" and "low" which were above and below the predicted desired regul (iteratively increasing or decreasing the value of regul until the values were above or below the desired $\Delta\chi^2$). Then two intermediate values were chosen: one, halfway between the high and low values and one-half again between the new value and the low value. This is different from the original code as it was found that having two intermediate fits allowed for quicker acquisition of the desired regul. These four values were then used with the `curve_fit` function from the `scipy.optimize` python package using the simple logarithm equation $f(x) = a \log(x + b) + c$ to fit a curve to them. This curve was then used to predict the desired regul value. The predicted value was then entered into BpPXF as a new regularisation estimation and a new curve was fitted until $\Delta\chi^2$ was within 0.1 of the desired value (this value was deemed acceptable as anything lower than this provided negligible difference in the calculated $\Delta\chi^2$). This typically took between 6 and 10 iterations but was significantly quicker than iterating manually. If the data points would not fit to the curve then the code resorted to a linear fit which would take longer to find the true solution but would always work.

It is common understanding when using pPXF that $regul > 100$ results in an un-physical fit. This is generally because the amount of smoothing of the solution results in an unrealistically large combination of SSP ages and metallicities. Thomas' iteration code physically stopped the value of regul exceeding this number. However, due to the decrease in signal-to-noise plus some of the poor sky subtractions, the

CHAPTER 3

regul value was sometimes driven to unrealistic values. Rather than forbid this, the regul value was allowed to achieve unrealistic values but have noted in the plots where these values are (Figures 3.8, 3.9 & 3.10 where the GCs with “bad” regul values are highlighted with a shaded box). Through tests where high SNR data was degraded to lower SNR data, it was found that when high regul values are used it generally does not change the output mean weighted age and metallicity values from the BpPXF fit. Rather, it just increases the smoothness of the fit, increasing the number of models used but not changing the output mean value except for when peak age or metallicity was at an extreme and the excess smoothing dragged the mean value away from the true value. Measurements made using BpPXF where regul is above the 100 mark are not used in mean calculations in the result figures (Figure 3.8, 3.9,& 3.10) but are, highlighted showing their measured values. Figure 3.7 shows the regularisation factors for each of the WAGGS GCs with the different wavelength regions. It shows that the only objects with $\text{SNR} \leq 100$ had regul values in excess of the 100 cap, reinforcing the need for high SNR data for the optimal extraction of stellar population information.

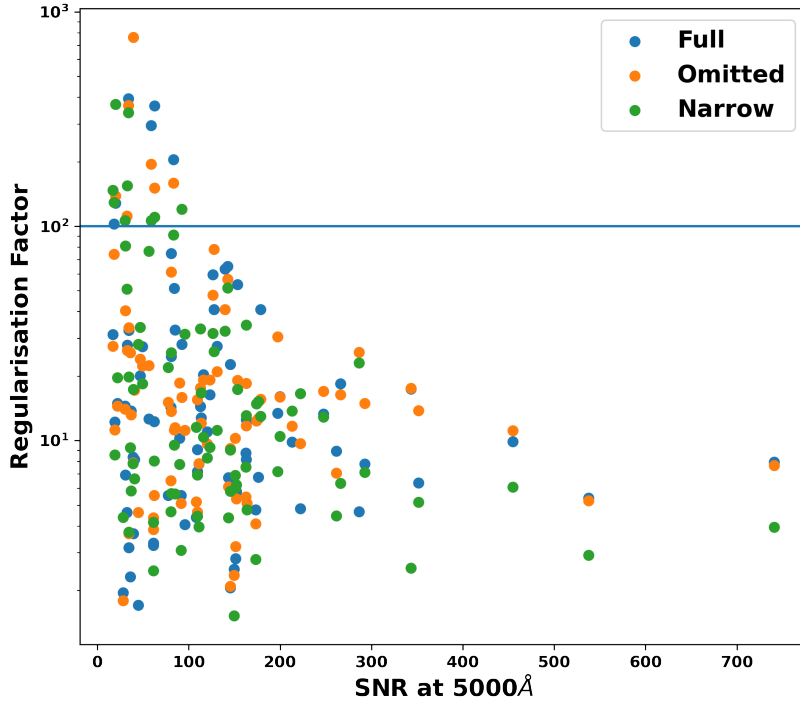


Figure 3.7: Regularisation factor against signal-to-noise for the WAGGS GCs using BpPXF in the different wavelength ranges introduced in Section 3.6.2. The blue horizontal line indicates the $\text{regul} = 100$ cutoff.

pPXF methods can take a significant time to run compared to LISM χ . This depends on many factors: fundamentally though, the number of SSP models used, the number of pixels in the wavelength range, and the value of the multiplicative Legendre polynomial all contributed to the run time significantly. A typical full run of non-regularised fit, regul iteration, final run with desired regul would require 5 - 10 minutes per spectrum. While this may seem quick, each object required three runs for the full, omitted, and narrow wavelength ranges and there were 86 GCs in the sample all of which required inspection for anomalous emission, absorption, or continuum effects before the GCs with bad data were trimmed. For the error calculations, it is recommended that Monte Carlo simulations be used to determine

CHAPTER 3

a spread in the output age and metallicities. This however increases the run time of this method considerably and should be considered when measuring the benefits of each method presented here.

3.6.4 Results

This section will cover the key findings of the BpPXF approach to age and metallicity estimation of the WAGGS GC spectra, the results of which can be found in Table B.1.

Firstly it should be said that this method can find both the kinematics of objects and the stellar population which make them up. For this section however, focus is put on the population study.

Metallicity in BpPXF is output as “[M/H]” as this is what the SSP models’ metallicity is measured in. For comparison with literature, metallicity will be measured in [Fe/H]. For this, the following conversion is used:

$$[M/H] = [Fe/H] + a[\alpha/Fe] + b[\alpha/Fe]^2 \quad (3.8)$$

where a is 0.66154 ± 0.00128 and b is 0.20465 ± 0.00218 from Knowles et al. (2023), in this case $[\alpha/Fe] = 0.3$ is used to convert the BpPXF output values.

Looking first at age, Figure 3.8 shows the results of BpPXF on the all of the GCs in the WAGGS sample for the “Full” wavelength range. The Figure shows the output age and metallicity values compared to literature values (which were measured from CMD fitting, presented in Table A.1). The results show a general underestimation in age from this method compared to the literature. The age residual has a general increase towards the lower metallicities but is present in almost all older GCs (with the exception of some metal-rich GCs whose age output was overestimated along with an overestimation of metallicity).

For the different wavelength ranges, Figures 3.9 & 3.10 show how the problem of age underestimation is present in all wavelength ranges. However, the effects

CHAPTER 3

of it are different in each. The ‘narrow’ wavelength range (4828 - 5464 Å) which used $H\beta$ as its main age indicator has a greater mean offset in ages than that of the ‘full’ spectrum (3800 - 6000 Å). The fits with the omitted region show greater residuals than the full region as well. This is because the removal of the poor fitting regions from the fit has caused the older GCs, which showed age overestimation and poor metallicity estimation, to have an age underestimation which agrees with the underestimations found in lower metallicities. This indicates that the poor metallicity estimations of the full region are likely due to MPs.

The measurements of age offset (literature age minus measured age) have been split to either side $[Fe/H] = -1.0$ (dex) (shown in all of the results figures of this section where metallicity is displayed as a black dashed line). This is because lower metallicities tend to have larger age underestimations than the more metal-rich GCs and the offsets seem to be larger after this metallicity value. The reasons for this are complex and are likely due to anomalous populations of stars skewing the age estimation, the fraction of which are dependent on cluster metallicity. This topic is explored further in Chapter 4 where SSP models are adapted in order to offer a partial solution to the age problem. The split in the GCs here also represents the more massive CSSs which will be studied later, which in general have higher metallicities equivalent to the more metal-rich GCs.

While there is a general age under-estimation trend with BpPXF, the metallicity is generally well predicted with a slight overestimation in metallicity in the ‘full’ wavelength range for the objects with age overestimation. The ‘narrow’ wavelength range identifies metallicity with the most accuracy with the lowest standard deviation in the residuals to literature (Figures 3.11 & 3.12). This is most likely due to there only being 3 key metallicity lines in the region Mgb, Fe5270 and Fe5335 where the ‘full’ region has many metal lines which could be affected by population issues and would contribute to the measured metallicity.

CHAPTER 3

Figures 3.8, 3.9 & 3.10 show that the GCs with poor regul values differed for each wavelength region. There are more omitted GCs with larger age residuals in the ‘narrow’ data compared to the ‘full’ data. This results in biasing in the mean residual and the standard deviation. When the GCs with bad regul values are included, the age underestimation is more apparent in the mean offset and the standard deviation is more in trend with the scatter that is seen in the Figures.

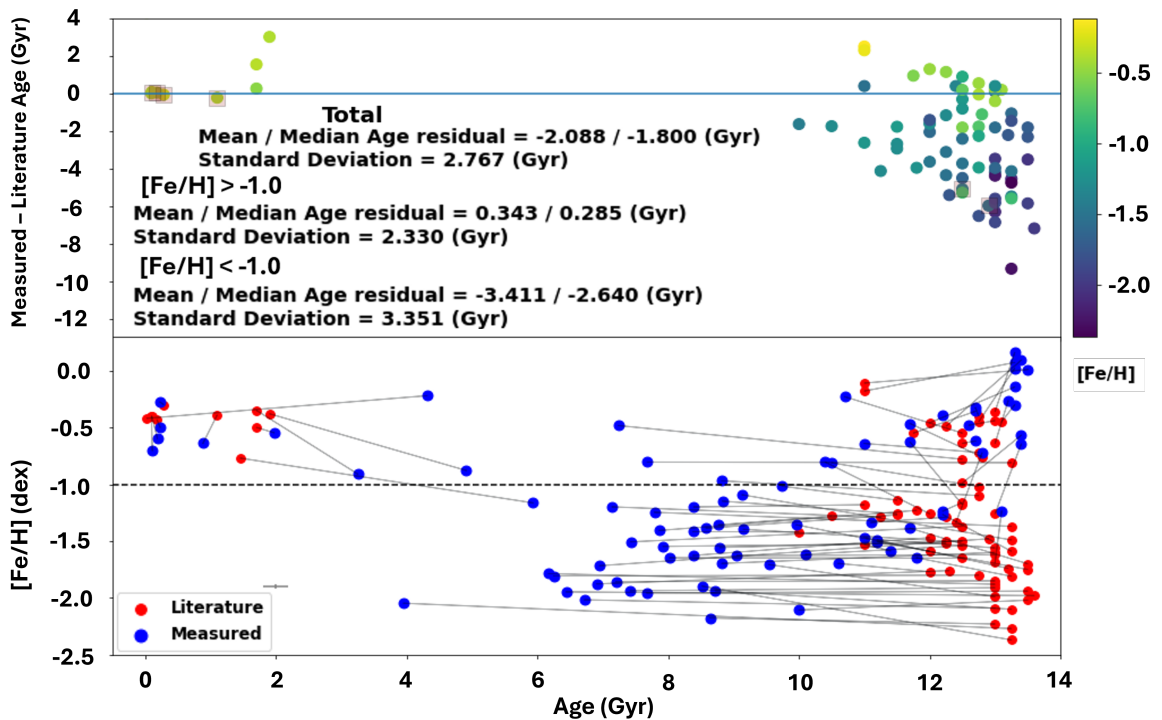


Figure 3.8: Plot of BpPXF outputs for the “Full” wavelength range 3800 - 6000Å using $[\alpha/\text{Fe}] = 0.3$ sMILES SSP models. Top: The literature age of the WAGGS GC sample against BpPXF age - literature age. Bottom: An age Vs $[\text{Fe}/\text{H}]$ plot showing the literature values for the WAGGS GC sample (red) and the BpPXF outputs (blue) with the grey lines indicating the differences between output and literature.

CHAPTER 3

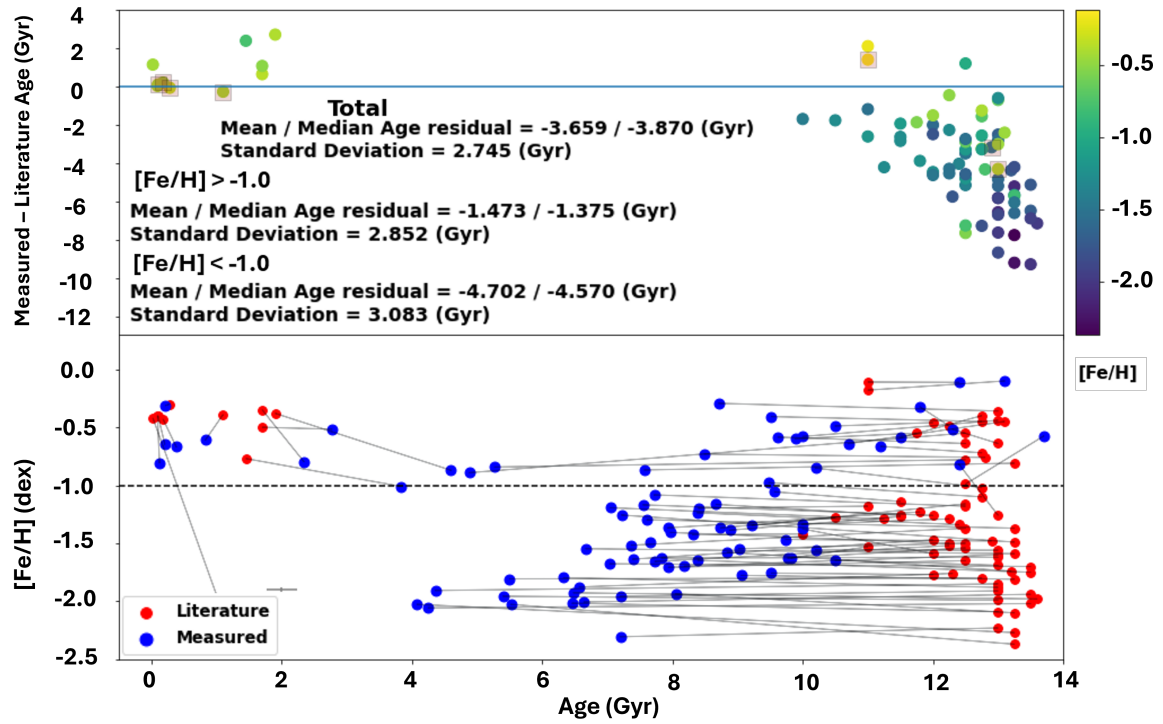


Figure 3.9: Plot of BpPXF outputs for the “Omitted” wavelength range 3800 - 6000Å using $[\alpha/\text{Fe}] = 0.3$ sMILES SSP models with the regions indicated in part b of Figure 3.6 omitted from the fit. Top: The literature age of the WAGGS GC sample against BpPXF age - literature age. Bottom: An age Vs $[\text{Fe}/\text{H}]$ plot showing the literature values for the WAGGS GC sample (red) and the BpPXF outputs (blue) with the grey lines indicating the differences between output and literature.

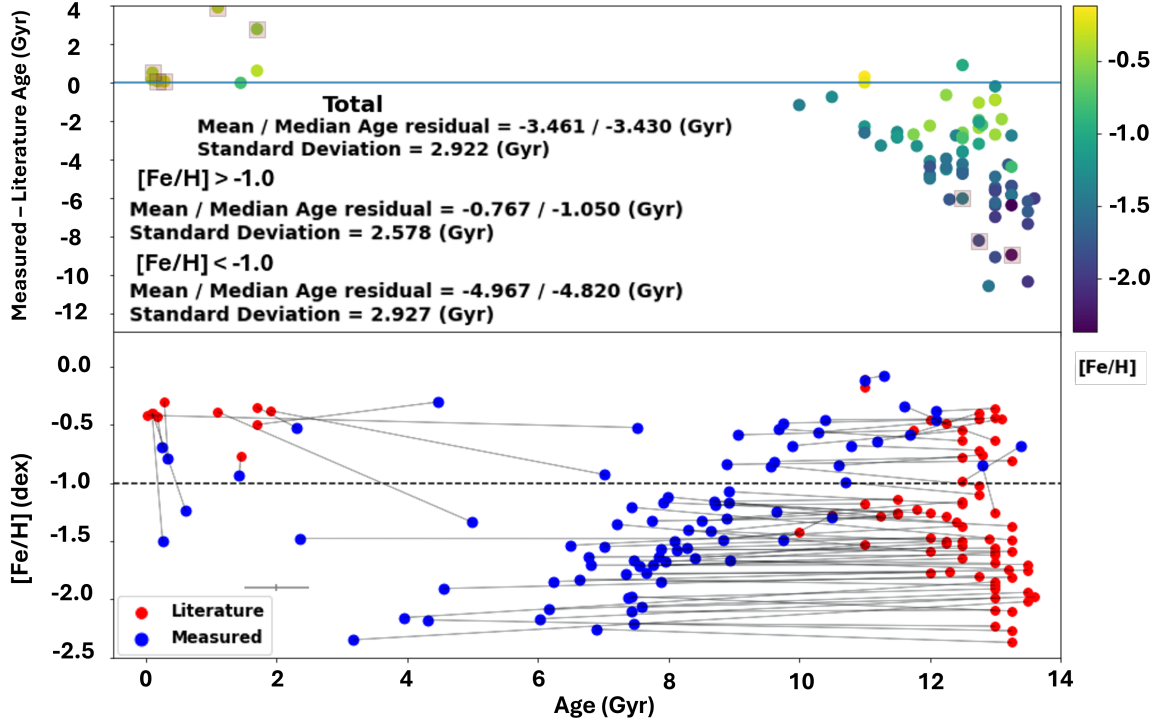


Figure 3.10: Plot of BpPXF outputs for the “Narrow” wavelength range 4828 - 5363Å using $[\alpha/\text{Fe}] = 0.3$ sMILES SSP models. Top: The literature age of the WAGGS GC sample against BpPXF age - literature age. Bottom: An age Vs [Fe/H] plot showing the literature values for the WAGGS GC sample (red) and the BpPXF outputs (blue) with the grey lines indicating the differences between output and literature.

Figure 3.11 shows how metallicity is generally very well fit using this method (especially for MW GCs in Figure 3.12). The narrow wavelength range show less scatter in general except for an anomalous group of GCs where there is strong metallicity underestimation. This group of GCs are young metal rich GCs from the Magellanic Clouds. Figure 3.12 and Table 3.2 show how the metallicity estimations are better for Milky Way GCs as opposed to extragalactic ones. This is most likely due to the $[\alpha/\text{Fe}]$ used for the SSP models. The $[\alpha/\text{Fe}]$ abundances of younger metal-rich GCs (for example, in the Magellanic Clouds) is lower than that of older

CHAPTER 3

GCs (Wallerstein, 1962; San Roman et al., 2015; Bentley et al., 2022; Mucciarelli et al., 2023a,b). With models that are too enhanced in $[\alpha/\text{Fe}]$, the output metallicity will be underestimated causing the GC to appear more metal-poor than it actually is.

The colour bar of Figures 3.11 & 3.12 show the correlation between age residual and cluster metallicity mentioned earlier. The causes of this phenomenon are discussed in Chapter 4 where methods of accounting for age under estimation and metallicity correlation are presented.

Table 3.2: The output age and metallicity residual values for BpPXF using only Milky Way GCs.

λ region	Δ_{Age} (Gyr)	$\sigma_{\Delta_{\text{Age}}}$ (Gyr)	$\Delta_{[\text{Fe}/\text{H}]}$ (dex)	$\sigma_{\Delta_{[\text{Fe}/\text{H}]}}$ (dex)
Full	-2.494	2.536	0.184	0.241
Omitted	-4.064	1.862	0.032	0.138
Narrow	-4.118	1.634	0.003	0.135

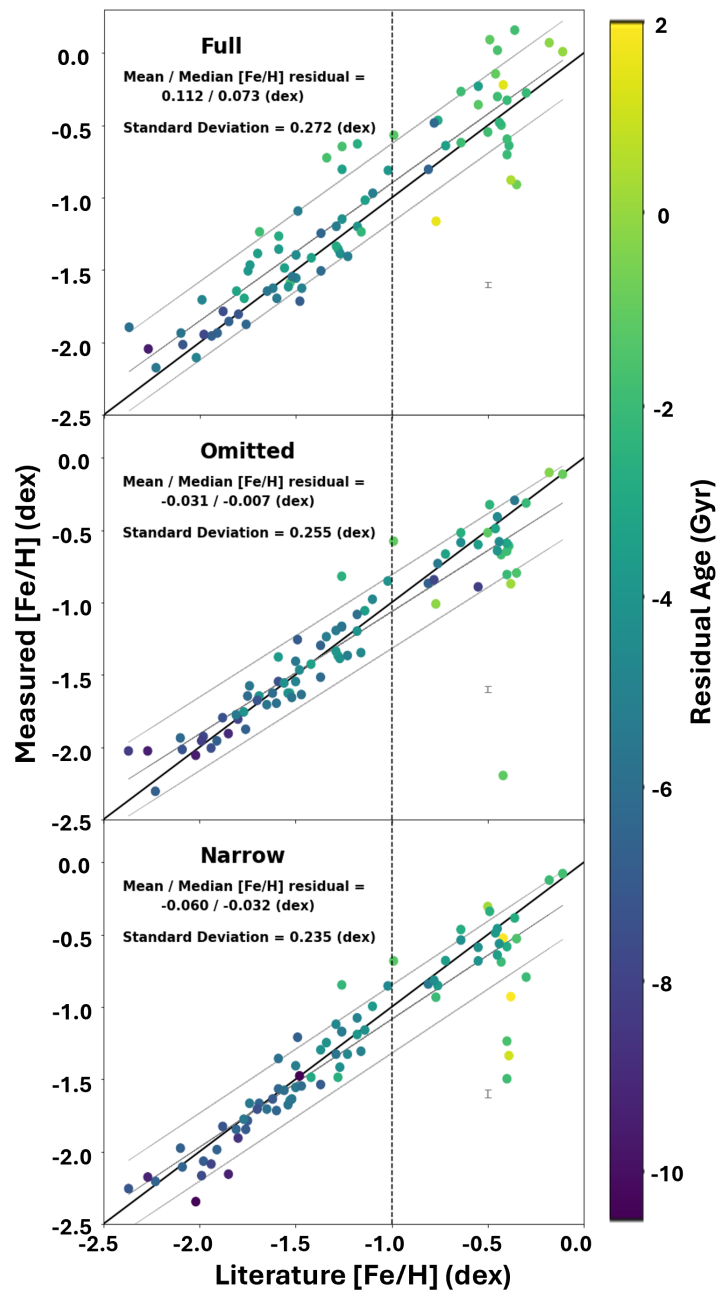


Figure 3.11: Literature [Fe/H] against BpPXF output [Fe/H] (converted from [M/H] using Equation 3.8) for the GCs of the WAGGS sample for the 3 different wavelength regions. The solid black line is a 1-to-1 positive correlation line going through [0,0], the black dashed line represents the metallicity split mentioned earlier, while the solid grey lines represent a linear least squares fit (middle grey line) and standard deviation (either side).

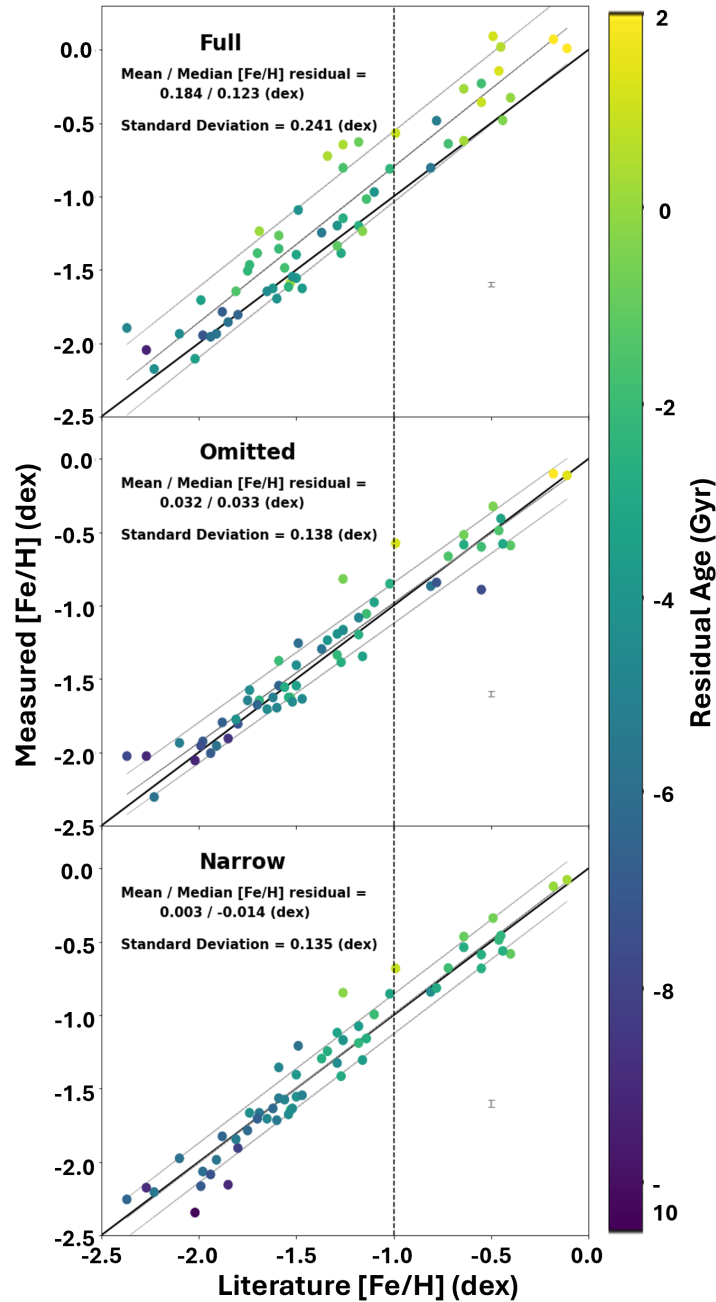


Figure 3.12: Similar to Figure 3.11. Literature $[\text{Fe}/\text{H}]$ against BpPXF output $[\text{Fe}/\text{H}]$ (converted from $[\text{M}/\text{H}]$ using Equation 3.8) for the Milky Way GCs of the WAGGS sample for the 3 different wavelength regions. The solid black line is a 1-to-1 positive correlation line going through $[0,0]$, the black dashed line represents the metallicity split mentioned earlier, while the solid grey lines represent a linear least squares fit (middle grey line) and standard deviation (either side).

3.6.5 Uncertainty Calculations

To measure the uncertainties of BpPXF Monte-Carló simulations were ran. The way this would work for BpPXF is to change the input spectra by a Gaussian distribution of the pixel error for each pixel by the equation:

$$\text{pixel}_{\text{new}} = \text{pixel} + \text{random number} \times \sigma_{\text{pixel}} \quad (3.9)$$

where each pixel in the spectrum is added with gaussian noise drawn from the $1\text{-}\sigma$ error spectrum. Then the BpPXF is run again. Ideally, many runs are completed for each object where the individual uncertainty of each GC can be measured. However, due to time constraints and the extended run time of BpPXF it was decided to run Monte-Carló simulations on a small sample of 10 GCs at a range of SNRs whose mean SNR was equivalent to the mean SNR of the whole WAGGS GC sample. The standard deviation of the Monte-Carló outputs was then the uncertainty of a specific object, and the mean of these values provided representative equivalent uncertainties for the whole sample.

50 iterations per Monte-Carló simulation were run, as is common practice for BpPXF Ge et al. (2018), the results of which are shown as grey errorbars in the Figures 3.8, 3.9, 3.10, 3.11, & 3.12. The uncertainties show that in general, the results for age and metallicity are precise in their measurements. As the wavelength range decreases the uncertainties increase, however. So while the larger wavelength range produces errors due to MPs it actually offers smaller uncertainties. Therefore it is concluded that the wavelength range which provides the most accurate information is the ‘‘Omitted’’ range which excludes the effects of MPs and still covers a large fraction of the wavelength range extracting useful spectral population information.

3.7 SpPXF

For this method, the same sample selected for BpPXF is used. Because this method uses pPXF as its base the same emission lines can be masked in the same way as the previous method.

SpPXF runs pPXF for an objects spectrum on each SSP model in the sample one at a time and produces a reduced χ^2 value for each model which is used as a representation of how well fit the model is to the object spectrum. The minimum value of reduced χ^2 represents the best-fitting model.

Normally for pPXF the noise spectrum is normalised and then iterations of the fit are run with different regularisation values in order to get $\Delta\chi^2 = \sqrt{2N_{pix}}$. This changes the error of the object’s spectrum for each different regularisation used and would make the χ^2_{red} values incomparable. Therefore the regularisation factor for each was set to zero and the noise spectrum not normalised.

The outputs of this method were the parameters of the selected “best fitting” SSP model meaning the binning of the SSP model grid directly influenced the precision of the results. For the sake of run time, however, the same model binning that Knowles et al. (2023) produced for the sMILES models was used.

For comparison with BpPXF this method was first run on sMILES SSP models with $[\alpha/Fe] = 0.3$. This method, however, can be used on SSPs with multiple $[\alpha/Fe]$ values at the same time. The binning of the $[\alpha/Fe]$ is every 0.1 dex. The output $[\alpha/Fe]$ value can ideally be used to identify which SSP models should be used with BpPXF. The results of this method for each object in the WAGGS sample are presented in Table B.2.

3.7.1 Using sMILES with $[\alpha/Fe] = 0.3$

Firstly, to compare with BpPXF this process was run with the same $[\alpha/Fe] = 0.3$ SSP models. Much like BpPXF, there is a large underestimation in age with a mean

CHAPTER 3

residual of $\Delta_{Age} = -2.51 \pm 3.81$ Gyr for 3800 - 6000 Å. BpPXF highlighted that non-MW GCs cause greater residuals, so here two sets of results are presented, one using all WAGGS GCs and the other using only MW GCs. Using only MW GCs produces a mean age underestimation of $\Delta_{Age} = -2.847 \pm 3.998$ for the full spectral range of 3800 - 6000 Å. This indicates that the younger non-MW GCs have better age estimations (Figure 3.13). Comparing the lower half of Table 3.3 and Table 3.2, the age residuals are on average ~ 0.5 Gyr larger for SpPXF with a larger spread with the standard deviation an average of 1.457 Gyr larger for SpPXF across all of the wavelength regions.

Table 3.3: The output age and metallicity residual values for SpPXF GCs and $[\alpha/Fe] = 0.3$ sMILES SSP models.

λ region	GCs	Δ_{Age} (Gyr)	$\sigma_{\Delta_{Age}}$ (Gyr)	$\Delta_{[Fe/H]}$ (dex)	$\sigma_{\Delta_{[Fe/H]}}$ (dex)
Full	All	-2.565	3.792	0.075	0.216
Omitted	All	-4.132	3.456	0.009	0.162
Narrow	All	-3.863	3.056	-0.036	0.188
Full	MW	-2.847	3.998	-0.117	0.206
Omitted	MW	-4.580	3.456	-0.042	0.150
Narrow	MW	-4.465	2.848	-0.005	0.160

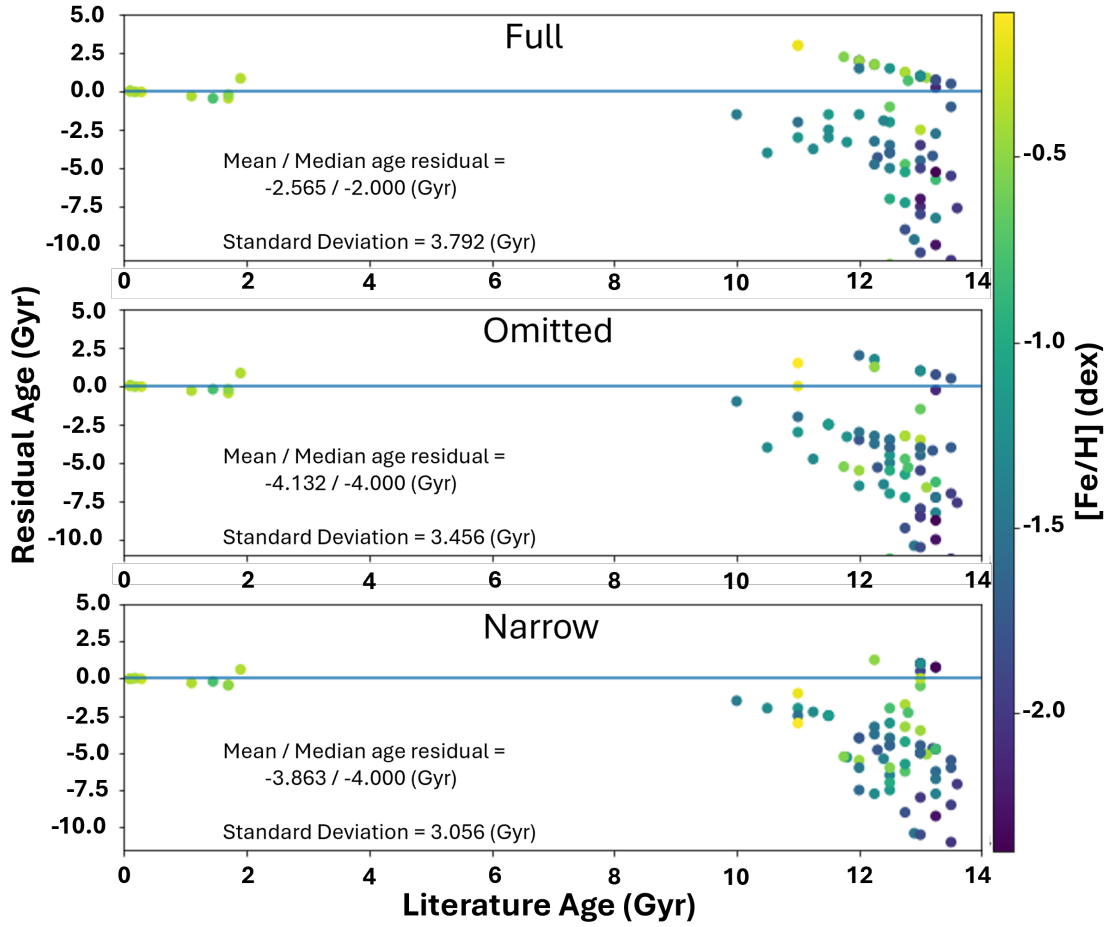


Figure 3.13: Similar to the top plots of Figures 3.8, 3.9, & 3.10. This plot shows SpPXF age minus Literature age against Literature age with literature $[Fe/H]$ shown in colour and the standard deviation of the residual as ‘std’. The plots are for the ‘full’, ‘omitted’ and ‘narrow’ spectral regions (top, middle and bottom respectively). Using sMILES models with $[\alpha/Fe]$ values of 0.3 dex. The age mean uncertainty values for the Full, Omitted and Narrow regions are 0.38, 0.40, & 1.43 Gyr respectively.

This tends to suggest that the SpPXF method is worse at finding age than BpPXF. It should be noted how the binning of the SSP models used (the cause of the horizontal banding shown best in Figure 3.14) will influence the standard deviation of the resulting age and metallicity residuals which could be an explanation for their

CHAPTER 3

increase in size. The age binning between models at ages above 4.5 Gyr is every 0.5 Gyr which would lead to the standard deviation being 0.5 Gyr worse if the larger standard deviation was only due to the larger binning. This is unlike BpPXF where the fitting techniques of combining multiple SSP models allow for a light weighted mean value of age and metallicity. Therefore it is concluded, that for age estimation, SpPXF is likely to be worse than BpPXF.

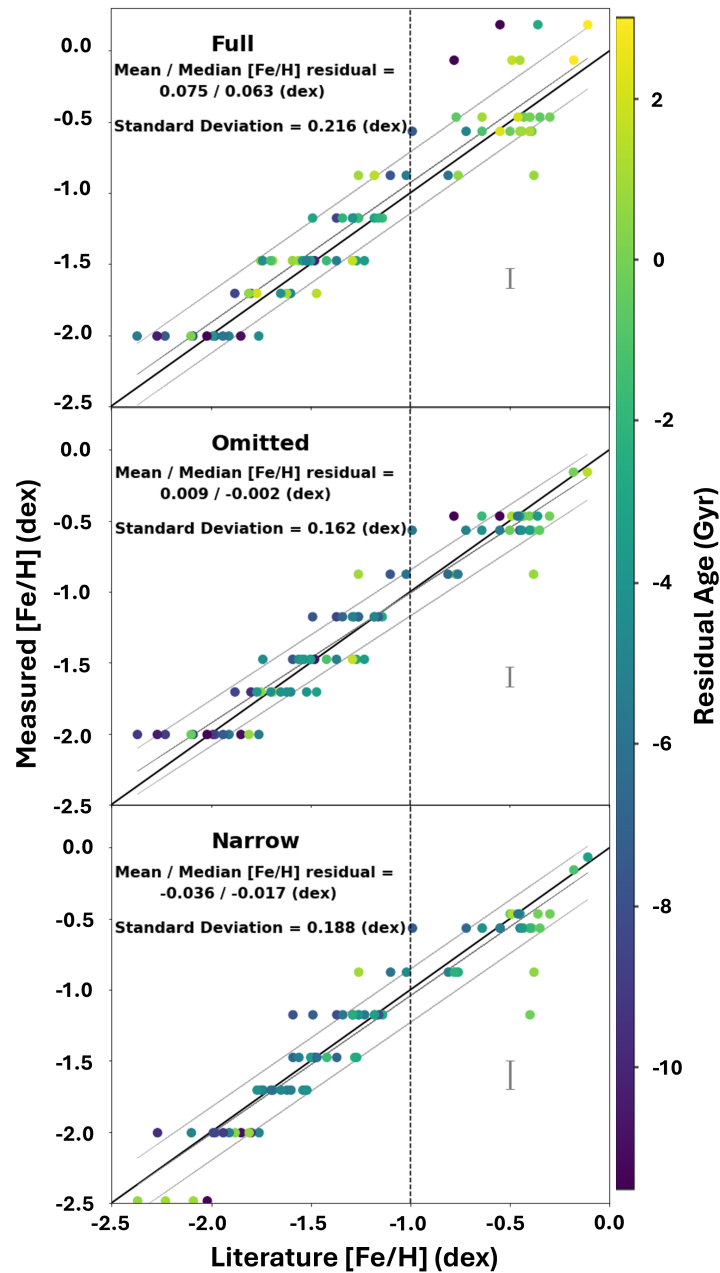


Figure 3.14: Similar to Figures 3.11 & 3.12. Literature $[\text{Fe}/\text{H}]$ against SpPXF output $[\text{Fe}/\text{H}]$ (converted from $[\text{M}/\text{H}]$ using Equation 3.8) for the WAGGS sample for the 3 different wavelength regions with literature age shown in colour. The solid black line is a 1-to-1 positive correlation line going through $[0,0]$, the black dashed line represents the metallicity split mentioned earlier, while the solid grey lines represent a linear least squares fit (middle grey line) and standard deviation (either side).

3.7.2 Using sMILES with all $[\alpha/\text{Fe}]$ Values

SpPXF was designed to allow fitting to models with multiple $[\alpha/\text{Fe}]$ values. Here SpPXF is run again using sMILES models with multiple $[\alpha/\text{Fe}]$ values ranging from -0.2 to 0.6 dex at a binning of 0.1 dex. The same binning for age and metallicity given in Knowles et al. (2023) is used. The mean residual values (measured minus literature) are presented in Table 3.4 and Figures 3.15 & 3.16. When using all of the GCs in the WAGGS sample (excluding those already eliminated during sample selection) it is found that the age residual is larger for the full spectrum (3800 - 6000 Å) than the narrow spectrum (4828 - 5363 Å). However, the standard deviation in age residual for SpPXF using $[\alpha/\text{Fe}] = 0.3$ (Table 3.3) and all $[\alpha/\text{Fe}]$ values are equivalent to each other, and are of the same order as the mean residuals themselves indicating very poor age estimation and scatter in the results. Allowing to freely fit to any alpha value does not effect the age estimation in any visibly significant way.

Table 3.4: The output age and metallicity residual values for SpPXF using all (top) and just MW (bottom) GCs and all $[\alpha/\text{Fe}]$ sMILES SSP models.

λ region	GCs	Δ_{Age} (Gyr)	$\sigma_{\Delta_{\text{Age}}}$ (Gyr)	$\Delta_{[\text{Fe}/\text{H}]}$ (dex)	$\sigma_{\Delta_{[\text{Fe}/\text{H}]}}$ (dex)
Full	All	-3.237	3.493	0.076	0.193
Omitted	All	-4.205	3.163	0.005	0.172
Narrow	All	-3.556	3.005	-0.048	0.209
Full	MW	-3.580	3.419	0.107	0.181
Omitted	MW	-4.741	2.981	0.0186	0.171
Narrow	MW	-4.050	2.867	0.000	0.180

CHAPTER 3

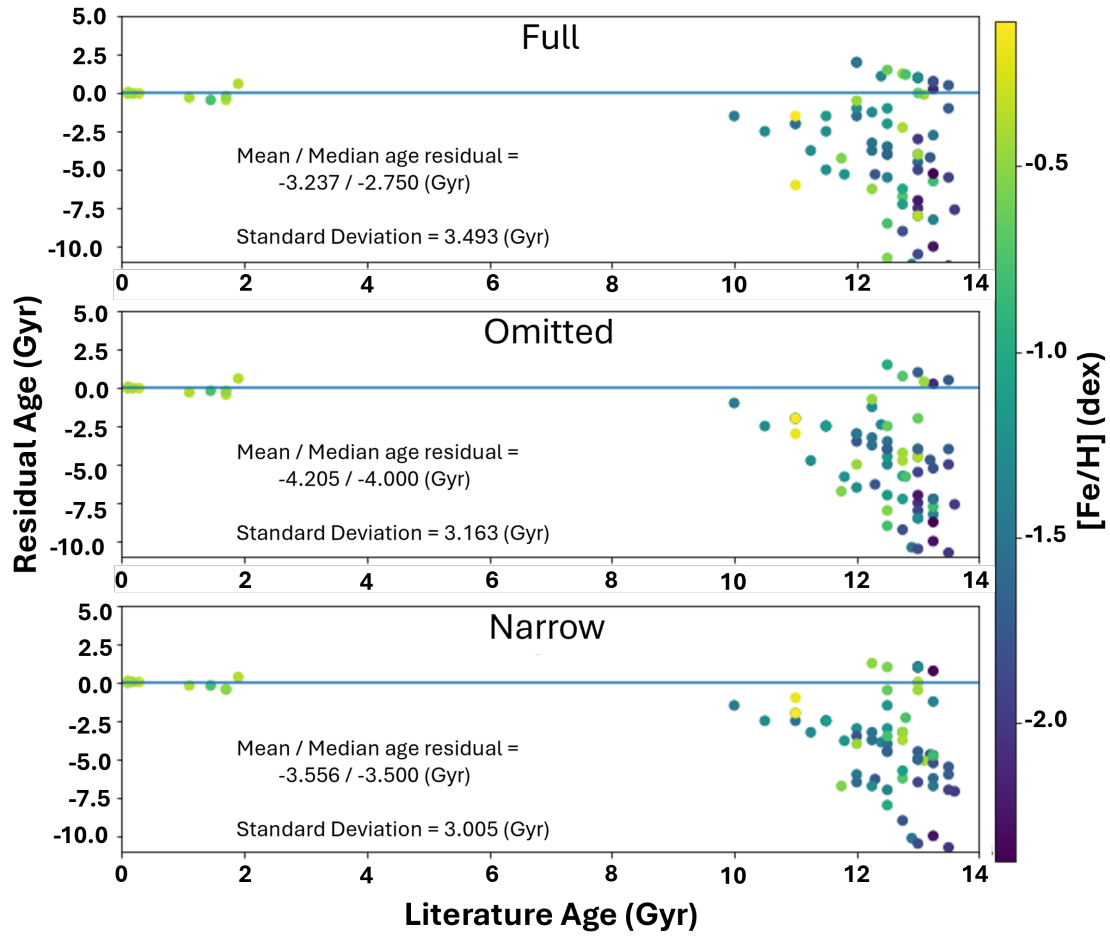


Figure 3.15: Similar to Figure 3.13. This plot shows SpPXF age minus Literature age against Literature age with literature $[Fe/H]$ shown in colour and the standard deviation of the residual as ‘std’. The plots are for the ‘full’, ‘omitted’ and ‘narrow’ spectral regions (top, middle and bottom respectively). Using sMILES models with $[\alpha/Fe]$ values from -0.2 to 0.6 (dex) every at 0.1 dex intervals. The mean age uncertainty values for the Full, Omitted and Narrow regions are 1.18, 0.37, & 1.02 Gyr respectively.

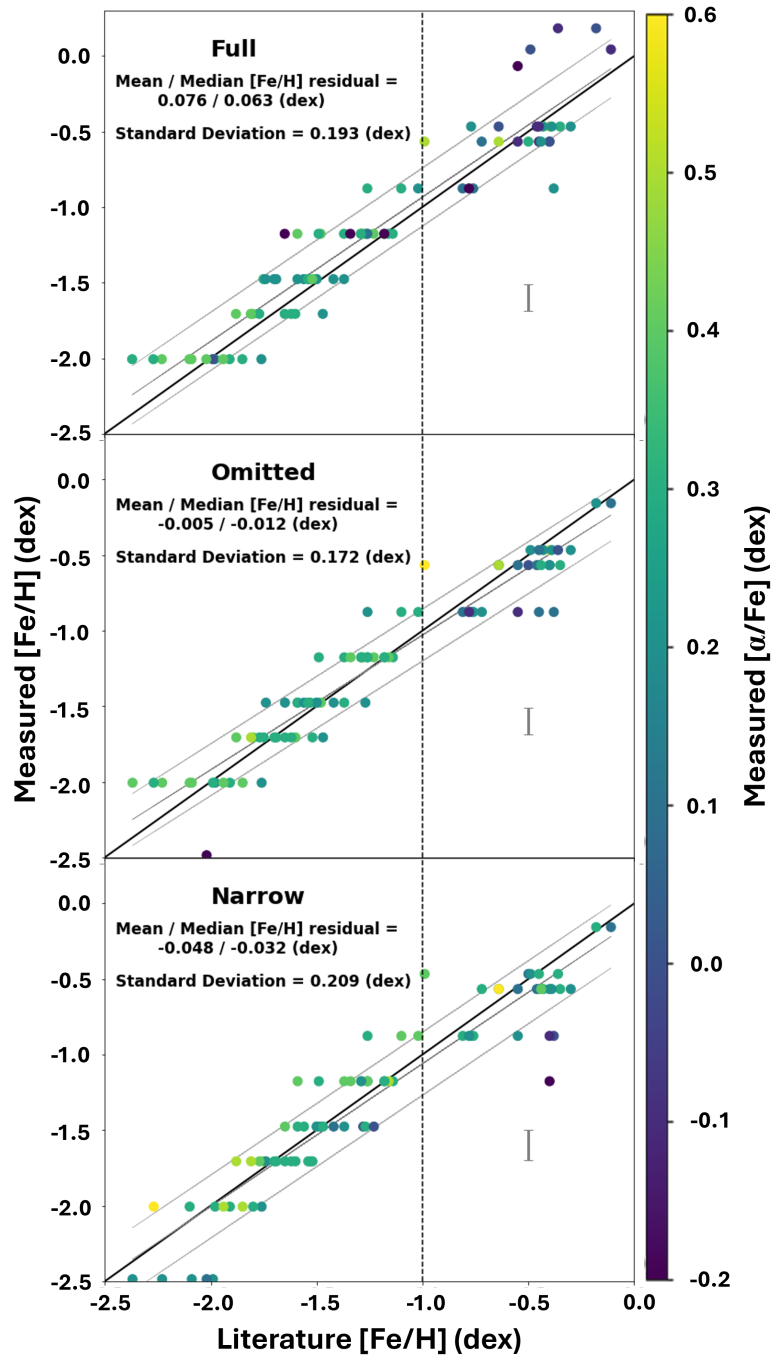


Figure 3.16: Similar to Figures 3.14. Literature $[\text{Fe}/\text{H}]$ against SpPXF output $[\text{Fe}/\text{H}]$ (converted from $[\text{M}/\text{H}]$ using Equation 3.8) for the WAGGS sample for the 3 different wavelength regions with output $[\alpha/\text{Fe}]$ shown in colour. SpPXF used sMILES models with $[\alpha/\text{Fe}]$ values from -0.2 to 0.6 (dex) every at 0.1 dex intervals.

CHAPTER 3

Comparing Tables 3.3 and 3.4 and the Figures 3.14 and 3.16 it can be seen that allowing SpPXF to fit $[\alpha/\text{Fe}]$ freely does not effect the measured metallicity. The mean residuals (measured minus literature) for both methods of SpPXF are minimal and the standard deviations of the residuals are similarly low.

However, Figures 3.14 and 3.16 show how the binning of the model grid can affect the output measurement. The long correlated horizontal lines of points in each plot are globular clusters of different literature metallicities selecting the same metallicity SSP model as each other. For example, the lowest metallicity point the middle plot of Figure 3.14 is the GC NGC 7078 which has $[\text{Fe}/\text{H}] = -2.37$ (Harris, 2010). The GC NGC 6273 with literature $[\text{Fe}/\text{H}] = -1.74$ had an SSP model with the same metallicity of $[\text{Fe}/\text{H}] = -2.05$ selected as its output metallicity (converted from the sMILES $[\text{M}/\text{H}]$ value using Equation 3.8). A finer metallicity binning will remove this correlation in the plot. This is plotted in Figure 3.17 for $[\alpha/\text{Fe}] = 0.3$ SSPs. But, this finer binning only reduces the standard deviation in the residuals by ~ 0.02 dex indicating that the scatter is mostly real and not an artefact of the binning.

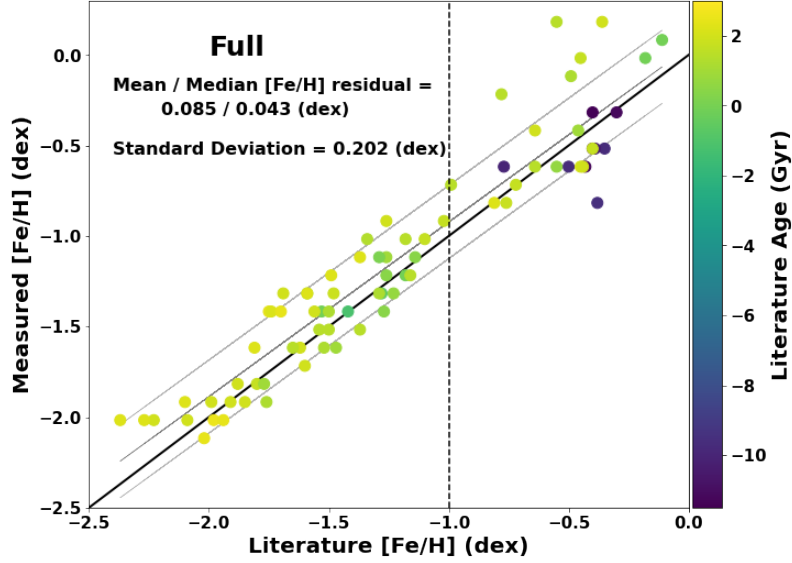


Figure 3.17: SpPXF $[\text{Fe}/\text{H}]$ residual for sMILES models with $[\alpha/\text{Fe}] = 0.3$ and a metallicity binning of 0.1 dex between $[\text{M}/\text{H}] = -2.2$ and $[\text{M}/\text{H}] = 0.4$ over the “Full” wavelength range. The solid black line is a 1-to-1 positive correlation line going through $[0,0]$, the black dashed line represents the metallicity split mentioned earlier, while the solid grey lines represent a linear least squares fit (middle grey line) and standard deviation (either side).

This method was designed to freely fit to the ‘best’ available $[\alpha/\text{Fe}]$ value for each GC. As has been shown so far this has not improved the estimation of age or metallicity. Table 3.5 shows the residual (measured minus literature) $[\alpha/\text{Fe}]$ value for each globular cluster with published alpha values.

Table 3.5: The SpPXF $[\alpha/\text{Fe}]$ outputs - the literature values (for GCs with known $[\alpha/\text{Fe}]$ values) with the standard deviation of the residuals.

λ region	$\Delta_{[\alpha/\text{Fe}]}$ (dex)	$\sigma_{\Delta[\alpha/\text{Fe}]}$ (dex)
Full	-0.075	0.204
Omitted	0.037	0.165
Narrow	-0.019	0.136

CHAPTER 3

It is clear From Figure 3.18 that there is still a large scatter in $[\alpha/\text{Fe}]$ selection even in the Narrow wavelength range which offers the best return for $[\alpha/\text{Fe}]$ and that this method (for the other two wavelength ranges) does not return $[\alpha/\text{Fe}]$ within levels comparable to literature (e.g. Dias et al. 2016). However, the Narrow range returns the best results out of the wavelength ranges with the mean uncertainty value (via Monte Carlo simulations of a sample of GCs, see Section 3.7.3) of ± 0.11 dex indicating a good fit for almost all of the objects.

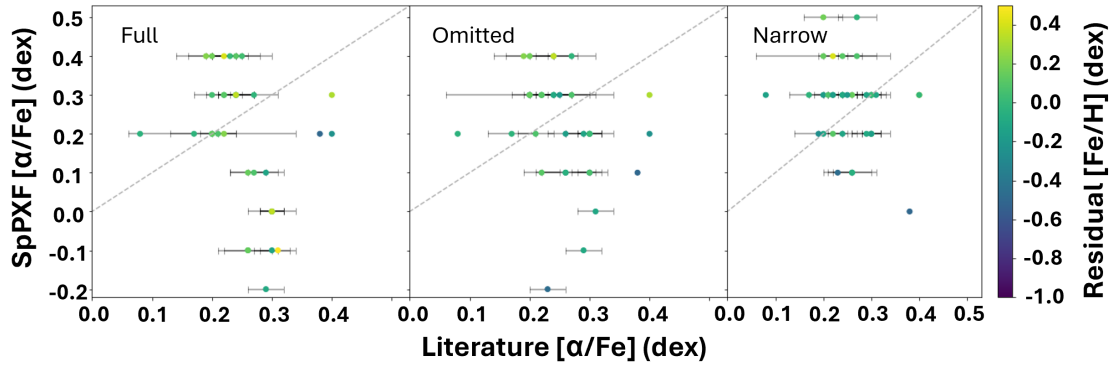


Figure 3.18: The output $[\alpha/\text{Fe}]$ values from SpPXF from the 3 different wavelength regions compared to values from the literature. Objects without error bars are literature values published with no uncertainty values. The mean $[\alpha/\text{Fe}]$ uncertainty values for the Full, Omitted and Narrow regions are 0.07, 0.08, & 0.11 dex respectively.

3.7.3 Uncertainty calculations

While each selected model had a reduced χ^2 value which indicated wellness of fit, the way to get accurate uncertainty in the output age, metallicity, and $[\alpha/\text{Fe}]$ is Monte Carlo simulations similar to those used for BpXF.

To properly analyse the uncertainties of each GC, sufficient runs need to be made. Common practice is to do at least 50 iterations when running pPXF (Ge et al., 2018) for each object being measured. For this method, however, the large

CHAPTER 3

sample of models and the large number of wavelength pixels made Monte Carlo simulations exceptionally long to run. Each measurement to compare the spectrum to a model took ~ 0.3 seconds. Multiply this by 50 iterations and 636 models and 82 GCs and the run time will be 9 days just for one wavelength range. This can be reduced with parallel processing, but this process also used sMILES models across multiple $[\alpha/\text{Fe}]$ values where the number of models was 3180. Therefore it was decided for this method to only run Monte Carlo simulations on a sample of GCs at a range of ages and metallicity with SNR values around the median to provide representative error bars.

The errorbars themselves are very small for age comparatively to BpPXF indicating that often the same SSP model was selected as the best fitting model regardless of how the spectrum had been changed within its noise. Only in the narrower ranges did uncertainty increase indicating that with less spectral information SpPXF is less precise with its “best” model prediction.

3.8 LISm χ

As stated before, this method has been used before by many authors, including Proctor, Forbes & Beasley (2004); Norris et al. (2008); Zhang et al. (2012), but due to the higher resolution of the spectra used, it has been possible to reproduce this method using a resolution only limited by the SSP models used. In this case, sMILES models are used again which have a resolution of 2.51 Å (FWHM). The sMILES models are first used with $[\alpha/\text{Fe}] = 0.3$ for comparison with all methods and then again with sMILES models of all $[\alpha/\text{Fe}]$ values.

3.8.1 LICK Indices

In examinations of the ages of the integrated light of star clusters and galaxies, Balmer hydrogen lines are the usual indicators of age due to their sensitivity to the effective temperature (Buzzoni, Mantegazza & Gariboldi, 1994)[¶]. In the chosen spectral range of 3800 - 6000 Å, only three lines are included: H γ , H δ and H β . The previous methods indicate that, at larger wavelength ranges, metallicity is less well identified by spectral analysis techniques for globular clusters, this could be due to chemical abundance issues being present in the longer spectra. Age is also poorly estimated at all wavelength ranges tested in the previous methods, with lower residuals (measured age minus literature age) for the longer wavelength ranges but with a larger scatter in the residuals. Therefore for this section, only 4 LICK indices are used: H β , Mgb, Fe5270, Fe5335 in an attempt to accurately infer metallicity and age with this new minimum reduced χ^2 technique, showing how only a few key spectral features are needed for accurate extraction of population details.

These indices were chosen because H β is the strongest hydrogen indicator in the larger spectral range. The other indices are Mgb, Fe5270 and Fe5335. These were chosen because they are the key component in the commonly used metallicity indicator [MgFe]' (Thomas, Maraston & Bender, 2003). Due to the indices' proximity, it is possible to make an equivalent wavelength range from the full spectrum which has been labelled above as the "narrow" wavelength band of 4828 - 5363 Å (Figure 3.19).

This method has the possibility of including multiple indices and as such a representative sample of a full spectrum could be used for a similar comparison with the larger wavelength range described in the above two methods. It was chosen to run this method on the 4 key indices selected for age and metallicity for the

[¶]For simple stellar populations, the temperature of the main sequence turn off indicates cluster age (Sandage, 1982)

CHAPTER 3

above reasoning. In a later chapter (Chapter 5), the lick indices of GCs and other objects will be used to identify chemical abundance anomalies and other details in the object's spectra. There, this same method is used to see if age and metallicity are better fit when other indicating indices are included.

3.8.2 Sample Selection

For this method, the same sample as BpPXF and SpPXF is used. However, some changes to the sample were needed. Section 3.6.1 identified several GCs which possessed OIII and H emission (and absorption) lines. Unlike the other two methods, emission lines cannot be masked in index measurement, therefore some objects had to be removed. Any object that possessed a visible hydrogen emission line was removed from the sample (shown in Figure 3.19). As well as this, the presence of OIII emission lines at 4959 and 5007 Å inferred the presence of ionised hydrogen gas which would affect the spectrum. Therefore if ionised gas emission lines were detected anywhere in the spectrum when running BpPXF, bad hydrogen lines were assumed, and that GC was removed from the sample.

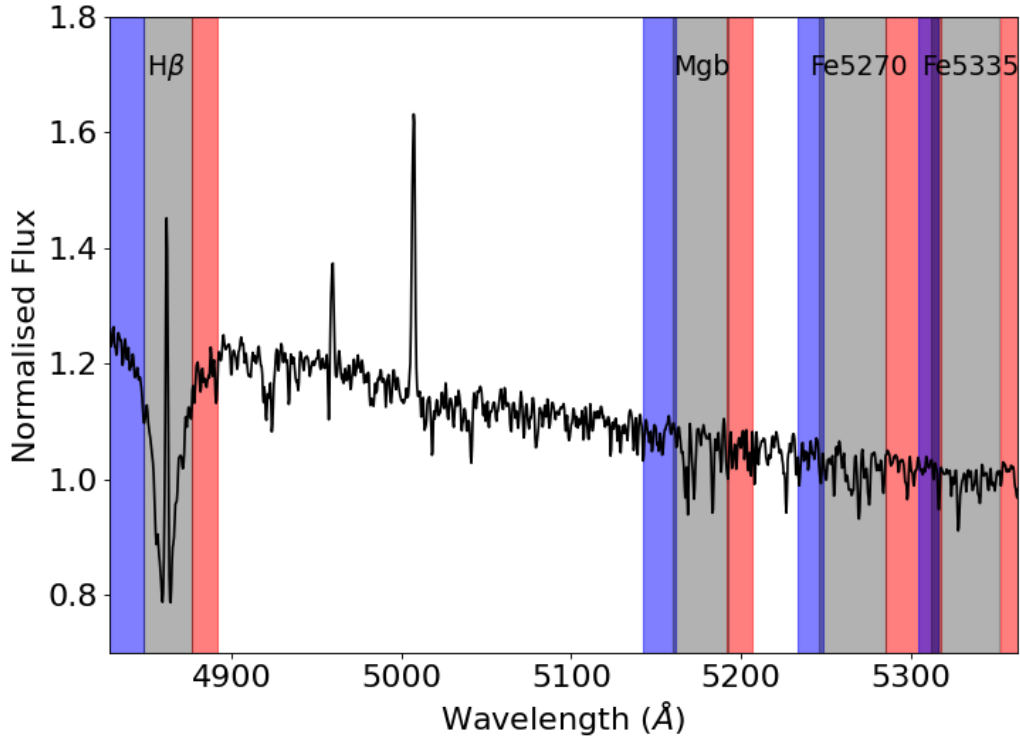


Figure 3.19: The “narrow” wavelength region used in BpPXF and SpPXF for the spectrum of NGC 1850. The LICK indices used in LISm χ are highlighted by grey regions with blue and red highlighted regions indicating the area where blue and red pseudo-continua are measured. This spectrum shows Balmer emission lines as well as OIII emission present in the spectrum.

Only 5 objects had to be removed from the sample, they are Fornax 5, NGC 1850, NGC 2100, NGC 6352 and NGC 6637. This is only 7.3% of the total sample used for the other two methods and should not significantly affect the comparison of age and metallicity residuals between the methods.

What is interesting to see is the presence of gas emission lines in the GCs Fornax 5, NGC 6352 and NGC 6637. Fornax 5 is a classic old metal-poor globular cluster, the presence of ionised OIII emission lines indicates the presence of an emission nebula or hot, young massive stars in star-forming regions (Suzuki et al., 2016)

CHAPTER 3

which is unlikely (but not impossible) in old globular clusters where star formation ceased billions of years ago. For Fornax 5 there is a possible background source of OIII from a PNe discovered in the Fornax dwarf spheroidal galaxy (Maran et al., 1984). However Larsen (2008) discovered PNe candidate within Fornax 5 itself which is likely the source of this anomalous emission.

NGC 6352 and NGC 6637 both possess hydrogen emission lines. They are old globular clusters but they have higher metallicities than the classic metal poor old GC, both at $[\text{Fe}/\text{H}] = -0.64$ dex. Schiavon et al. (2005) discovered the presence of OII emission in NGC 6352 spectra, which was due to foreground B and A stars. The position of the Hydrogen emission line in the spectrum for NGC 6352 indicates that the source of the emission is not within the GC: the emission line lies 1.53 \AA redder than $\text{H}\beta$ which seems to agree with this hypothesis. The $\text{H}\beta$ emission in NGC 6637 also lies slightly to the redder side of $\text{H}\beta$, also indicating the presence of young hot stars with a gaseous envelope. Both of these GCs have negative recession velocities which have been corrected to zero, therefore any artefacts due to foreground stars are going to appear redder (or bluer depending on the motion of the star relative to Earth) than they normally would. It can be concluded that the hydrogen emission in these objects is not due to the population of the GCs and is most likely due to foreground stars. These foreground stars are not classified and their effects cannot be removed without access to the original WAGGS data cubes where they can be identified and masked.

3.8.3 Results

This method used a finer binning of age and metallicity of 0.1 Gyr, 0.1 dex and 0.1 dex for age, metallicity, and $[\alpha/\text{Fe}]$ due to the relatively low computational power this method needed, outlined in Section 3.8.4. For easy comparison with SpPXF and BpPXF, LISm χ is first run with sMILES models at this finer binning but with

CHAPTER 3

$[\alpha/\text{Fe}] = 0.3$. The results for each GC are presented in Table B.3 with the mean residual values given in Table 3.6. Figure 3.20 shows the results of this. The same age underestimation trend seen in the other two methods is seen here, while the metallicity seems underestimated (this is best shown in Figure 3.21). Comparison with the ‘narrow’ wavelength range used for SpPXF and BpPXF shows a similar outcome for all three methods. However, for this method, some old, metal-poor GCs have age over-estimation. These over-estimated GCs have large uncertainty values which could indicate that fitting to the extreme age value may not be the correct value. Fitting to the extreme of age is also produced from SpPXF for some GCs and this appears to be something that finer age bins cannot remove.

Figure 3.21 shows how the metallicity is mostly well estimated using $[\alpha/\text{Fe}] = 0.3$, Figure 3.23 also shows fairly good agreement with literature metallicity. However, there is a larger scatter in metallicity for Figure 3.23 where all $[\alpha/\text{Fe}]$ models have been used.

Table 3.6: mean offsets of age (Δ_{Age}) and metallicity ($\Delta_{[\text{Fe}/\text{H}]}$) with their standard deviations ($\sigma_{\Delta_{\text{Age}}}$ & $\sigma_{\Delta_{[\text{Fe}/\text{H}]}}$ respectively) for LISm χ using the indices $\text{H}\beta$, Mg_b , $\text{Fe}5270$, & $\text{Fe}5335$ with sMILES models at $[\alpha/\text{Fe}] = 0.3$.

Δ_{Age} (Gyr)	$\sigma_{\Delta_{\text{Age}}}$ (Gyr)	$\Delta_{[\text{Fe}/\text{H}]}$ (dex)	$\sigma_{\Delta_{[\text{Fe}/\text{H}]}}$ (dex)
-3.177	2.856	-0.066	0.158

CHAPTER 3

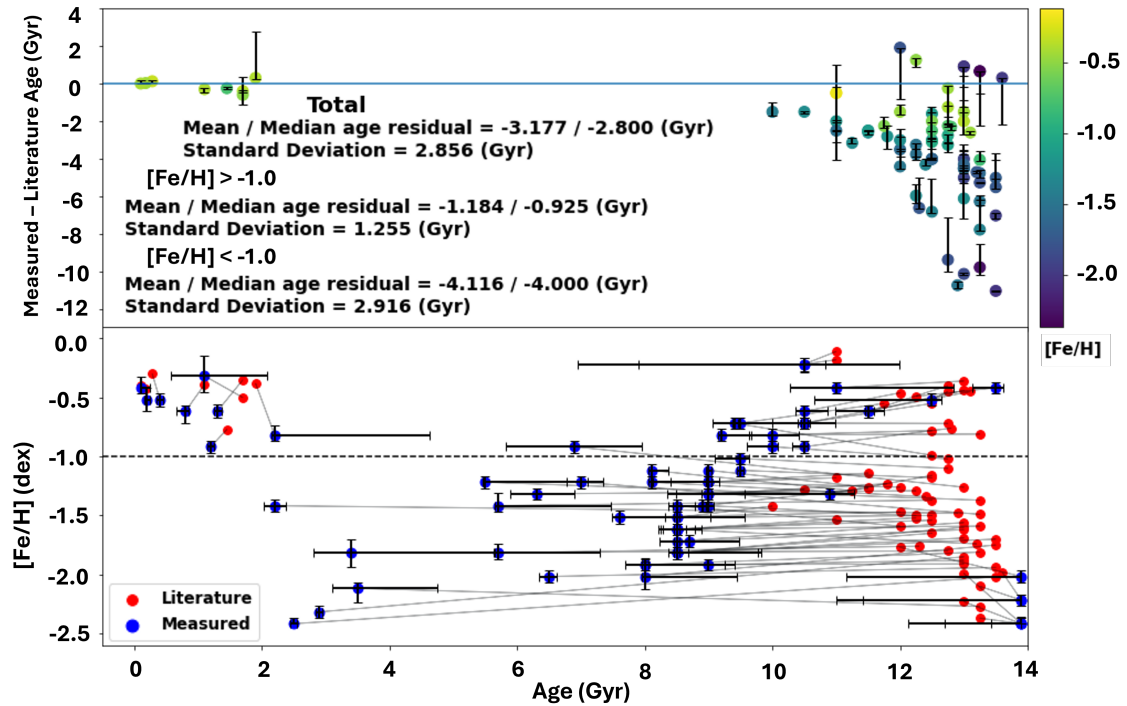


Figure 3.20: LISm χ output plots using sMILES SSP models with $[\alpha/\text{Fe}] = 0.3$ (dex) showing: Top, the residual in age measurement (measured age - literature age) against literature age with std as the standard deviation of the scatter and literature $[\text{Fe}/\text{H}]$ as the colour bar. Bottom, the age/metallicity plot showing the measured values for age and $[\text{Fe}/\text{H}]$ (blue) and the literature values for the GCs (red) with the grey lines connecting literature to measured points. Error bars for each point are measured from Monte Carlo simulations.

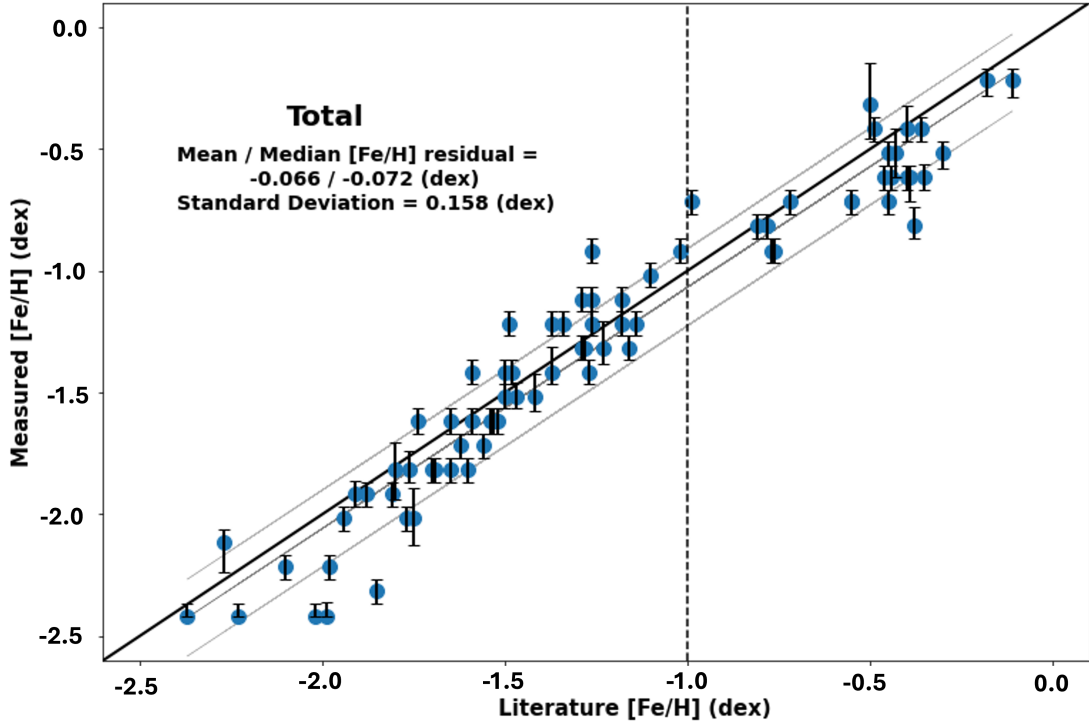


Figure 3.21: LISm χ [Fe/H] against literature [Fe/H] using sMILES SSP models with $[\alpha/\text{Fe}] = 0.03$ (dex). Error bar values are measured from Monte Carlo simulations. The solid black line represents a 1:1 correlation while the grey lines show the best fit \pm the standard deviation of the scatter from that best fit. The vertical dashed line shows the $[\text{Fe}/\text{H}] = -1.0$ split in age residual measurements from Figure 3.20.

[Fe/H] is calculated based on Equation 3.8 which relies upon the $[\alpha/\text{Fe}]$ of the model. Therefore it was hoped that when using the models with all $[\alpha/\text{Fe}]$ the correct alpha value would be chosen and the metallicity measurement would have a smaller scatter in the results. This was inconclusive from the SpPXF method as the metallicity values for both sets of models are similar in magnitude and uncertainty. For LISm χ , when multiple $[\alpha/\text{Fe}]$ values are allowed, the standard deviation of the residual (measured minus literature) increases shown via comparison of Figures 3.22 & 3.23. This suggests that $[\alpha/\text{Fe}]$ is not estimated well. Table 3.7 shows the residuals (measured minus literature) of age, [Fe/H] and $[\alpha/\text{Fe}]$. Comparison of

CHAPTER 3

Table 3.6 and Table 3.7 shows that mean age residuals for both $[\alpha/\text{Fe}] = 0.3$ and all $[\alpha/\text{Fe}]$ values are within error of each other and from this it can be concluded that the age indicators are not correlated to alpha elements. This makes sense as the only age indicator used is the $\text{H}\beta$ which is mostly alpha insensitive (The LICK index $\text{H}\beta_0$ is claimed to be truly alpha insensitive (Cervantes & Vazdekis, 2009) but for this purpose, the LICK index $\text{H}\beta$ is enough to indicate age).

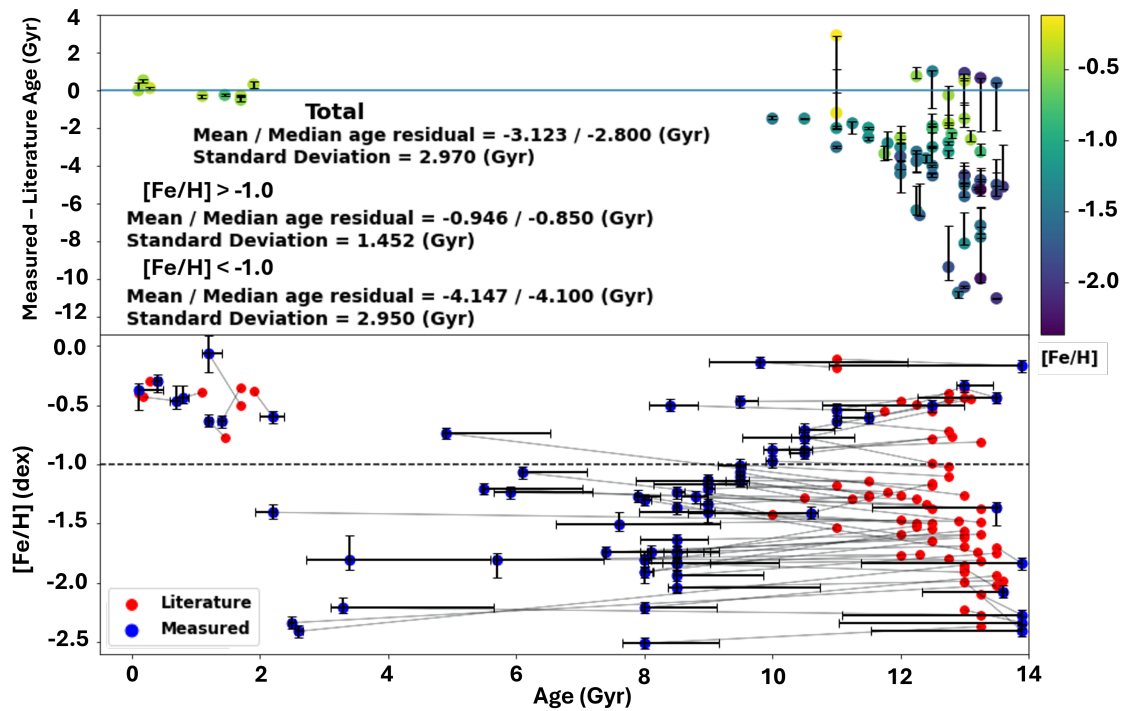


Figure 3.22: LISm χ output plots using sMILES SSP models with $[\alpha/\text{Fe}] = -0.2$ to 0.6 (dex) at 0.1 dex intervals with age and $[\text{M}/\text{H}]$ interpolated to every 0.1 (Gyr) and (0.1) dex respectively showing: Top, the residual in age measurement (measured age - literature age) against literature age with std as the standard deviation of the scatter and literature $[\text{Fe}/\text{H}]$ as the colour bar. Bottom, the age/metallicity plot showing the measured values for age and $[\text{Fe}/\text{H}]$ (blue) and the literature values for the GCs (red) with the grey lines connecting literature to measured points. Error bars for each point are measured from Monte Carlo simulations.

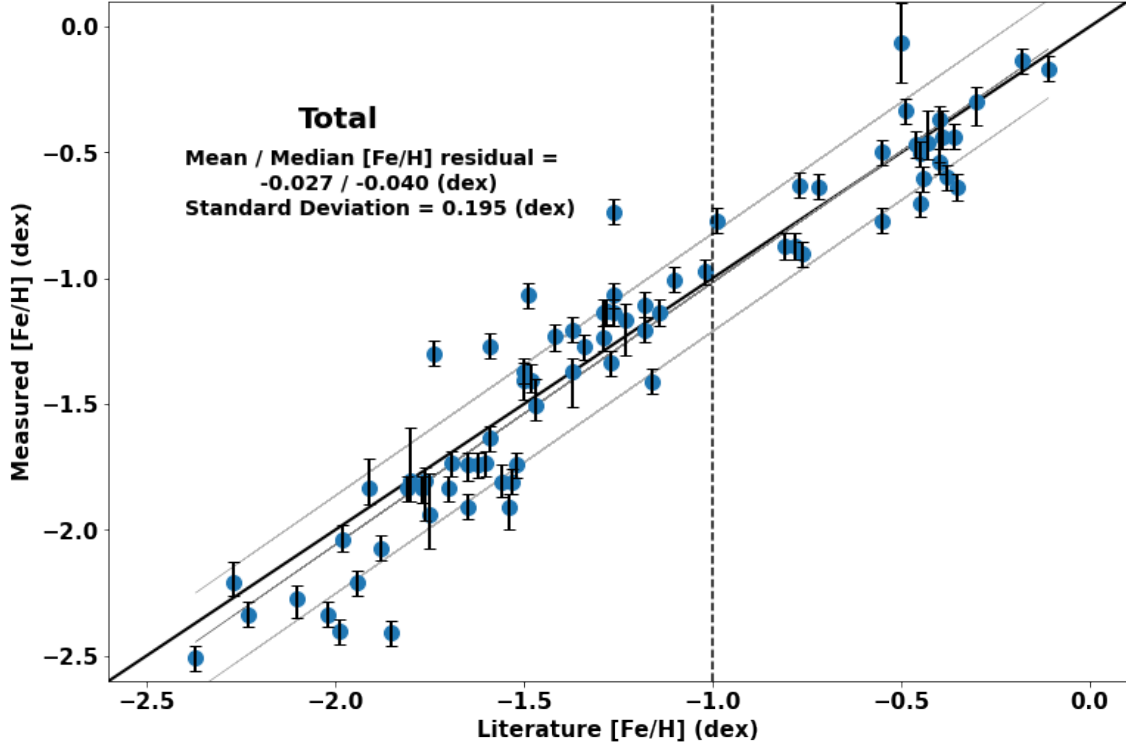


Figure 3.23: LISm χ [Fe/H] against literature [Fe/H] using sMILES SSP models with $[\alpha/\text{Fe}] = -0.2$ to 0.6 (dex) at 0.1 dex intervals with age and $[M/H]$ interpolated to every 0.1 (Gyr) and (0.1) dex respectively. Error bar values are measured from Monte Carlo simulations. The solid black line represents a 1:1 correlation while the grey lines show the best fit \pm the standard deviation of the scatter from that best fit. The vertical dashed line shows the $[\text{Fe}/\text{H}] = -1.0$ split in age residual measurements from Figure 3.22.

Table 3.7: mean offsets of age (Δ_{Age}), metallicity ($\Delta_{[\text{Fe}/\text{H}]}$) and alpha abundance ($\Delta_{[\alpha/\text{Fe}]}$) with their standard deviations ($\sigma_{\Delta_{\text{Age}}}$, $\sigma_{\Delta_{[\text{Fe}/\text{H}]}}$, & $\sigma_{\Delta_{[\alpha/\text{Fe}]}}$ respectively) for LISm χ using the indices $H\beta$, Mg_b , $\text{Fe}5270$, & $\text{Fe}5335$ with sMILES models at $[\alpha/\text{Fe}]$ values between -0.2 and 0.6 binned to every 0.1 dex.

Δ_{Age} (Gyr)	$\sigma_{\Delta_{\text{Age}}}$ (Gyr)	$\Delta_{[\text{Fe}/\text{H}]}$ (dex)	$\sigma_{\Delta_{[\text{Fe}/\text{H}]}}$ (dex)	$\Delta_{[\alpha/\text{Fe}]}$ (dex)	$\sigma_{\Delta_{[\alpha/\text{Fe}]}}$ (dex)
-3.123	2.970	-0.027	0.195	-0.073	0.201

CHAPTER 3

Figure 3.24 shows the measured $[\alpha/\text{Fe}]$ against the literature value, as can be seen is a very large scatter in the measured value. This is most likely due to the indices used being mostly alpha-insensitive with only Mg_b being alpha sensitive. It has already been stated that the index $\text{H}\beta$ is almost completely alpha-insensitive (Korn, Maraston & Thomas, 2005; Cervantes & Vazdekis, 2009). Korn, Maraston & Thomas (2005) also indicates that $\text{Fe}5270$ and $\text{Fe}5335$ are mostly alpha insensitive too. Thomas, Maraston & Johansson (2011) states that Mg_b is alpha sensitive but this is mostly due to an Fe anti-correlation and Thomas, Maraston & Bender (2003) state that the metallicity index $[\text{MgFe}]'$ which comprised of Mg_b $\text{Fe}5270$ and $\text{Fe}5335$ (Equation 3.7) is alpha insensitive. Therefore it can be expected that alpha estimations from this process will be inaccurate. Figure 3.18 and Table 3.5 show how the $[\alpha/\text{Fe}]$ measurements from SpPXF for the three wavelength ranges still have a large scatter. The narrow region with SpPXF shows the least amount of scatter which would indicate that the indices used here would give similar results. The increased scatter, however, shows that there are other features in the narrow wavelength range which contribute to alpha element sensitivity.

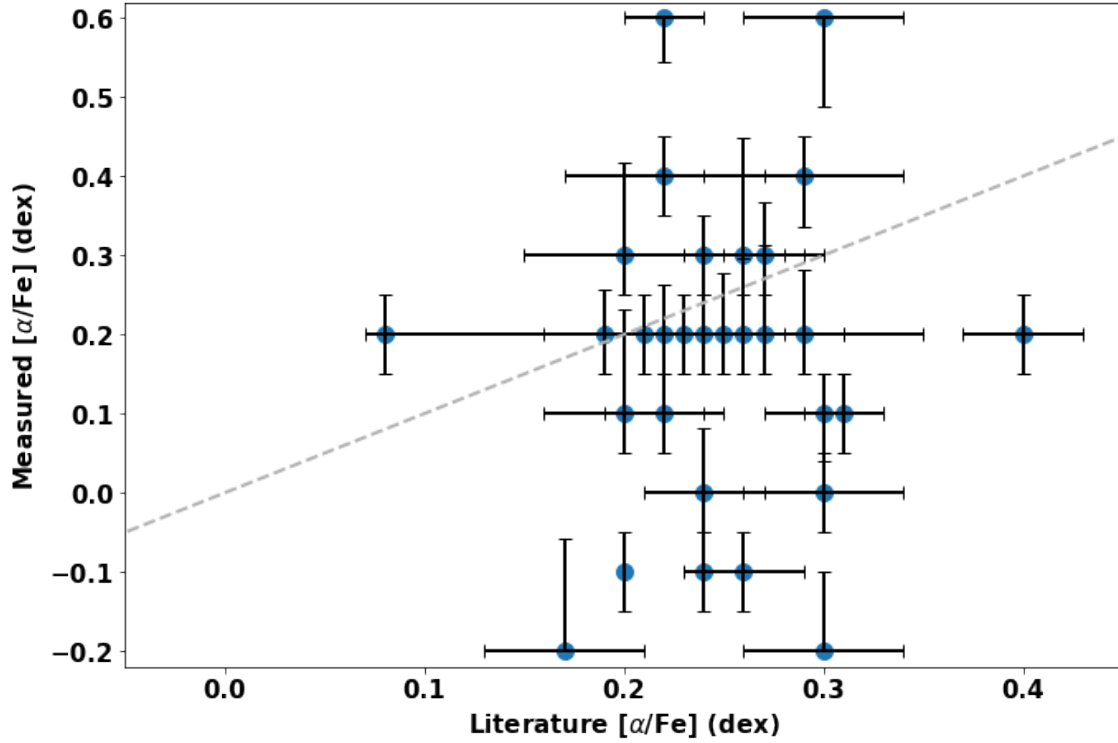


Figure 3.24: LISm χ $[\alpha/\text{Fe}]$ against literature $[\alpha/\text{Fe}]$ using sMILES SSP models with $[\alpha/\text{Fe}] = -0.2$ to 0.6 (dex) at 0.1 dex intervals with age and $[M/H]$ interpolated to every 0.1 (Gyr) and (0.1) dex respectively. Error bar values are measured from Monte Carlo simulations.

3.8.4 Uncertainty Analysis

To measure the uncertainty of the outputs of LISm χ a Monte Carlo simulation is used. This method is considerably quicker to run a Monte Carlo than the other methods as only a limited number of indices are used as opposed to the thousands of pixels from fitting an SED. The reduced run time allowed us to fit the higher binning of age and metallicity in the SSP models that have been used.

Firstly each index measured had its error calculated by a Monte Carlo simulation of 300 iterations. The spectrum of each GC was changed in the same way described in Section 3.7.3. Each pixel in the spectrum was changed following Equation 3.9.

CHAPTER 3

The indices were then measured as described in Section 3.2 and the $1\text{-}\sigma$ standard deviation was used as the uncertainty for each index.

For the minimum reduced χ^2 uncertainty calculation each index was changed by the Gaussian multiplication of its error similarly to Equation 3.9 but for just the used indices not every pixel in a spectrum. Then finding the standard deviation of the results around the median of the Monte Carlo runs and using this as the $1\text{-}\sigma$ uncertainty (Figure 3.25). Occasionally the standard deviation of the MC runs around the median would not overlap with the ‘true’ value (the ‘true’ value being the output of LISm χ here) in this case the errors have been extended past the true value to half of the binning of the SSP models. For GCs where the MC gave uncertainties less than half of the model binning, the uncertainties were increased to match half of the binning of 0.05 Gyr, 0.05 dex and 0.05 dex for age, [M/H] and [α /Fe] respectively.

CHAPTER 3

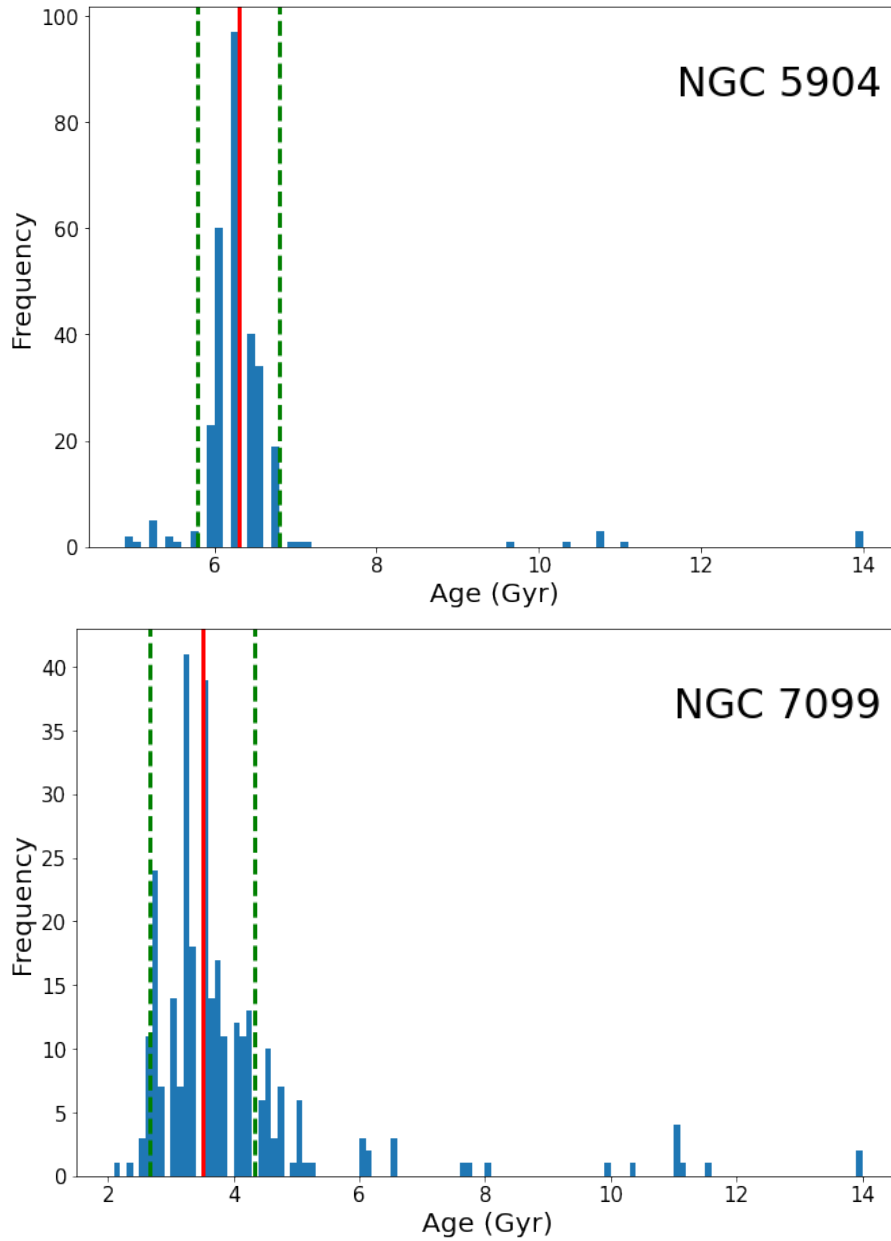


Figure 3.25: A Histogram of the Monte Carlo runs of (top) NGC 5904 & (bottom) NGC 7099 showing their age estimations. The solid red line marks the mean value of the MC iterations while the dashed green lines show the standard deviation of the iterations around the mean value. The age value and error for these objects are 6.3 ± 0.5 Gyr and 3.5 ± 0.85 Gyr for NGC 5904 and NGC 7099 respectively. These uncertainties correlate with the GCs SNRs of 221.19 and 30.37 (at 5000 \AA).

CHAPTER 3

Monte Carlo simulations for this method were significantly quicker than for the other methods. Where SpPXF would take 9 days of run time a Monte Carlo for all GCs for just one wavelength range at 100 iterations, for LISm χ using $[\alpha/\text{Fe}] = 0.3$, it would take 11 hours and 37 minutes using four indices with 300 iterations. This is still quite a long time (as there were limitations in computational power) but it is a significant decrease in run time compared to SpPXF and this allowed the estimation of errors for LISm χ with the finer binned models (33,777 SSP models). For these Monte Carlo runs, only 100 iterations were used to save run time and the parameter uncertainties have been calculated in the same way as the single alpha value models, but including $[\alpha/\text{Fe}]$ uncertainty.

The uncertainty values for metallicity and $[\alpha/\text{Fe}]$ are equivalent with both SpPXF and BpPXF. However, the uncertainty values for age are different between each method, with LISm χ showing the largest uncertainty in its ages average uncertainty. The larger LISm χ uncertainties show, however, that this method does not get locked into choosing the same ‘best’ model through each Monte-Carló iteration and when compared to the residuals seen in age, this comparative increase in uncertainty highlights (along with the decreased average residual and scatter compared to the literature) that for age, LISm χ is preferable to SpPXF.

3.9 Conclusion

This section has introduced three methods for the analysis of the integrated light spectra of compact stellar systems and shown the use of them on a large sample of local globular clusters with known parameters from resolved star studies.

The key finding from all three methods is that from integrated light spectra identifying age is incredibly difficult, there is a common age underestimation for all old globular clusters (with the older clusters showing the best age estimations with residuals in the range of $\sim 1\text{-}3$ Gyr). This is a common problem in spectral analysis

CHAPTER 3

of GCs (Puzia, Perrett & Bridges, 2005; Koleva et al., 2008; Cervantes & Vazdekis, 2009; Usher et al., 2019b; Boecker et al., 2020; Goudfrooij & Asa'd, 2021; Leath et al., 2022).

Metallicity was generally fit well with these techniques which shows that accurate parameters of these GCs can be extracted via integrated light spectral analysis but there was often a scatter in the metallicity residuals which is likely due to poor $[\alpha/\text{Fe}]$ estimation. $[\alpha/\text{Fe}]$ was fit well using SpPXF only for those GCs with very high signal to noise and this is in common with the results of LISm χ where the GCs with the highest signal to noise had the lowest residual to the literature value of $[\alpha/\text{Fe}]$. The solution to this is either to get more, higher SNR, data or to look elsewhere in the current data wavelength range for alpha-sensitive features which will increase the accuracy of the measurements. Although, for the narrow region SpPXF generally fit $[\alpha/\text{Fe}]$ well and within uncertainty indicating that the larger wavelength regions possess features which essentially confuse the $[\alpha/\text{Fe}]$ signal.

The solution to the age problem is complex. For all of the GCs which experienced an underestimation in age, there was poor fitting to the hydrogen lines (larger residuals around hydrogen lines between the object spectrum and model spectrum). There was $\text{H}\beta$ over and underestimation for almost all GCs which showed poor age estimations with the most metal-poor GCs with the highest age underestimations having very large $\text{H}\beta$ overestimations in the fit. This was also present in the lick indices, shown in Figure 3.26 is the mean of the residuals (χ s) of each index used in the fit. Hydrogen is shown as a clear outlier with the largest spread in χ values.

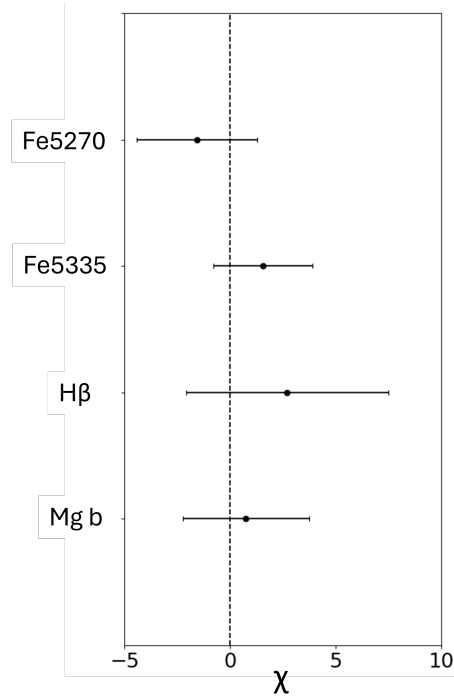


Figure 3.26: Figure based on Proctor, Forbes & Beasley (2004) showing the mean χ value for each index used with LISM χ for each GC in the sample. the error bars represent the standard deviation of the index values across the GCs.

This indicates that there is something wrong with the models used where the line strength of hydrogen is too weak in the models making the object appear younger than it actually should. A trend which has been found is that for higher metallicity GCs ($[\text{Fe}/\text{H}] \geq -1.0$) the age residual is significantly smaller (although still present) with a trend of increased age residual as metallicity decreases. Even for simple GCs, the techniques described in this chapter are not providing answers consistent with those derived from resolved GC constituent stars. There are a few objects in GCs which would make the GC appear younger than they should when compared to models that do not take them into account. One is Blue Horizontal Branch stars and the other is Blue straggler stars. This is examined in the next chapter where models which take into account blue stars are created to probe a solution to the age underestimation problem.

CHAPTER 3

What can be confidently measured using any of these methods is the metallicity. This project has a very large sample of CSSs and other objects, and the techniques used here will assist in the study of these objects. The last chapter of this work will take these techniques and the conclusions of Chapter 4 and analyse the large group of data looking to find common chemical abundance issues in CSSs and classify formation scenarios based on physical (mass-radius) parameters and parameters obtained through the analysis of the integrated light spectra of these objects (age, metallicity, specific chemical abundances).

Chapter 4

Simple SSP Models with Blue Straggler Stars

4.1 Introduction

The methods used in the previous chapter were tested on GCs because these are the “simplest” CSS and therefore should be subject to few anomalous population issues during spectral analysis. During the conduct of this project, it became clear that it has proven difficult to robustly estimate GC ages, which is a common theme in spectral energy distribution analysis (Puzia, Perrett & Bridges, 2005; Koleva et al., 2008; Cervantes & Vazdekis, 2009; Usher et al., 2019b; Boecker et al., 2020; Leath et al., 2022). Determining abundance anomalies relies on observational data with well-understood ages and metallicities to show that the ‘population’ of stars that cause this anomalous chemical abundance are either in-situ stars that have evolved differently or were later additions to the stellar system via star-burst formation or pollution of the chemical interstellar environment from an external source. Robustly determining age from the integrated light of objects is especially important for extragalactic objects where age cannot be determined by resolved star studies.

4.2 Sources of Age uncertainties

Firstly it should be noted that throughout this project the “age problem” is referred to age underestimation. It is assumed that the literature values of age provided via photometric studies (Usher et al., 2019a) are accurate and that the age values measured in this work are underestimated. This is well founded as other publications (see above) have also found similar age uncertainties. This section will look at the previous explanations of poor age estimation in integrated light spectrum analysis and probe other possible explanations.

A long-standing problem in spectral analysis was age-metallicity degeneracy (Worthey, 1994, 1999). This is the phenomenon where a single-age, single-metallicity stellar population can be spectrally similar to another single-age, single-metallicity population that is 3 times older and half as metal-rich as the first population. In Worthey (1994), it is described as “If the percentage change $\Delta \text{age}/\Delta Z$ approximately equals $3/2$ for two populations, they will appear almost identical in most indices.”. This phenomenon could explain the elongated curve upwards in metallicity as age decreases in the reduced χ^2 values of the data in Figure 4.1. This Figure shows how the younger SSP models have a similar reduced χ^2 to those of older more metal-poor SSP models. Although age-metallicity degeneracy can be countered by the presence of certain strong indices which are more sensitive to metallicity (LICK indices: Fe4668, Fe5015, Fe5709, Fe5782) or more sensitive to age such as G4300 and $H\beta$ (Worthey, 1994). For LISM χ (Section 3.8) $H\beta$ is used as one of the four indices used and this should counter the effects of age-metallicity degeneracy. In LISM χ this effect may not be completely removed due to the presence of the curved trend mentioned in Figure 4.1 but the presence of this trend is not enough to explain the large systematic underestimation in age.

The reduced χ^2 lines are extended in age in Figure 4.1. This can be explained by the similarity in the spectra for ages above ~ 4 Gyrs. This is another long-running

CHAPTER 4

problem in measuring age spectroscopically, in that the spectral features that indicate age have very small differences in intermediate-old ages. This would explain large uncertainties in the age estimation, but what is seen in this project is a systematic underestimation of age, which the similarity in old age spectra cannot explain. The age insensitivity at ages above ~ 4 Gyrs is a key problem here. The underestimated ages are likely to be the result of there being many more SSP models younger than the true age which Figure 4.1 shows as being as equally likely as the true value. This is a caveat to studying these spectra and must be considered. This chapter will attempt to address this insensitivity by discussing and implementing different stellar types (see below in Sections 4.2.1 & 4.2.2) which are not typically used in SSP models.

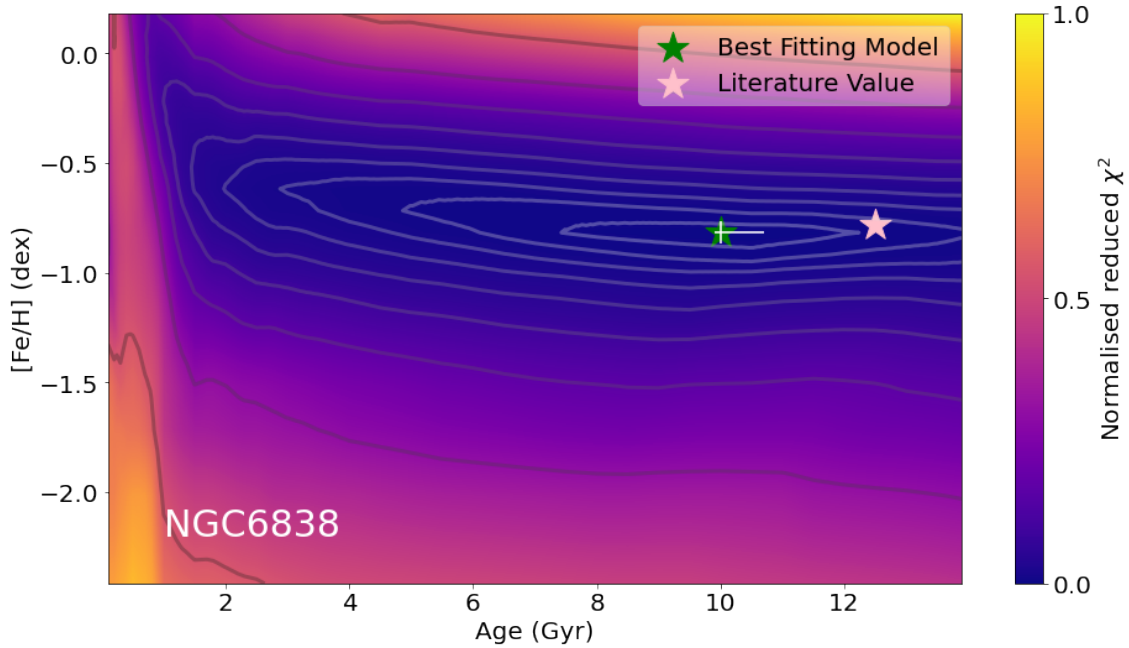


Figure 4.1: LISm χ contour age-metallicity plot of NGC 6838 showing the best fitting SSP and the normalised reduced χ^2 value of each SSP model. The lower normalised reduced χ^2 values indicate the better fitting models. The grey contour lines are the logarithm of the reduced χ^2 values and show detail at lower χ^2 .

CHAPTER 4

Another cause for the age underestimation could be poor sampling of the stellar environment causing only core light to be observed which will not provide full coverage of the stellar environment of the cluster and will skew the results to the parameters of just those core stars. As stated in Section 2.2.3, WAGGS data sometimes poorly samples the stellar environment of the observed GC by looking at the interior light. However, comparing the fraction of the GC mass in the field of view with the age underestimation, no obvious correlation was found. This work suggests this could be because stars that will affect age estimation (e.g. blue straggler stars; Singh & Yadav 2019) have complex bimodal radial distributions concentrating in the core and the outer regions of the GC. So different field-of-views will have different amounts of BSSs (Blue Straggler Stars) but without a linear correlation to the observed GC mass fraction. Another type of age-influencing star, the blue horizontal branch (BHB) star (see below), is loosely concentrated in the core (to a lesser proportion than red giants; Woolf 1964) but does extend significantly to the outer annuli of GCs (Krogsrud, Sandquist & Kato, 2013). Therefore poor stellar sampling would not have a consistent effect on the BHB's contribution to the GC integrated light. However, there is mass segregation in low mass stellar populations such as GCs (Fregeau et al., 2002) where the most massive (and therefore brightest) stars sink towards the centre. Therefore, different observations of the same object will have different stellar populations contributing to the integrated light depending on the size of the field-of-view.

4.2.1 Blue Horizontal Branch Stars

The age underestimation may be due to populations of stars within the GC itself causing the integrated light spectra to appear younger than it actually is.

One type of star that may be responsible for this is the BHB star. These stars have evolved from low-mass stars and after the red giant branch, have undergone a

CHAPTER 4

helium flash (Moehler, 2001; Culpan, Pelisoli & Geier, 2021). They lie on the blue side of the instability strip (purple oval in Figure 4.2).

It is well studied that BHB stars cause large uncertainties in the age estimations of GCs via their integrated light (Koleva et al., 2008; Percival & Salaris, 2011; Cabrera-Ziri & Conroy, 2022; Leath et al., 2022; Sharina et al., 2024). They are relatively bright, and blue in colour (i.e. hot) which will bias the continuum and cause increases in the Balmer absorption line strengths leading to younger age estimations.

For SSP models such as MILES (Vazdekis et al., 2010) and sMILES (Knowles et al., 2023), BHB stars are not taken into account and this could be a leading cause of the age underestimation (in low metallicity objects). Cabrera-Ziri & Conroy (2022) added the light of BHB stars to SSP models using the “alf” code (Conroy & van Dokkum, 2012; Choi et al., 2014; Conroy, Graves & van Dokkum, 2014; Conroy et al., 2018) which was originally designed to fit the absorption lines of old massive galaxies but which they adapted for modelling GCs. They did this by “includ(ing) the flux contribution of a hot HB star *over and above* the [predicted flux] from a standard isochrone” (Cabrera-Ziri & Conroy, 2022). They found that the age estimation improved significantly with their models used with high SNR, low-resolution optical integrated light spectra of GCs.

There is a correlation between age underestimation in this work and the metallicity of the GC (e.g. Figures 3.11 & 3.12). This can be explained by the relationship between BHB population and cluster metallicity, where BHB star percentage increases as metallicity decreases (Kodaira & Philip, 1984; Kafle et al., 2013; Chung, Lee & Pasquato, 2016; Ju et al., 2024). In addition, the presence of multiple stellar populations in globular clusters have not been taken into account where helium overabundance is often a signature (Milone, 2015; Fare, Webb & Sills, 2018). According to Chung, Lee & Pasquato (2016), stellar evolution theory indicates that BHB stars

CHAPTER 4

(which have enhanced helium; Gross 1973; Paunzen et al. 2019; Culpan, Pelisoli & Geier 2021) would appear even bluer on the HR diagram leading to an increased age under-estimation.

The evidence discussed in this Chapter suggests that BHB stars are the leading cause of age under-estimation. It is known that BHB stars are only present in metal-poor stellar environments (Kodaira & Philip, 1984; Kafle et al., 2013; Chung, Lee & Pasquato, 2016; Culpan, Pelisoli & Geier, 2021; Ju et al., 2024) with Figure 4.2 showing the BHB population/metallicity correlation, with no BHB stars with metallicities above $[\text{Fe}/\text{H}] = -1.0$. In the previous chapter, it is found that there is also an age underestimation (although less significant) in more metal-rich GCs (For example NGC 6838 in Figure 4.1). The age under-estimation at higher metallicities should not be due to BHB stars, so another star that will affect the apparent age of a cluster must be considered. Some metal-rich GCs have BHB stars (i.e. NGC 6441 Krogsrud, Sandquist & Kato 2013) but this is thought to be due to GC mass (NGC 6441 being the second most massive GC in the WAGGS sample), and a population of high helium abundance stars.

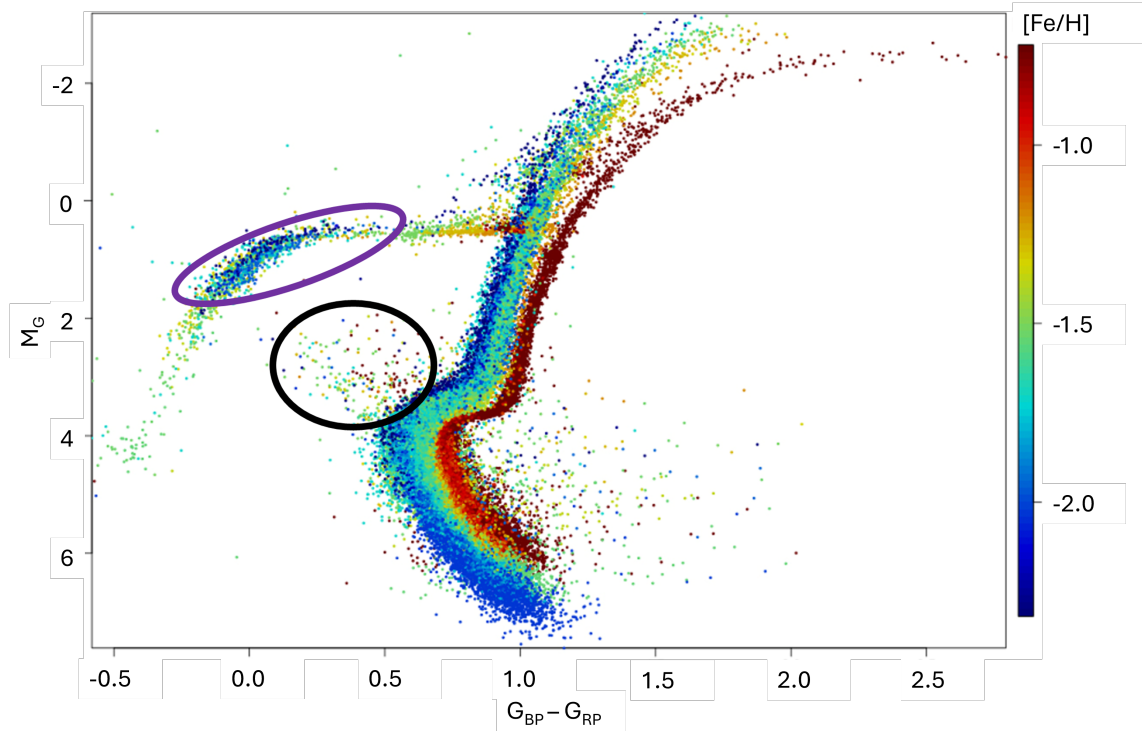


Figure 4.2: A combined Hertzsprung-Russell diagram of 14 metal poor ($-2.3 \leq [Fe/H] \leq -0.72$) GCs using GAIA DR2 photometry, they are coloured according to metallicity. This image is Figure 3 from Gaia Collaboration et al. (2018). Two ovals have been added which indicate the Blue Horizontal Branch stars (purple) and Blue Straggler stars (black). The only GC here with ‘high’ metallicity is NGC 104 (47 Tuc) whose red clump (associated with more metal-rich populations) is hidden under the more metal-poor populations.

4.2.2 Blue Stragglers

Blue Straggler stars lie along the main sequence on the HR diagram but appear to lie after the main sequence turn-off of their host GC (Figure 4.2). Unlike BHB stars they can exist at all metallicities Cennaro et al. (2008); Wyse, Moe & Kratter (2020). Given their mass (Shara, Saffer & Livio, 1997), they should have evolved off the main sequence long ago, but instead they “straggle” behind the stellar evolution

CHAPTER 4

of the rest of the cluster making them appear much younger than they actually are.

There are two main avenues for BSS formation. They are thought to form from the coalescence of stars in dense stellar environments (Hills & Day, 1976) where the collision and stars combining leads to a more massive star which naturally burns brighter and has a higher surface temperature (making it bluer). The second method of formation is a ‘vampire’ (McCrea, 1964) formation scenario resulting from mass transfer in binary star systems where a more massive star accretes the mass of another star extending its core hydrogen burning phase. There has been much research into the topic of BSS formation paths and the BSS populations of GCs (McCrea, 1964; Hills & Day, 1976; De Marco et al., 2005; Chatterjee et al., 2013; Portegies Zwart, 2019).

Portegies Zwart (2019) looks into the origin of two populations of BSSs in NGC 7099 (M30) finding that the populations can be separated by their formation scenarios. They speculate that a younger (bluer) population formed in a short burst of stellar collisions from a GC core-collapse scenario around 3.2 Gyr ago, with a formation rate of around 30 stars per Gyr. The other BSSs which they call ‘red stragglers’ lie redder than the young population on the HR diagram. They are generally older and are the result of constant BSS formation of around 2.8 BSSs per Gyr over the last ~ 10 Gyr. The older population formed from the mass transfer between binary systems and they conclude that about half of all binary systems in this cluster result in BSSs. This is supported by what was found in Chatterjee et al. (2013) that for low-density clusters mass transfer of binaries is the leading formation path of BSS stars (up to 60% of total cluster BSS population). While for the collision model, central densities above $\sim 10^3 M_{\odot} \text{pc}^{-3}$ are needed for this to be the dominant formation channel. It should be noted that Ferraro et al. (2009) states that the core collapse scenario of NGC 7099 created both of the populations of BSSs as the collision rate and binary interaction rate would have increased. Both Ferraro

CHAPTER 4

et al. (2009) and Portegies Zwart (2019) agree, however, that the bluer population was formed via stellar collision and the redder population by binary mass transfer.

Both BSS formation scenarios create stars that appear younger than the rest of the GC. These stars are bright (typically from the turnoff to 2 magnitudes brighter, with the brightest being 3 magnitudes brighter than the turnoff, Rain, Ahumada & Carraro 2021) and when studying spectra of specifically high SNRs, their light can influence the integrated light of these objects significantly (Deng et al., 1999; Ferraro et al., 2006; Koleva et al., 2008; Cenarro et al., 2008). BSSs are much fainter than other stars in the system such as red giant branch (RGB) stars so it could be questioned how much these stars actually affect the spectrum. However, in the blue wavelength ranges, which are more sensitive to age (Koleva et al., 2008), BSSs can contribute more light to the spectrum than RGB stars and therefore these stars need to be considered and as stated in Cenarro et al. (2008) BSSs can contribute significantly in the V band.

The findings of binary mass transfer and the light of BSSs influencing the integrated light are interesting as binary systems exist in all stellar environments. This indicates that there are, potentially, populations of blue straggler stars in every stellar environment which could affect the light of these environments. From this theory, in well-mixed stellar environments (like the disk of the milky way) BSSs still exist but it would be hard to identify them as they would appear similar to any other young stars in the system. They only stand out in GCs because they are anomalously young in appearance. They would still affect the integrated light of these objects and work should be done to identify how much the light of BSSs contributes to the total integrated light of these objects. Portegies Zwart (2019) states that half of all binary systems in the GC NGC 7099 create blue straggler stars and the importance of the presence of BSSs in massive, well-mixed, stellar populations needs to be fully understood, for example, in studies that seek to determine the star-formation

CHAPTER 4

histories of galaxies such as Davison (2021).

One study on this topic (Wyse, Moe & Kratter, 2020) studies the populations of BSSs in low-density stellar environments such as dwarf spheroidal (dSph) galaxies and agrees with Chatterjee et al. (2013) & Portegies Zwart (2019) that the dominant BSS formation scenario for low-density environments is mass transfer between close binary interactions. They also find a correlation between metallicity and BSS fraction stating that lower metallicity environments have higher BSS populations matching the metallicity anti-correlation of close binary fraction in the field population of the Milky-Way (Moe, Kratter & Badenes, 2019). The author recommends that future work to identify the population of BSSs formed this way in less stellar dense environments should be undertaken.

Examining how BSSs affect the light of GCs; Cenarro et al. (2008) finds that for the GC, NGC 6342, 13% of the V band flux within the core comes from light off just 7 BSSs. This is a significant percentage of the core light. NGC 6342 is a low mass GC compared to other galactic GCs Harris (2010). Flux contribution of this amount shows clear correlation with $H\beta$ (Cenarro et al., 2008) and will lead to younger spectroscopic age estimations.

Previously it was described how Cabrera-Ziri & Conroy (2022) created models that take into account the light of BHB stars and correct for age. Koleva et al. (2008) does a similar experiment where they perform full spectral fitting of GC spectra (taken from Schiavon et al. 2005) using SSP models from multiple sources (Bruzual & Charlot, 2003; Le Borgne et al., 2004; Vazdekis et al., 2010) along with the spectra of hot blue young stars, freely fitting to any combination of spectra. They find that the measured age of a GC is very sensitive to the presence of BHB and BSSs spectroscopically.

The contribution of BHB stellar light has been studied well and it is beyond the scale of this thesis to further examine their contributions to integrated light of

GCs. The majority of the CSS in this thesis are relatively metal rich and would contain BSSs, not BHB stars. Therefore below, simple population models that include the light of BSSs at realistic proportions are created and implemented to observe the effects on age estimations of the methods presented in the previous chapter (BpPXF and LISm χ , SpPXF is excluded because of its extended run time and because the information extracted from this method can be extracted with the other two methods).

4.3 Making BSsMILES Models

To understand the effects of BSS light on the integrated light of GCs simple models have been created for this work that include their light which are here named BSsMILES. The models created were based on the sMILES SSP models (Knowles et al., 2023) as these models were created internally in the institute and there was access to their base ingredients. They also had a large range of metallicities, ages and alpha values and had a relatively high MILES resolution of 2.51 Å (FWHM). As stated in Chapter 2, sMILES models are semi-empirical SSP models that cover a large range of metallicities, ages, and $[\alpha/\text{Fe}]$ abundances, the stellar sample they used for their creation was lacking BHB star candidates and so the horizontal branch is not well modelled. This is fine for purposes of this chapter as light representing blue straggler populations will be added which are uncorrelated to populations of BHB stars. As well as this, the sMILES SSP models were the ones used in the previous chapter so the same models are used to allow a direct comparison.

The most concise way to describe the process of model creation is to state that the light of blue, empirical or theoretical, main sequence stars of the correct effective temperature (T_{eff}), surface gravity ($\log g$), metallicity and $[\alpha/\text{Fe}]$ as a predicted blue straggler were added to an SSP model of set age, metallicity and $[\alpha/\text{Fe}]$.

4.3.1 Blue-Star Sample

For the ‘BSsMILES’ models that are created here, the light of a representative “blue straggler” star was added to the light of the SSP models at a range of proportions. The parameters of the added BSS are defined here.

De Marco et al. (2005) showed that most blue stragglers in a system have effective temperatures between 6300 to 14000 K and have surface gravities of around $\log(g) = 4.5$ at the hottest effective temperatures, going down to $\log(g) = 3.8$ at lower effective temperatures. While Chatterjee et al. (2013) agrees, stating $T_{\text{eff}} = 6300$ and $\log(g) = 4.0$ and Cenarro et al. (2008) states the hottest BSS had a temp around 7500 K for NGC 6342 (at age = 12.5 Gyr, De Angeli et al. 2005). The surface gravity and temperature for BSSs are generally less than that of BHB stars (although there can be some ambiguous overlap in these stars, De Marco et al. 2005). Because of this the stellar samples used were limited to these ranges and below the horizontal branch on the HR diagram that De Marco et al. (2005) used defined from VandenBerg et al. (2000).

A catalogue of stars that could be used as potential blue straggler candidates was needed. The logical first step for this was to look at the stellar library used for MILES and sMILES. The MILES stellar library (Sánchez-Blázquez et al., 2006) consists of ~ 1000 stars at a large range of atmospheric parameters and evolutionary phases. For BSSs only main sequence V-type stars are needed so this limited the number of stars immediately to a stellar sample of only 281 stars (Figure 4.3). The sample of stars did not need to be limited further, as limiting the stars to the main-sequence only, meant that any light added would automatically represent a Blue Straggler population (when the desired BSS parameters are accurately calculated).

Due to being drawn from the stars of the Milky Way, there are no MILES stars in the high-temperature low metallicity region so other stars were needed. For this theoretical stars from Coelho (2014) were used. These stars offered high-temperature

CHAPTER 4

stellar spectra at lower metallicities than the MILES stellar library and at specific surface gravities. Shown in Figure 4.3, the selected values are $\log(g) = 4.0$ for temperatures below 11,000 K, and $\log(g) = 4.5$ for temperatures above this to avoid spectra from theoretical stars which have similar temperatures and gravities to HB stars.

CHAPTER 4

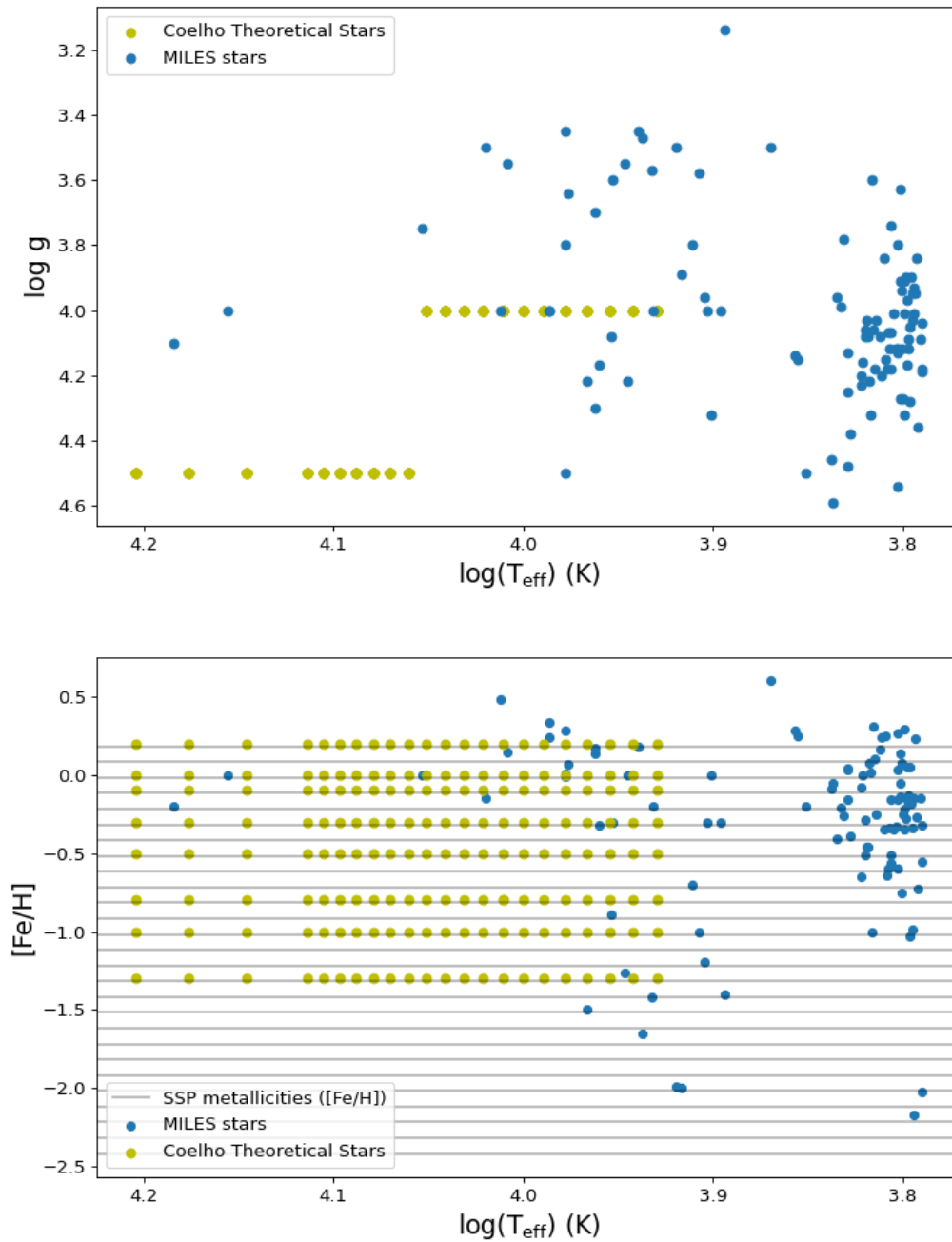


Figure 4.3: The plot of the effective temperature against the surface gravity (upper) and effective temperature against the metallicity (lower) for the stellar library used in the construction of the BSsMILES models.

The Coelho theoretical stars cover a metallicity range of $[\text{Fe}/\text{H}] = 0.2$ to $[\text{Fe}/\text{H}] = -1.3$.

CHAPTER 4

Figure 4.3 shows that at higher effective temperatures there is still an absence in low metallicity spectra. Accurate, high SNR spectra of blue stragglers in low metallicity GCs are needed to fill this gap. However, Leath et al. (2022) states that age underestimation is not due to BSSs at metallicities lower than $[M/H] = -1$ and is instead due to helium overabundance (likely from BHB stars; Gross 1973; Paunzen et al. 2019; Culpan, Pelisoli & Geier 2021), so a lack of hot, low metallicity stars will not affect the results if metal-poor GCs are ignored. But slight metallicity overabundance will have to be accepted in the low metallicity SSPs if they are used for an object with low metallicity. Increased metallicity has only a small effect on the spectroscopic age, changing the continuum to appear cooler and thus slightly older (Conroy, 2013) (a symptom of age metallicity degeneracy; Worthey 1994). This is a small effect compared to the effective temperature which dominates Balmer line strength. So for the creation of BSsMILES, finding a blue star with the correct T_{eff} is a higher priority than finding one with the correct metallicity.

The Coelho stars can either be alpha-enhanced to 0.4 or solar-scaled. It was chosen to have the stars as alpha enhanced to match the general enhancement of GCs. The median alpha enhancement of the metal-rich ($[Fe/H] \geq -1$) GCs in the WAGGS sample (with published $[\alpha/Fe]$ values) was $[\alpha/Fe] = + 0.295$. For simplicity, the same alpha-enhanced $[\alpha/Fe]=0.3$ sMILES SSP models used in the previous Chapter will be used. This means however that as BSS proportion increases the alpha abundance of the spectrum will increase causing an overestimation of metallicity when Coelho (2014) stars are used. The alpha enhancement of MILES stars is well measured, with a correlation between reduced alpha abundance as $[Fe/H]$ increases at metallicities above $[Fe/H] = -1.0$ (Knowles et al., 2023). Their alpha abundance mostly matches that of the GCs in the sample so it can be assumed that there are no effects due to poor alpha selection in BSsMILES models where MILES stars were used.

4.3.2 Blue-Star Selection

For each SSP model, a star from the sample needed to be identified which would best represent the brightest BSS from a population of that age and metallicity. To do this the effective temperature of a star formed by the complete collision of two stars with mass equivalent to that of the MSTO (Main Sequence Turn Off) (being the most massive star still on the main sequence), where the resulting star has double the MSTO mass was calculated. Portegies Zwart (2019) showed how stellar collisions create hotter, brighter BSSs justifying the use of this formation scenario for the BSS Teff calculation used here. This, therefore can be considered a simplistic “worst case” scenario where the light to be added is the most discrepant compared to the expected light of an SSP.

This formation scenario assumes an idealistic 100% mass conservation in the collision. This is probably not realistic as during collisions there is inevitably a small amount of mass loss (Davies, Benz & Hills, 1993; Freitag & Benz, 2005; Genzel, Eisenhauer & Gillessen, 2010). However, the mass loss does not represent a significant change in mass of the final product of collision (Vergara et al., 2021). De Marco et al. (2005) also supports the BSS mass being double the MSTO mass. While their calculated mean BSS mass is slightly less than double, the variance of this result allows for a star of double the MSTO mass.

Stellar mass was calculated using the mass-light ratio. The main sequence turn-off mass of intermediate to old GCs is less than $2 M_{\odot}$ thus the M/L equation (Equation 4.1) can be used.

$$\frac{L}{L_{\odot}} = \frac{M}{M_{\odot}}^4 \quad (4.1)$$

Using alpha enhanced BaSti isochrones (Figure 4.4) (Pietrinferni et al., 2021) with helium abundance $Y = 0.275$ (based on data from Leath et al. 2022) and $[\text{Fe}/\text{H}] = -0.9$ (to match the more metal-rich GCs where BSS light is the dominant cause of the age underestimation as discussed earlier), the luminosity of the peak

CHAPTER 4

temperature on the MSTO was used as the luminosity of the most massive star on the main sequence which was then used to calculate the mass.

To calculate the effective temperature of the blue straggler the luminosity - radius - temperature relation for stars

$$T_{eff} = \sqrt[4]{\frac{L_{BS}}{4\pi\sigma R_{BS}^2}} \quad (4.2)$$

can be used, where L_{BS} is the luminosity of the BSS in watts (calculated by the inverse of 4.1 with its exponent changed to 3.5 to account for the increased mass of the BSS*). In this equation, σ is the Stephan-Boltzman constant and R_{BS} is the radius of the BSS.

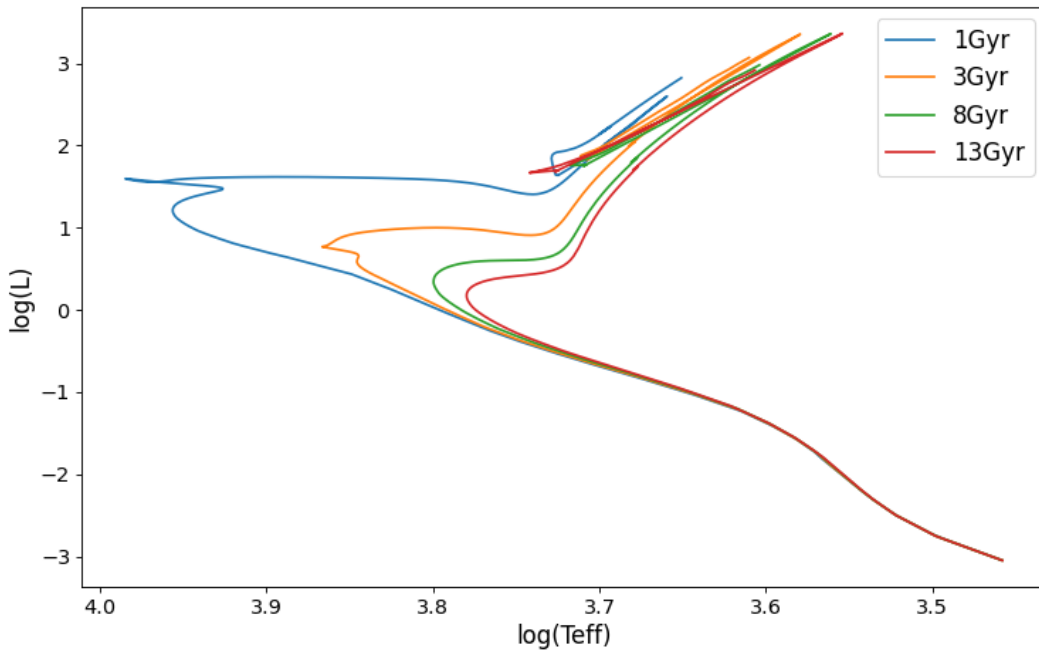


Figure 4.4: BaSt Isochrones (Pietrinferni et al., 2021) at different ages, $[\text{Fe}/\text{H}] = -0.9$, & $Y = 0.275$.

To calculate BSS radius the radius of the initial stars before the collision needs to be calculated. Using the inverse of 4.2, the MSTO effective temperature and

*These values for the mass-luminosity relation are broad estimates and it is acknowledged that future work should use more accurate, specific values for the calculated BSS masses where possible.

CHAPTER 4

luminosity (from the Pietrinferni et al. 2021 isochrones) the radius of one of the initial stars is produced. Assuming that the BSS formation comes from the collision of two of the most massive stars on the main sequence, these stars therefore have the same mass and radius. The equation

$$R_{BS} = R_0 \left(1 + \frac{M_1}{M_2} \right)^{\frac{1}{3}} \quad (4.3)$$

is used to calculate BSS radius where R_0 MSTO radius. M_1 and M_2 are the same so this equation goes to $R_{BS} = R_0 \cdot 2^{\frac{1}{3}}$.

It should be noted that this equation is based on work presented in Vergara et al. (2021) for population III star collisions. However, it is found that the radius resulting from this equation agrees with the radius calculated from stars with the same T_{eff} and luminosity as BSSs (using equation 4.2 and mass and temperature values from De Marco et al. 2005).

There are a lot of calculations used here to estimate the effective temperature of theoretical blue straggler stars for single stellar populations at different ages, the values of which are shown in Figure 4.5. These values are consistent with those presented in De Marco et al. (2005), Chatterjee et al. (2013), and Portegies Zwart (2019) for the most massive BSSs in a GC. However, to do so the MSTO masses have had to be increased compared to isochrones of the same age (e.g. the isochrones used to estimate MSTO temperature: Pietrinferni et al. 2021). The increased mass compared to the isochrone values is due to the equations presented above and so the values of mass can be relied upon.

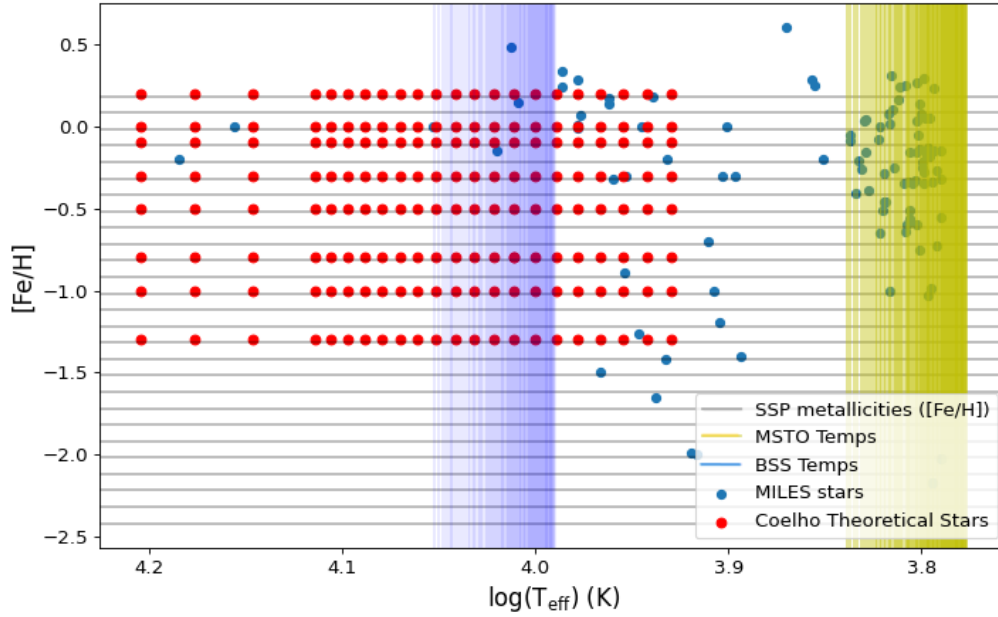


Figure 4.5: The plot of the effective temperature against the metallicity for the stellar sample, showing (yellow vertical lines) the effective temperature of the sMILES models MSTO (at different ages) and the effective temperature of the calculated ‘most massive’ Blue straggler star for each sMILES model age (blue vertical lines).

This method does not account for the full population of BSSs in a SSP, it just represents the most luminous, youngest seeming BSS present. For a more comprehensive inclusion of BSS light in SSP spectra a combination of BSSs of different ages representing the whole of BSS formation is needed. Chatterjee et al. (2013) states that BSS formation has been occurring over an 8 Gyr period while Portegies Zwart (2019) suggests the GC NGC 7099 has been forming BSSs consistently for ~ 10 Gyr. Here, the simple case of including only the light of the most massive BSS in the system as a representation for the population as a whole is used. This has only been done to increase understanding of the general effects of BSSs on integrated light spectra. Because of the BSS formation rates found in Chatterjee

CHAPTER 4

et al. (2013) and Portegies Zwart (2019), the age of the collision formation trigger of core-collapse found in Portegies Zwart (2019), the increase in central BSS percentage with increased GC relaxation time (Ferraro et al., 2018, 2023) and the low BSS fraction in the young GC NGC 419 (Dresbach et al., 2022) the SSP construction process only added the light of BSSs to SSPs that were 3 Gyr and older.

Now the desired BSS parameters have been calculated, the library of empirical and theoretical stars is searched for the star with the closest effective temperature and metallicity and add that light to the SSP spectrum as a fraction representative of a real BSS population.

4.3.3 BSS SSP Combination

Cenarro et al. (2008) states that in the core of the GC NGC 6342, 13% of the light in the V band comes from BSSs. As relaxation time increases for a GC, the central concentration of BSSs increases (Ferraro et al., 2018), so for the GC sample of this work, differences in mass fractions in the FOV may affect the fraction of the integrated light contributed by BSSs. Therefore, for this project, initial BSS contributions of 0.1, 0.5, 1.0, 5.0, and 10.0 percent in the V band were chosen to probe how different BSS fractions affect the spectrum of different GCs. However, it should be noted as stated in Section 4.2 no correlation between mass fraction in the FOV and age underestimation was found so it was unsure if there would be an observed correlation between mass fraction in the observed FOV and ‘ideal’ BSS fraction.

To create these models, the first step was to smooth the stellar and SSP model spectra to the same resolution and limit it to the same wavelength range. A resolution of $\Delta\lambda = 2.51 \text{ \AA}$ was used to match the sMILES models. The MILES stars were already at this resolution, but the Coelho stars have a much higher resolution of $R = 20,000$ (Coelho, 2014) and had to be smoothed using the same

CHAPTER 4

method described in section 3.4.1. The flux of the selected BSS and SSP model were normalised to the same flux value at the midpoint of the sMILES wavelength range (the spectra were in different units and therefore had different pixel values as the Coelho stellar flux corresponded to stellar surface fluxes and were in units of $\text{erg cm}^{-2} \text{s}^{-1} \text{\AA}^{-1}$ (Coelho, 2014) while the SSP models and the MILES stars were already normalised; Sánchez-Blázquez et al. 2006). The flux of the contributing star in the V band was then calculated by multiplying the BSS spectrum by a normalised V band transmission curve[†], and summed the total flux in the V band. After doing the same process for the SSP model, the BSS total V band flux was multiplied by the desired contribution percentage and multiplied the BSS spectrum by this value. Then the SSP V band flux was multiplied by the opposite fraction (so if 1% BSS fraction was desired the summed SSP V band flux would be multiplied by 0.99) and multiplied the SSP model spectrum by this value and added the new BSS and SSP spectra together. This process is shown in Figure 4.6 for a 10% BSS contribution but can be best described by the equation

$$SSP_{new} = (0.1 \cdot \Sigma(V_{BSS})) \cdot BSS + (0.99 \cdot \Sigma(V_{SSP_0})) \cdot SSP_0 \quad (4.4)$$

where $\Sigma(V_{BSS})$ is the summation of the BSS spectrum multiplied by the V band transmission curve, $\Sigma(V_{SSP_0})$ is the summation of the SSP spectrum multiplied by the V band transmission curve, SSP_0 is the original SSP model spectrum and BSS is the original blue star spectrum.

Under ideal circumstances, the sum of the initial V band flux for the blue star and the SSP model were identical, causing the proportions of each spectrum added together in Equation 4.4 to be accurate. However, there was often a 1-6% flux difference in these due to large continuum differences between the SSP and the blue star and non-ideal flux normalisation. This was corrected for by re-scaling one side

[†]Calculated in Python with the Johnson et al. (1966) V band transmission curve provided by the package PyAstronomy pyasl.

CHAPTER 4

of the addition in equation 4.4 so that $\Sigma(V_{BSS})$ was equal to $\Sigma(V_{SSP0})$ (which would ideally have been achieved by the initial normalisation between the models).

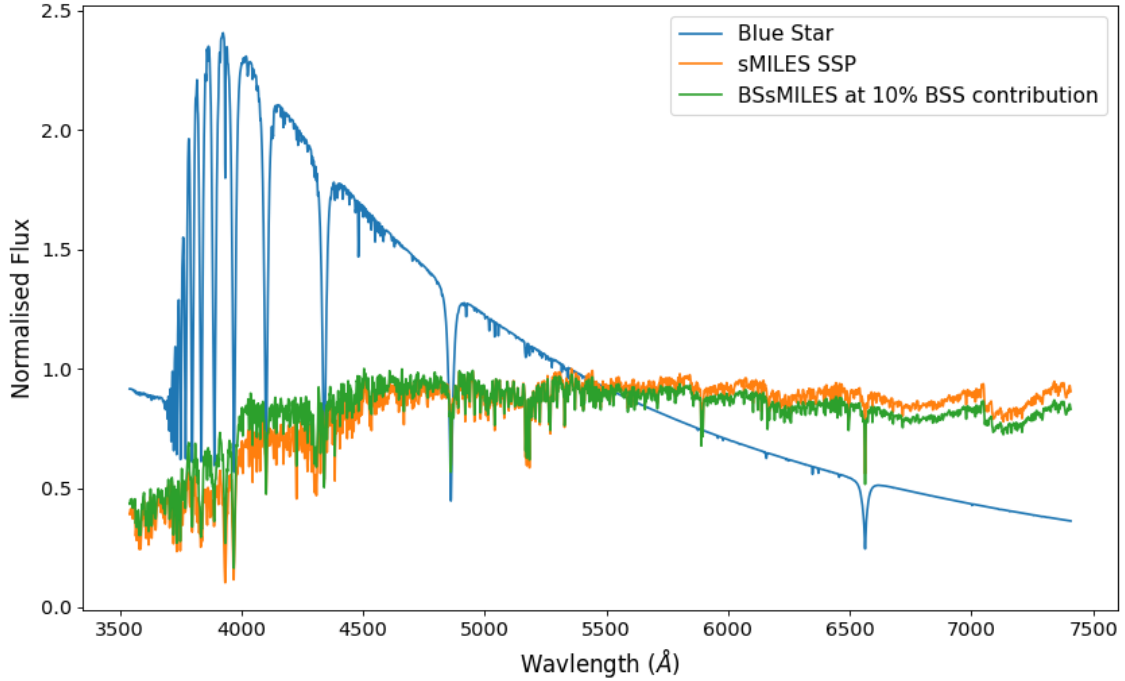


Figure 4.6: The creation of BSsMILES. Blue shows the spectrum of the blue star, in this case, it is a Coelho theoretical star (Coelho, 2014) with $T_{eff} = 10000$ K and $[Fe/H] = -0.5$. Orange is the sMILES model the blue star is added to, it shows an 8 Gyr SSP with $[Fe/H] = -0.5169$. Green is the combination of both the BSS and the original SSP with the blue star contributing 10% (from the Vband flux ratio between the two spectra) to the SSP model.

Shown in Figure 4.7 is the $H\beta - [MgFe]'$ plot of the WAGGS sample. Overlaid onto this plot are single age grids of the LICK indices measurements of sMILES and BSsMILES SSP models. Shown are the ages and metallicities for three different percentages of BSS light contribution 0%, 1%, and 5%. As BSS light contribution is increased, $H\beta$ strength increases while $[MgFe]'$ does not show significant change. As stated previously $H\beta$ is the key age indicator used with the LISm χ and the plot shows an increase in $H\beta$ can be considered a decrease in age. The GCs lie below the

CHAPTER 4

12 Gyr model at all BSS percentages, as BSS percentage increases the GCs appear to lie lower and lower than the SSP models indicating an increase in GC estimated age.

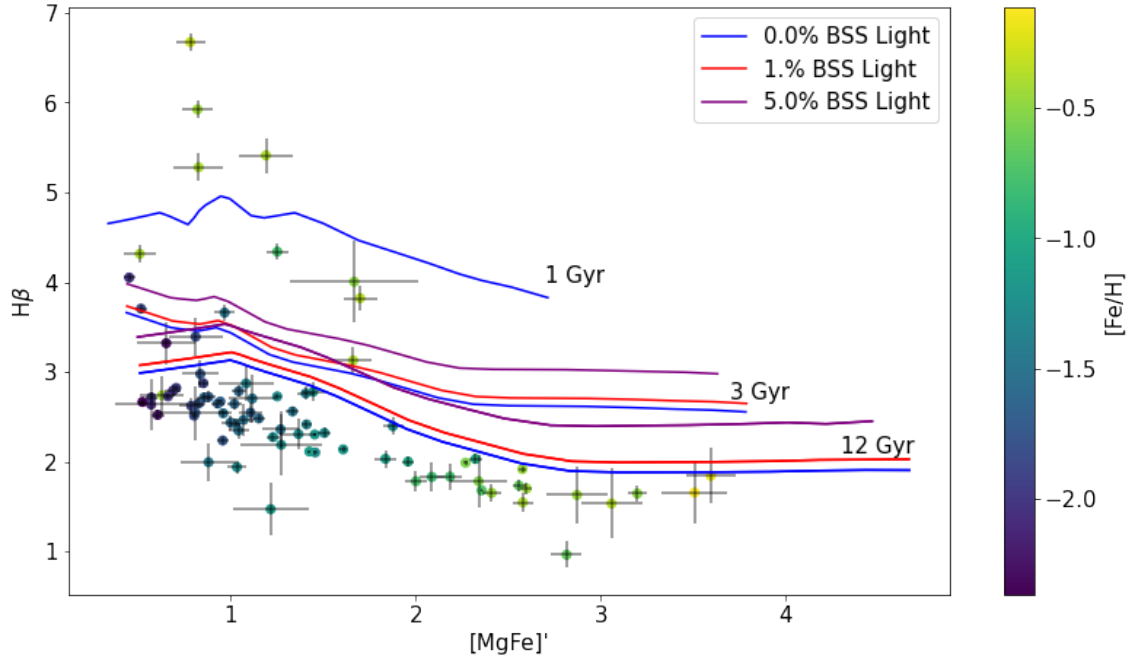


Figure 4.7: Plot of $H\beta$ against $[MgFe]'$ indices showing the sMILES and BSsMILES models at different ages. No BSsMILES models were made at ages below 3 Gyr and this is shown in the figure. Also shown are the measured values of WAGGS (Usher et al., 2017) GCs. Model and GC indices are measured at a resolution of 2.51 \AA (FWHM).

Figure 4.7 shows that it can be expected that (when the full spectrum is fitted) the $H\beta$ absorption line will fit less well as BSS percentage increases due to there being a correlation between $H\beta$ over estimation and BSS percentage. This is shown best in figures of Section 4.5. This phenomenon seems counterintuitive as one would expect better fits of $H\beta$ if there was a significant contribution of light from BSS populations. However, as shown in the next sections, with increased BSS percentage there is an improvement in the age estimation compared to the standard sMILES

CHAPTER 4

SSP models.

4.4 LISm χ

First, the BSsMILES models are used with the LISm χ method defined in Section 3.8. The results of which are shown in Figures 4.8, 4.9, 4.10 & 4.11 and presented in Table B.4. In these plots, the residual estimations for age and metallicity have been split to above and below $[\text{Fe}/\text{H}] = -1$. This was done to represent the separation between where blue stragglers affect the age estimation of GCs and where BHB stars start to dominate (Cenarro et al., 2008; Kafle et al., 2013; Leath et al., 2022; Cabrera-Ziri & Conroy, 2022).

4.4.1 Age

SSP models with BSS contribution percentages of 0.1 and 0.5 % were made for this project but their effect in the age vs metallicity domain was found to be minimal and so are not plotted or tabulated here.

Shown in Section 3.8 and again in Figure 4.8 it is found that for normal sMILES SSP models, above the $[\text{Fe}/\text{H}] = -1$ cutoff the age residual is significantly smaller than for metallicities below this cutoff. This trend continues in results utilising higher BSS percentages. In Section 3.8 (Figure 3.20) sMILES models are used at an age binning of 0.1 Gyr between 0.1 and 13.9 Gyr. For this section, younger GCs are not being used and as such the SSP age range has been limited to be between 3.0 and 13.9 Gyr (with the same 1 Gyr binning).

The higher metallicity sections of Figures 4.8, 4.9, 4.10 & 4.11 show that as BSS fraction increases the age residual generally gets smaller. There are a few exceptions to this and it is hypothesised here that this is due to different proportions of BSS contribution to the integrated spectra of these objects. At BSS percentages

CHAPTER 4

of 10% at the highest metallicities the age is over-estimated, indicating that at higher percentages, potentially too much BSS light has been introduced to the SSP models. More metal-rich GCs may have fewer BSSs according to the close binary fraction/metallicity relation Moe, Kratter & Badenes (2019). But they will still have BSSs due to stellar collisions which would explain the smaller (but none-zero) BSS fraction needed.

Below the metallicity cutoff, as BSS fraction increases, measured age increases but does not completely correct the age underestimation problem. This is in agreement with the literature which states that BSSs are not a dominant contributor to age estimation problems at lower metallicities (Leath et al., 2022). It is expected that the ages below the metallicity cutoff will increase as there is still the addition of a fraction of hotter, bluer stars to the SSP spectra which would affect the age estimations regardless of stellar type, but BHB stars are hotter and brighter than BSSs and dominate the integrated light of stellar systems at higher proportions than BSSs would.

Figures 4.8, 4.9, 4.10 & 4.11 also show the output measured metallicity of the GCs and this is covered below, and shown in Figures 4.12, 4.13, 4.14 & 4.15.

CHAPTER 4

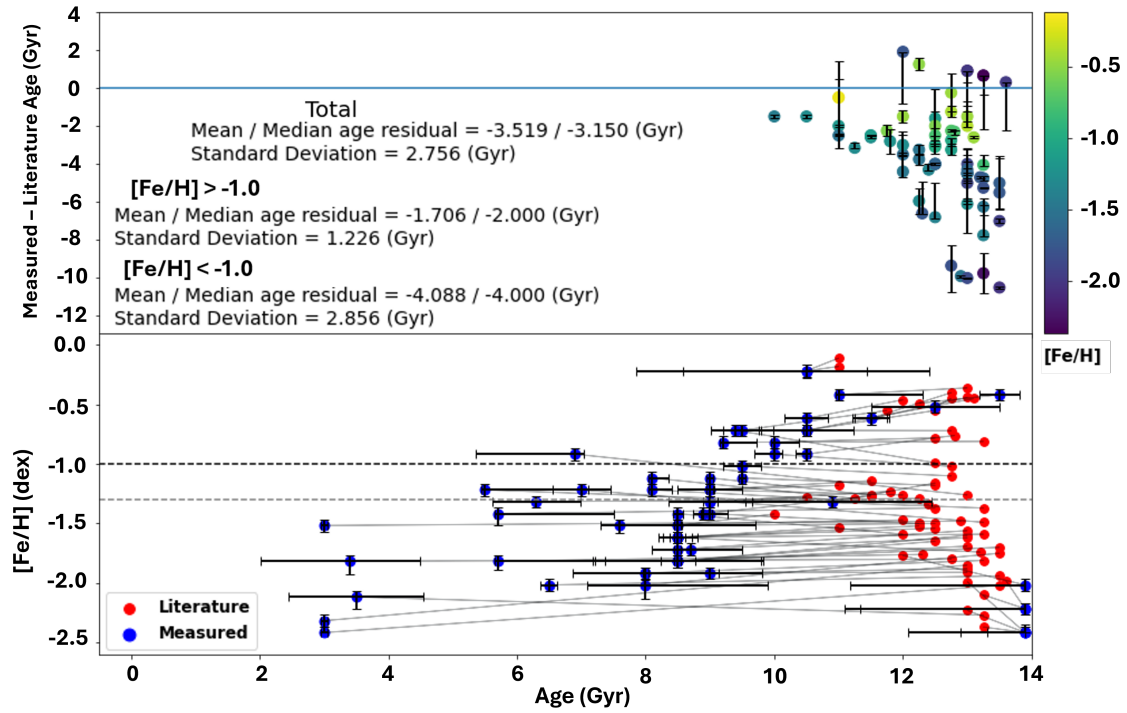


Figure 4.8: LISm χ output values using sMILES models with 0% BSS addition. The models and WAGGS GCs are limited to ≥ 3 Gyr. The top panel shows the literature age against the residual age (measured - literature). The bottom panel shows the output and literature values in the age vs metallicity space. The black dashed line represents a continuum at $[\text{Fe}/\text{H}] = -1.0$ dex, the grey dashed line represents a continuum at $[\text{Fe}/\text{H}] = -1.3$ dex to show the lowest metallicity star added to the SSP models.

CHAPTER 4

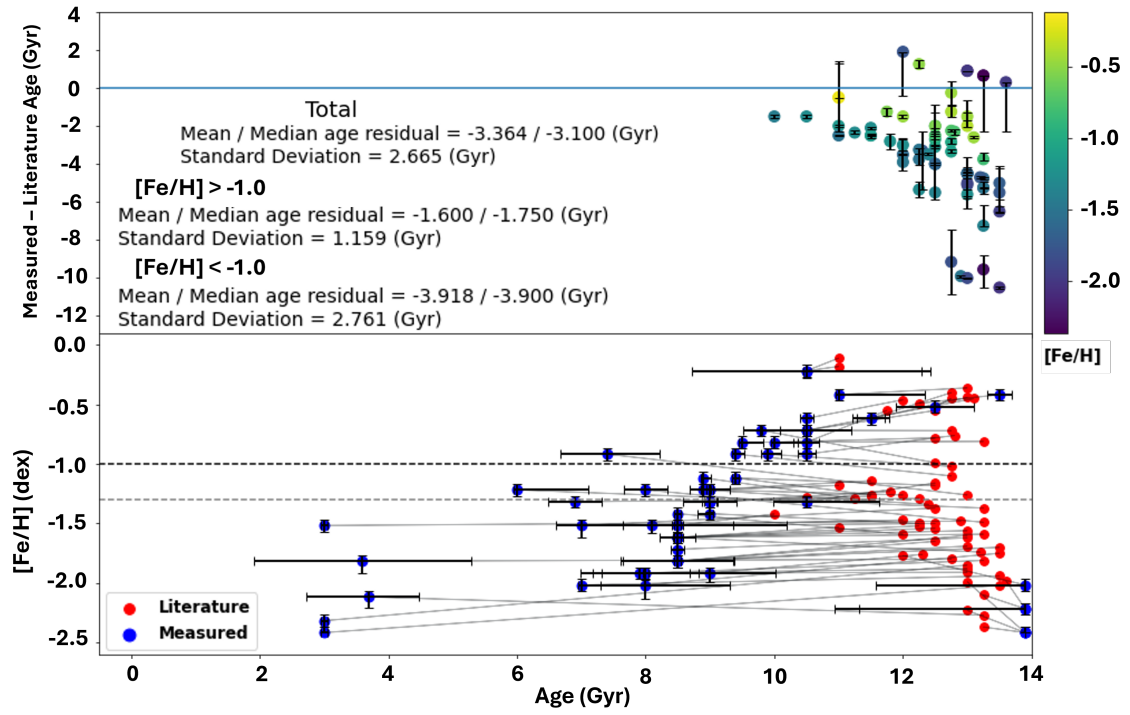


Figure 4.9: Same as Figure 4.8 but using BsMILES models with 1% BSS addition

CHAPTER 4

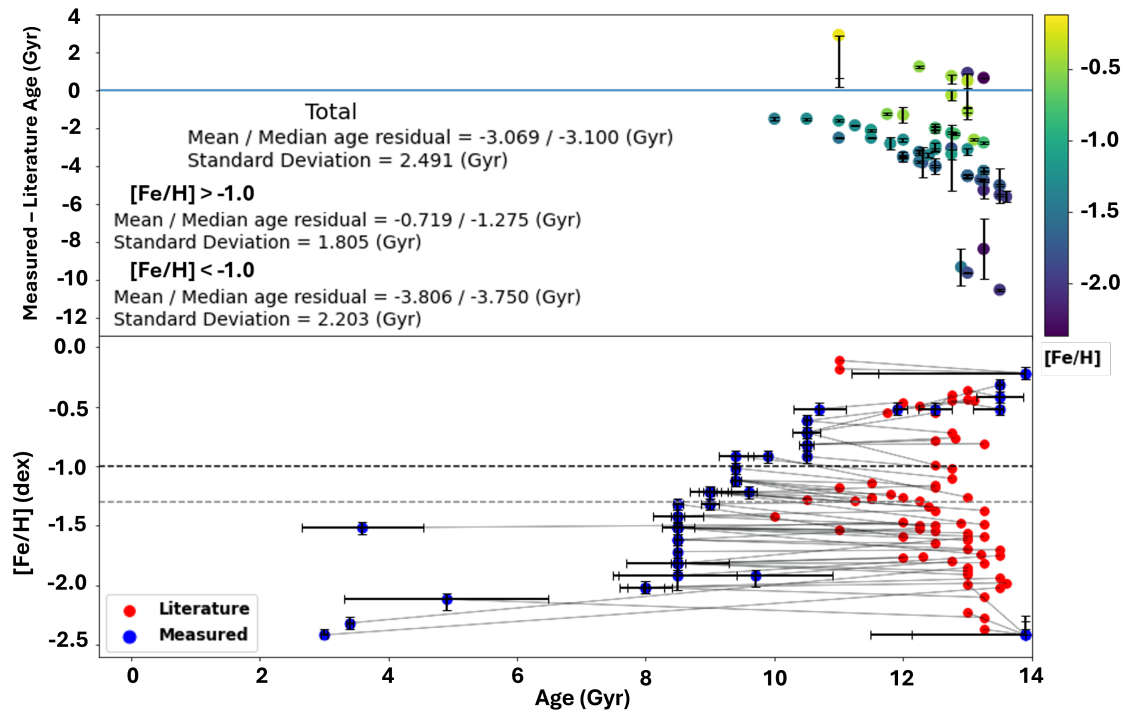


Figure 4.10: Same as Figures 4.8 & 4.9 but using BsMILES models with 5% BSS addition

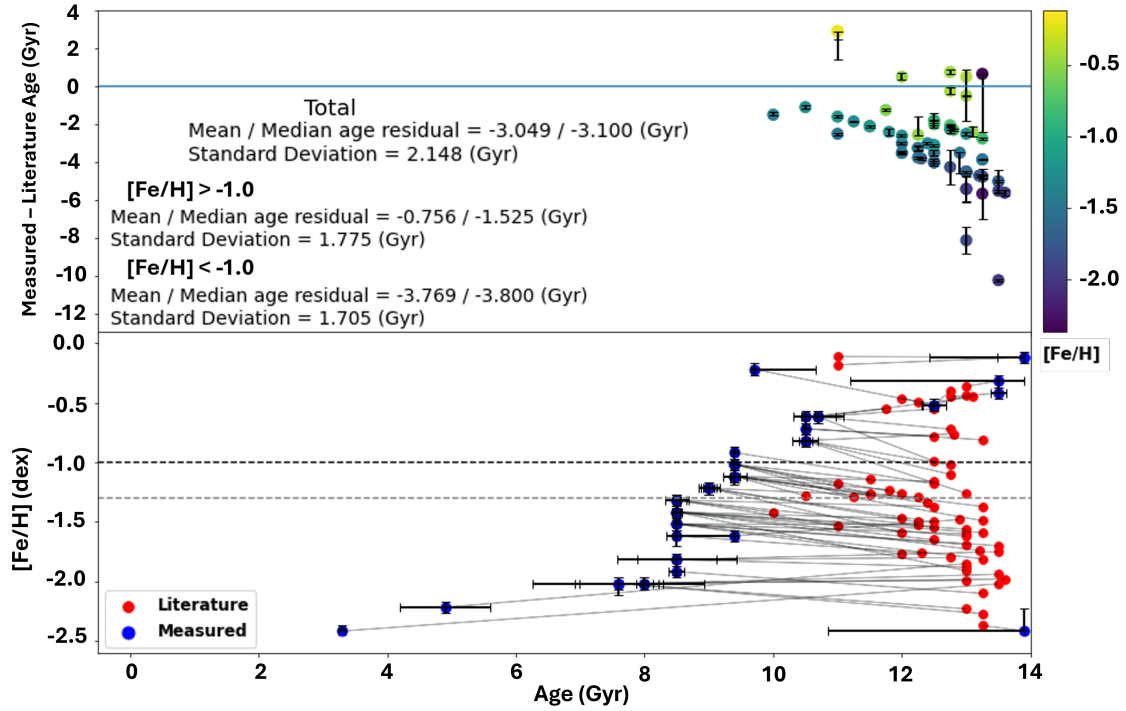


Figure 4.11: Same as Figures 4.8, 4.9, & 4.10 but using BsMILES models with 10% BSS addition.

4.4.2 Metallicity

The Coelho stars (Coelho, 2014) used for BSsMILES were alpha enhanced to match the alpha enhancement of globular clusters (Salaris, Chieffi & Straniero, 1993; Worthey et al., 1994; Lee & Worthey, 2005). However, the alpha enhancement of the Coelho theoretical stars was $[\alpha/\text{Fe}] = +0.4$ while the median alpha enhancement of the metal-rich ($[\text{Fe}/\text{H}] \geq -1$) GCs in the WAGGS sample (with published $[\alpha/\text{Fe}]$ values) was $[\alpha/\text{Fe}] = +0.295$. This would potentially cause an over-estimation in metallicity at higher BSS fractions.

The stars used as BSS examples only had metallicity upwards of $[\text{Fe}/\text{H}] = -1.3$ at the effective temperatures indicated in Figure 4.5. Therefore at metallicities below this value, the output results are not reliable. But as explained before it was not

CHAPTER 4

expected that there will be to improvements to the fits for metal-poor objects so this did not matter. The $[\text{Fe}/\text{H}] = -1.3$ minimum BSS metallicity is shown as a grey dashed line in all plots in this section.

In general, the measured metallicity from LISm χ is comparatively well estimated compared to age and this is in agreement with the other methods defined in Chapter 3. However, For the metal-rich GCs ($[\text{Fe}/\text{H}] \geq -1.0$), using sMILES SSPs with 0% BSS light there is a metallicity underestimation (Figures 3.21 & 4.12). As BSS percentage increases (Figures 4.13, 4.14 & 4.15) the output metallicity increases with a minimum median residual when there is 10% BSS light. The scatter in the metallicity (for $[\text{Fe}/\text{H}] \geq -1.0$) is at a minimum at 5% BSS light. There is no correlation between metallicity residual (to the literature) and BSS percentage and metallicity appears to scale near linearly as BSS percentage increases at all (high) metallicities. Figure 3.21 also shows the metallicity of young GCs that do not have BSS populations (Rain, Ahumada & Carraro, 2021), and these GCs also show metallicity underestimation. So it is likely that the metallicity correction shown here is not realistic and is a symptom of non-ideal models and the added stars' alpha abundance.

As predicted, the measured metallicity for GCs below $[\text{Fe}/\text{H}] = -1.0$ increases where BSS percentage increases to 10% contribution, the estimated metallicity of the low metallicity GCs becomes vastly overestimated (except for the most metal-poor GCs where metallicity has always been underestimated for all BSS percentages including 0%). It is unclear why the lowest metallicity GCs have underestimated metallicity at all BSS percentages. It is predicted that it is due to the use of only 4 line indices in the method, BpPXF also shows metallicity underestimation at the lowest metallicities when only the limited “narrow” wavelength range (4828 - 5363 Å) is used (i.e. Figures 3.11 & 3.12).

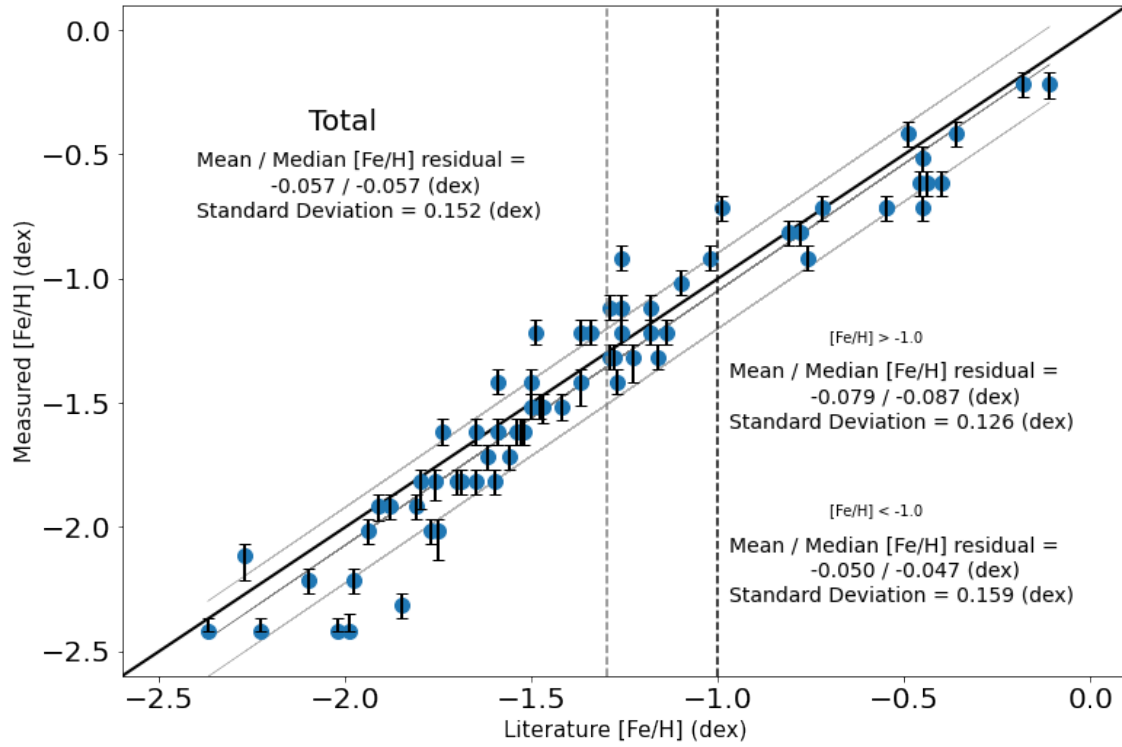


Figure 4.12: LISm χ output [Fe/H] (calculated via Equation 3.8) values using sMILES models with 0% BSS addition. The models and WAGGS GCs are limited to ≥ 3 Gyr. The black dashed line represents a continuum at [Fe/H] = -1.0 dex, the grey dashed line represents a continuum at [Fe/H] = -1.0 dex to show the lowest metallicity star added to the SSP models.

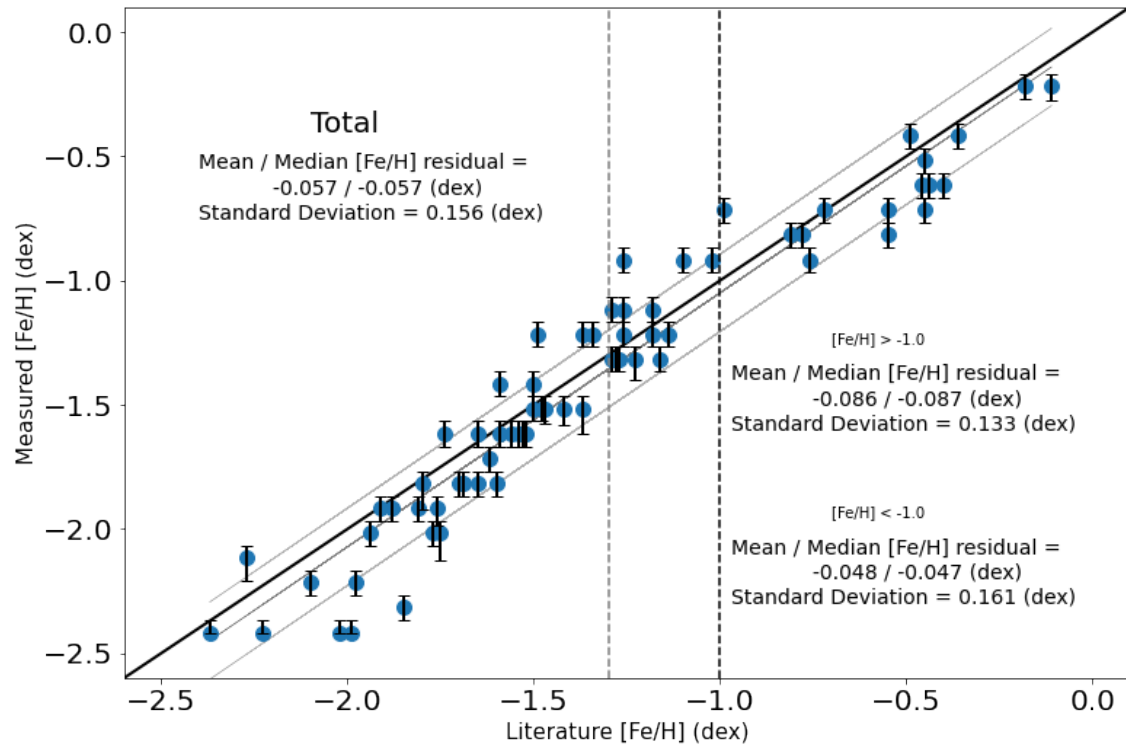


Figure 4.13: Same as Figure 4.12 but using BSMILES models with 1% BSS addition

CHAPTER 4

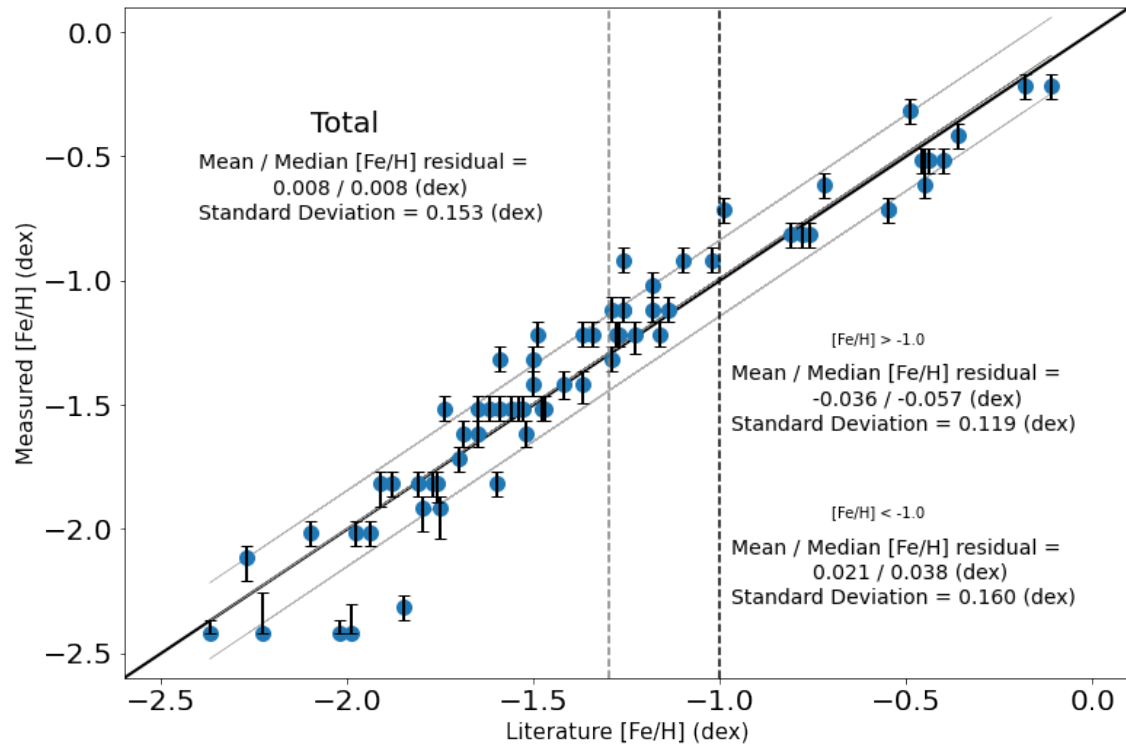


Figure 4.14: Same as Figures 4.12 & 4.13 but using BsMILES models with 5% BSS addition

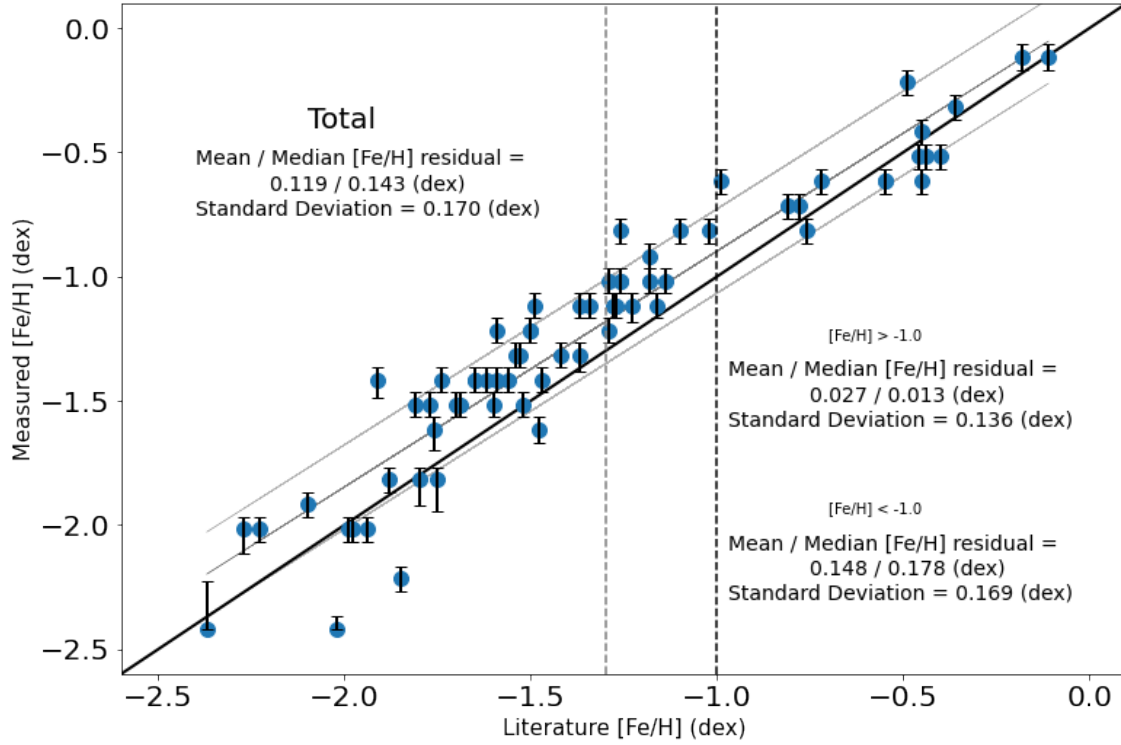


Figure 4.15: Same as Figures 4.12, 4.13, & 4.14 but using BsMILES models with 10% BSS addition.

4.5 BpPXF

The LISm χ method is used with just four indices to see what information can be obtained from a few, simple, age and metallicity indicators. To get a deeper understanding of how BSsMILES models represent the spectra of GCs more indices can be used in the fit (as is done in Chapter 5 for the other CSSs in the sample) or BpPXF can be used. Chapter 3 uses 3 different wavelength regions for BpPXF, in this section, however, the “omitted” region (see Section 3.6.2) is used. In this way, more spectral information is obtained while avoiding effects due to MPs. Ferraro et al. (2006) states that some BSSs possess depleted carbon and oxygen which is a key indicator of MPs in GCs. Because of this, it can be assumed that MPs also affect the blue straggler populations of GCs and that for spectral analysis the regions

CHAPTER 4

which MPs affect should be omitted.

BpPXF takes significantly longer to run than LISM χ so this method is only used on a small sample of GCs. Figures 4.16, 4.17 & 4.18 show the GCs NGC 104, NGC 6356, and NGC 5927. These specific GCs are chosen due to the range of SNRs between them, and their metallicity of $[\text{Fe}/\text{H}] \geq -1.0$. NGC 5927 was chosen because unlike the other GCs in the sample as BSS percentage increases, the age estimation with LISM χ decreases.

NGC 104

Figure 4.16 shows an agreement with LISM χ . As the BSS percentage increases, so does the age estimation. However, at 1% BSS contribution, the measured age does not change from 0% BSS contribution. In this BSS percentage interval, there is only a very small increase in metallicity. Age only starts to increase properly at 5-10% BSS contribution with the most accurate (to the literature) age measurement with 10% BSS contribution. Looking at the bottom 4 panels of Figure 4.16, there appears to be \sim two peaks in mass fraction one at \sim 10.5 Gyr and another at \sim 13 Gyr and as BSS percentage increases the older peak increases in mass fraction. The metallicity increases as BSS percentage increases but Figure 4.16 indicates that this is due to the swapping between mass fraction peaks. In the plot with 0% BSS contribution, the metal-rich older models are selected for the best-fitting SSP combination but to a lesser extent than for the 10% BSS models.

Looking at the upper panels of Figure 4.16 it can be seen that as BSS percentage increases, so to do the Balmer line residuals. This was expected as explained earlier with Figure 4.7 where, as BSS percentage increases, the models move further away from the $H\beta$ values of the GCs. Therefore it can be said that while increasing BSS percentage increases the age estimations to more accurate (to the literature) levels, it also increases the residuals indicating the fit is less accurate, which is a

CHAPTER 4

counterintuitive but interesting result. Also shown in the upper panels of Figure 4.16 is the fit for Ca H&K absorption lines and as BSS percentage increases the ratio between the two lines increases. A large ratio between Ca H&K is the case with the spectra of young GCs (Pimblet, Crossett & Fraser-McKelvie, 2019) but the increased ratio between the lines is not present in the spectra of these older GCs indicating that calcium is being fit incorrectly with this method. However, Ca H&K are in the unfitted region so pPXF has not been allowed to fit to these lines. If it was allowed to fit to Ca H&K, the results may be different, and further work to understand the implications on the SSP metallicity by the addition of bluer light needs to be undertaken.

NGC 6356

This GC shows very similar results to those of NGC 104, there appears to be \sim two mass fraction peaks in the age-metallicity plain in the lower panels of Figure 4.17 that bias towards the older population as BSS percentage increases. However, the measured age and metallicity for this globular cluster is almost completely corrected by the addition of 10% BSS light to the SSP models. But the increase in residuals that is seen in the spectral fit of the upper panels (Figure 4.17) is the same that is seen in the same plot for NGC 104.

Something notable for this GC, is that at 1% BSS contribution, the estimated age and metallicity decreases compared to the 0% BSS SSPs. This goes against the trend seen at higher BSS percentages and more work needs to be done to understand why this is happening.

NGC 5927

In LISM χ , initially, the age of this GC is over-estimated by about 1 Gyr with 0% BSS contribution and continued to be over-estimated until 10% BSS contribution

CHAPTER 4

where it suddenly became under-estimated in age by ~ 2 Gyr. For that reason, this GC was selected for analysis with BpPXF where more information would be extracted.

The lower panels of Figure 4.18 show that at 0-1% BSS contribution, the measured best-fitting combination of SSP models accurately reproduces the literature values of age and metallicity. As BSS contribution increases the age measurement also increases with the peak of the mass-weighted fraction being at the extreme SSP age. Leigh, Sills & Knigge (2007) states that this GC has an average amount of BSSs according to their measurements of galactic GCs and this globular cluster has a high SNR in the WAGGS dataset of 108.22 (at 5000Å). GCs which are more metal-rich have fewer BSSs according to the close binary fraction/metallicity relation (Moe, Kratter & Badenes, 2019; Wyse, Moe & Kratter, 2020). This could explain NGC 5927 preferring smaller BSS percentages, but as stated NGC 5927 has an average number of BSSs according to Leigh, Sills & Knigge (2007). Why this GC appears to have a smaller BSS population according to these methods is not known.

What should be noted is that in all cases with BpPXF, as BSS percentage increase the spurious younger populations go away, and an older population is preferred.

CHAPTER 4

NGC 104

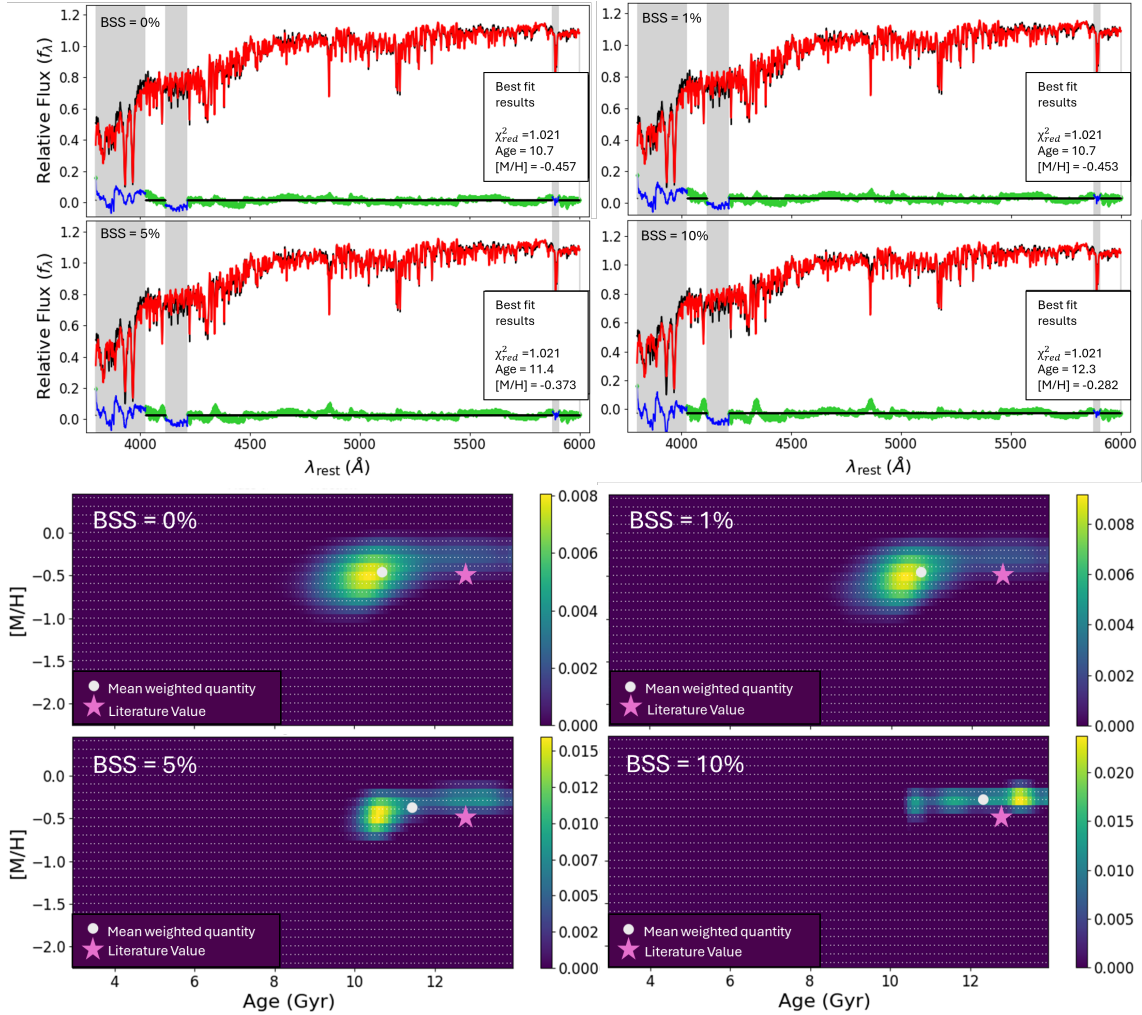


Figure 4.16: “Omitted” region, BpPXF output for NGC 104. The upper panels show the spectrum (black), the best-fitting combination of SSP models (red), and the residual between the two (green), the grey regions and blue residuals show regions of the spectrum that have been masked from the fit. The panels show the outputs for BpPXF for 0, 1, 5, and 10 % BSS light contribution to the SSP models. The lower panels show the mass-weighted fraction of the best-fit SSP model combination for each BSS percentage, showing the mean weighted value (white spot) and the literature value (pink star).

CHAPTER 4

NGC 6356

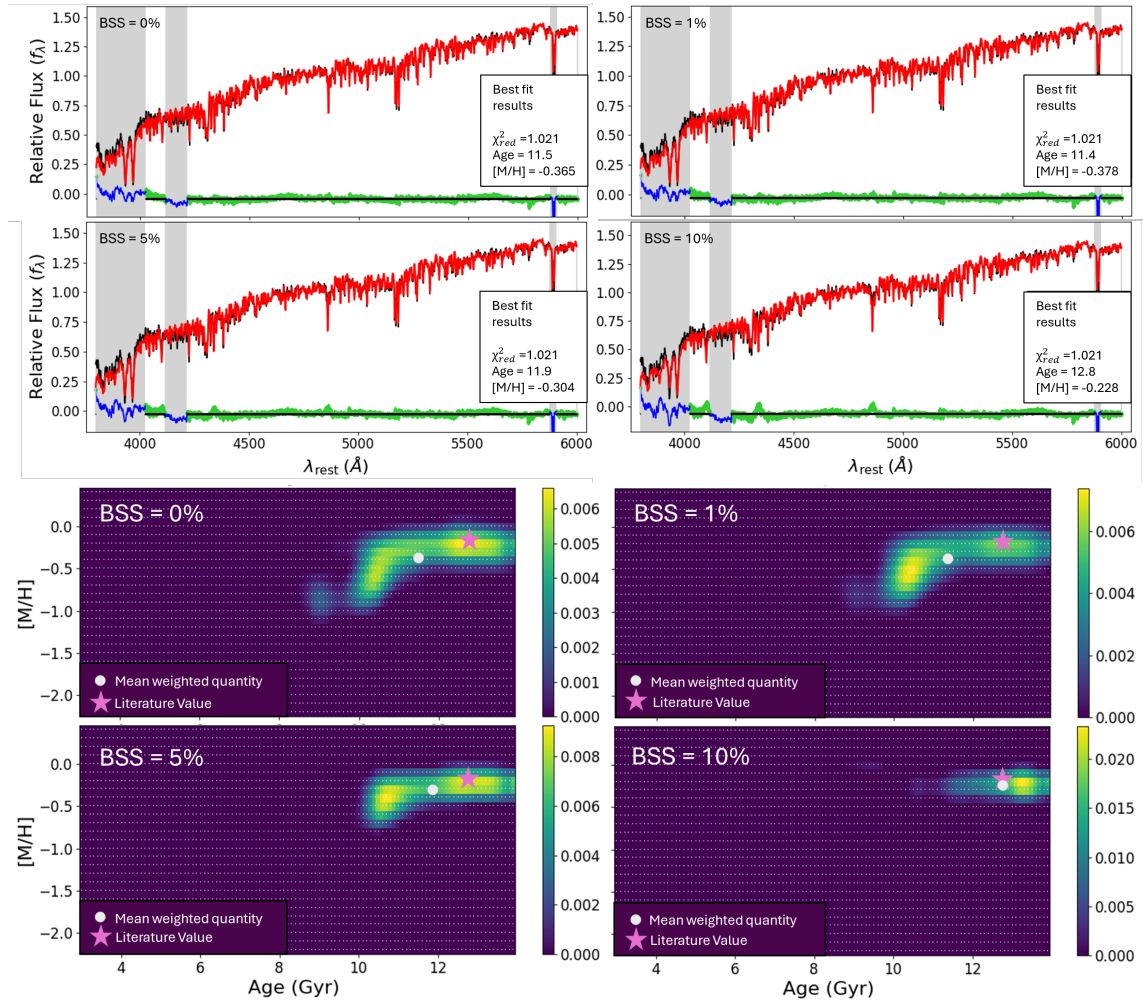


Figure 4.17: Same as Figure 4.16 but for the GC NGC 6365.

NGC 5927

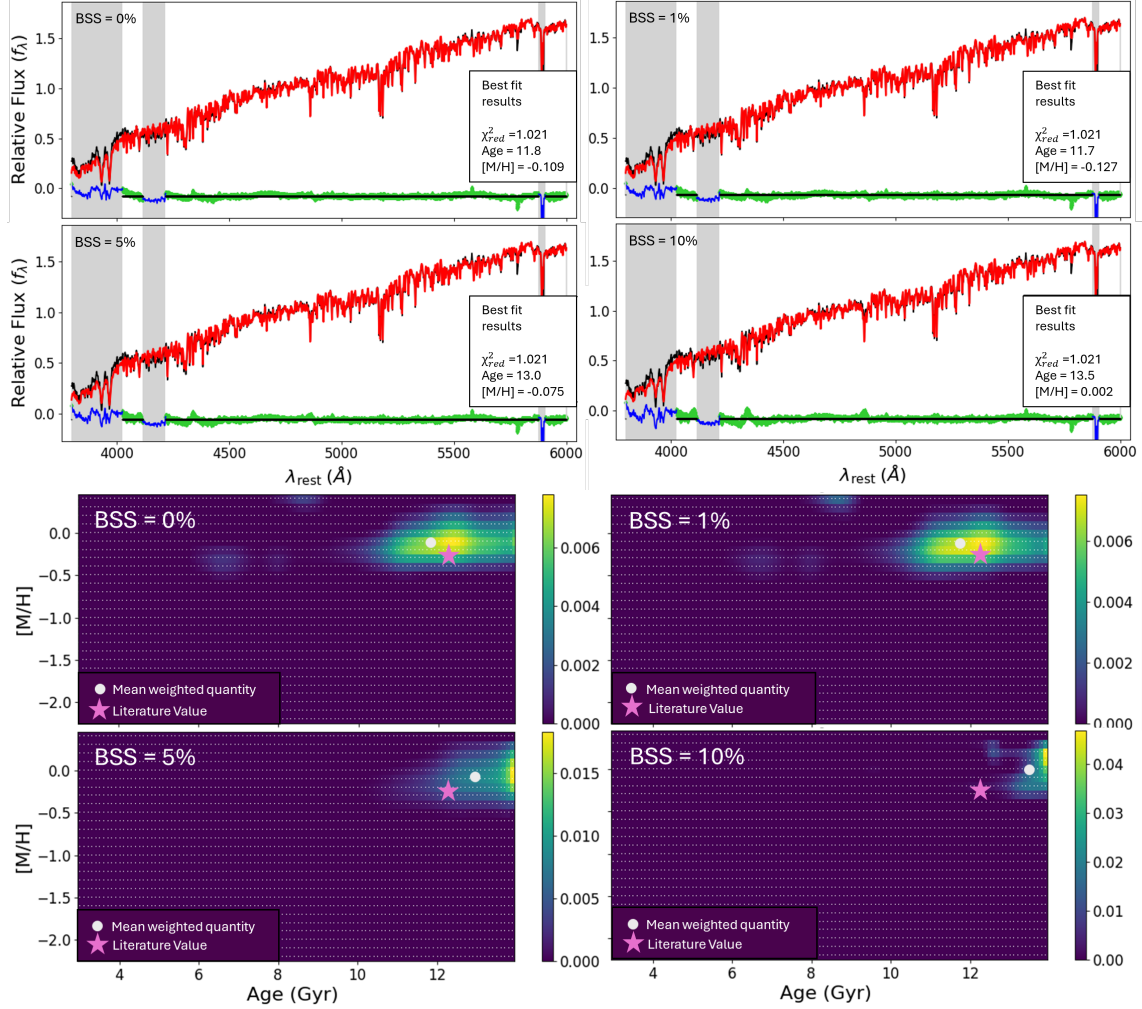


Figure 4.18: Same as Figures 4.16 & 4.17 but for the GC NGC 5927.

4.6 Conclusion

This Chapter has probed the causes of age underestimation in integrated light spectral analysis and created models intending to correct for current SSP models not accounting for blue straggler stars.

It is concluded that for low metallicity GCs, BHB stars are likely the leading cause of age underestimation. While for more metal-rich GCs, the contribution

CHAPTER 4

of BSSs can be considered to account for some age underestimation and in full spectral fitting the addition of BSS light removes the presence of spurious younger populations in the age vs metallicity mass fraction plots. More work needs to be done to model simple stellar populations so accurate SSP models can be created that represent the contribution of BSS light realistically. The mass fraction of BSS populations increases with age and with events such as core-collapse (Chatterjee et al., 2013; Ferraro et al., 2018; Portegies Zwart, 2019), indicating there may be a density relation to BSS population size and the stochastic issues of poor sampling in some observations might have effects which cannot be detected here which are not modelled by simply adding a percentage of blue light to pre-existing SSP models. This work proposes future simulations of globular cluster evolution focusing on BSS production from binary interactions and collisions for a mixture of ages and metallicities with the aim of creating a new simple stellar population library. This is unfortunately outside of the scope of this project and it is left to future work. What has been found here is that as the percentage of BSS light in a set of SSP models is increased, the measured age of globular clusters increases. For this work, it is found that BsMILES models with 5% BSS population give the most accurate age results with minimal sacrifice in the accuracy and precision of metallicity estimations for GCs with $[\text{Fe}/\text{H}] \geq -1.0$ dex. Therefore these models will be used going forward when studying compact stellar systems (although it is noted how the percentage BSS contribution to the integrated light is probably different on a cluster-to-cluster basis i.e the difference between BpPXF measurements of NGC 104 and NGC 5927). What should be discussed, however, is that given the overall fits to the spectra are worse when BSSs are included, BSSs may not be driving the issue of age underestimation physically. What cannot be denied however is that when the light of younger stars is introduced the age underestimation is reduced, often completely. As stated above, more work is needed to understand the effects

CHAPTER 4

of BSSs on the integrated spectra of CSSs. The main goal of this future work is to understand why the age estimation is increasing in accuracy while the accuracy of the fit in the hydrogen lines is decreasing.

It was discussed earlier (Section 4.2) that the cause of the age underestimation is due to the many more models, younger than the true value, which have equivalent reduced χ^2 values. The attempt to account for BSS was hoped to reduce the age insensitivity of the SSP models. Due to the increased accuracy of the age estimations when BSSs are introduced it is indicated that the age sensitivity is increased when BSSs are considered. It should also be considered that BSSs will have more of an effect in the blue region of the spectra than the red so it is possible that the use of a different wavelength range (red-NIR where the effects of younger bluer stars are minimal) instead of having to account for the light of these bluer stars will also account for some of the age underestimation and this is left for future work where longer wavelength range models can be used.

Another aspect to consider is the implications of the fact that BSSs form via stellar collisions and via close binary interactions (Portegies Zwart, 2019). While stellar collisions are exclusive to the most stellar-dense environments, binary stellar interactions are very common throughout all stellar systems. If there is significant contribution of blue stragglers formed this way, age estimations of many stellar systems (via integrated light) may be underestimated (i.e. Wyse, Moe & Kratter 2020). It is possible that the UV-upturn seen in many early-type galaxies (Code & Welch, 1979; Bertola, Capaccioli & Oke, 1982; O’Connell, 1999), thought to be from BHB stars in the dense central stellar bulges could also have some contribution from anomalous blue straggler populations.

What has been found from integrated light analysis is that in general there is an issue in measuring age for these, apparently, simplest stellar populations. There is not, however, an issue in measuring metallicity and multiple techniques can be used

CHAPTER 4

to identify and measure regions in the spectrum where there are specific chemical abundance anomalies. The next Chapter will probe these chemical abundance anomalies for GCs and the other CSSs in the sample obtained for this project, probing the complexity of the chemical analysis of CSSs via their integrated light.

Chapter 5

Further Analysis of Compact Stellar Systems

5.1 Introduction

The previous chapters, have analysed the integrated light spectra of globular clusters, testing analysis methods and creating models to account for inaccuracies in their measurements. This chapter will apply the fruits of this research to the full zoo of compact stellar systems and further extend the analysis to look into common chemical abundance issues with the goal of defining classification parameters for different CSS types based on the formation mechanisms.

5.2 Initial CSS Sample Analysis

Figure 5.1 shows the mass-size plane for the objects from the following surveys, MODS, GHTS, XShooter, WAGGS and the M87 objects from Forbes et al. (2020). This data also includes objects such as the relatively compact dE NGC 52-dE and the red nugget candidate MRK1216. The dE galaxy is of equivalent mass to the most massive cEs in the sample but the red nugget has mass equivalent to massive

CHAPTER 5

galaxies (represented by the inclusion of the SDSS21 binned galaxy parameters in the figure).

Figure 5.1 shows an overlap in mass and radius for the GCs and UCDs and NSCs. A good example of this is the M31 ‘GC’ B023-G078 which has an average effective radius for a GC but is very massive ($M_* \approx 6.79 \times 10^6 M_\odot$, Norris et al. 2014). This ‘GC’ has been shown to possess a massive ($M_* \approx 100,000 M_\odot$, Pechetti et al. 2022) black hole at its centre indicating it is the tidally stripped nucleus of a galaxy that Pechetti et al. (2022) predicts had a mass of $M_* \geq 10^9 M_\odot$. Therefore this CSS should not be considered a GC but actually a low-mass UCD which formed via tidal stripping of a galactic nucleus. Another example is the ‘GC’ Ω Cen (NGC 5139) which has been shown to have an extended star formation history and metallicity spreads which are indicative of being a stripped object (Majewski et al., 2000; Hilker & Richtler, 2000; Bekki & Freeman, 2003; Fellhauer, 2004; Seth et al., 2021). Ω Cen may also have a massive BH in its core (van der Marel & Anderson, 2010), however, there are large uncertainties in the location of the centre of the CSS and the retention of stellar remnants, and from velocity dispersion measurements, Pechetti et al. (2024) found no evidence for a central intermediate-mass BH. The presence of massive black holes in UCDs is a key indicator of their formation path. Figure 5.1 shows (highlighted) GCs and UCDs in the sample which are known to possess massive black holes at their centre (M59c0, VUCD3, M60-UCD1, NGC4621-UCD3, B023-G078 Ahn et al. 2017; Seth et al. 2014; Norris et al. 2014; Ahn et al. 2018; Majewski et al. 2000; Hilker & Richtler 2000; Bekki & Freeman 2003) or have evidence of extended star formation or spreads in metallicity (NGC4546-UCD1, & Ω Centauri, Norris et al. 2015; Seth et al. 2021). As has just been discussed, this indicates that these formed as the result of tidal stripping from a more massive galaxy. Via the mass-radius plot, it is hard to separate UCD formation types (one being the massive end of GC formation, the other being tidal stripping, see Section 1.4). Norris et al.

CHAPTER 5

(2019) suggests an upper mass limit for GC-like cluster formation of $M_* \sim 5 \times 10^7 M_\odot$. In the sample presented here, the UCDs which are the stripped nuclei of larger galaxies tend to be more massive than the other UCDs and lie over the limit set by Norris et al. (2019). Works like Norris et al. (2014) show how this is not always the case and the presence of low mass stripped nuclei (Ω Cen and B023-G078) indicates that there is significant overlap between objects which are and are not stripped nuclei and stripped nuclei likely exist at all masses (with GC formation dominating at lower masses). Later in this chapter, another avenue to separate UCD formation types is probed, one which uses chemical abundances (Section 5.7).

What can be noted from the CSS sample, is the apparent lack of objects in the radius range between the UCD sample and cE sample. There are known UCDs and cEs in this region (i.e. M32, Norris et al. 2014), however, the spectra for these objects has not been obtained yet. A combination of COVID-19, lack of access to telescopes in the correct hemisphere and weather conspired to stop further acquisition of more data. A future goal for this project will be to fill in the gap so that there is continuous coverage across the mass-size plane.

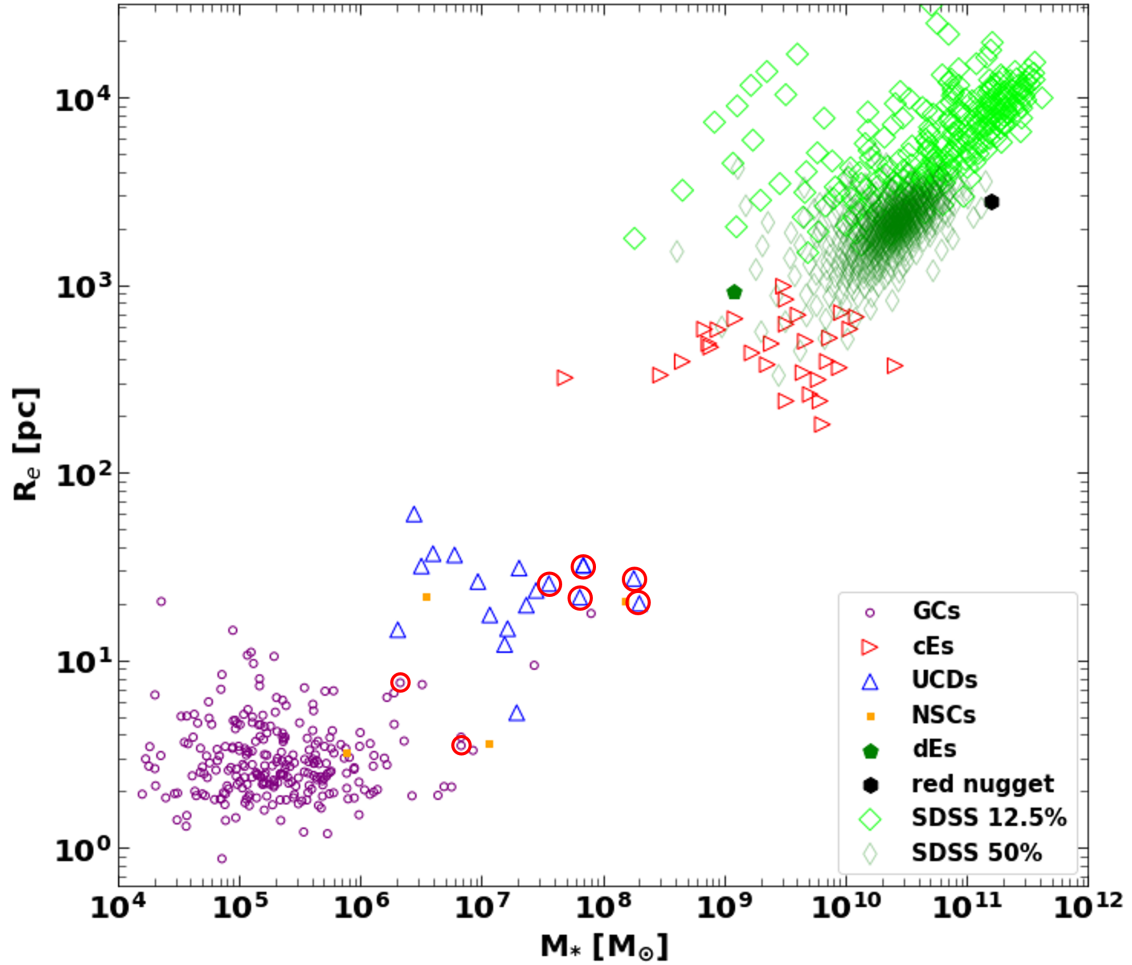


Figure 5.1: Effective radius versus stellar mass plot of the sample of CSSs. Also included in this plot are the SDSS21 galaxies (representing the most massive galaxies) and the dE and red nugget from MODS and GHTS respectively. The points highlighted by a red circle show GCs and UCDs known to possess evidence indicating a ‘stripped nucleus’ formation path.

Another feature of Figure 5.1 that can be noted, is the overlap between NSCs and the GCs and UCDs. While they may overlap in this plot, NSCs are very easy to identify observationally as they are, by definition, located in the centres of more massive galaxies. Separating how they formed, however, is another task and later measurements are used of their ages and metallicities in combination with literature

mass measurements to suggest how the NSCs in the sample formed and go further to analyse the chemical abundances of these objects.

5.3 Age & Metallicity Measurements

Chapter 3 3 methods were defined to determine the age metallicity and alpha abundance of a CSS via its spectrum. It was found that while metallicity can be reliably returned using all methods, $[\alpha/\text{Fe}]$ values were generally not accurate compared to literature values derived from high-resolution single-star studies (e.g. Dias et al. 2016) except for using a narrow wavelength range where a reduced residual scatter and increased uncertainty showed good agreement with $[\alpha/\text{Fe}]$, and age was routinely underestimated to some degree for almost all of the GC sample. To combat this age underestimation the BSsMILES models were created which take into account the light of BSS populations in the observed object. These models improved age estimation for GCs, especially at higher metallicities of $[\text{Fe}/\text{H}] \geq -1.0$. This section will use these methods on the extended CSS sample.

It was decided that the results given by SpPXF were not unique compared to the other two methods, they did not provide any more information than could be taken from BpPXF and LISm χ . While SpPXF with models at different alpha values returned acceptable alpha values, here LISm χ is used with a greater number of indices to probe if alpha measurement is plausible through this method. For that reason, in this section, only the BpPXF and LISm χ methods are used for comparison between full spectral fitting and line index measurement. To provide useful insight into the effectiveness of the BSsMILES models on more massive CSSs than GCs, both methods were run on each object using normal sMILES models and with BSsMILES models with 5% BSS contribution (as this was the optimal fraction identified in Chapter 4) with all models interpolated in age to 0.1 Gyr and in metallicity to 0.1 dex and with $[\alpha/\text{Fe}] = 0.3$ to represent the general alpha

CHAPTER 5

enhancement seen in most CSSs. If more time were available, the alpha abundance of each object would be determined either via index measurements or through iteration refinements of the methods presented in this Thesis, then interpolate the SSP $[\alpha/\text{Fe}]$ to match the object value.

5.3.1 BpPXF

A short wavelength range is used here in continuation with previous chapters, where the omitted wavelength range has been used to exclude regions of the spectrum which generally provided poor SNR and had regions susceptible to anomalous chemical abundances such as the CN region and NaD. In this section, the wavelength range of 4000 - 5500 Å is used with the extended CN region (defined in section 3.6.2) omitted for the fit where possible. This was done to get the maximum amount of spectral information while keeping the same wavelength range for each source of data. In some spectra there were bad pixel columns which were masked and where emission lines were detected (such as in MRK1216, Section 5.8) these were all masked from the fit using pPXF’s inbuilt emission line masking code.

Following the same procedure for BpPXF outlined in Section 3.6, first a run which is un-normalised with no regularisation is done followed by iterating runs with different regularisation values until the desired $\Delta\chi^2$ value is reached. However, this was not always possible.

Earlier, an upper limit was set for what classified a “realistic” regularisation value (Section 3.6.3) and for the majority of these spectra, of which many had relatively low SNRs (compared to the WAGGS GCs)*, regularisation often needed to be above 100 to reach the desired $\Delta\chi^2$. Earlier methods allowed the regularisation value to go to unrealistic values and highlighted them in the plots, in this case where the

*The median SNR of the data in this sample (at 5000 Å) is ~ 49 with many objects having significantly lower SNRs compared to WAGGS with a median SNR (at 5000 Å) of ~ 109 .

CHAPTER 5

majority of objects had high regularisation values, a different approach was taken.

For this data, when regularisation required values higher than 100, 'regul', the regularisation factor was simply capped at 100 and ran BpPXF. This was done because the output mean weighted age and metallicity values between BpPXF runs with a 'regul' value of 100 and runs with the 'true' desired value (when this value was ≥ 100) showed little difference. The only effect observed was an increase in the smoothing of the weights fraction. This means that more models were used in the fit, effectively blurring the stellar populations that are contributing to the integrated spectrum.

The results of the BpPXF fit for the sample are presented in Table B.5 and in the bottom panels of Figure 5.2 with comparison to literature values in the bottom panels of Figures 5.6 & 5.8 in Section 5.4.

5.3.2 LISM χ

In Chapters 3 & 4, this method (defined in Section 3.8) was used on WAGGS GC data using just 4 LIS indices, $H\beta$, Fe5270, Fe5335, and Mg_b . This was done to see what population information could be extracted from the minimal spectral details (which was hopefully clean from chemical anomalous populations due to the MPs phenomenon). In this section, this will be taken further using the indices used in Proctor, Forbes & Beasley (2004) which all of the measured CSSs had in common (as different redshifts caused some indices on the edges of other CSS wavelengths to be cut off and be non-measurable). For the same reasons mentioned above, the CN indices have not been included in the fits for this method as it was predicted that there may be populations with enhanced CN in some of these UCDs in a similar abundance pattern to that of the MPs of GCs which may affect the output measurements of the LISm χ method. After these indices were removed 17 indices were left which are presented in Table 5.1. These 17 indices are used for all of

CHAPTER 5

the objects except the M31 GCs where only the $H\beta$ index was provided originally (on the LICK/IDS system which has been converted to the LIS system here at the common resolution of 5 \AA).

Each object had a different resolution which was dependent on the instrumental resolution and its velocity dispersion. The LIS system has 3 resolution options described in Section 3.3 which the data needed to be blurred to, for accurate index measurements. The indices of each object were measured using the velocity dispersion of the object measured from BpPXF fits (with the additive polynomial parameter set to 4, matching the multiplicative Legendre polynomial parameter which is needed for kinematic measurements, see Section 3.4.2) or the instrumental resolution (whichever value was larger) as the base resolution for ‘blurring’ to the appropriate LIS resolution.

The results of this method are presented in Table B.5 and in the top panels of Figure 5.2 with comparison to literature values in the top panels of Figures 5.6 & 5.8. Discussion on the results of these methods is given in Section 5.4. One disadvantage of this method is that bad pixels or anomalous emission/absorption lines will skew the line index measurements of indices which have those bad emission lines. One example of this which could not be avoided is the case of MRK1216 which has been found in this thesis to show emission in its OIII and H Balmer lines. These emission lines could be masked in BpPXF, but the Balmer line emission may have caused an underprediction of hydrogen abundance and therefore increased the metallicity and age of the output measurements. The case of MRK1216 is discussed in Section 5.8.

Table 5.1: Table of LICK/IDS indices used for the LISm χ analysis.

Name	Index	Min	Max	Min blue	Max blue	Min red	Max red
	units	Å	Å	Å	Å	Å	Å
Ca4227	EW	4222.250	4234.750	4211.000	4219.750	4241.000	4251.000
Ca4455	EW	4452.125	4474.625	4445.875	4454.625	4477.125	4492.125
Fe4383	EW	4369.125	4420.375	4359.125	4370.375	4442.875	4455.375
Fe4531	EW	4514.250	4559.250	4504.250	4514.250	4560.500	4579.250
Fe5015	EW	4977.750	5054.000	4946.500	4977.750	5054.000	5065.250
Fe5270	EW	5245.650	5285.650	5233.150	5248.150	5285.650	5318.150
Fe5335	EW	5312.125	5352.125	5304.625	5315.875	5353.375	5363.375
G4300	EW	4281.375	4316.375	4266.375	4282.625	4318.875	4335.125
H β	EW	4847.875	4876.625	4827.875	4847.875	4876.625	4891.625
H β_0	EW	4839.275	4877.097	4821.175	4838.404	4897.445	4915.845
H δ_A	EW	4083.500	4122.250	4041.600	4079.750	4128.500	4161.000
H δ_F	EW	4091.000	4112.250	4057.250	4088.500	4114.750	4137.250
H γ_A	EW	4319.750	4363.500	4283.500	4319.750	4367.250	4419.750
H γ_F	EW	4331.250	4352.250	4283.500	4319.750	4354.750	4384.750
Mg ₁	Mag	5069.125	5134.125	4895.125	4957.625	5301.125	5366.125
Mg ₂	Mag	5154.125	5196.625	4895.125	4957.625	5301.125	5366.125
Mg _b	EW	5160.125	5192.625	5142.625	5161.375	5191.375	5206.375

5.4 Age and Metallicity Results

The output age and metallicity values for the CSS sample are presented in Table B.5 and Figure 5.2. To better understand the outputs of the BpPXF and LISm χ methods on the CSS spectra the output values need to be compared to the literature. Literature age metallicity and alpha abundance values for many of these objects have been obtained from other surveys which performed spectroscopic analysis (references

for which are in Table A.3).

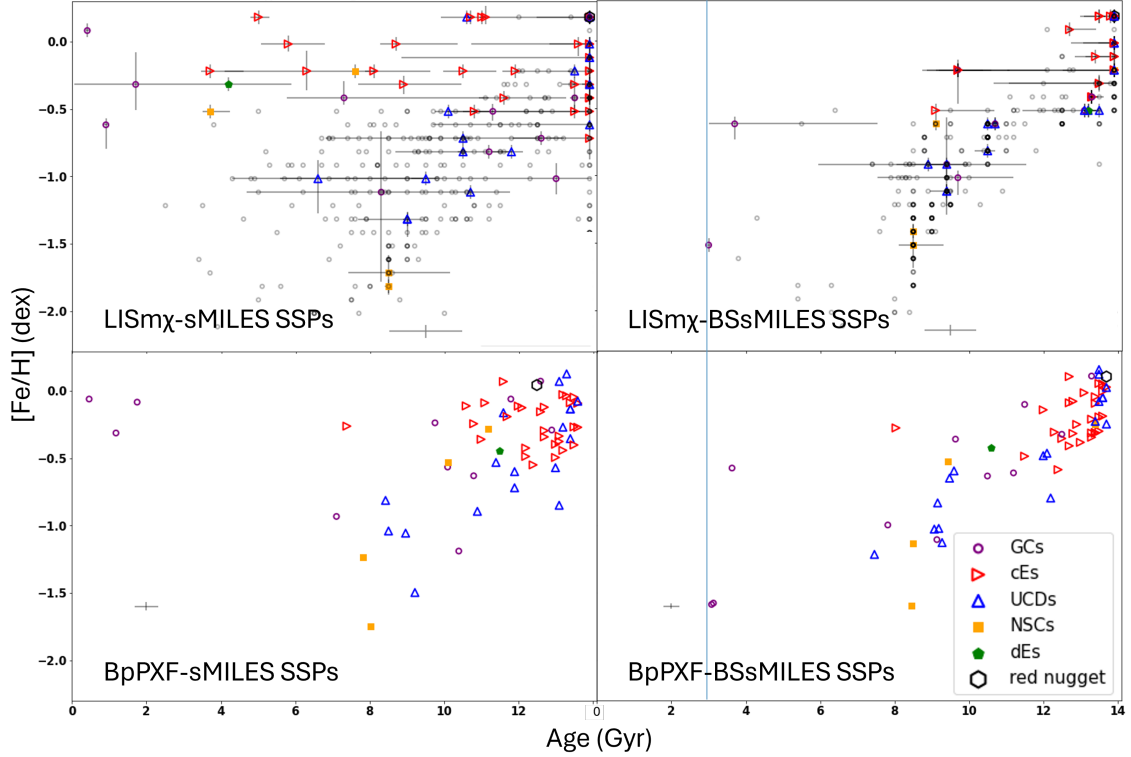


Figure 5.2: Plots of output $[\text{Fe}/\text{H}]$ against output age for the 4 method / model combinations. The top left shows the output results from the LISm χ method using interpolated sMILES SSP models, and the top right shows the same method using the interpolated BSsMILES SSP models. The bottom left panel shows the results from BpPXF using sMILES SSP models and the bottom right panel shows the BpPXF results with BSsMILES SSPs. In the left panels, the blue vertical line represents the minimum age of the BSsMILES models. The grey error bars in the top two panels show the mean uncertainty for the M31 GCs.

5.4.1 M31 Residuals

The accuracy of literature values for parameters such as age are questionable. These objects, which are located at significantly greater distances than the GCs of the previous sections cannot be examined using resolved star observations (except for the

CHAPTER 5

brightest stars observed with Hubble, Peacock et al. 2018). So the observed “true” age and metallicities from the literature cannot be trusted to the level available of the MW GCs. Because of this, relatively large offsets and scatter between the results of this work and those given in other studies could be expected. In Figure 5.3, the comparison of values from previous studies (which in this case utilise different methods of measurement) show very poor agreement for everything except for the metallicities of Caldwell & Romanowsky (2016) and Wang, Chen & Ma (2021).

Figures 5.3, 5.4, & 5.5 show the results from these different studies compared to each other and compared to the results in this work. In the top panels of Figures 5.4 & 5.5 the results of this to Fan, de Grijs & Zhou (2010). In this study they measured the ages and metallicities of GCs by the comparison of photometric spectral energy distributions to SSP models. Their ages do not agree well with the ages measured in this work while there is a loose correlation found with $[\text{Fe}/\text{H}]$ there is a large deviation larger than the uncertainty values of the points. There may be large discrepancies in age for estimations based on SED-SSP comparison as there is no available information from the spectral lines. It is found via Figure 5.3 that Fan, de Grijs & Zhou (2010) generally has large disagreements with other surveys and therefore the results from this study are probably not accurate.

The middle panels of Figures 5.4 & 5.5 show the comparison to Caldwell et al. (2011) (for age) & Caldwell & Romanowsky (2016) (for metallicity) with both being the same study where metallicity measurements were updated with supplementary new data in the later study. In Caldwell et al. (2011) they measure age and adopt a similar process used here via comparison of the same LICK indices used in this project (S12) to SSP models from Schiavon (2007). There is some agreement in age, but due to the large uncertainties involved, all but the most extreme objects agree in age. Since the same data was used, the disagreements in age must be due to the different models used, differences in the age measurement techniques (they

CHAPTER 5

used the stellar population analyses program EZ_Ages (Graves & Schiavon 2008) and a different combination of LICK indices used in the fit. There are a large number of objects whose age is listed as 14 Gyr, this was the case when they could not return an age estimation due to limitations in their code not being able to fit below a metallicity of $[\text{Fe}/\text{H}] = -1$ (dex) and any other condition where their code would not work. When this happened, they assumed an age of 14 Gyr. They updated this study in Caldwell & Romanowsky (2016) making use of higher resolution spectra as well as the older indices used in Caldwell et al. (2011). The comparison showing in Figure 5.5 shows very strong agreement with both sets of models in this work while the measurements with BSsMILES have a slightly larger offset at the lower metallicity objects echoing what was found for MW GCs at higher BSS percentages.

The bottom panels in Figures 5.4 & 5.5 show comparison with Wang, Chen & Ma (2021). This study uses a combination of photometric and spectral analysis comparison with SSP models to derive ages and metallicities. It is found that due to the large age uncertainties of their work, the results of this work agree in age with theirs, although it should be noted that none of their predicted ages value above 10 Gyr in age. $[\text{Fe}/\text{H}]$ is in relatively good agreement with this work. There is slightly larger scatter in the residuals than with the Caldwell & Romanowsky (2016) values but due to the large uncertainties, there is reasonable agreement with this work although it is noticeable that they do not cover as large of a metallicity range as is done here or in Caldwell & Romanowsky (2016) which may be a contributing factor to the comparatively large scatter seen in the results.

CHAPTER 5

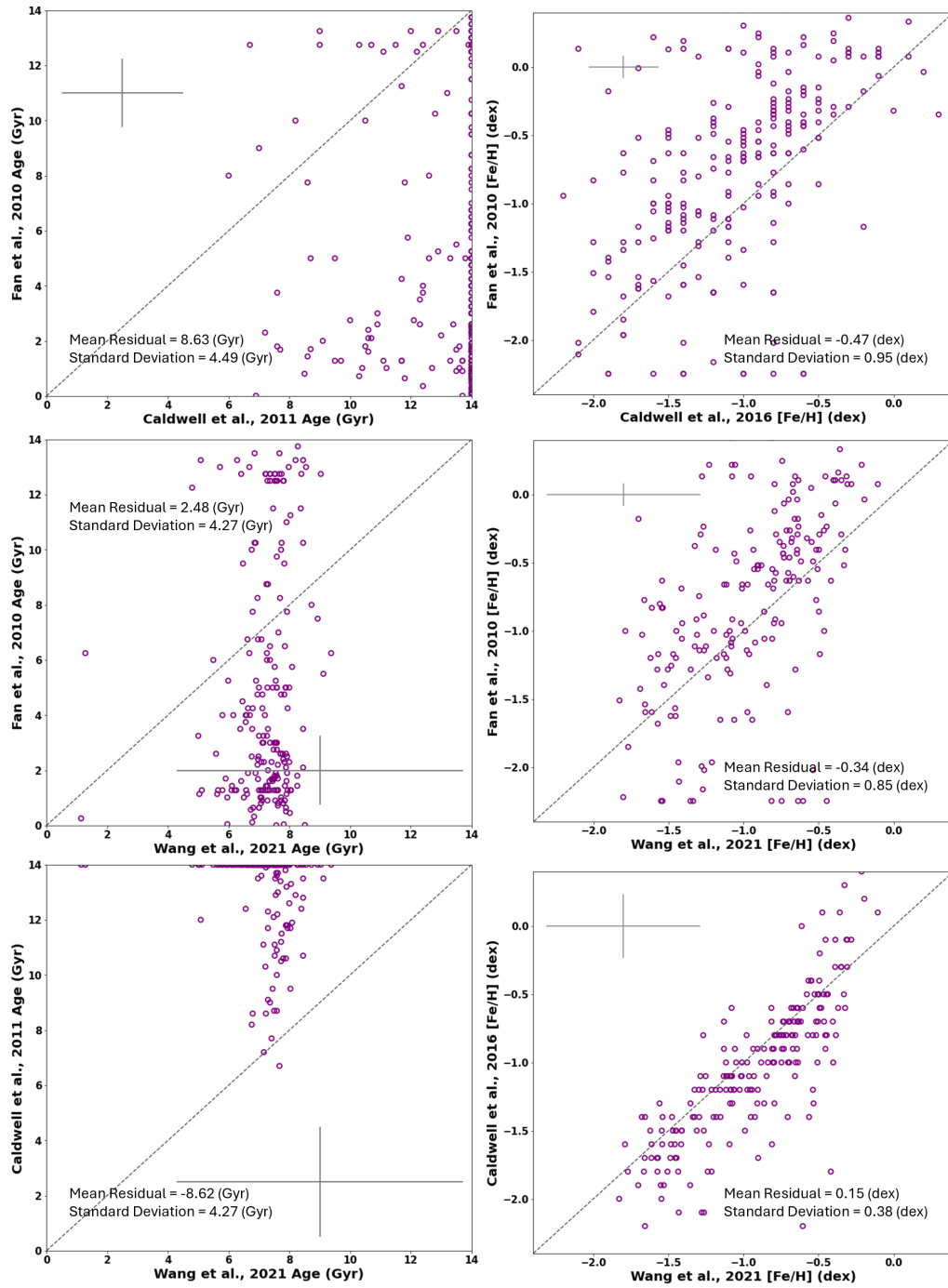


Figure 5.3: A comparison between age and metallicity values from the literature (Fan, de Grijs & Zhou, 2010; Caldwell & Romanowsky, 2016; Wang, Chen & Ma, 2021) for M31 GCs. The errorbars in each frame show mean uncertainty values.

CHAPTER 5

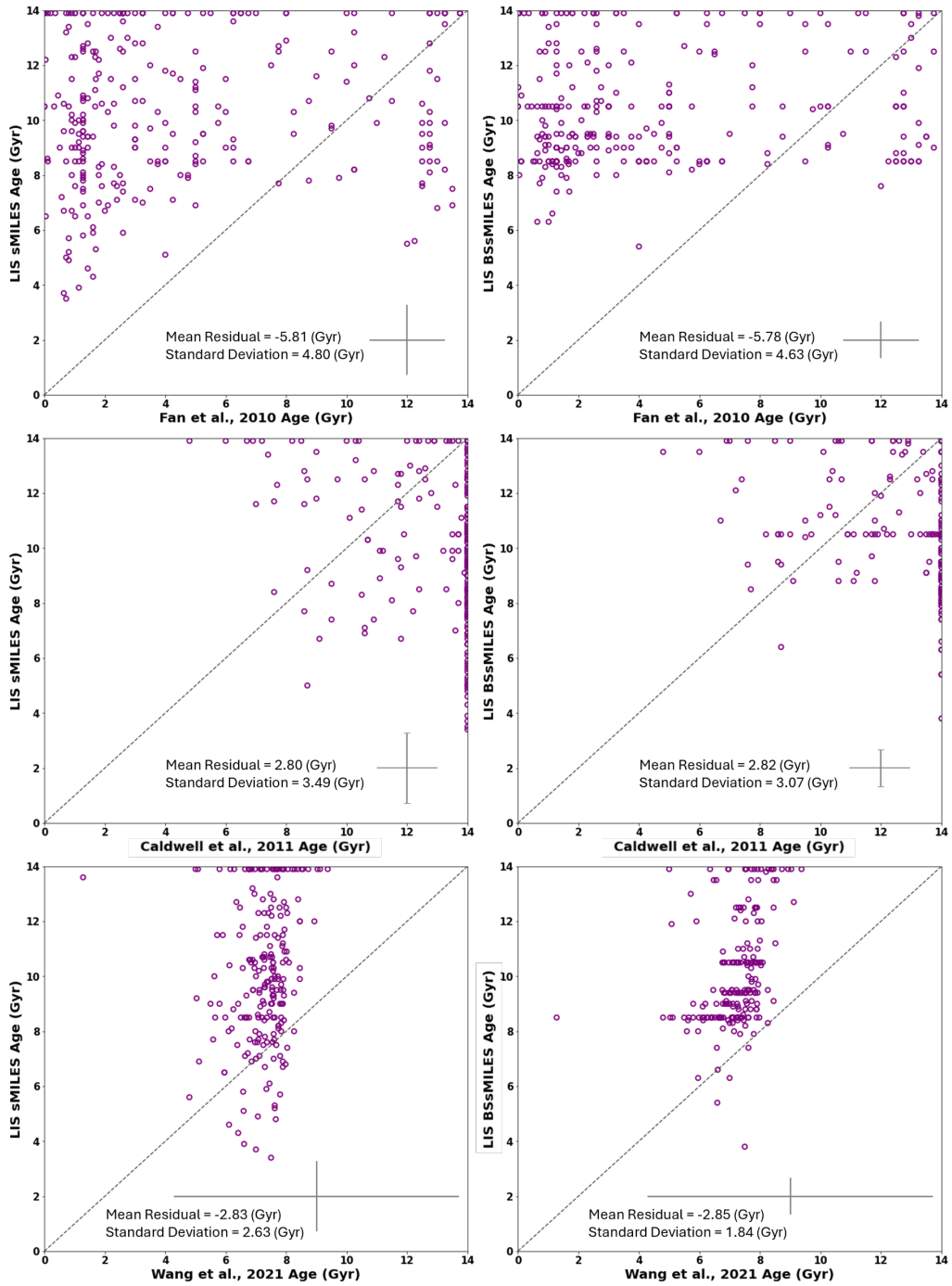


Figure 5.4: A comparison between the measured age of this work for the S12 M31 GCs using both sMILES and BSsMILES models with the LISm χ method against values from the literature (Fan, de Grijs & Zhou, 2010; Caldwell et al., 2011; Wang, Chen & Ma, 2021). The errorbars in each frame show mean uncertainty values.

CHAPTER 5

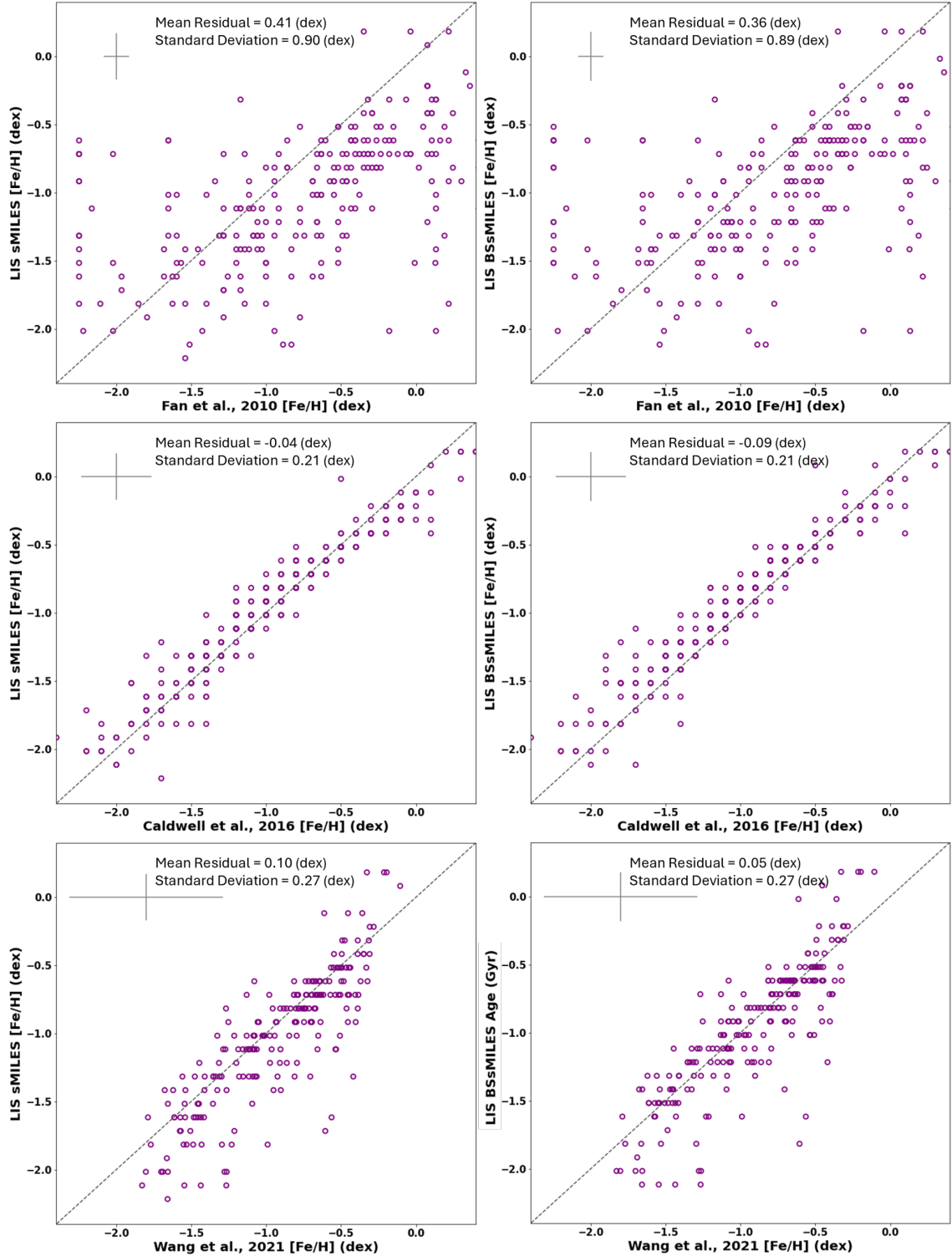


Figure 5.5: A comparison between the measured $[\text{Fe}/\text{H}]$ of this work for the S12 M31 GCs using both sMILES and BSsMILES models with the LISmX method against values from the literature (Fan, de Grijs & Zhou, 2010; Caldwell & Romanowsky, 2016; Wang, Chen & Ma, 2021). The errorbars in each frame show mean uncertainty values.

CHAPTER 5

What has been found from the comparison with literature is that age is poorly estimated even when studies use the same set of data (i.e. this work and Caldwell et al. 2011), while metallicity can be relatively accurately returned for all of the M31 objects and the measurements found here are in agreement with many literature sources. What has been shown is that the work of Chapter 4 has assisted in the reduction of the scatter in the age measurements when compared to work from other sources. The use of BSsMILES models routinely increases the age estimations of GCs who have underestimated age while maintaining metallicity measurements within error of literature values.

5.4.2 Other CSS Residuals

In this Chapter, the previous methods are used on CSSs much more massive than GCs. Figure 5.6 compares the literature $[\text{Fe}/\text{H}]$ to the $[\text{Fe}/\text{H}]$ measured from the methods used here (where $[\text{Fe}/\text{H}]$ has been calculated for the models using equation 3.8). All 4 plots show that metallicity is in relatively good agreement (for the objects with literature values). The relatively large uncertainties in both the measurements of this work and the literature measurements mean that in most cases, the measurements agree within the mutual error. Section 3.6.4 states that the scatter in metallicity selection may be due to different alpha values of the objects, where only a fixed alpha value of $[\alpha/\text{Fe}] = 0.3$ has been used for the fit. Figure 5.7 shows how the metallicity residual (literature minus measured values) correlates with the literature $[\alpha/\text{Fe}]$ of the object indicating that a large portion of the scatter is due to poor alpha selection. This could be fixed by the application of SSP models with appropriate $[\alpha/\text{Fe}]$ values as discussed earlier.

The residual metallicity - $[\alpha/\text{Fe}]$ relation shown in Figure 5.7 is present in all of the method / SSP model combinations. This is in agreement with what was found using the methods in Chapter 3 when only one $[\alpha/\text{Fe}]$ value was used. Importantly

CHAPTER 5

this indicates that the LISm χ method can measure $[\alpha/\text{Fe}]$ when more indices are used (than the 4 used in Chapters 3 & 4) and future work, will go back to the WAGGS GC sample that these methods were tested on and try to estimate $[\alpha/\text{Fe}]$ abundances for all of the CSS in the sample. Unfortunately, there is sufficient time to attempt this, so it is recommended for future work.

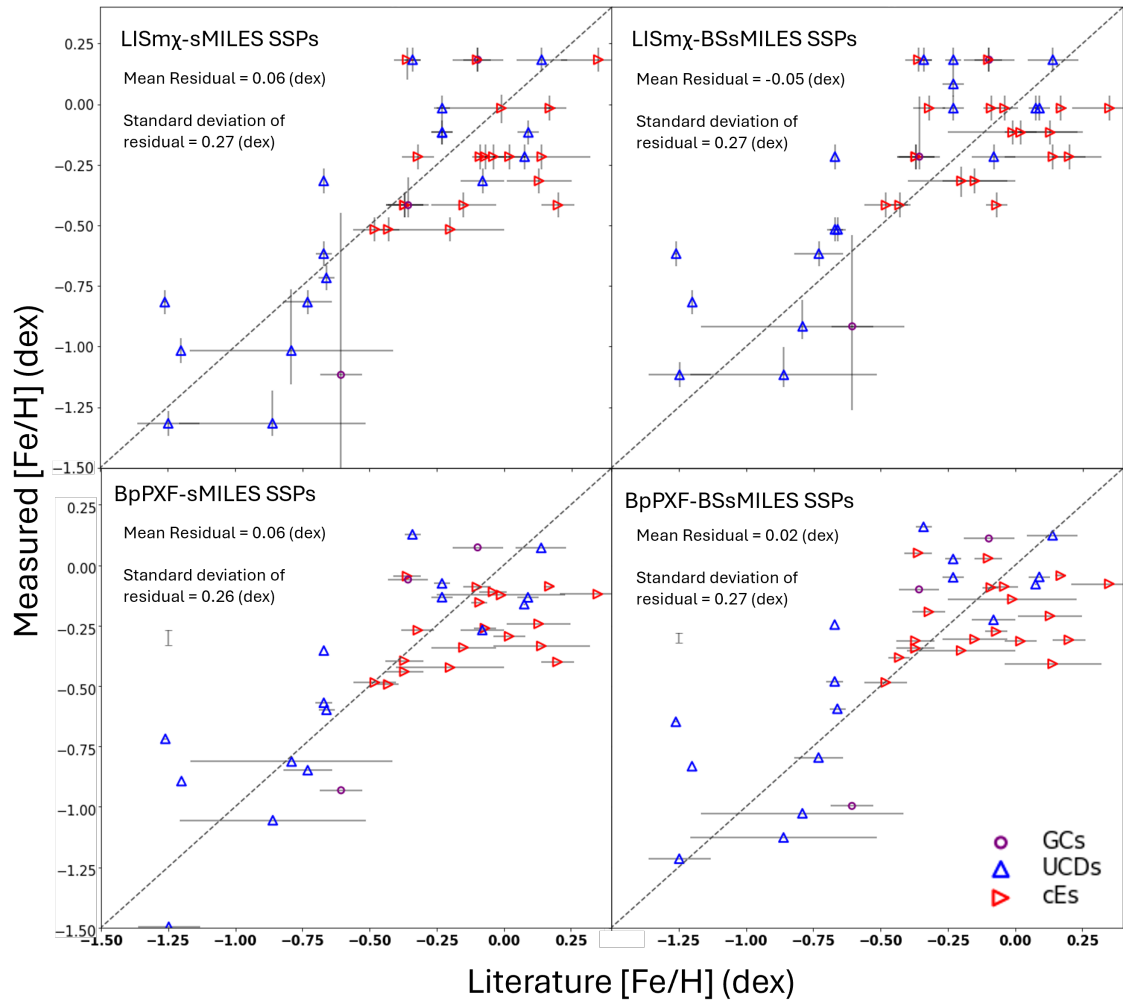


Figure 5.6: The measured $[\text{Fe}/\text{H}]$ and against literature $[\text{Fe}/\text{H}]$ for some GCs, UCDs, & cEs in the CSS sample. The top left shows the output results from the LISm χ method using interpolated sMILES SSP models, and the top right show the same method using the interpolated BSsMILES SSP models. The bottom left panel shows the results from BpPXF using sMILES SSP models and the bottom right panel shows the BpPXF results with BSsMILES SSPs.

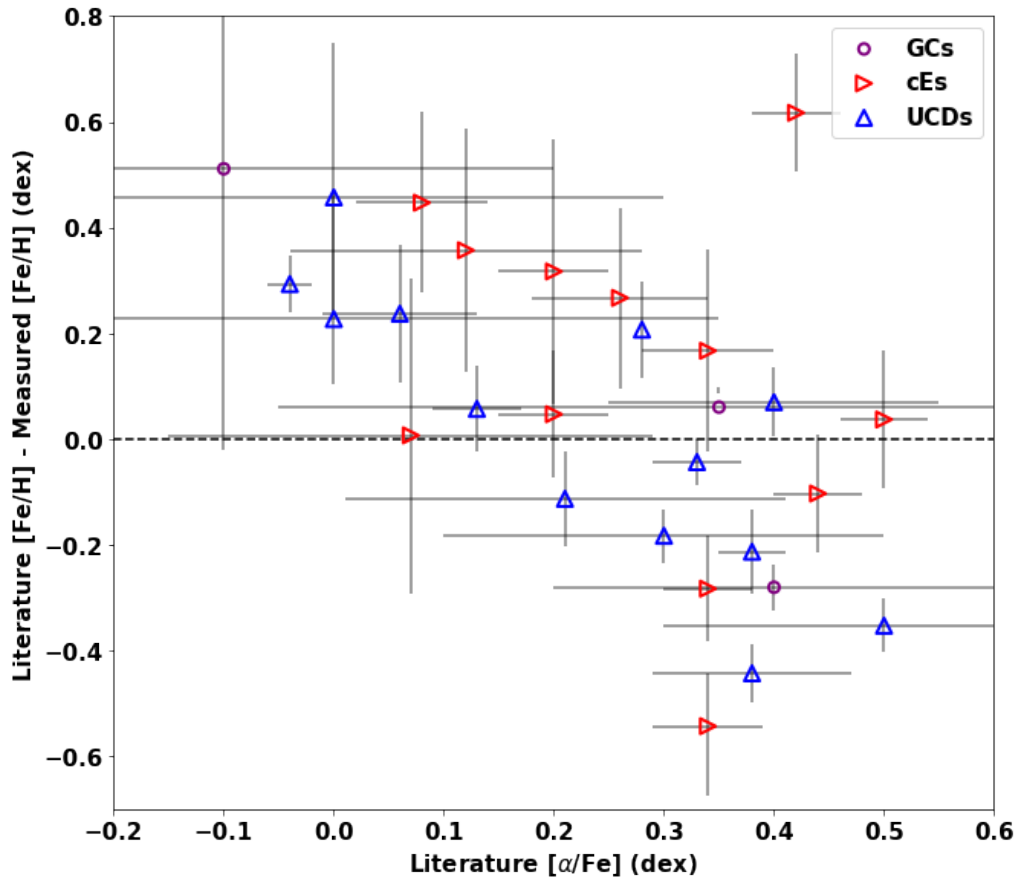


Figure 5.7: Residual $[\text{Fe}/\text{H}]$ (literature minus measured) against literature $[\alpha/\text{Fe}]$ for GCs, UCDs, & cEs. The $[\text{Fe}/\text{H}]$ values are measured using the LISm χ method with sMILES SSP models.

CHAPTER 5

Comparisons of measured and literature age (Figure 5.8) show how age estimation is still a very large problem with spectroscopic data. The accuracy of literature values for parameters such as age are questionable due to the large scatter between different literature values for the same objects (i.e. Figure 5.3). In this section, the measured values of age are compared against those in other works. Where it is generally referred to that the values of this work are overestimated in age, this may not be the case and the literature may actually be underestimated. This is especially important when it is considered that the population models used for the measurements of these objects in other studies did not contain any BSS fractions which may be present in these populations. This will cause an underestimation in age as has been shown in Chapter 4.

Through analysis of the results of this work with both methods and both sets of models, the only method which returned age estimations comparable to literature for the majority of the GCs, UCDs, and cEs (within error) was LISm χ using sMILES SSP models (top left panel of Figure 5.8). The interesting effect is that in general in all methods / SSP combinations, cE ages are ‘overestimated’ while there is a split between the metal-poor UCDs which have age measurements accurate to the literature and metal-rich UCDs with age ‘over-estimations’ similar to the cEs. If the age residual (literature minus measured) is plotted against literature metallicity for these objects (Figure 5.9) it can be seen that as CSS metallicity increases the measured age becomes more over-estimated. The source of this is unknown but may be due to age metallicity degeneracy (Worthey, 1999) as the cEs which are ‘overestimated’ in age are also generally ‘underestimated’ in metallicity compared to the literature (Figure C.1), although this correlation is loose with large uncertainties in both the literature values and the values found here.

The introduction of BSsMILES SSPs which were originally designed to represent a population of BSSs contributing a (in this case 5%) proportion of the integrated

CHAPTER 5

light does not seem to have much effect on the measured ages of the more metal-poor UCDs. BSsMILES models' impact on the populations of cEs increases their measured age significantly with LISm χ (this echoes what happened with the metal-rich WAGGS GCs in Chapter 4). The use of BSsMILES with BpPXF, however, only shows a minor age increase for the more metal-rich objects. In both methods, BSsMILES models increase the average age value of the CSSs but they also increase the scatter in measurements compared to literature (Figure 5.8). In both cases where BSsMILES models are used, the young GCs are forced to 3 Gyr and produce much lower metallicity measurements which increases the residual and standard deviation of the residuals and future work should make sure to include young models in the BSsMILES sample (this is discussed further in Section 6.2).

Overall, the use of BSsMILES models increases the age estimation of these CSSs, especially the metal-rich CSSs while there is an increase in metallicity outputs with BSsMILES but this is generally negligible compared to the uncertainty. More work needs to be undertaken to probe if BSSs contribute significant light to the integrated light of CSSs more massive than GCs. If it is found that BSSs contribute significantly then many studies which use SSP models which do not consider BSSs will have produced inaccurate ages.

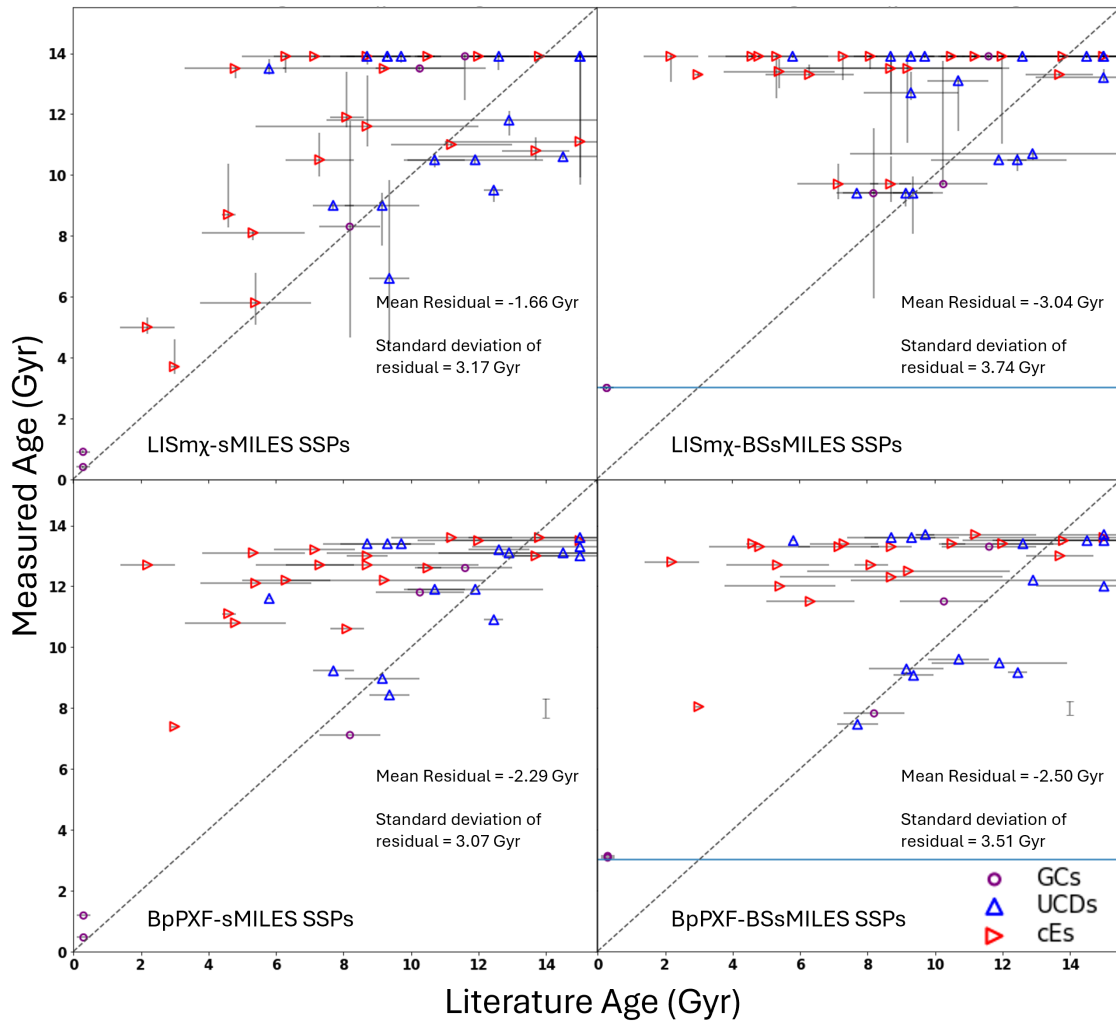


Figure 5.8: The measured age and against literature age for the GCs, UCDs, & cEs in the CSS sample. The top left is the output results from the LISm χ method using interpolated sMILES SSP models, and the top right is the same method using the interpolated BSsMILES SSP models. The bottom left panel shows the results from BpPXF using sMILES SSP models and the bottom right panel shows the BpPXF results with BSsMILES SSPs. In the left panels, the blue horizontal line represents the minimum age of the BSsMILES models.

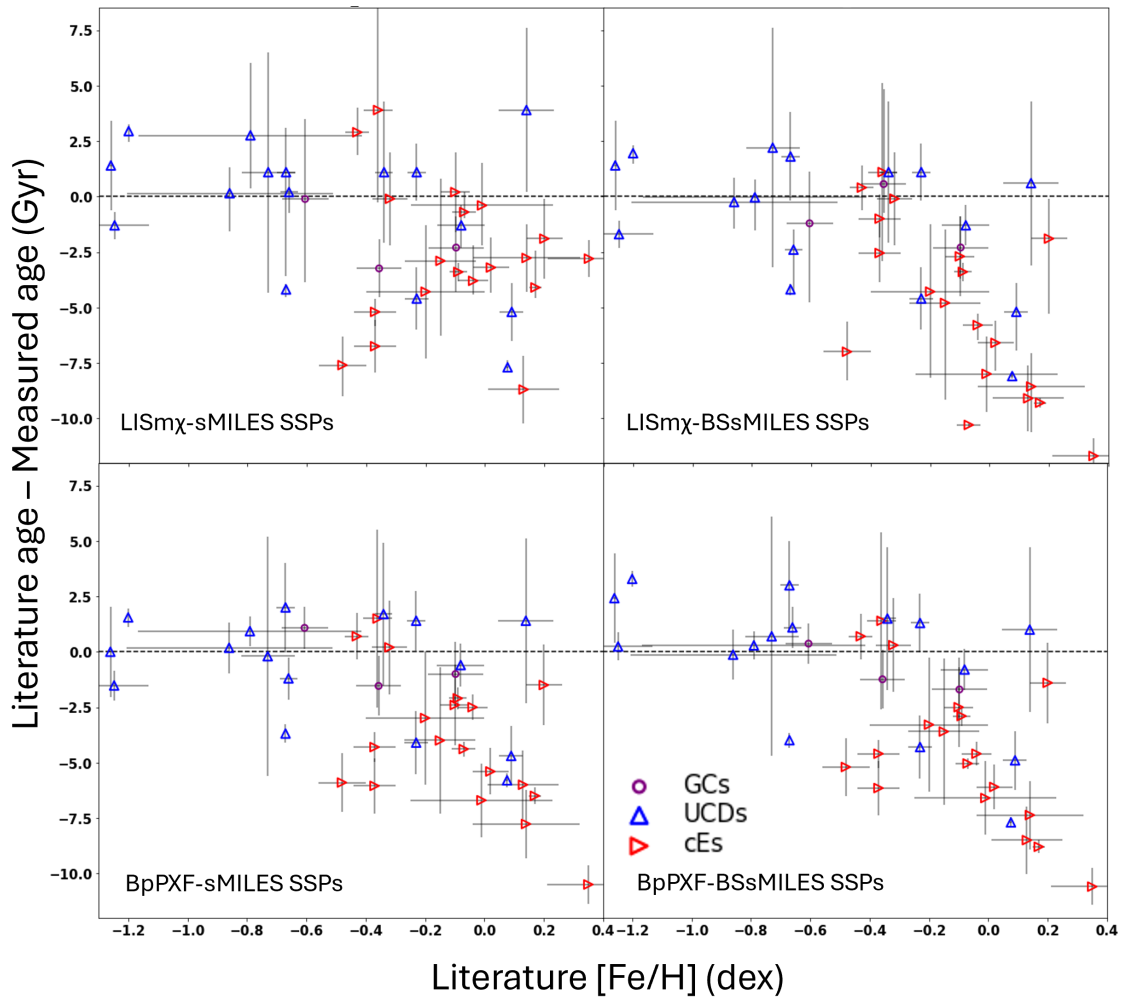


Figure 5.9: Residual age (literature minus measured) against literature $[\text{Fe}/\text{H}]$ for GCs, UCDs, & cEs. The top left shows the output results from the LISm χ method using interpolated sMILES SSP models, and the top right shows the same method using the interpolated BSsMILES SSP models. The bottom left panel shows the results from BpPXF using sMILES SSP models and the bottom right panel shows the BpPXF results with BSsMILES SSPs. The uncertainty in residual ages have been calculated by adding the measured uncertainty in quadrature to the literature value (for BpPXF the mean estimated value from Monte Carlo runs of a sample of CSSs from each data source has been added, and a range of SNRs with the same mean SNR as the whole CSS sample).

5.5 Age and Metallicity Evidence of CSS Stripping

In Section 5.2, the separation of formation scenario based on the presence of extended star-formation history and massive black holes in the cores of CSSs is discussed. The metallicity of these CSSs has been measured and it is found that it can be returned reliably.

If Figure 5.1 is remade colour-coding for measured metallicity (Figure 5.10) it can be seen that there is a clear correlation between mass and metallicity where the more massive objects trend to higher metallicities (e.g. Tremonti et al. 2004; Thomas et al. 2010; Ma et al. 2016; Janz et al. 2016). This figure shows the measured metallicities of the larger radii SDSS binned galaxies using LISm χ with sMILES models at $[\alpha/\text{Fe}] = 0.3$ to match the general alpha enhancement trend found in massive galaxies (Segers et al., 2016). The metallicities of these galaxies are included for comparison with the lower mass CSSs indicating how, as mass increases, so too does metallicity.

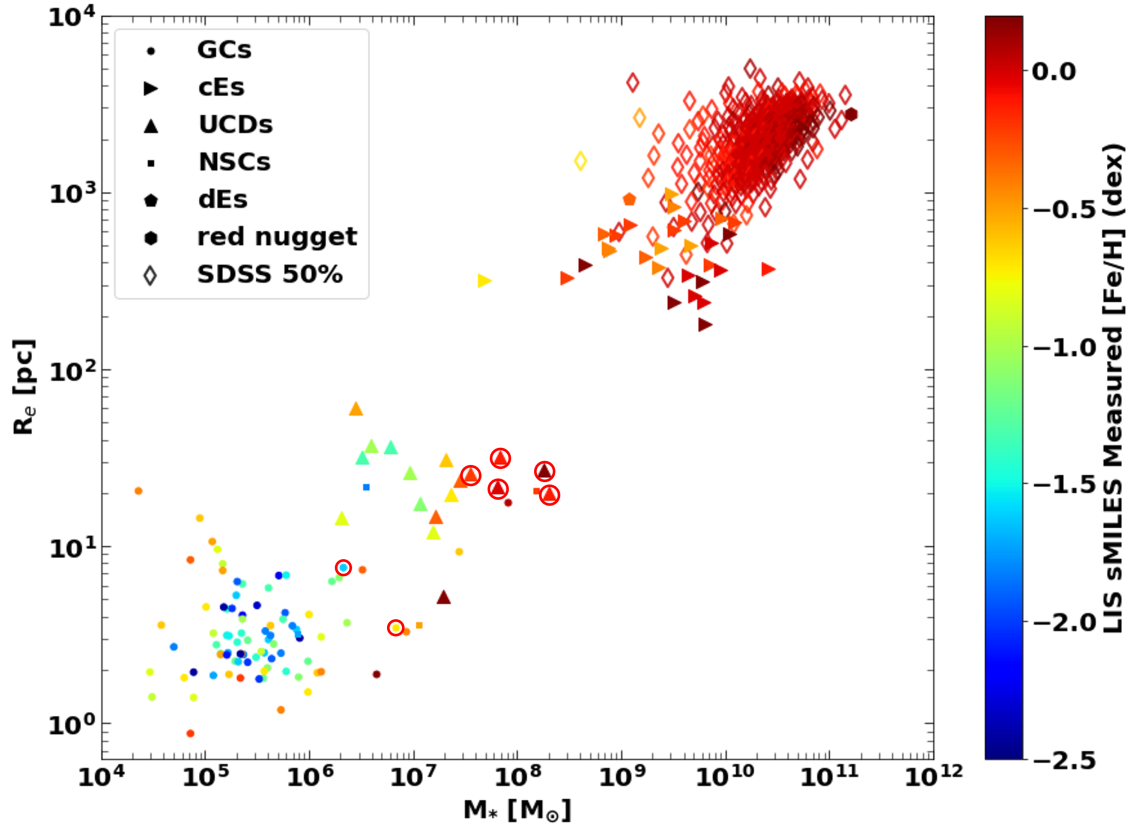


Figure 5.10: The mass vs radius plot of the CSS sample, shown in Figure 5.1 with $[\text{Fe}/\text{H}]$ as the colour. The $[\text{Fe}/\text{H}]$ values returned by LISm χ using sMILES models are used to account for the young ages of some of the GCs.

For cEs, similar result to Janz et al. (2016) are found, where the most massive cEs are more metal-rich. In comparison to the mass of the SDSS galaxies, there is a split. The more massive cEs are generally more metal-rich than galaxies with similar mass but the less massive cEs with larger effective radii have generally lower metallicities. The split in metallicity could be an indicator of formation scenario. Kim et al. (2020) states that cEs that are near a larger host galaxy are typically more metal-rich than cEs which are isolated. Isolated cEs tend to follow the mass-metallicity relation of larger elliptical galaxies indicating they formed in-situ (likely through compaction events) rather than through the galaxy cluster formation scenario of Du et al. (2019)

CHAPTER 5

where a more massive (and therefore more metal-rich, Tremonti et al. 2004) galaxy was stripped. In the cE sample, 5 cEs are identified which are likely isolated (their names in the sample of this work, provided in Table A.3, are AHcE0, AHcE53, cE1, cE547, & Chillingarian 117). In Figure 5.11 the mass metallicity relation for the cEs is plotted, highlighting the isolated cEs. Loose agreement with Kim et al. (2020) is found where the isolated cEs are more metal-poor than cluster cEs of the same mass but there is significant overlap where cluster cEs with similar mass also have low metallicities equivalent to the isolated cEs.

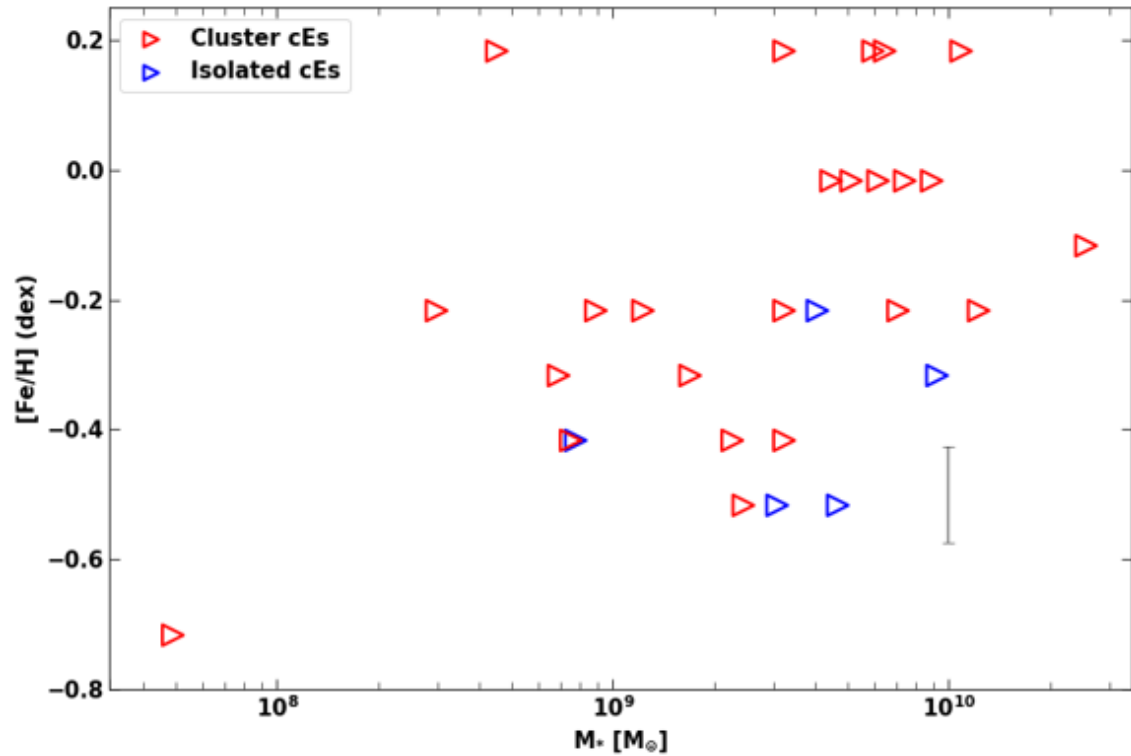


Figure 5.11: Mass against $[Fe/H]$ for the cEs in the CSS sample separated by their environment. The error bar is the mean uncertainty of the cEs $[Fe/H]$ measurements.

At low masses, dEs can have very high metallicities compared to the classic stellar mass-metallicity relation (Janz et al., 2016). However, with a sample size of 1, it is impossible to see a trend in this relation for dEs. The red nugget candidate MRK1216, is predictably very metal-rich and all of the methods used returned

extreme old ages with little to no extended star formation present in the mass fraction plots returned by BpPXF for this object. This fits with the general scenario that such “red nugget” galaxies are extremely ancient fossils of the earliest phase of galaxy formation. In this scenario the galaxy formed from a gas-rich starburst, but was then cut off from the typical accretion that enlarges galaxies over time.

5.5.1 Confirming Age & Metallicity Spreads in 2 GCs

The UCDs previously highlighted as stripped nuclei of larger galaxies, all stand out as unusually high metallicity objects compared to typical GCs. This is expected as there is a clear correlation between more massive objects and higher metallicities, an object which has evolved from the core of a more massive object is likely to be more metal-rich than similar objects formed from other pathways (e.g. high mass cluster UCDs). However, it is noticeable that the GCs highlighted as stripped objects do not show anomalously high metallicities. This potentially indicates that their formation was in lower mass galaxies (as supported by their relatively low IMBH/SMBH masses) than the more massive UCDs.

This is somewhat misleading as Ω Cen is known to have a large spread in its metallicity (Majewski et al., 2000; Hilker & Richtler, 2000; Fellhauer, 2004) but still has a relatively low peak in metallicity around $[\text{Fe}/\text{H}] = -1.7$ (dex) and spread up to $[\text{Fe}/\text{H}] = -0.7$ (dex) for a younger population up to 6 Gyr younger (Hilker & Richtler, 2000). Using BpPXF with sMILES models a spread in metallicities is found (top panel of Figure 5.12) although no evidence is found of the spread in ages (the same is also found with BSsMILES models with little difference between the selected models). However, when the larger wavelength range is used, an older population appeared on the edge of the age grid at 13.9 Gyr and with a metallicity of $[\text{M}/\text{H}] = -1.6$ (dex) indicating that with a larger wavelength range evidence of the older metal-poor population mentioned in Hilker & Richtler (2000) becomes more

CHAPTER 5

apparent, likely due to the increasing contribution low mass stars make at longer wavelengths.

The M31 GC B023-G078 has a literature metallicity of $[\text{Fe}/\text{H}] = -0.7$ (Caldwell & Romanowsky, 2016) (which is in agreement with the work here). For this CSS, a spread in ages and metallicity is returned with BpPXF (bottom panel of Figure 5.12). This figure shows a spread in ages of ~ 8 Gyr and with the younger population being slightly more metal-poor with the older population having $[\text{M}/\text{H}] \approx -0.1$ (dex) and the younger population with $[\text{M}/\text{H}] \approx -0.8$ (dex).

Given the poor constraint on age, these spreads in age may not be meaningful. However, what they do show is multiple peaks in the age axis whereas the other GCs, which do not have age spreads in the literature, return only single-peak age populations. This indicates the spread in ages where separate, multiple, populations of SSPs are needed to accurately fit the spectrum of these objects as opposed to a single age selection with a large spread (due to the poor age constraint).

While it is shown that age estimations via integrated light spectra can often be poorly estimated, metallicity is generally, accurately extracted. Because of this, it can be assumed that the extended metallicity spreads shown in Figure 5.12 are accurate and that metallicity spreads measured this way may be a valid method for the detection of CSSs formed via stripped nuclei.

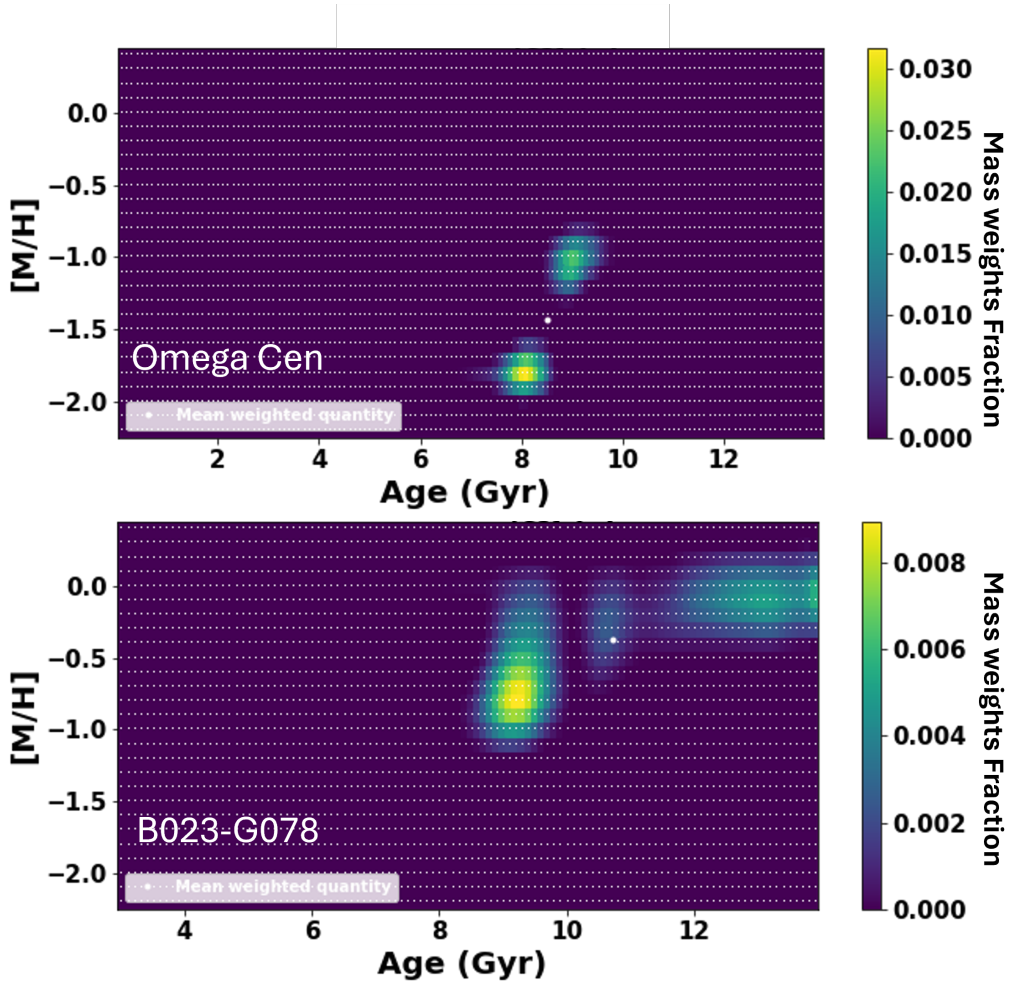


Figure 5.12: The output model fraction weights plots from BpPXF for the CSSs Ω Centauri (top) and B023-G078 (bottom, showing the selected models used in the best-fit run. smILES models are used for Ω Cen due to its $[\text{Fe}/\text{H}] \leq -1$ metallicity (Hilker & Richtler, 2000) and BSsmILES are used for B023-G078 due to its $[\text{Fe}/\text{H}] \geq -1$ metallicity (Caldwell & Romanowsky, 2016). For both objects, the wavelength range 4000-5500 Å is used with the extended CN region omitted. The models use $[\alpha/\text{Fe}] = 0.3$.

For comparison with an object also known to have an extended star formation history identified using integrated light spectral analysis, the BpPXF age-metallicity mass fraction plot of the UCD NGC 4546-UCD1 is plotted (Figure 5.13) which has

been shown to possess an extended star formation history (Norris et al., 2015) with which agreement is found here.

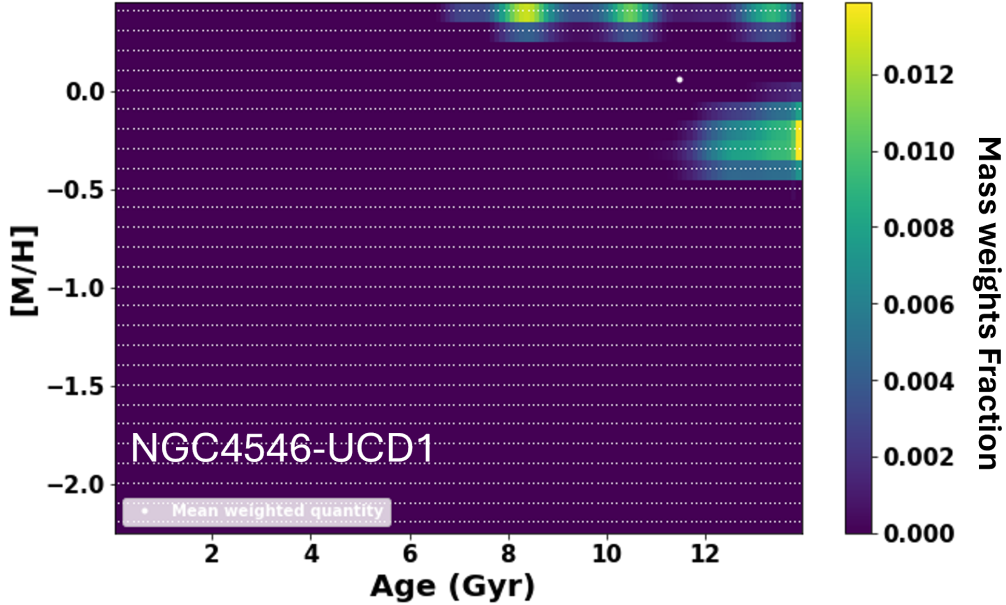


Figure 5.13: The BpPXF output mass-fraction weights plots for the CSSs NGC4546-UCD1. The plot here shows the resulting BpPXF fit for a wavelength range of 4000-5500 Å using interpolated sMILES models with an alpha value of $[\alpha/\text{Fe}] = 0.3$.

An example of an object which shows no extended star formation history is shown in the next section.

5.5.2 An Anomalous Metal-Rich UCD

As previously stated, Figure 5.10 shows how the UCDs previously highlighted as stripped remnants are all very metal-rich. This figure also highlights an anomalously metal-rich UCD with a low effective radius of $r_e = 5.24$ and mass of $M_* = 1.95 \times 10^7 M_\odot$ (Mieske et al., 2008). This is the CSS UCD-FORS 45 (CSS-969 from the XShooter data in Table A.3) and is the UCD with the smallest effective radius despite it having a mass around the average value for the sample. With LISm χ using

CHAPTER 5

sMILES models, its metallicity is measured as $[\text{Fe}/\text{H}] = 0.18 \pm 0.05$ (dex). This is an anomalously high metallicity for its mass and unlike the other high metallicity UCDs in the sample, there has previously been no published evidence of a stripped formation path. This UCD is in the Fornax galaxy cluster so could feasibly have undergone a tidal stripping event in its history.

Using BpPXF, it has been shown (Figure 5.12) how extended star formation and metallicity spreads can be identified via integrated light spectra. Using the same method, it is attempted here to identify metallicity spreads or extended star formation histories in UCD-FORS 45. Figure 5.14 shows the mass fraction plot of BpPXF using the $[\alpha/\text{Fe}] = 0.3$ interpolated sMILES models. This figure shows no extended star formation histories and no spreads in metallicity indicating that either this object is not a stripped nucleus, or that star formation ceased very early in its formation, before a later stripping event (possibly due to its location in a galaxy cluster). Figure 5.14 also shows the fit from BpPXF, it is fairly well fit but there are a few regions, especially on the red end of the spectrum where BpPXF has had trouble being able to fit this spectrum. This may be due to continuum effects from the reduction process that the “mdegree” polynomial has not been able to remove or this may be a physical effect due to a chemical overabundance causing more absorption in that wavelength range than the models predict. The age-indicating lines ($\text{H}\beta, \gamma, \delta$) seem to generally fit well.

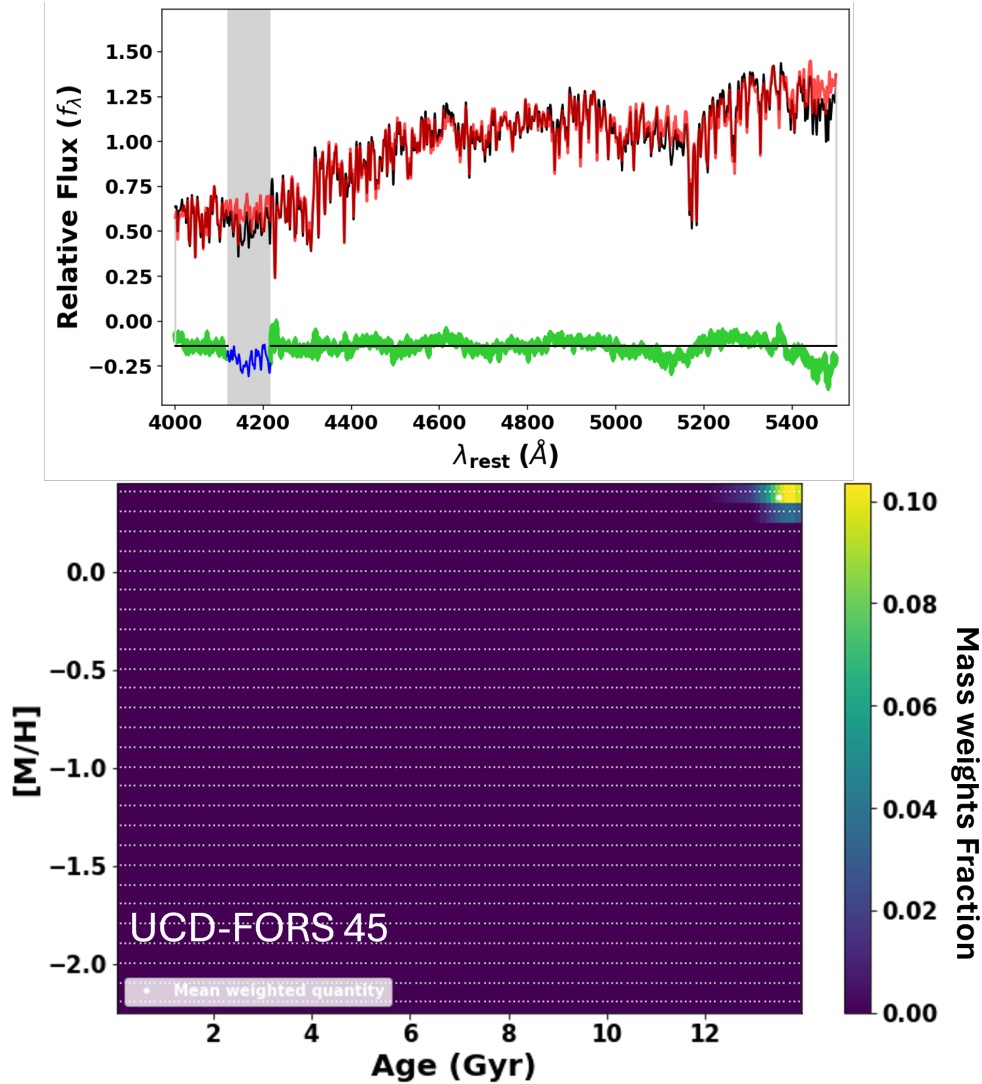


Figure 5.14: Mass fraction age vs metallicity plot and spectral fit from BpPXF for UCD-FORS 45 using sMILES models with $[\alpha/\text{Fe}] = 0.3$. the poor-fitting regions of the "Ommited" region used before have been removed from the fit and highlighted with a shaded box.

There is evidence of a less-than-simple history for this UCD. Via analysis of its surface brightness profile Voggel, Hilker & Richtler (2016) showed that this object had faint residuals on its outer annuli and they disagree with the effective radius calculation from Mieske et al. (2008) stating a much larger radius of $r_e = 33.83$

CHAPTER 5

± 0.14 pc which places it back with the other UCDs and in close proximity with the UCDs with stripped nuclei formation pathways. The presence of faint extended residuals indicates that this object possibly had previous stellar populations at larger radii which have since been (at least partially) stripped away.

This UCD was observed by XShooter which offers very high resolutions. This data has a resolution of $R \sim 5400$ and therefore it was possible to measure the velocity dispersion of this UCD. Velocity dispersions can be a good indicator of whether a CSS possesses a massive black hole in its core (Seth et al., 2014; Ahn et al., 2017). The presence of SMBHs were found in the UCDs M59c0 and VUCD3 via analysis of the change in radial velocity dispersions at different radii from the core (Ahn et al., 2017). They found peak central velocity dispersions of 52.9 ± 2.5 kms^{-1} and 40.2 ± 1.6 kms^{-1} for VUCD3 and M59c0 respectively, while they found integrated dispersions (velocity dispersions from the integrated light spectrum) of 39.7 ± 1.2 kms^{-1} and 31.3 ± 0.5 kms^{-1} respectively. They applied double sérsic profiles to HST imagery to obtain mass density and luminosity for their UCDs and combined their mass models with their velocity dispersion profiles to obtain mass estimates for a central black hole.

Using BpPXF with a fourth-order additive polynomial (as is done in Ahn et al. 2017), an integrated dispersion of $\sigma = 37.2 \pm 1.4$ kms^{-1} is found. The uncertainties were calculated using 50 Monte-Carlo runs where the uncertainty was calculated using the standard deviation of the output values. This value is in agreement with Mieske et al. (2008) who measure a velocity dispersion of $\sigma = 35.6 \pm 2.9$ kms^{-1} . This velocity dispersion value is equivalent to those given for M59c0 and VUCD3. M59c0 and VUCD3 are more massive than UCD-FORS 45 so an equivalent velocity dispersion is highly suggestive of the presence of a SMBH.

For comparison with UCDs of similar mass with no known SMBH at their centre the velocity dispersion of CSS-756 and VUCD7 was also measured with the same

CHAPTER 5

method and found velocity dispersions of $\sigma = 26.5 \pm 3.2 \text{ kms}^{-1}$ and $\sigma = 30.7 \pm 4.5 \text{ kms}^{-1}$ respectively (also shown in Figure 5.15). The masses of the UCDs are shown in Table A.3 and Figure 5.15 and are comparable with (and slightly more massive than) UCD-FORS-45. Figure 5.15 shows mass against velocity dispersion (σ) for UCDs from Mieske et al. (2008, 2013) along with the UCDs from Ahn et al. (2017). The effective radii of the UCDs can contribute to the measured velocity dispersion and as such has been plotted as colour. This again shows that the velocity dispersion of UCD-FORS-45 is anomalously high for its mass. There are three interesting objects in Figure 5.15 which have anomalously high σ for their masses. These objects are (in order of ascending mass) “S314”, “0330”, and “S490” from Mieske et al. (2013) and these objects also have very small radii. This radii is comparable to that of other UCDs of similar mass but their σ is much larger. This could indicate that these objects are stripped, and what is seen in the figure is the very high velocity dispersion of the interior regions of a previously more massive object. Work should be done to identify evidence of tidal stripping in these objects such as the presence of a SMBH, age or metallicity spreads or faint extended features such as those found for UCD FORS 45 in Voggel, Hilker & Richtler (2016).

This thesis is limited in what it can achieve with this, seeing limited, XShooter data. The seeing of the observations, and the small size of the objects means that it isn't possible to measure spatially resolved kinematic profiles for these CSSs. So the velocity dispersion cannot be corrected by system rotation as they did in Ahn et al. (2017) and velocity dispersion cannot be measured at different radial distances so peak velocity dispersion cannot be measured. This is left to future work where it is hoped adaptive optics (AO) high-resolution spectroscopy will reveal high central velocities indicative of an SMBH.

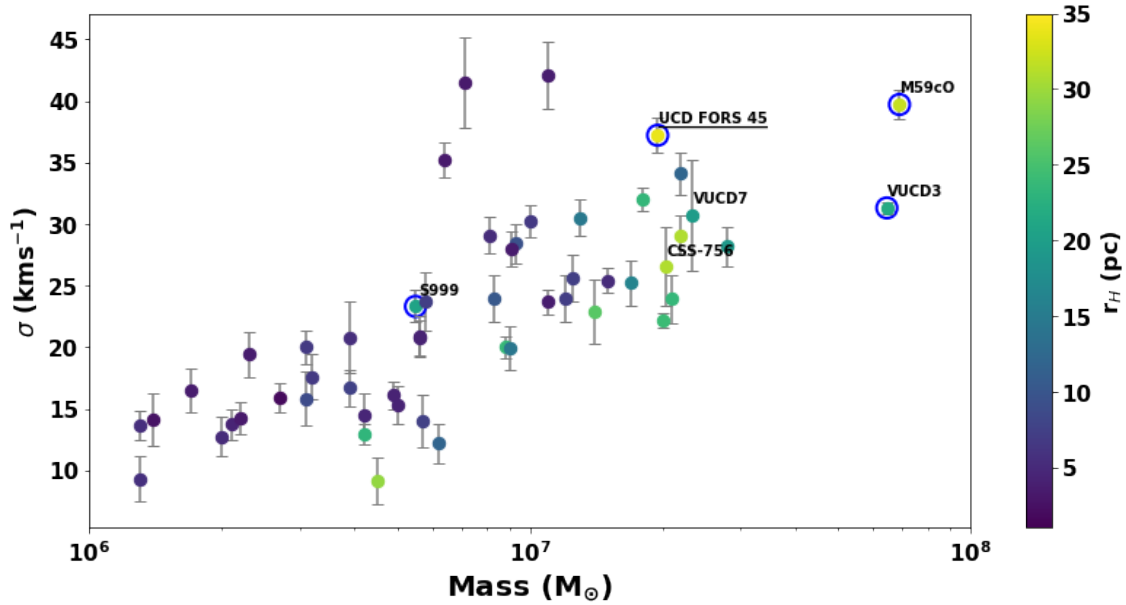


Figure 5.15: Mass against velocity dispersion plot for UCDs with half-light radius as colour. Most of the UCD data came from Mieske et al. (2008, 2013) as well as the UCDs from Ahn et al. (2017) and the σ measurements of VUCD7, CSS-756 and UCD FORS 45 made in this thesis (with the larger radius value of Voggel, Hilker & Richtler (2016) for UCD FORS 45 which takes into account its extended outer annuli). Objects with known (or suspected for UCD FORS 45) central SMBHs are circled in blue.

It is found that the UCDs which are definitive stripped objects are all massive and metal-rich. There was a metal-rich outlier at lower masses and low effective radii. This work suggests that this UCD may in fact be the result of a stripped more massive galaxy. Through analysis in this section, no evidence of an extended star-formation or metallicity spreads have been found indicative of some stripped objects. However, through its high-resolution XShooter spectra, it has been found that this UCD has a large velocity dispersion for its mass, which could suggest the presence of a SMBH. Further study of this object is suggested.

5.6 NSC Formation Classification

Figure 5.2 shows the separation in metallicity of the majority of UCDs and the cEs, but it also shows a spread in the metallicity of the NSCs.

As stated in Section 1.5 there are two main formation pathways for NSC. One lower mass path that is caused by the infalling of GCs to the central regions of a galaxy via tidal friction (Fahrion et al., 2022). NSCs formed this way are typically of intermediate - old ages (equivalent to GCs) and have low masses and low metallicities (Tremaine, Ostriker & Spitzer, 1975; Capuzzo-Dolcetta, 1993; Capuzzo-Dolcetta & Miocchi, 2008; Agarwal & Milosavljević, 2011; Portaluri et al., 2013; Antonini, 2013; Arca-Sedda & Capuzzo-Dolcetta, 2014; Gnedin, Ostriker & Tremaine, 2014). The other formation pathway for NSCs is via directly forming in the galactic centre from the dense gas and dust in the galactic core. NSCs formed this way are typically more massive and metal-rich than the NSCs formed via GC infalling. In-situ NSCs are also typically older (Loose, Kruegel & Tutukov, 1982; Milosavljević, 2004; Bekki, Couch & Shioya, 2006; Bekki, 2007; Antonini, Barausse & Silk, 2015). There is also the pathway of NSC formed via the combination of both of these methods resulting in a well-mixed, stellar dense environment which attributes of both of the other formation types with extended metallicities and formation ages.

In the CSS sample, there are 4 NSCs. These are NGC 628 (M74)-NSC, NGC 2344-NSC, EVCC1320 (mislabelled as LEDA4573336-NSC in the MODS data) and UGC 12732-NSC. These NSCs do not have published age or metallicity values for comparison with the measurements made in the work presented here but they do have published masses and effective radii. Combined with the age and metallicity measurements from this work, the formation scenarios are probed, based on the parameters of formation mentioned.

5.6.1 NGC 628 - NSC

This NSC has a literature effective radii of $r_e = 3.6$ pc and mass of $M_* = 1.313 \pm 0.533 \times 10^7 M_\odot$ (Georgiev et al., 2016) and is the second most massive NSC in the sample (Figure 5.1). Using LISM χ with BSsMILES models with $[\alpha/\text{Fe}] = 0.3$, its metallicity was measured to be relatively high at $[\text{Fe}/\text{H}] = -0.62 \pm 0.05$ (dex) which lies in the lower end of the “metal-rich” high mass NSCs defined in Neumayer, Seth & Böker (2020).

The measured age for this NSC (like most objects presented in this thesis) is uncertain. However, the method which gave the most accurate (to literature) ages of the available methods (LISM χ with sMILES models with $[\alpha/\text{Fe}] = 0.3$) gives this object an age of $3.7_{-0.2}^{+0.5}$ Gyr. However, Neumayer, Seth & Böker (2020) states that spectroscopic ages of NSC should not be used as an age estimate due to the age metallicity degeneracy and state that many NSC are likely to have large spreads in ages due to an extended star formation history (e.g. Alfaro-Cuello et al. 2020). The BSsMILES models give it an age of 9.1 ± 0.05 Gyr and the mass fraction plot of BpPXF shows evidence of extended star formation (Figure C.2).

The metallicity measured here is equivalent to the core metallicity of NGC 628 provided by Sánchez-Blázquez et al. (2014). The metallicity combined with the large mass of this NSC and the extended star formation inferred via BpPXF indicates that this NSC probably formed in-situ at the core of its host galaxy.

5.6.2 NGC 2344-NSC

This is the most massive NSC in the CSS sample. It has a mass of $M_* = 1.51_{-1.18}^{+0.15} \times 10^8 M_\odot$ and an effective radius of $r_e = 20.5_{-20.5}^{+1.1}$ pc (Georgiev et al., 2016) laying in the similar mass-radius space as the most massive UCDs in Figure 5.1. Although due to this NSCs larger effective radius, it is less stellar dense than NGC 628-NSC.

In the output age-metallicity plots of Figure 5.2, this NSC is shown to be

CHAPTER 5

metal-rich ($[\text{Fe}/\text{H}] = -0.22 \pm 0.05$ [dex] using the LISm χ method with BSsMILES models at $[\alpha/\text{Fe}] = 0.3$) and have older ages than the other metal-rich NSC (although there is large spread in measured ages between the different method / model combinations). BpPXF does not show clear evidence of extended star formation (Figure C.3) but it does show very old ages and high metallicities.

Due to the high mass and high metallicity, it is predicted here that this NSC formed via in-situ star-formation from material in the core of NGC 2344.

5.6.3 UGC 12732-NSC

Of the 4 NSCs in the CSS sample, this has the lowest mass and radius ($M_* = 7.68_{-0.19}^{+2.82} \times 10^5 M_\odot$ and $r_e = 3.2 \pm 0.1$ pc, Georgiev et al. 2016). The classification for NSC formation stated earlier suggests that the less massive NSCs formed via infalling of GCs via dynamical friction and that NSCs formed this way would appear older and more metal-poor than their surrounding galaxy.

The measured metallicity from the LISm χ method with BSsMILES models at $[\alpha/\text{Fe}] = 0.3$ is $[\text{Fe}/\text{H}] = -1.51_{-0.16}^{+0.17}$ (dex). This value is significantly more metal-poor than the previous two NSCs. It should be noted that metallicity produced via BpPXF is higher than that produced with LISm χ by ~ 0.4 dex. However, the spectrum of this object has a very low SNR for MODS data (SNR = 7.4 at 5000 Å) so any measurements based on this particular spectrum may not be reliable. This low SNR is apparent in the BpPXF mass fraction plot (Figure C.4) where this object appears to have a large spread in age and metallicity which is due a very large regul value needed for BpPXF to acquire the correct $\Delta\chi^2$ value.

There are no published metallicity values for the host galaxy, UGC 12732. However, due to the low metallicity and low mass of this NSC, it is speculated here that it formed via the dynamical friction-driven GC infall formation method, but due to the low SNR of this object, this cannot be certain.

5.6.4 EVCC1320

EVCC1320 lies within the Virgo cluster. There was no literature mass value for this object. Therefore, to calculate this the SDSS r band luminosity and the distance[†] are used, calculating absolute magnitude. Then using the mass-luminosity relation a mass of $M_* = 3.47 \pm 0.87 \times 10^6 M_\odot$ is calculated. Combined with its effective radius of $r_e = 21.75$ pc, this NSC is placed in the low mass end of the UCD sample in Figure 5.1.

This NSC is low mass compared to the others in the sample and has a relatively large effective radius meaning that is among the less dense CSSs and is the least dense NSC in the sample. The output for all four method / model combinations give this NSC intermediate age. All 4 outputs give this NSC a metal-poor value with the metallicity from the LISM χ method with BSsMILES models at $[\alpha/\text{Fe}] = 0.3$ being $[\text{Fe}/\text{H}] = -1.42 \pm 0.051$ (dex). The low mass and low metallicity indicate that this NSC formed as the result of dynamical friction-driven GC infall.

Intriguingly, this NSC shows very similar metallicity spreads to the stripped nucleus candidate ‘GC’ Ω Cen with a large spread in metallicity at ~ 8 Gyr (Figure C.5). The low metallicity indicates that it could be due to GC infall but the large spread in metallicity indicates that it has accreted material from many sources becoming a mixed stellar environment of potentially many populations (distinct from the MPs phenomenon of GCs). This object could be very similar to a pre-stripped version of Ω Cen.

5.6.5 NSC Summary

The suggested formation paths given here for each NSC are speculations based on their mass and metallicity relative to their host galaxy (where host galaxy metallicity

[†]Assuming its distance is equivalent to Virgo ± 2 Mpc due to its presence in the Extended Virgo Cluster Catalog (EVCC).

is known). There is currently no robust way to measure NSC formation paths with the data available in this sample, and more evidence must be collected in order to increase confidence in the predictions presented here.

It is possible that the chemical signatures present in globular clusters (i.e. MPs in the form of specific chemical enhancements) would be present in the spectra of NSCs formed via GC infalling. However, it should be mentioned that Neumayer, Seth & Böker (2020) states that NSCs which form this way may still be well-mixed environments which undergo bursts of star formation later in their life from accreted gas from the polluted cores of their host galaxy, and the influence of the MPs of the GCs the NSC formed from may be diluted by these younger populations of stars.

5.7 CN Abundance as a Signature of Formation

Previous work (Banister, 2020) has shown how the enhanced nitrogen signature of MPs for GCs is visible in the integrated light spectra (highlighted in Figure 5.16). This was done via plotting the LIS index CN_1 against the alpha insensitive metallicity index $[MgFe]'$ showing nitrogen enhancement with the TMJ (Thomas, Maraston & Johansson, 2011) SSP models (enhanced in nitrogen by 0.3 dex). Figure 5.17 shows this nitrogen enhancement compared to TMJ and Conroy (Conroy et al., 2018) models both enhanced in nitrogen by 0.3 dex (LIS indices measured with a resolution of 5\AA FWHM) and it is seen that the N overabundance only becomes apparent at higher metallicities.

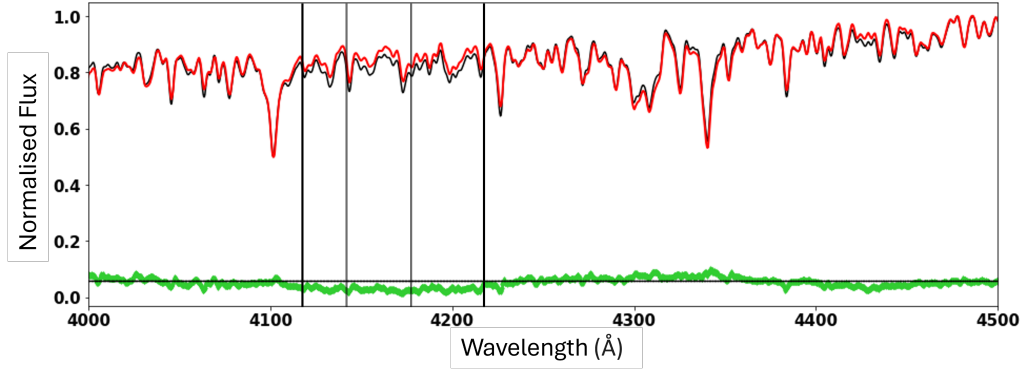


Figure 5.16: BpPXF fit over the CN enhanced region for NGC6864. Highlighted with vertical columns are the central region of the CN₁ LIS index (grey) and the extended CN region introduced in Banister (2020) (black).

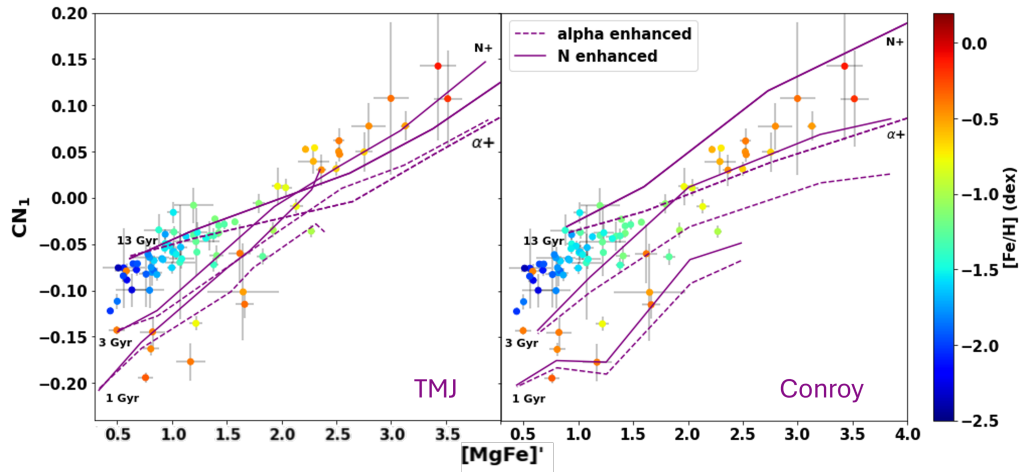


Figure 5.17: CN₁ against $[\text{MgFe}]'$ for the WAGGS GC sample (Usher et al., 2017). The left panel shows alpha-enhanced (dashed line) and nitrogen-enhanced (solid line) TMJ (Thomas, Maraston & Johansson, 2011) SSP models at 3 different ages (1, 3 and 14 Gyr). The right panel shows alpha-enhanced (+0.3 dex) and nitrogen-enhanced (+0.3 dex) Conroy (Conroy et al., 2018) models at the same ages as the TMJ models. The colourbar shows $[\text{Fe}/\text{H}]$ (Measured using LISm χ using sMILES models to allow accurate fitting of low metallicity GCs) as a comparison to the metallicity indicator $[\text{MgFe}]'$.

CHAPTER 5

There is some dependency on CSS age shown in the figure, the young WAGGS GCs are metal-rich when measured with $[\text{Fe}/\text{H}]$ but have low $[\text{MgFe}]'$ values indicating that for these young GCs, magnesium is not as strong as iron in the object's spectrum. If the TMJ models are compared to Conroy it can be seen that TMJ predict that when $[\text{MgFe}]'$ increases ($\gtrsim 2$) the CN_1 value becomes insensitive to cluster age. This is not the case with the Conroy models where there is consistent separation in age at all ranges of $[\text{MgFe}]'$. Comparison of the CN abundances of the two model sets at different metallicities shows that while the oldest age line for the alpha-enhanced models generally agree with each other at high metallicities, the Conroy models N enhanced SSP models have considerably larger CN absorption regions resulting in the GCs appearing less enhanced than the TMJ models suggest they are (while still appearing enhanced). The GCs start to appear enhanced at $[\text{MgFe}]' \gtrsim 1.3$ dex for TMJ, yet only start to appear enhanced at $[\text{MgFe}]' \gtrsim 2$ dex in the Conroy models. For the rest of this section, Conroy models are used as they offer a more conservative estimation of CN enhancement while showing a dependence on age which may appear in other objects.

The CN region is controlled by both carbon and nitrogen abundance, however using the residuals of carbon-enhanced and nitrogen-enhanced spectra to a solar spectrum (Figure C.6), it is seen that there are residuals in the carbon-enhanced spectrum at larger wavelengths (4220-4400 Å) which are not generally shown as poor fitting regions in BpPXF fits (there were occasional small overestimations of the continuum in this region but these were often smaller than the pixel uncertainty and so were not omitted from any fits). Nitrogen-enhanced spectra only have residuals in the extended CN region that is omitted from the fits, indicating that the enhancements seen are the result of nitrogen enhancement. This correlates with the MPs phenomenon where there is an anti-correlation between nitrogen and carbon with an overabundance of nitrogen and depleted carbon. If the depleted carbon were

CHAPTER 5

a dominant signature the CN region would be overestimated in Figure 5.16. In this Figure, small overestimations are seen in wavelengths to the red side of the CN region and this correlates with Figure C.6 where the wavelength range $\lambda \sim 4250 - 4400 \text{ \AA}$ is dominated by the signatures of carbon. This region is weak (oversampled by the model) which indicates that this region may be depleted in carbon. In future work, the hope is to be able to account for this poor fitting region, and there is current work with sMILES models to allow for individual elemental abundance changes where the combination of different element amounts (i.e. enhanced nitrogen and depleted carbon) may be available.

It has been shown that the abundance variations of nitrogen are significantly larger than those of carbon in the CN region (Thomas, Maraston & Johansson, 2011; Bastian & Lardo, 2018; Milone & Marino, 2022) which supports the inference that abundance issues in this region are dominated by nitrogen overabundance.

5.7.1 NSC CN Enhancement

Section 5.6 speculates the formation of the NSCs of the sample suggesting two are the result of in-situ star formation in the core of their host galaxy while the other two are the result of GC infalling. The theory here is that the NSCs which formed via GC infalling may have the same spectroscopic signatures of MPs that GCs have, showing nitrogen enhancement. The LIS indices of these objects are measured and CN abundance is plotted against $[\text{MgFe}]'$ in Figure 5.18. The spectrum of UGC 12732-NSC as a very low SNR for MODS data ($\text{SNR} = 7.4$ at 5000 \AA) and the resulting index measurements resulted in negative values for the index Fe5270. Therefore Equation 3.7 could not calculate $[\text{MgFe}]'$ for this object and is not plotted.

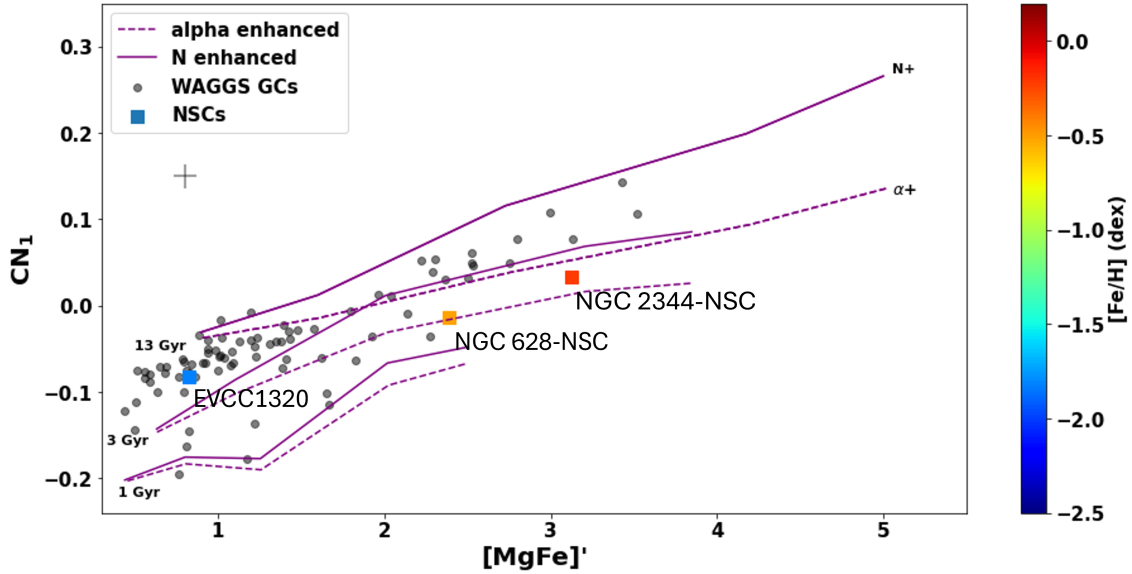


Figure 5.18: Similar to Figure 5.17 using only Conroy (Conroy et al., 2018) SSP models. This figure shows the CN abundance of the NSCs in the CSS sample along with the WAGGS GCs (grey) for comparison with objects which are enhanced in the CN region.

If the spectrum of NSC EVCC1320 is compared to the N-enhanced models (Figure 5.18) it is seen that it does not appear to be nitrogen-enhanced. However, this NSC is metal-poor and it sits with the GCs which are metal-poor but are known to have enhanced nitrogen (from single star studies Milone & Marino 2022). This indicates that this object may be enhanced in nitrogen but it is not possible to tell from the integrated light. The two metal-rich NSCs NGC 628-NSC and NGC 2344-NSC do not appear to show N enhancement. They sit well below the enhancement line and the nitrogen-enhanced GCs of similar metallicities. If the theory is assumed that N enhancement will be seen in NSCs formed via GC infalling then this supports the earlier assumptions that these NSCs are the result of in-situ star formation in the metal-rich cores of their host galaxies, or at least that some in-situ formation occurred to dilute the N overabundance.

5.7.2 UCD CN Abundance

Section 5.5 identified that the UCDs which were the result of tidal stripping stood out as very metal-rich (Figure 5.10) while the UCDs which have not had any indicators of a stripped formation scenario were more metal-poor. Evidence for other UCD formation scenarios will now be discussed. UCDs are more massive than GCs and therefore the presence of actual multiple stellar populations (not just the chemical abundance variations seen in GC MPs) is highly likely as they will be massive enough to retain mass during the usual matter ejection scenario which quenches star formation (Goodman & Bekki, 2018). What can also be expected to be seen for these GC type UCDs is the same evidence of MPs seen in GCs. By plotting CN_1 against $[MgFe]'$ (Figure 5.19) the CN abundances of the UCDs in the sample are shown.

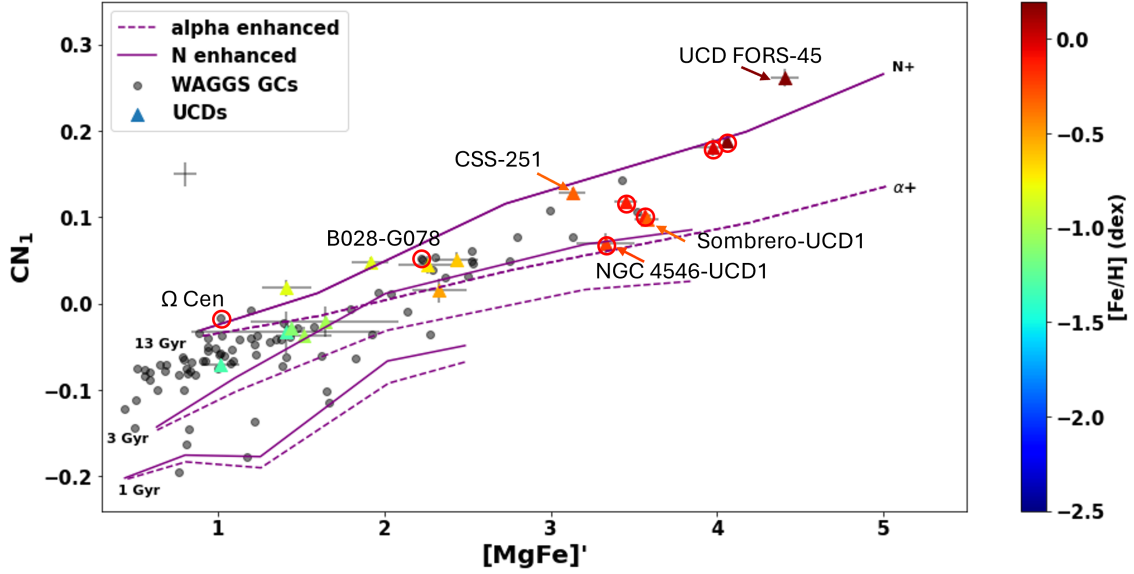


Figure 5.19: Similar to Figure 5.18 but showing the UCDs from the CSS sample. Highlighted in red circles are the UCDs and GCs identified as being stripped nuclei. The two metal-rich UCDs which have not had published evidence of stripped formation, The UCD investigated in Section 5.5.2 and the stripped UCD NGC 4546-UCD1 which does not appear to show much CN enhancement relative to the other stripped UCDs have all been labelled.

There is an apparent metallicity split in the UCDs on either side of $[\text{MgFe}]' \approx 3$. The metal-poor UCDs generally agree with the GC CN abundance or are otherwise more enhanced. This is good evidence to indicate the presence of the same MP abundance issues present in GCs and supports the theory that these objects are the massive end of GC formation. However, Ω Cen and B023-G078 fit well with the other GCs even though they are likely stripped objects.

The metal-rich UCDs ($[\text{MgFe}]' \gtrsim 3$) also show anomalous enhanced CN. There is an increasing CN trend as $[\text{MgFe}]'$ increases which is apparently greater than the models predict. Only one stripped UCD (NGC 4546-UCD1 which has an extended star formation history) does not appear to show CN enhancement. The presence of CN enhancement in almost all UCDs despite their formation scenario forces us

CHAPTER 5

to conclude that CN abundance cannot be used to separate UCDs by formation scenarios. It does, however, bring up the question of why these UCDs, which are not related to GCs in their formation possess anomalously high abundances in the CN region. UCDs are very stellar dense objects. This could be for a number of reasons. These values could just be the natural relation between metallicity and CN abundance, indicating that the SSP models are incorrect. Or it could be that stellar dense environments lead to stellar populations with enhanced nitrogen. This phenomenon of anomalously enhanced CN in other CSSs is explored in the next few sections.

The UCD identified in Section 5.5.2 as being anomalously metal-rich for its mass has both the highest CN value and $[\text{MgFe}]'$ value which adds interest to this object to understand what has driven this intermediate-mass UCD to such high metallicity values. Earlier it was suggested that this UCD potentially is the stripped nucleus of a previously more massive galaxy. There are two other UCDs which are classified here as metal-rich from Figure 5.19 ($[\text{MgFe}]' \gtrsim 3$), Sombrero UCD1 and CSS-251 and due to their high metallicity, future work is proposed to search for signatures of tidally stripped formation.

5.7.3 cE CN Abundances

Since unexpected CN overabundance was found in the metal-rich uCDs formed via tidal stripping, the CN values of the cEs were measured to see if they display similar abundance patterns. Plotted in Figure 5.20 is the CN against $[\text{MgFe}]'$ plot for the sample of cEs compared with WAGGS GCs and Conroy alpha and nitrogen enhanced SSP models at 3 different ages, similar to Figures 5.18 & 5.19.

Figure 5.20 shows that the cEs in the sample have a large spread of CN with some cEs appearing CN enhanced with others not. There is a very loose correlation with $[\text{Fe}/\text{H}]$ with the most metal-rich being the more CN enhanced cEs. To check

CHAPTER 5

for correlation with formation, the cEs identified to be isolated are highlighted. It is found that these cEs do not show any particularly strong CN enhancements with only two lying with the GC abundances above the 14 Gyr alpha-enhanced models. No correlation is identified between cE formation and CN line strength.

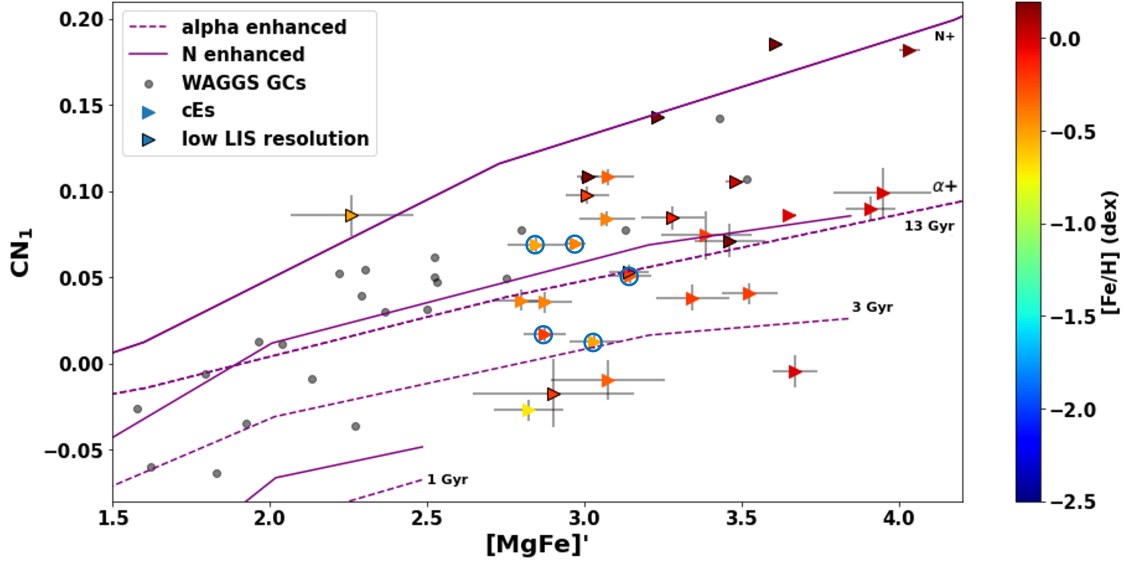


Figure 5.20: Similar to Figures 5.18 & 5.19 showing the cEs in the sample. Isolated cEs have been highlighted with blue circles. The objects with a black outline are CSSs whose velocity dispersion measurements with BpPXF were too large for their spectra to be smoothed to the LIS standard of 5\AA and were therefore smoothed to a lower resolution.

Using the lower resolution LIS indices did not change the results much when other objects were smoothed to the lower resolutions for comparison. There was a small (less than error) increase in the indices for the objects that were smoothed for comparison and therefore these lower LIS resolution objects are included for comparison with the 5\AA objects and models.

5.7.4 A Possible CN - Density relation

The origins of the anomalous enhanced CN regions in these objects are uncertain. Here potential correlations are investigated. As well as the previous loose metallicity relation identified here another common trend with these CSSs is probed, their large mass, small radii and therefore high densities.

Figure 5.21 shows the mass and effective stellar mass surface density, Σ (where $\Sigma = M_*/2\pi R^2$, Norris et al. 2014) of the cE sample. There is only a loose correlation seen here where increased mass increases CN abundance, this was expected however due to the relation between mass and metallicity identified in Figure 5.10. The figure showing density shows a stronger correlation, however with many exceptions such as the lower density, CN enhanced cEs at $[\text{MgFe}]' \approx 3$ and the higher density, low CN cE at $cE \approx 0$.

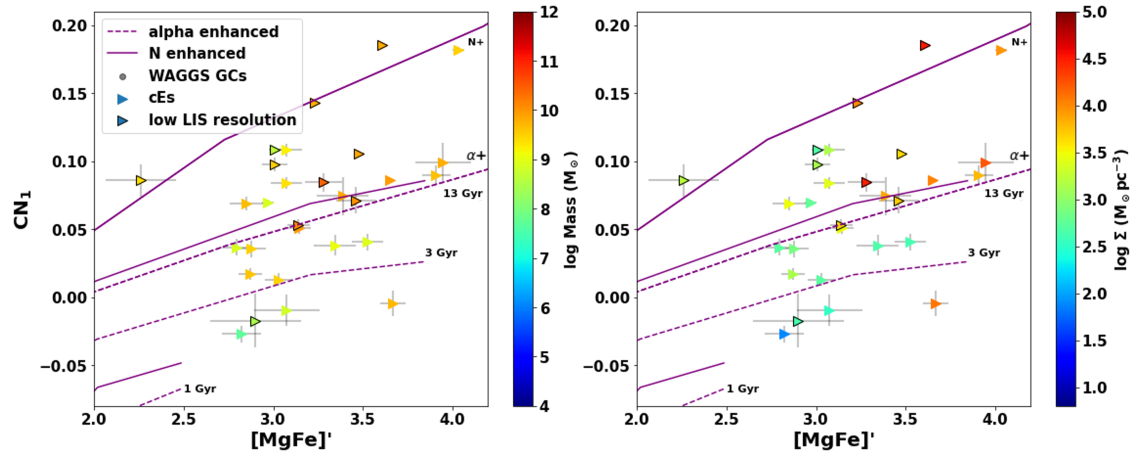


Figure 5.21: These plots are similar to Figure 5.20 showing (left) the stellar mass and (right) the effective stellar mass surface density (Σ).

There may be effects due to age. As stated earlier, the Conroy models indicate that CN region is somewhat sensitive to age where younger ages show weaker CN region abundances. The low CN dense cE is AHcE2 and has a literature age of 5.4 ± 1.64 Gyr (Janz et al., 2016) indicating that it may not have as strong a CN region

as older cEs. However there are younger cEs which have higher CN values and as is shown in this work, age is difficult to measure accurately so age measurements often cannot be deemed reliable. AHcE2 has a low SNR in the CN region (~ 18) which could influence poor index measurements, however, BpPXF fitting where the CN region was excluded to allow the models to fit freely in that region showed no anomalous residuals indicating this object has very little CN.

Figure 5.22 includes all of the CSSs in the CN - $[\text{MgFe}]'$ - Σ plot to further investigate if there is a relation between stellar density and CN (and therefore nitrogen) abundance. It is found that when including GCs and UCDs there becomes a clearer correlation between CN overabundance and density, however, there is still a large scatter with many outliers making it hard to confirm the relation.

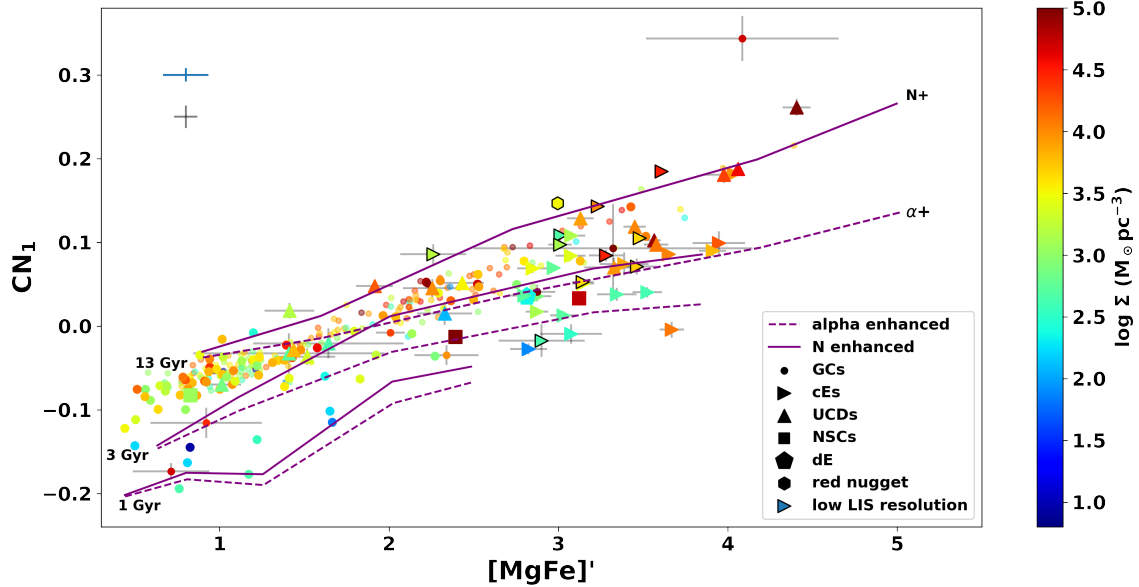


Figure 5.22: Similar to the right panel of Figure 5.21, showing CN_1 against $[\text{MgFe}]'$ for all of the CSSs in the sample and the red nugget and dE with effective stellar mass surface density (Σ) as the colourbar. The grey errorbars in the top left are for the WAGGS GCs, and the blue error bars are for the M31 GCs.

The NSCs actively disagree with the density - CN theory where they are incredibly

CHAPTER 5

stellar dense but show no CN enhancement. This could be because NSCs are well-mixed environments often containing many populations of stars with a polluted ISM (Neumayer, Seth & Böker, 2020). The effect of this may be the ‘drowning out’ of anomalous populations.

When the binned SDSS galaxies (inner 12.5% light) are plotted onto the CN vs $[\text{MgFe}]'$ plot (Figure 5.23) the lower density cEs which are enhanced in nitrogen can be seen to agree with the higher density inner light of the SDSS binned galaxies. The galaxies and the GCs have a clearly different trend as metallicity increases. For low metallicity, the galaxies are not CN enhanced at all but as metallicity increases the inner light of these galaxies show CN enhancement increasing sharply, with levels becoming equivalent to that of the GCs, UCDs and cEs. There is also a trend with increasing Σ as CN becomes more enhanced with densities equivalent to the lower density, CN-enhanced cEs. The enhanced nitrogen in the central regions of these galaxies agrees with N enhancement found in Parikh et al. (2024).

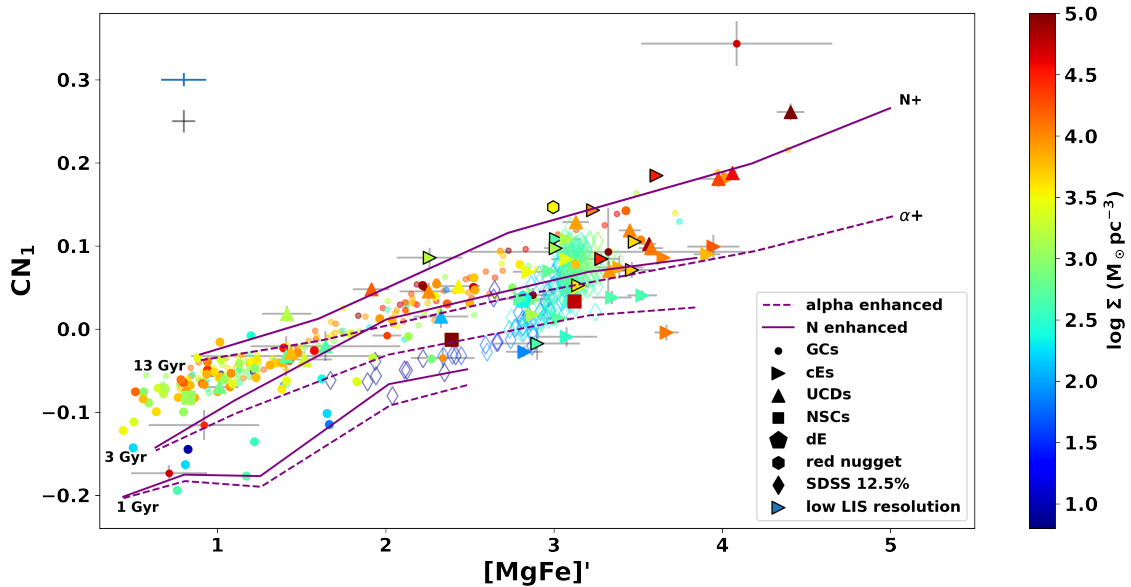


Figure 5.23: The same plot as Figure 5.22, now including SDSS binned galaxies of inner 12.5% light coloured for their stellar density within the 12.5% light radius.

CHAPTER 5

In summary, the CN abundance of the CSS sample has been measured and it has been found that the nitrogen enhancement, found in the MPs of GCs, cannot be used as a definition for GCs or GC-like formation and that a large proportion of CSSs measured (all metal-rich GCs, all UCD, some cEs) show CN enhancements similar to those seen in the MP phenomenon of GCs and CN enhancement is visible even the high-density end of the SDSS galaxies. The origin of the enhancements is as of yet unknown but a loose correlation to stellar density is found, indicating a self-polluting mechanism similar to those discussed for the formation of MPs in GCs (D’Ercole et al., 2008; D’Ercole, D’Antona & Vesperini, 2016; Bekki, 2017; Bastian & Lardo, 2018; Milone & Marino, 2022) may be at work. The next steps for this process would be to quantify the exact amount of N enhancement seen by interpolating the models to different levels of N enhancement and then comparing this value to density to further investigate any correlations.

5.8 OIII Emission in Two Red & Dead Galaxies

A number of objects in the CSS catalogue show signs of ionised gas in their ISM. For example, the WAGGS spectra for the GCs Fornax 5, NGC 1850, NGC 2100, and NGC 6352 all possess evidence of either OIII or hydrogen Balmer line emissions or both. This is due to many factors discussed in Section 3.8.2 such as the presence of a PNe in Fornax 5 or hot A B stars with a gaseous envelope in the foreground for NGC 6352 and NGC 6637. As well as these objects emission is identified in two other objects providing potential evidence for the presence of an active galactic nucleus (AGN).

5.8.1 MRK1216 Red & Dead, Redemption?

MRK1216 is thought to be a local descendant of the distant early-type red-nugget galaxies discovered with Hubble in 2005 (Daddi et al., 2005; Damjanov et al., 2009; Buote & Barth, 2019). These objects are meant to be the end of the first phase of early-type galaxy formation where gas infall leads to a rapid burst of star formation. MRK 1216 is thought to have not formed any stars since its initial star formation and is considered isolated with no major merger history. It is effectively dead of all-star formation. MRK is known to have an episodic AGN (Buote & Barth, 2019) and is actively accreting cold gas onto its central black hole (Fabian et al., 2023).

AGN have optical emission in the hydrogen Balmer lines and in OIII (Comerford et al., 2022) which is what is observed for MRK1216. Through BpPXF, fits were done across the wavelength region containing $H\beta$ and the OIII emission lines at 4959 and 5007 Å at different radial distances either side of the core (Figure 5.24). In each fit pPXF was forced to fit with an emission spectrum at fixed ratios defined by Storey & Hummer (1995); Osterbrock & Ferland (2005). In the central regions, strong emission lines are found which decrease with radial distance. Emission line detection at distances greater than 1.41'' from the core are spurious as their strengths are equivalent to the scatter in the residuals to the fit and are probably due to BpPXF being forced to fit emission spectra where there are not any.

Emissions are observed in both the core spectra and at larger radii. This could be attributed to blurring of the central source due to poor seeing. However, the seeing for the spectra of MRK1216 is very good at $\sim 0.6''$ which could indicate that the emission seen at greater radial distances are real. At the distance of MR1216 (94 Mpc, Walsh et al. 2017) a radial distance of 1.41'' is equivalent to ~ 630 pc where the effective radius of this object is 2300 pc (Walsh et al., 2017). The emission is confined to the central regions of this galaxy but is, however, extended beyond the core light more than the blurring from the seeing can account for. Further study on

CHAPTER 5

this object is needed to identify the cause of the extended emission. The accreted matter in this galaxy (Fabian et al., 2023) could be fuelling star formation in areas around the core.

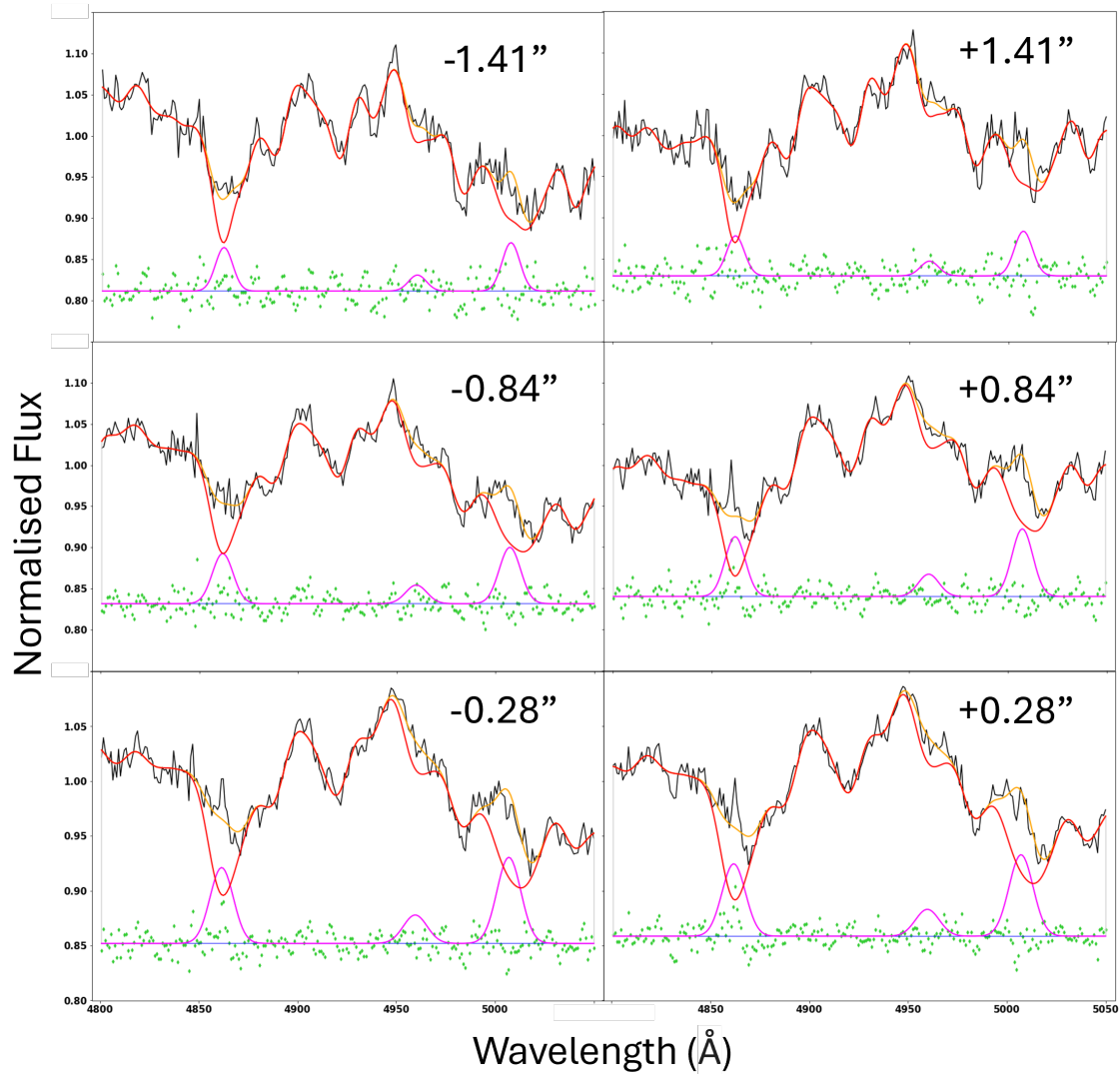


Figure 5.24: BpPXF output plots showing $H\beta$ and $OIII$ emission the wavelength range 4800-5050 \AA at different radii either side of the core (individually de-redshifted). Black is the spectrum while the red line shows the best-fitting model. Orange and pink lines represent the fit over the omitted emission and the residual between the best fit (red) and the masked (orange) fit. The green points show the pixel residual to the combination of the best-fit and the masked fit.

5.8.2 AHcE0 AGN Candidate

One of the cEs identified as isolated (Section 5.5) also shows evidence of $H\beta$ and OIII emission in its spectra. Using the same technique as adopted for MRK1216, the detected emission in this cE was investigated. It is found (Figure 5.25) that there is strong emission in OIII at 5007\AA . However the secondary emission of the OIII doublet at 4959\AA is equivalent to the noise of the best fit so cannot be relied upon, but the existence of the emission at 5007\AA implies the existence of emission 4959\AA . Emission on the $H\beta$ line is also measured. This indicates that there is ionised gas present in the cE.

Due to having equivalent redshifts, the source of the emission is known to be from within the cE. Unfortunately, the spectrum is too low SNR (~ 56 at 5000\AA) and too low spatial resolution for separation by radial distance from the core as was done for MRK1216 so the structural position of the emission source in the cE cannot be measured. However, in Asmus et al. (2020), via a combination of $12\mu\text{m}$ and xray observation, AHcE0 is selected as a potential AGN candidate. AGN have only been found in a few cEs (Rey, Oh & Kim, 2021) and future study on this object with new high SNR spectra is planned to follow up on this.

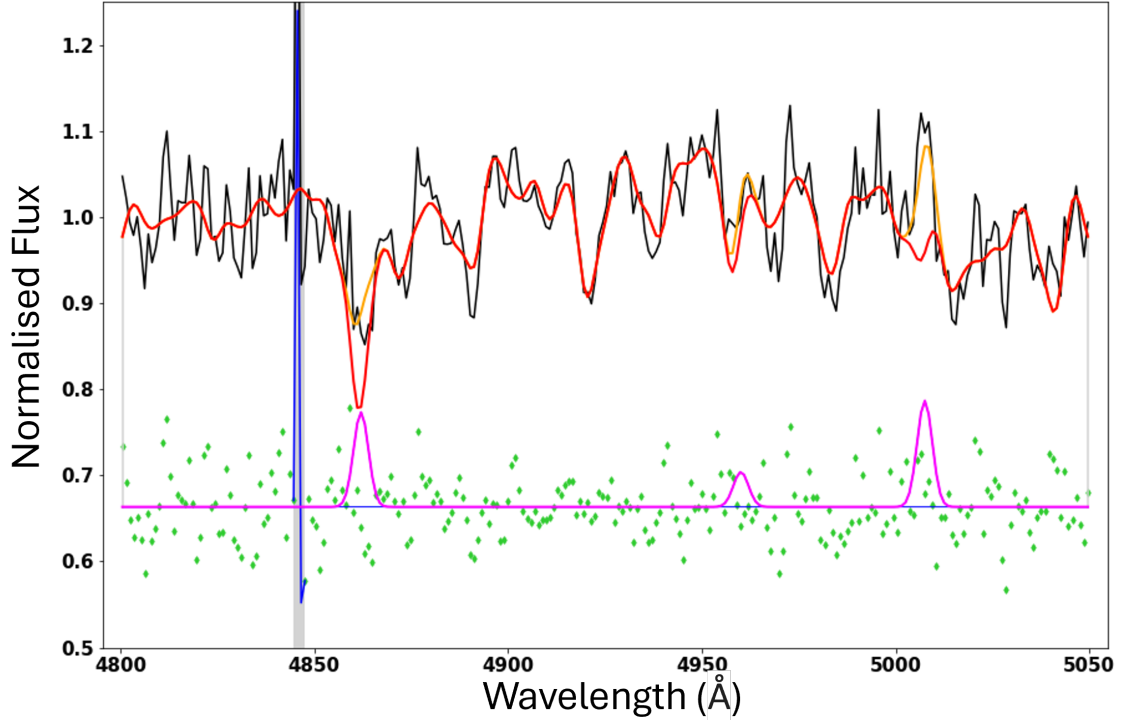


Figure 5.25: Similar to Figure 5.24 showing the BpPXF fit of the integrated spectrum of AHcE0 including the emission line mask. The grey area and blue line indicate a masked bad pixel column.

5.9 Conclusion

This chapter has used the analysis techniques and models developed in the previous chapters on the extended CSS sample prepared for this Thesis. Simple parameters such as mass, radius, age, and metallicity have been utilised to define clear separation for different CSSs and to suggest different formation scenarios. CSS were separated by their known formation and probed for trends separating the systems. For UCDs, it was identified that the UCDs that formed via tidal stripping are all metal-rich compared to those formed at the high mass end of GC formation. One very high metallicity UCD was identified which has not had any published formation theory for it and possible signatures of stripping via a large integrated velocity dispersion were

CHAPTER 5

identified, future work is suggested for this with AO-assisted high-resolution high SNR spectra to accurately measure velocity dispersion at different radial distances (e.g. Ahn et al. 2017).

The formation scenarios of the 4 NSCs in the CSS sample were probed by correlation of mass and metallicity and suggest that both NGC 628-NSC and NGC 2344-NSC formed via in-situ star formation in the cores of their host galaxy while UGC 12732-NSC and EVCC1320 are both the result of GC infalling although UGC 12732-NSC is too low SNR for its metallicity values to be considered as evidence for its formation.

The specific chemical abundances of the CSSs were probed, focusing on the CN region, and found that a large number of CSSs show CN enhancement. No correlation between UCD formation scenario and CN abundance (where almost all appear enhanced) was found along with no correlation with the cEs, where there is a larger spread in CN abundances but with some significantly enhanced in CN. It can be tentatively suggested that there is a correlation with stellar density for this phenomenon although there are many outliers to this suggestion and further work should be undertaken to provide a more in-depth analysis of each object individually.

Finally, in this chapter, two objects have been identified which have ionised gas emission lines in the form of Balmer and OIII emission. Through radial spectral analysis, it was found that the red nugget galaxy shows emission up to ~ 630 pc from its core with an AGN as the source for the ionised gas (although the radial extent of the emission suggests other mechanisms are at work). Similar emissions in the cE AHcE0 were also found and this is considered evidence for the suspected AGN it hosts.

Analysing this many CSSs has highlighted many issues with the techniques and models used. No issue is more pressing than the inability to accurately measure ages between different studies and even different methods in the same study. BpPXF and

CHAPTER 5

LISm χ were used to measure the ages and metallicities of the CSS sample using both sMILES and BSsMILES models with age and metallicity interpolated to every 0.1 (Gyr) and 0.1 (dex) respectively. It is found that while metallicity can be repeatedly returned accurately with both methods and both sets of models age is rarely in good agreement with comparative values to literature with a correlation with increased metallicity and increased residual age. The source of this age - metallicity correlation is potentially due to residuals in the metallicity measurements to literature where a loose correlation to the residuals in age was found. Future work intends to use other high-resolution SSP model spectra to identify if this issue is only common to sMILES and sMILES-based models.

While metallicity was generally returned well, a correlation with literature alpha abundance was found (Figure 5.7) indicating that $[\alpha/\text{Fe}]$ can be returned accurately through these methods. Chapter 3 showed the attempt to measure $[\alpha/\text{Fe}]$ using LISm χ and found it is not returned accurately when compared to literature for many of the WAGGS GCs. However, with the increased number of indices used for LISm χ in this chapter, it is seen that $[\alpha/\text{Fe}]$ can influence the output parameters. Therefore future improvements to this work would involve interactively solving for the $[\alpha/\text{Fe}]$ by estimating $[\alpha/\text{Fe}]$ directly from indices and using those values to select the ideal set SSP models to fit with that object.

For the comparison between sMILES and BSsMILES SSP models it is found that for the M31 GCs, while they reduce in the spread of the output ages compared to literature, literature ages are too varied to be used as a measurement of accuracy. There is little to no agreement between literature measurements of the same GCs. However, the BSsMILES models increase the age estimations of these GCs in the same trend as they do for the WAGGS local GCs indicating that the presence of BSSs in M31 GCs is being at least partially accounted for. For more massive CSSs, the metal-poor objects did not seem to be affected in age with the use of BSsMILES

CHAPTER 5

while the more metal-rich objects generally ‘overestimated’ the age compared to the literature values. Although as was discussed, the literature age values are generally not reliable for comparison. The metallicity measurements with BSsMILES models show negligible differences.

The analysis of the full zoo of CSSs in this chapter has highlighted how none of these objects can be thought of as simple stellar populations and even the smallest are subject to phenomena which cannot be adequately modelled by modern model spectra.

Chapter 6

Thesis Overview and Discussion

This thesis assembled, reduced and analysed high SNR spectroscopy of a sample of 150 CSSs. To this, it added literature line index measurements of 313 additional CSSs. The combined sample ranged from the least massive CGs to massive compact ellipticals and beyond. This is a very large sample which can provide excellent research opportunities for the CSS community. For this project, the sample has provided an excellent probe into the analyses of CSSs (and perhaps stellar populations in general), highlighting the issues in the measurement of their integrated light spectra which are common between all CSSs, and providing signatures which in some cases can help discriminate between different formation scenarios which cannot be distinguished via the object's outward appearance (such as deciphering the star formation rate or identifying anomalous chemical signatures indicating formation history and evolution). This chapter will explore, summarise and suggest improvements to the work produced in this thesis and conclude on what has been learnt.

For the data catalogue, a large percentage of sources of data did not provide reduced data. Because of this, a large part of the initial work of this project was spent producing a data reduction pipeline which could reduce MODS 1 and MODS 2 spectra. This pipeline was later adapted for the spectra from GHTS when its own reduction pipeline failed to reduce the spectra adequately. It should be highlighted

that the custom reduction pipeline produced for this thesis allowed, for the first time, analysis of MODS 2 spectra which had never been reduced before, increasing the SNR of the MODS data considerably.

6.1 Methods of CSS Spectral Analysis

In this Thesis, three methods for the analysis of the integrated light spectra of compact stellar systems were introduced and used them on a large sample of local globular clusters and then two of them on the rest of the sample.

Looking at these methods first with the local GC sample, the key finding is that age was underestimated in all of the objects with an increasing trend in age underestimation as metallicity decreased. This is a common problem in spectral analysis of GCs (Puzia, Perrett & Bridges, 2005; Koleva et al., 2008; Cervantes & Vazdekis, 2009; Usher et al., 2019b; Boecker et al., 2020; Goudfrooij & Asa'd, 2021; Leath et al., 2022) where Boecker et al. (2020) found a similar age value to this work using full spectral fitting of the same WAGGS data for NGC 6715. For high SNR, metal-rich ($[\text{Fe}/\text{H}] \geq -1.0$) age was returned relatively well compared to the other data. however there was still a general age underestimation for the old GCs. For the more massive CSSs problems were also found with age estimation. However, comparisons with the literature here are less reliable than with the GC sample as the more massive CSSs can only be measured via their integrated light spectra. It therefore cannot be concluded, for the non-WAGGS CSSs, that ages measured in this work are poorly estimated. For CSS analysis three methods were used, here they are discussed.

6.1.1 BpPXF

The BpPXF method utilises full spectral fitting through the Python package pPXF. This method is a very useful tool for understanding both chemical abundances and stellar populations/star formation history. While age was measured poorly, with the aforementioned age underestimation-metallicity relation. BpPXF measured metallicity well but was not designed to measure alpha abundance. Future work plans to utilise CSS $[\alpha/\text{Fe}]$ values to further refine the metallicity estimations selecting SSP models with $[\alpha/\text{Fe}]$ values closest to literature (or values measured through other means such as individual line index measurements).

While it is important to acknowledge that age cannot necessarily be accurately measured with BpPXF, the age-metallicity mass fraction plots (e.g. Figure 5.14 are powerful tools for the extraction of star formation histories and metallicity spreads which are key probes into CSS formation and therefore essential for any formation-based object categorisation (i.e. Section 5.5.2). The spectrum of the best-fitting combination of SSP models which the mass-fraction plots represent is another powerful tool BpPXF provides. It has been used in this project to identify chemically anomalous regions where there are large residuals between the best fit and the observed spectrum. It has also identified spectral emission in what could otherwise have been classed as noise or missed entirely (i.e. MRK1216 and AHcE0).

The downside of BpPXF, for this project, is that it requires high amounts of customisation for each observed object where poor-fitting regions and emission lines must be masked. When very large samples are used, BpPXF can take a considerable amount of time. This is especially noticeable with lower SNR data where the regularisation iteration process takes significant time. As well as this, estimating uncertainty values for large sets of data takes a considerable amount of time and in this thesis, Monte Carlo simulations had to be run on only a representative sample due to time limitations. In future, work will be undertaken to assess the uncertainties

CHAPTER 6

with BpPXF and other methods (i.e. bootstrapping) will be utilised to probe the most efficient way to calculate uncertainty values.

Overall BpPXF is a very useful tool in an astronomer’s arsenal and future work will undoubtedly include BpPXF as one of its core analysis tools.

6.1.2 SpPXF

SpPXF was initially implemented in order to find a method which could provide BpPXF with initial $[\alpha/\text{Fe}]$ estimations but its design also allowed it to identify a best-fitting age and metallicity value. SpPXF used the same base program as BpPXF but where BpPXF used the combination of SSP models to find the best fit, SpPXF used the reduced χ^2 of the residuals between the object spectrum and each SSP model in the model library. This method also did not estimate age well comparatively to the literature for galactic GCs but estimated metallicity well and in the ‘Narrow’ wavelength range returned alpha values accurate to literature (within error) for the majority of GCs with published $[\alpha/\text{Fe}]$ values.

Unfortunately, compared to BpPXF, SpPXF does not return as much information as can be extracted with BpPXF (i.e. star formation histories and chemical abundance anomalies) and the increased run time compared to the well-optimised, well-supported “basic” pPXF programme makes this method less preferable. If further work were to be undertaken with SpPXF more attention would be taken into making the process more efficient. The initial improvement would involve narrowing down the best fitting model selection via active analysis of each object’s reduced χ^2 value where one model is selected, the adjacent (+ or - a single unit in age, metallicity, $[\alpha/\text{Fe}]$) models are measured, and the model with the lowest reduced χ^2 value is then selected, repeating the process until the model with the lowest reduced χ^2 is selected. Although this method can easily fall into the trap of a local minimum where the best model is not selected, more work is needed on this topic.

CHAPTER 6

Comparatively with BpPXF and LISm χ , SpPXF is the slowest method of CSS analyses. While SpPXF did return $[\alpha/\text{Fe}]$ values with the most accuracy (to literature) it was found that LISm χ may also be able to return $[\alpha/\text{Fe}]$ accurately with the correct combination of indices. However, the next steps will be to simply measure $[\alpha/\text{Fe}]$ via the LIS index values of alpha elements. Therefore the other two methods are preferred, hence SpPXF is not used for analysis after Chapter 3.

6.1.3 LISm χ

The third method introduced in Chapter 3 is LISm χ , this method used a similar reduced χ^2 to SpPXF but instead of using the full spectrum it used a few selected indices. Only four indices were selected initially for GC analysis, H β , Fe5270, Fe5335, & Mg $_b$. These indices were selected to avoid potentially chemically anomalous features and to probe the simplest combination of indices for the adequate acquisition of CSS parameters (age, metallicity, alpha abundance).

The results of LISm χ with galactic GCs show the same age underestimations apparent with the other methods while also showing good metallicity agreement with literature and with the other methods. Due to the mostly good $[\alpha/\text{Fe}]$ selection of the Narrow wavelength region with SpPXF, it was hoped that the four index LISm χ method would also return good $[\alpha/\text{Fe}]$. It was found that while most of the GCs with published values it returned alpha within uncertainty, there was a large scatter equivalent to that seen for the larger wavelength ranges used with SpPXF. If the analysis was done again only models with $0.1 \leq [\alpha/\text{Fe}] \leq 0.4$ would be included to match published GC alpha abundances. Clearly (Figure 3.24), in some cases the preferred alpha value is in the extreme lows or extreme highs. In Chapter 5 LISm χ was used with a larger range of indices but only using models with a fixed alpha abundance, and a correlation with metallicity residual (measured - literature) was found, indicating that with more indices, $[\alpha/\text{Fe}]$ may be returned well. In future,

CHAPTER 6

the aim is to use more indices and models with a range of $[\alpha/\text{Fe}]$ values with all of the objects in the CSS sample to firstly identify the alpha abundance of these objects and also to get more accurate and precise metallicity measurements.

LISm χ was very quick to run, and if future work used the same SSP model selection technique suggested for SpPXF, the run-time could be reduced even further. Due to the shorter runtime compared to BpPXF and SpPXF, it is possible to use this method with a much larger SSP sample and run large iteration Monte Carlo simulations for each CSS observed.

Out of the three methods used for the analysis of CSSs in this thesis, BpPXF provides the most detail in terms of star formation histories and chemical abundance anomalies while LISm χ provides ages and metallicities similar to BpPXF for each object but is considerably quicker to run and is better for quick analysis of large datasets. SpPXF provides measurements equivalent to LISm χ but takes considerably more time to run and is therefore less ideal for large datasets such as in this thesis and therefore in any further work, SpPXF will not be used and the use of BpPXF and LISm χ will be used where appropriate.

6.2 BSsMILES

In order to compensate for the presence of blue straggler stars in CSSs, a fraction of ‘blue’ stellar light was introduced into the sMILES SSP models used in this thesis. These new models are named BSsMILES and they come in a range of BSS contribution percentages to probe the BSS abundance of the CSS sample. It was found that in the majority of cases for GCs where BSsMILES models were used, the higher the BSS percentage the lower the age residual to literature, and with high metallicity ($[\text{Fe}/\text{H}] \geq -1.0$) age became quite well measured for GCs. Age estimations improved up to 10% BSS contribution, where effects on age decrease in magnitude and the metallicity becomes more enhanced. In general, when these

CHAPTER 6

models are used the metallicity increases and this is possibly due to the theoretical stars being used having, a) enhanced alpha abundance of $[\alpha/\text{Fe}] = 0.4$ where the models used had $[\alpha/\text{Fe}] = 0.3$, b) in low metallicity models young low metallicity stars were not available to add to the models, and c) where a trade-off was made between the residual to the poorly fit age indicators and metallicity lines, where models with larger metallicity lines provided smaller overall χ^2 values. All three of these factors would cause metallicity overestimation. However, the increase in metallicity between 0% and 10% BSS contribution for GCs was equivalent to the scatter in the residual to literature, indicating that even with mixed metallicity levels in the models, metallicity is generally measured well. In this work it is found that 5% BSS contribution best describes the GCs in the sample, however, it should be acknowledged that due to many aspects, such as field-of-view differences between data sources and objects and different CSS formation histories, each object in the sample will have different BSS contribution to the integrated light.

To improve upon these models, future work will adopt a number of things. Firstly the Coehlo theoretical stars would simply be interpolated between $[\alpha/\text{Fe}] = 0.0$ and 0.4 to match the alpha abundance of the models the stars are being added to. As well as this, to accommodate the BSS populations of metal-poor SSPs, a search will be done for more metal-poor hot stars such as those of Knowles et al. (2021) which were developed for the sMILES SSP models, or the stars of Allende Prieto et al. (2018). It was initially not considered to add low metallicity stars to the BSsMILES models because it was determined that the age underestimations at metallicities of $[\text{Fe}/\text{H}] \leq -1.0$ dex were due to BHB stars which have been modelled well in other studies (e.g. Cabrera-Ziri & Conroy 2022). However, this is an avenue that is intended to be explored in future.

Another aspect of the BSsMILES models is that they have a lower age cutoff of 3 Gyr, this was done to represent an increased BSS percentage of the core light

CHAPTER 6

of CSSs as they age (Chatterjee et al., 2013; Ferraro et al., 2018; Portegies Zwart, 2019). However, this hindered analysis of the full zoo of CSSs available in this thesis (i.e. young, Magellanic Cloud GCs or the young massive GCs NGC7252-W3 & W30). Therefore, it is suggested that future iterations of these models probe the BSS populations of these young clusters and give a more representative sample of BSS contribution of the integrated light at different ages, and (ideally) at different field-of-views to match those observed with the spectrograph to take into account the bimodality of BSS distribution in GCs Sollima & Ferraro (2019) and the distributions in CSSs. In order to do this, however, full, high-resolution self-consistent modelling of CSSs formation and evolution would need to be undertaken, where the BSSs formed via binary interaction and collisions and BHB stars are modelled accurately as the system ages. This is outside the scope of this project however, what has been shown is how when the light of BSSs are taken into account, the measured ages of GCs improve relative to the literature and the measured ages of more massive, more metal-rich CSSs increase similarly to the ages of GCs.

For CSSs more massive than GCs the BSsMILES models increase their age estimations (especially for the higher metallicity cEs). The literature values of age for these objects are questionable as they use models which do not include BSS fractions. Work needs to be done to understand BSS prevalence in CSSs and in galaxies in general. Therefore the it is suggested that future iterations of these models which use the population simulations described before also look into BSS fractions in high-mass systems, looking for a density-BSS fraction relation, following the logic of increased stellar density increases BSS populations due to increased numbers of stellar collisions. Also, considering that BSSs form via binary interactions, every stellar environment will possess “blue-straggler” stars which, in massive, well-mixed stellar systems, will appear non-anomalous. If BSSs formed via binary interactions are prevalent in these objects then age estimations using SSP

models will undoubtedly underestimate system age.

6.3 CN Overabundance in CSSs

During the BpPXF analysis of the CSS sample, it was noted how many objects had poorly fit CN regions. This poor fitting was in common with those seen in GCs as signatures of the MPs phenomena where there is a spread in the chemical abundances in the supposed single stellar population of GCs. All old (and higher metallicity) GCs show nitrogen enhancement visible via the CN LIS index, and therefore it is expected that any old CSS which does not show CN enhancement can probably be ruled out as having formed as being formed at the massive end of GC formation.

However, it was found that there is not a correlation with GC-like formation and CN abundance but there is a general CN overabundance for many CSSs. All UCDs show strong CN enhancement despite their formation scenario and from these objects alone it is concluded that the nitrogen enhancement, found in the MPs of GCs, cannot be used as a definition for GCs or GC-like formation. As well as UCDs, it was also found that the more massive CSS, cEs, also show enhanced nitrogen. It is tentatively suggested that a correlation with stellar density for this phenomenon although there are many outliers to this suggestion with some low-density cEs being enhanced in the CN region. When the inner light of SDSS galaxies are included however, they agree with the cEs and show similar CN enhancements with similar densities to the least dense cEs indicating that that even the most massive galaxies show similar abundance anomalies seen in the CSS sample. Recent work has shown how the inner cores of some galaxies can be enhanced in nitrogen (Parikh et al., 2024) agreeing with the findings in this work for SDSS galaxies. The enhanced nitrogen has been suggested to be due to differences in the IMF in the central regions (Parikh et al., 2024). It is possible that the enhanced nitrogen of GCs, UCDs and cEs could

be due to the same mechanisms causing enhanced nitrogen in the cores of massive galaxies as well as the MP mechanisms suggested in Section 1.3 (if they are not the same mechanisms all together) and further work should be undertaken to analyse any density - chemical abundance correlations.

Further analysis of potential anomalous regions common in CSSs is planned, where extended wavelength ranges may expose more regions in the integrated spectra which BpPXF identifies as anomalous. Figure 5.16 also shows other (smaller) poor-fitting regions near the CN region, and work to identify the elements associated with other poor-fitting regions should be done to possibly identify other signatures of chemical abundance issues.

6.4 Anomalous Objects

The work in Chapter 5 highlighted several objects which showed anomalous behaviour in their ages, metallicities or chemical abundances. Three objects are highlighted where further analysis has been done.

For the UCD, UCD-FORS 45 (CSS-969 in this works catalogue) its anomalously high metallicity for its mass relative to the other UCDs is noted (UCD-FORS 45 is also the UCD with the largest CN overabundance). Because a trend in higher metallicity UCDs being the result of tidal stripping was noted, it is speculated that this object may also have a similar formation. While BpPXF analysis does not show any extended star formation or metallicity spreads common in stripped objects (i.e. Ω cen, Fellhauer 2004; Seth et al. 2021). Xshooter provided high-resolution spectra and through BpPXF, a large integrated velocity dispersion of $\sigma = 37.2 \pm 1.4 \text{ kms}^{-1}$ was measured which is equivalent to the integrated velocity dispersions of two more massive UCDs which possess SMBHs, VUCD3 and M59cO (Ahn et al., 2017). This indicates that there could be a SMBH in the core of this object and follow-up high-resolution AO assisted IFU spectroscopy of this object is suggested to allow

CHAPTER 6

for spatial analysis to determine velocity dispersions in the very central regions and calculate the mass of a potential centrally located massive black hole which would indicate a stripped formation history.

Another object which was analysed was not necessarily a CSS, having mass equivalent to the most massive galaxies (Walsh et al., 2017). It was added to the SOAR observation list in an attempt to understand compact nugget galaxies and their relationship with CSSs. During regular BpPXF analysis of this object, potential OIII emission lines in the spectrum were detected which, when excluded from the fit using pPXF’s gas emission masking routine, showed large emission which extends from the core to a radius of ~ 630 pc. Emission in the core is likely due to an AGN (Walsh et al., 2017; Fabian et al., 2023) however, the presence of OIII and Balmer line emissions at radii outside of the core likely indicates star formation taking place, if this is true, then this object cannot be considered a dead (in star formation) galaxy like red nuggets are assumed to be (Martín-Navarro, van de Ven & Yıldırım, 2019). In future, it is suggested that obtaining AO-assisted IFU spectroscopy (similarly to UCD-FORS 45) of this object be done in order to investigate the radial distribution of the emission spectra in more detail probing to see if star formation is indeed happening.

The final object that was investigated was the cE, AHcE0. This object had relatively low SNR for MODS spectra but there was clear OIII emission at 5007 Å and a potentially infilling of the H β absorption line in the BpPXF fit indicating emission. Unfortunately, the SNR of the spectrum of this object is too low for the radial analysis to observe where (spatially) in the cE the emission is coming from, so similarly to MRK1216 and UCD-FORS 45 further observations of this object are proposed. If the emission is centrally located this could be the evidence for the first ever AGN in the core of a cE.

6.5 Final Conclusions

Compact Stellar systems (CSSs) are small, but incredibly stellar dense objects and cover a broad range of object types. In Chapter 2 the large data sample available for this project was introduced, with detail on how reduction pipelines for much of this data were produced, and how new data has been observed and reduced via GHTS and with never before reduced MODS2 spectral data. Chapter 3, introduced and used multiple techniques to analyse the integrated light spectrum of GCs finding that at different wavelength ranges age is poorly estimated, metallicity is well estimated and alpha abundance is well estimated only under certain conditions. In Chapter 4 the BSsMILES SSP models were created which attempt to account for populations of BSSs which are present in potentially all stellar systems (due to formation via binary interactions). When using these models, a general increase in the age estimations for the majority of the CSS sample is found which decreases the residual between measured age and literature age for local GCs where literature ages can be trusted. Using what was learnt from the previous two chapters, in Chapter 5 other parameters of CSSs such as their mass, radius, metallicity and specific chemical abundances are analysed. Mass-metallicity correlations similar to Norris et al. (2014); Janz et al. (2016); Ma et al. (2016) were found. Potential correlations between density and CN abundance were found and key chemical features in the spectra of these objects which indicate formation scenario for UCDs were identified, the potential presence of star formation in a red nugget and potentially the presence of an AGN in a cE. It is concluded that CSSs are individually unique and that the complexity of the information needed for “simple” single stellar population models to accurately describe even the most “simple” GCs shows how these objects are complex with many different mechanisms and formation scenarios creating unique parameters which differ from object to object. Compact stellar systems are small but powerful, and as has been shown, they are far from simple.

Bibliography

- Abadi M. G., Navarro J. F., Steinmetz M., 2006, *MNRAS*, 365, 747
- Agarwal M., Milosavljević M., 2011, *ApJ*, 729, 35
- Aguado D. S. et al., 2019, *ApJS*, 240, 23
- Ahn C. P. et al., 2018, *ApJ*, 858, 102
- , 2017, *ApJ*, 839, 72
- Alfaro-Cuello M. et al., 2020, *ApJ*, 892, 20
- Allende Prieto C. et al., 2018, *A&A*, 618, A25
- Anderson J. et al., 2008, *AJ*, 135, 2055
- Anguiano B. et al., 2015, *MNRAS*, 451, 1229
- Antonini F., 2013, *ApJ*, 763, 62
- Antonini F., Barausse E., Silk J., 2015, *ApJ*, 812, 72
- Arca-Sedda M., Capuzzo-Dolcetta R., 2014, *ApJ*, 785, 51
- Asmus D. et al., 2020, *MNRAS*, 494, 1784
- Bacon R. et al., 2010, in *Society of Photo-Optical Instrumentation Engineers (SPIE) Conference Series*, Vol. 7735, *Ground-based and Airborne Instrumentation for Astronomy III*, McLean I. S., Ramsay S. K., Takami H., eds., p. 773508
- , 2001, *MNRAS*, 326, 23
- Baldry I. K., Bland-Hawthorn J., Robertson J. G., 2004, *PASP*, 116, 403
- Banister J. T., 2020, University of Central Lancashire, MSc Thesis
- Barden S. C. et al., 2000, *PASP*, 112, 809

Barkhouser R. H., Arns J., Gunn J. E., 2014, in Society of Photo-Optical Instrumentation Engineers (SPIE) Conference Series, Vol. 9147, Ground-based and Airborne Instrumentation for Astronomy V, Ramsay S. K., McLean I. S., Takami H., eds., p. 91475X

Bastian N., Lardo C., 2018, ARA&A, 56, 83

Baumgardt H., De Marchi G., Kroupa P., 2008, ApJ, 685, 247

Baumgardt H. et al., 2022, MNRAS, 510, 3531

Baumgardt H., Hilker M., 2018, MNRAS, 478, 1520

Bekki K., 2007, PASA, 24, 77

—, 2017, MNRAS, 467, 1857

Bekki K. et al., 2004, , 610, L93

Bekki K., Couch W. J., Drinkwater M. J., 2001, ApJL, 552, L105

Bekki K. et al., 2003, MNRAS, 344, 399

Bekki K., Couch W. J., Shioya Y., 2006, ApJL, 642, L133

Bekki K., Freeman K. C., 2003, MNRAS, 346, L11

Bekki K., Stanimirović S., 2009, , 395, 342

Bentley R. O. et al., 2022, ApJ, 925, 77

Bertola F., Capaccioli M., Oke J. B., 1982, ApJ, 254, 494

Boecker A. et al., 2020, ApJ, 896, 13

Breen P. G., 2018, MNRAS, 481, L110

Bruzual G., Charlot S., 2003, MNRAS, 344, 1000

Buote D. A., Barth A. J., 2019, ApJ, 877, 91

Burstein D. et al., 1984, ApJ, 287, 586

Buzzoni A., Mantegazza L., Gariboldi G., 1994, AJ, 107, 513

Byler N. et al., 2017, ApJ, 840, 44

Cabrera-Ziri I., Conroy C., 2022, MNRAS, 511, 341

Caldwell N., Romanowsky A. J., 2016, ApJ, 824, 42

Caldwell N. et al., 2011, *AJ*, 141, 61

Cappellari M., 2017, *MNRAS*, 466, 798

—, 2023, *MNRAS*, 526, 3273

Cappellari M., Emsellem E., 2004, *PASP*, 116, 138

Cappellari M. et al., 2011, *MNRAS*, 413, 813

Capuzzo-Dolcetta R., 1993, *ApJ*, 415, 616

Capuzzo-Dolcetta R., Miocchi P., 2008, *ApJ*, 681, 1136

Carollo C. M., Stiavelli M., Mack J., 1998, *AJ*, 116, 68

Carrera R. et al., 2008, *AJ*, 135, 836

Carretta E., 2021, *A&A*, 649, A154

Cenarro A. J. et al., 2008, *ApJL*, 689, L29

—, 2007, , 374, 664

Cervantes J. L., Vazdekis A., 2009, *MNRAS*, 392, 691

Cezario E. et al., 2013, *A&A*, 549, A60

Chatterjee S. et al., 2013, *ApJ*, 777, 106

Chevalier R. A., Oegerle W. R., 1979, *ApJ*, 227, 398

Chiboucas K. et al., 2011, , 737, 86

Childress M. J. et al., 2014, *Astrophys. Space Sci.*, 349, 617

Chilingarian I. et al., 2007, *A&A*, 466, L21

—, 2009, *Science*, 326, 1379

Chilingarian I., Zolotukhin I., 2015, *Science*, 348, 418

Chilingarian I. V., Cayatte V., Bergond G., 2008, *MNRAS*, 390, 906

Choi J. et al., 2014, *ApJ*, 792, 95

—, 2016, *ApJ*, 823, 102

Chung C., Lee Y.-W., Pasquato M., 2016, *MNRAS*, 456, L1

Clemens J. C., Crain J. A., Anderson R., 2004, in Society of Photo-Optical Instrumentation Engineers (SPIE) Conference Series, Vol. 5492, Ground-based Instrumentation for Astronomy, Moorwood A. F. M., Iye M., eds., pp. 331–340

Code A. D., Welch G. A., 1979, *ApJ*, 228, 95

Coelho P. R. T., 2014, *MNRAS*, 440, 1027

Colucci J. E. et al., 2009, *ApJ*, 704, 385

—, 2012, *ApJ*, 746, 29

Colucci J. E., Bernstein R. A., McWilliam A., 2017, *ApJ*, 834, 105

Comerford J. M. et al., 2022, *ApJ*, 927, 23

Conroy C., 2013, *ARA&A*, 51, 393

Conroy C., Graves G. J., van Dokkum P. G., 2014, *ApJ*, 780, 33

Conroy C., van Dokkum P., 2012, *ApJ*, 747, 69

Conroy C. et al., 2018, *ApJ*, 854, 139

Costantin L., 2022, in *Inward Bound: Bulges from High Redshifts to the Milky Way*, p. 19

Côté P. et al., 2004, *ApJS*, 153, 223

—, 2006, *ApJS*, 165, 57

Crnojević D. et al., 2016, *ApJ*, 823, 19

Culpan R., Pelisoli I., Geier S., 2021, *A&A*, 654, A107

da Silva R. L., Fumagalli M., Krumholz M., 2012, *ApJ*, 745, 145

Dabringhausen J., Kroupa P., Baumgardt H., 2009, *MNRAS*, 394, 1529

Daddi E. et al., 2005, *ApJ*, 626, 680

Damjanov I. et al., 2009, *ApJ*, 695, 101

Davies M. B., Benz W., Hills J. G., 1993, *ApJ*, 411, 285

Davison T. A., 2021, University of Central Lancashire, PhD Thesis

Davison T. A. et al., 2021a, *MNRAS*, 502, 2296

—, 2021b, *MNRAS*, 507, 3089

De Angeli F. et al., 2005, *AJ*, 130, 116

de Grijs R., 2001, *A&G*, 42, 4.12

De Marco O. et al., 2005, *ApJ*, 632, 894

de Mink S. E. et al., 2009, *A&A*, 507, L1

Deeley S. et al., 2023, *MNRAS*, 525, 1192

Deng L. et al., 1999, *ApJ*, 524, 824

D’Ercole A., D’Antona F., Vesperini E., 2016, *MNRAS*, 461, 4088

D’Ercole A. et al., 2008, *MNRAS*, 391, 825

Dias B. et al., 2016, *A&A*, 590, A9

Dib S. et al., 2022, *A&A*, 664, A145

Dotter A., 2016, *ApJS*, 222, 8

Dotter A. et al., 2010, , 708, 698

Douglas N. G. et al., 2002, *PASP*, 114, 1234

Dresbach F. et al., 2022, *ApJ*, 928, 47

Drinkwater M. J. et al., 2003, *Nature*, 423, 519

—, 2000, *PASA*, 17, 227

Du M. et al., 2019, *ApJ*, 875, 58

ESO/VISTA, 2017, eso1714a. [Online; accessed January, 2024]

Fabian A. C. et al., 2023, *MNRAS*, 524, 716

Fabricant D. et al., 2005, *PASP*, 117, 1411

Fahrion K. et al., 2022, *A&A*, 667, A101

—, 2021, *A&A*, 650, A137

Faifer F. R. et al., 2011, *MNRAS*, 416, 155

Falcón-Barroso J. et al., 2011, *A&A*, 532, A95

Fan Z. et al., 2016, *AJ*, 152, 208

Fan Z., de Grijs R., Zhou X., 2010, *ApJ*, 725, 200

Fare A., Webb J. J., Sills A., 2018, *MNRAS*, 481, 3027

Fellhauer M., 2004, arXiv e-prints, astro

Fellhauer M., Kroupa P., 2002, *MNRAS*, 330, 642

—, 2005, *MNRAS*, 359, 223

Ferraro F. R. et al., 2009, *Nature*, 462, 1028

—, 2018, *ApJ*, 860, 36

—, 2023, *Nat. Commun.*, 14, 2584

Ferraro F. R. et al., 2006, *ApJ*, 647, L53

Forbes D. A. et al., 2018, *Proc. R. Soc. Lond.*, 474, 20170616

Forbes D. A., Bridges T., 2010, *MNRAS*, 404, 1203

Forbes D. A. et al., 2020, *MNRAS*, 497, 765

—, 2008, *MNRAS*, 389, 1924

—, 2014, *MNRAS*, 444, 2993

Fregeau J. M. et al., 2002, *ApJ*, 570, 171

Freitag M., Benz W., 2005, *MNRAS*, 358, 1133

Gaia Collaboration et al., 2018, *A&A*, 616, A10

Garro E. R. et al., 2020, *A&A*, 642, L19

Ge J. et al., 2018, *MNRAS*, 478, 2633

Genzel R., Eisenhauer F., Gillessen S., 2010, *RMP*, 82, 3121

Georgiev I. Y. et al., 2016, *MNRAS*, 457, 2122

Gilbert K. M. et al., 2012, *ApJ*, 760, 76

—, 2014, *ApJ*, 796, 76

—, 2018, *ApJ*, 852, 128

Gnedin O. Y., Ostriker J. P., Tremaine S., 2014, *ApJ*, 785, 71

GoerdT T. et al., 2008, MNRAS, 385, 2136

Goodman M., Bekki K., 2018, MNRAS, 478, 3564

Gorgas J. et al., 1993, ApJS, 86, 153

Göttgens F. et al., 2019, A&A, 626, A69

Goudfrooij P., Asa'd R. S., 2021, MNRAS, 501, 440

Goudfrooij P. et al., 2014, ApJ, 797, 35

Graczyk D. et al., 2013, ApJ, 780, 59

Grasser N. et al., 2023, arXiv e-prints, arXiv:2312.09850

Gratton R. et al., 2019, A&A Rev., 27, 8

Gratton R., Sneden C., Carretta E., 2004, ARA&A, 42, 385

Graves G. J., Schiavon R. P., 2008, ApJS, 177, 446

Gross P. G., 1973, MNRAS, 164, 65

Hannon S. et al., 2019, MNRAS, 490, 4648

Harris W. E., 1991, ARA&A, 29, 543

—, 1996, AJ, 112, 1487

—, 2010, arXiv e-prints, arXiv:1012.3224

Harris W. E., van den Bergh S., 1981, AJ, 86, 1627

Herschel W., 1789, Philosophical Transactions of the Royal Society of London, 79, 212

Hilker M., 2009, Reviews in Modern Astronomy, 21, 199

Hilker M. et al., 1999, A&AS, 134, 75

Hilker M., Richtler T., 2000, A&A, 362, 895

Hills J. G., Day C. A., 1976, ApLetters, 17, 87

Horne K., 1986, PASP, 98, 609

Hu T., Peng Q., 2008, ApJ, 681, 96

Huxor A. P. et al., 2011a, in EAS Publications Series, Vol. 48, EAS Publications Series, Koleva M., Prugniel P., Vauglin I., eds., pp. 257–258

—, 2011b, MNRAS, 414, 3557

Janz J. et al., 2016, MNRAS, 456, 617

Johnson H. L. et al., 1966, Communications of the Lunar and Planetary Laboratory, 4, 99

Ju J. et al., 2024, ApJS, 270, 11

Kafle P. R. et al., 2013, MNRAS, 430, 2973

Kang J., Lee M. G., 2021, ApJ, 914, 20

Kim H.-S. et al., 2016, ApJS, 227, 24

Kim J. J., Lee Y.-W., 2018, ApJ, 869, 35

Kim S. et al., 2020, ApJ, 903, 65

King I. R. et al., 2012, AJ, 144, 5

Kirch G., 1681, 47

Knowles A. T. et al., 2021, MNRAS, 504, 2286

—, 2023, MNRAS, 523, 3450

Kodaira K., Philip A. G. D., 1984, ApJ, 278, 201

Koleva M. et al., 2008, MNRAS, 385, 1998

Koo J.-R. et al., 2022, ApJ, 925, 35

Korn A. J., Maraston C., Thomas D., 2005, A&A, 438, 685

Kravtsov V. et al., 2022, MNRAS, 512, 2936

Kremer K. et al., 2020, ApJ, 903, 45

Krogsrud D. A., Sandquist E. L., Kato T., 2013, ApJL, 767, L27

Kronberg C., Frommert H., 2019, Milky way globular clusters. First published in June 2011. last modified on 06/01/2019

Kroupa P., 2001, MNRAS, 322, 231

Larsen S. S., 2008, A&A, 477, L17

- Larsen S. S. et al., 2015, *ApJ*, 804, 71
- , 2014, *ApJ*, 797, 15
- Le Borgne D. et al., 2004, *A&A*, 425, 881
- Le Fèvre O. et al., 2003, in *Society of Photo-Optical Instrumentation Engineers (SPIE) Conference Series*, Vol. 4841, *Instrument Design and Performance for Optical/Infrared Ground-based Telescopes*, Iye M., Moorwood A. F. M., eds., pp. 1670–1681
- Leath H. J. et al., 2022, *MNRAS*, 512, 548
- Lee H.-c., Worthey G., 2005, *ApJS*, 160, 176
- Leigh N., Sills A., Knigge C., 2007, *ApJ*, 661, 210
- Lin D. N. C., Murray S. D., 1991, in *Astronomical Society of the Pacific Conference Series*, Vol. 13, *The Formation and Evolution of Star Clusters*, Janes K., ed., pp. 55–72
- Liu Y., 2020, *MNRAS*, 497, 3011
- Loose H. H., Kruegel E., Tutukov A., 1982, *A&A*, 105, 342
- Ma X. et al., 2016, *MNRAS*, 456, 2140
- Mackey A. D., 2009, in *IAU Symposium*, Vol. 258, *The Ages of Stars*, Mamajek E. E., Soderblom D. R., Wyse R. F. G., eds., pp. 275–286
- Mackey A. D., Broby Nielsen P., 2007, *MNRAS*, 379, 151
- Majewski S. R. et al., 2000, in *Liege International Astrophysical Colloquia*, Vol. 35, *Liege International Astrophysical Colloquia*, Noels A., Magain P., Caro D., Jehin E., Parmentier G., Thoul A. A., eds., p. 619
- Maran S. P. et al., 1984, *ApJ*, 280, 615
- Maraston C. et al., 2004, *A&A*, 416, 467
- Martín-Navarro I., van de Ven G., Yıldırım A., 2019, *MNRAS*, 487, 4939
- Massari D., Koppelman H. H., Helmi A., 2019, *A&A*, 630, L4
- Matthews L. D. et al., 1999, *AJ*, 118, 208
- Mayes R., 2019, in *Linking Galaxies from the Epoch of Initial Star Formation to Today*, p. 33
- Mayes R. J. et al., 2021, *MNRAS*, 506, 2459

McCrea W. H., 1964, MNRAS, 128, 147

McLaughlin D. E., van der Marel R. P., 2005, ApJS, 161, 304

Merritt D., 1997, AJ, 114, 228

Merritt D., Schnittman J. D., Komossa S., 2009, ApJ, 699, 1690

Messier C., 1771, Memoirs of the French Academy of Sciences for 1771, 435, translated version available at: <https://www.messier.seds.org/xtra/history/m-cat71.html>

Mészáros S. et al., 2015, AJ, 149, 153

Mieske S. et al., 2013, A&A, 558, A14

Mieske S., Hilker M., Infante L., 2002, A&A, 383, 823

Mieske S. et al., 2008, A&A, 487, 921

Mieske S., Hilker M., Misgeld I., 2012, A&A, 537, A3

Mieske S. et al., 2005, A&A, 430, L25

Miller B. W. et al., 1998, ApJL, 508, L133

Milone A. P., 2015, MNRAS, 446, 1672

Milone A. P., Marino A. F., 2022, Universe, 8, 359

Milone A. P. et al., 2020, MNRAS, 491, 515

—, 2018, MNRAS, 477, 2640

Milosavljević M., 2004, ApJL, 605, L13

Moe M., Kratter K. M., Badenes C., 2019, ApJ, 875, 61

Moehler S., 2001, PASP, 113, 1162

Morrissey P. et al., 2018, ApJ, 864, 93

Mucciarelli A. et al., 2023a, A&A, 671, A124

—, 2023b, A&A, 677, A61

Muratov A. L., Gnedin O. Y., 2010, ApJ, 718, 1266

Murray N., 2009, ApJ, 691, 946

Naab T., Johansson P. H., Ostriker J. P., 2009, *ApJL*, 699, L178

Nardiello D. et al., 2015, *MNRAS*, 451, 312

NASA/IPAC, 2013, Galactic dust reddening and extinction tool. [Online; accessed November 30, 2023]

Neumayer N., Seth A., Böker T., 2020, *A&AR*, 28, 4

Niederhofer F. et al., 2015, *A*, 575, A62

NOIRLab, 2015a, Soar optics. [Online; accessed November 8, 2023]

—, 2015b, Soar schematic. [Online; accessed November 8, 2023]

—, 2018, Goodman schematic 3d. [Online; accessed November 22, 2023]

Norris M. A. et al., 2015, *MNRAS*, 451, 3615

—, 2014, *MNRAS*, 443, 1151

—, 2008, *MNRAS*, 385, 40

—, 2019, *MNRAS*, 488, 5400

O’Connell R. W., 1999, , 37, 603

Oh K. S., Lin D. N. C., Aarseth S. J., 1995, *ApJ*, 442, 142

Oldham L. J., Auger M. W., 2016, *MNRAS*, 455, 820

Osterbrock, D E., Ferland, G J., 2005, *Astrophysics of Gaseous Nebulae and Active Galactic Nuclei*, second edition. University Science Books; 2nd ed. 2005 edition

Pallanca C. et al., 2021, *ApJ*, 913, 137

Parikh T. et al., 2024, *MNRAS*, 528, 7338

Paudel S. et al., 2013, *ApJ*, 767, 133

Paunzen E. et al., 2019, *A&A*, 622, A77

Peacock M. B. et al., 2018, *MNRAS*, 481, 3313

Pechetti R. et al., 2024, *MNRAS*, 528, 4941

—, 2022, *ApJ*, 924, 48

Peebles P. J. E., Dicke R. H., 1968, *ApJ*, 154, 891

Percival S. M., Salaris M., 2011, MNRAS, 412, 2445

Pfeffer J., Baumgardt H., 2013, MNRAS, 433, 1997

Phillips A. C. et al., 1996, AJ, 111, 1566

Piatti A. E., 2022, MNRAS, 511, L72

Pietrinferni A. et al., 2004, ApJ, 612, 168–190

Pietrinferni A. et al., 2021, ApJ, 908, 102

Pietrzyński G. et al., 2019, Nature, 567, 200–203

Pimblet K. A., Crossett J. P., Fraser-McKelvie A., 2019, MNRAS, 490, 455

Pogge R., 2019, modsCCDRed. Zenodo

Pogge R. W. et al., 2010, in Society of Photo-Optical Instrumentation Engineers (SPIE) Conference Series, Vol. 7735, Ground-based and Airborne Instrumentation for Astronomy III, McLean I. S., Ramsay S. K., Takami H., eds., p. 77350A

Portaluri E. et al., 2013, MNRAS, 433, 434

Portegies Zwart S., 2019, A&A, 621, L10

Price J. et al., 2009, MNRAS, 397, 1816

Prochaska J. et al., 2020a, The Journal of Open Source Software, 5, 2308

Prochaska J. X. et al., 2020b, pypeit/PypeIt: Release 1.0.0. Zenodo

Proctor R. N., Forbes D. A., Beasley M. A., 2004, MNRAS, 355, 1327

Puzia T. H., 2011, Observing run with xshooter: The stellar populations of ultra-compact dwarfs - galaxies or star clusters? 087.B-0758(B)

Puzia T. H., Perrett K. M., Bridges T. J., 2005, A&A, 434, 909

Puzia T. H. et al., 2002, A&A, 395, 45

Rain M. J., Ahumada J. A., Carraro G., 2021, A&A, 650, A67

Renaud F., Agertz O., Gieles M., 2017, MNRAS, 465, 3622

Renaud F., Bournaud F., Duc P.-A., 2015, MNRAS, 446, 2038

Retseck G., 2012, ancient-stars-how-does-spectrograph-work.2.jpg. [Online; accessed march 31, 2024]

Rey S.-C., Oh K., Kim S., 2021, ApJL, 917, L9

Rodgers A. W., Conroy P., Bloxham G., 1988, PASP, 100, 626

Salaris M., Chieffi A., Straniero O., 1993, ApJ, 414, 580

San Roman I. et al., 2015, A&A, 579, A6

Sánchez-Blázquez P. et al., 2006, MNRAS, 371, 703

—, 2014, MNRAS, 437, 1534

Sandage A., 1982, ApJ, 252, 553

Saracino S. et al., 2019, ApJ, 874, 86

Schiavon R. P., 2007, ApJS, 171, 146

Schiavon R. P. et al., 2012, AJ, 143, 14

—, 2005, ApJS, 160, 163

Schlafly E. F., Finkbeiner D. P., 2011, ApJ, 737, 103

Schödel R., Merritt D., Eckart A., 2009, A&A, 502, 91

Segers M. C. et al., 2016, MNRAS, 461, L102

Seth A. C. et al., 2021, Deciphering the Formation History of Omega Cen with a Comprehensive Stellar Kinematic and Population Dataset. HST Proposal. Cycle 29, ID. #16777

—, 2014, Nature, 513, 398

Shajn G., 1934, , 94, 642

Shapley H., 1918, , 30, 42

Shara M. M., Saffer R. A., Livio M., 1997, ApJL, 489, L59

Sharina M. E. et al., 2024, MNRAS, stae426

Shipp N. et al., 2021, ApJ, 923, 149

Shirazi A. R., Khalaj P., Haghi H., 2023, MNRAS

Sills A. et al., 1997, ApJ, 487, 290

Singh G., Yadav R. K. S., 2019, MNRAS, 482, 4874

Sirianni M. et al., 2002, *ApJ*, 579, 275

Smecker-Hane T. A. et al., 2002, *ApJ*, 566, 239

Smith Castelli A. V. et al., 2008, *MNRAS*, 391, 685

Sollima A., Ferraro F. R., 2019, *MNRAS*, 483, 1523

Stanway E. R., Eldridge J. J., 2023, *MNRAS*, 522, 4430

Storey P. J., Hummer D. G., 1995, *MNRAS*, 272, 41

Surdin V. G., 1994, *Astron. Lett.*, 20, 398

Suzuki T. L. et al., 2016, *MNRAS*, 462, 181

Theureau G. et al., 2007, *A&A*, 465, 71

Thomas D., Maraston C., Bender R., 2003, *MNRAS*, 339, 897

Thomas D., Maraston C., Johansson J., 2011, *MNRAS*, 412, 2183

Thomas D. et al., 2010, *MNRAS*, 404, 1775

Tonini C., 2013, *ApJ*, 762, 39

Torres-Robledo, S., Briceño C., 2019, in *Astronomical Data Analysis Software and Systems XXVIII*, Vol. 523, pp. 203–206

Trager S. C. et al., 1998, *ApJS*, 116, 1

Tremaine S. D., Ostriker J. P., Spitzer, L. J., 1975, *ApJ*, 196, 407

Tremonti C. A. et al., 2004, *ApJ*, 613, 898

Usher C. et al., 2019a, *MNRAS*, 482, 1275

—, 2019b, *MNRAS*, 490, 491

—, 2017, *MNRAS*, 468, 3828

van der Marel R. P., Anderson J., 2010, *ApJ*, 710, 1063

van der Marel R. P., Franx M., 1993, *ApJ*, 407, 525

van der Wel A. et al., 2014, *ApJ*, 788, 28

van Dokkum P. G., 2001, *PASP*, 113, 1420

VandenBerg D. A. et al., 2000, *ApJ*, 532, 430

Vazdekis A. et al., 1996, *ApJS*, 106, 307

—, 2010, *MNRAS*, 404, 1639

Veitch–Michaelis J., Lam M. C., 2020, in *Astronomical Society of the Pacific Conference Series*, Vol. 527, *Astronomical Data Analysis Software and Systems XXIX*, Pizzo R., Deul E. R., Mol J. D., de Plaa J., Verkouter H., eds., p. 627

Vergara M. Z. C. et al., 2021, , 649, A160

Vernet J. et al., 2011, *A&A*, 536, A105

Vilardell F. et al., 2010, *A&A*, 509, A70

Villanova S. et al., 2014, , 791, 107

Voggel K., Hilker M., Richtler T., 2016, *A&A*, 586, A102

Wallerstein G., 1962, *ApJS*, 6, 407

Walsh J. L. et al., 2017, *ApJ*, 835, 208

Wang S., Chen B., Ma J., 2021, *A&A*, 645, A115

Wei D. et al., 2020, *MNRAS*, 493, 5479

Welsh B. Y., Vedder P. W., Vallergera J. V., 1990, *ApJ*, 358, 473

Woolf N. J., 1964, *ApJ*, 139, 1081

Worthey G., 1994, , 95, 107

—, 1999, in *Astronomical Society of the Pacific Conference Series*, Vol. 192, *Spectrophotometric Dating of Stars and Galaxies*, Hubeny I., Heap S., Cornett R., eds., p. 283

Worthey G. et al., 1994, *ApJS*, 94, 687

Worthey G., Ottaviani D. L., 1997, *ApJS*, 111, 377

Wyse R. F. G., Moe M., Kratter K. M., 2020, *MNRAS*, 493, 6109

Zhang Y. et al., 2012, *MNRAS*, 421, 1678

Zheng Z. et al., 2019, *ApJ*, 873, 63

Zolotov A. et al., 2015, *MNRAS*, 450, 2327

Appendix A

Compact Stellar systems

Information

This thesis used the data of many CSSs, in this appendix chapter we will list most of the objects used with important information. For the sake of space we have not included the list of 754 SDSS binned galaxies or the 313 M31 GCs in this appendix chapter or the following appendices showing the results of this work. If the enquiring reader would like to request this data it will be made available in a second volume* or as a supplementary data files.

A.1 Local Globular Clusters

Firstly we introduce the WAGGS GC data, this data contained high SNR spectra of local group globular clusters. It contained 86 GCs, 64 from the MW, 14 LMC, 5 SMC and 3 from the Fornax dSph galaxy.

Table A.1: Part 1 of the table of WAGGS globular cluster data used in this project.

Name	Galaxy	Ra	Dec D	[Fe/H] ^(w) (dex)	Age ^(w) (Gyr)	[α /Fe] (dex)
Fornax 3	Fornax	39.95067	-34.25794	-2.33	12	
Fornax 4	Fornax	40.03208	-34.53627	-1.42	10	
Fornax 5	Fornax	40.58796	-34.10161	-2.09	13	
NGC 0104	MW	6.02233	-72.08144	-0.72	12.75	$0.26 \pm 0.03^{(b)}$
NGC 0121	SMC	6.70417	-71.53611	-1.28	10.5	

*please dont make me make a second volume

Table A.1 Continued						
Name	Galaxy	Ra	Dec	[Fe/H] ^(w)	Age ^(w)	[α /Fe]
			D	(dex)	(Gyr)	(dex)
NGC 0330	SMC	14.08579	-72.45347	-0.81	0.03	
NGC 0361	SMC	15.55346	-71.60450	-1.16	6.8	
NGC 0362	MW	15.80942	-70.84878	-1.26	11.5	
NGC 0416	SMC	16.99583	-72.35556	-1.22	6	
NGC 0419	SMC	17.07412	-72.88411	-0.77	1.45	
NGC 1261	MW	48.06754	-55.21622	-1.27	11.5	
NGC 1783	LMC	74.78579	-65.98773	-0.35	1.7	
NGC 1786	LMC	74.78112	-67.74596	-1.76	12.3	
NGC 1846	LMC	76.89542	-67.45901	-0.5	1.7	
NGC 1850	LMC	77.20913	-68.75990	-0.4	0.093	
NGC 1851	MW	78.52817	-40.04656	-1.18	11	
NGC 1856	LMC	77.37621	-69.12919	-0.3	0.281	
NGC 1866	LMC	78.41217	-65.46465	-0.43	0.177	0.08 ^(c)
NGC 1868	LMC	78.65250	-63.95714	-0.39	1.1	
NGC 1898	LMC	79.18908	-69.65466	-1.23	11.8	
NGC 1904	MW	81.04413	-24.52425	-1.6	13	
NGC 1916	LMC	79.65779	-69.40636	-1.48	12.9	
NGC 1978	LMC	82.18888	-66.23668	-0.38	1.9	0.02 or 0.38 ^(c)
NGC 2004	LMC	82.67225	-67.28940	-0.58	0.02	
NGC 2019	LMC	82.98533	-70.15903	-1.37	12.5	0.2 ^(c)
NGC 2100	LMC	85.53000	-69.20750	-0.42	0.021	-0.06 ^(c)
NGC 2136	LMC	88.25750	-69.49007	-0.4	0.1	
NGC 2808	MW	138.01292	-64.86350	-1.14	11.5	0.24 \pm 0.03 ^(b)
NGC 3201	MW	154.40342	-46.41247	-1.59	12	0.22 \pm 0.03 ^(b)
NGC 4147	MW	182.52563	18.54216	-1.8	12.75	
NGC 4590	MW	189.86658	-26.74406	-2.23	13	0.19 \pm 0.05 ^(b)
NGC 4833	MW	194.89133	-70.87650	-1.85	13	
NGC 5024	MW	198.23021	18.16817	-2.1	13.25	
NGC 5139	MW	201.69700	-47.47947	-1.53	11	\sim 0.2 ^(d)
NGC 5272	MW	205.54842	28.37728	-1.5	12.5	
NGC 5286	MW	206.61171	-51.37425	-1.69	13	
NGC 5634	MW	217.40533	-5.97642	-1.88	13	0.20 \pm 0.04 ^(b)
NGC 5694	MW	219.90217	-26.53833	-1.98	13.6	0.17 \pm 0.04 ^(b)
NGC 5824	MW	225.99421	-33.06853	-1.91	13	0.24 \pm 0.03 ^(b)
NGC 5904	MW	229.63842	2.08103	-1.29	12.25	0.24 \pm 0.04 ^(b)
NGC 5927	MW	232.00288	-50.67303	-0.49	12.25	0.30 \pm 0.04 ^(b)
NGC 5986	MW	236.51250	-37.78642	-1.59	13.25	

Table A.1 Continued

Name	Galaxy	Ra	Dec D	[Fe/H] ^(w) (dex)	Age ^(w) (Gyr)	[α /Fe] (dex)
NGC 6093	MW	244.26004	-22.97608	-1.75	13.5	
NGC 6121	MW	245.89675	-26.52575	-1.16	12.5	0.27 \pm 0.04 ^(b)
NGC 6139	MW	246.91663	-38.84918	-1.65		
NGC 6171	MW	248.13275	-13.05378	-1.02	12.75	0.20 \pm 0.14 ^(b)
NGC 6218	MW	251.80908	-1.94853	-1.37	13.25	
NGC 6254	MW	254.28771	-4.10031	-1.56	13	0.21 \pm 0.03 ^(b)
NGC 6266	MW	255.30250	-30.11236	-1.18	12.5	
NGC 6273	MW	255.65704	-26.26794	-1.74	13.2	
NGC 6284	MW	256.11979	-24.76423	-1.26	12	0.27 \pm 0.04 ^(b)
NGC 6293	MW	257.54342	-26.58172	-1.99	13	
NGC 6304	MW	258.63437	-29.46203	-0.45	12.75	
NGC 6316	MW	259.15592	-28.14000	-0.45	13.1	0.30 \pm 0.03 ^(b)
NGC 6333	MW	259.79908	-18.51625	-1.77	12	
NGC 6342	MW	260.29225	-19.58742	-0.55	12.5	
NGC 6352	MW	261.37129	-48.42217	-0.64	13	0.30 \pm 0.02 ^(b)
NGC 6356	MW	260.89579	-17.81303	-0.4	12.75	0.30 \pm 0.02 ^(b)
NGC 6362	MW	262.97912	-67.04833	-0.99	12.5	
NGC 6388	MW	264.07275	-44.73565	-0.55	11.75	
NGC 6397	MW	265.17538	-53.67433	-2.02	13.5	0.23 \pm 0.03 ^(b)
NGC 6440	MW	267.21946	-20.35958	-0.36	13 ^(e)	0.31 \pm 0.03 ^(b)
NGC 6441	MW	267.55442	-37.05144	-0.46	12	0.26 \pm 0.04 ^(b)
NGC 6522	MW	270.89200	-30.03397	-1.34	12.4	
NGC 6528	MW	271.20671	-30.05578	-0.11	11	0.26 \pm 0.05 ^(b)
NGC 6541	MW	272.00983	-43.71489	-1.81	13.25	
NGC 6553	MW	272.31533	-25.90775	-0.18	11	0.30 \pm 0.02 ^(b)
NGC 6569	MW	273.41200	-31.82644	-0.76	12.8 ^(f)	0.29 \pm 0.03 ^(b)
NGC 6584	MW	274.65667	-52.21578	-1.5	12.25	
NGC 6624	MW	275.91879	-30.36103	-0.44	13	
NGC 6637	MW	277.84625	-32.34808	-0.64	12.5	
NGC 6652	MW	278.94013	-32.99072	-0.81	13.25	
NGC 6656	MW	279.09975	-23.90475	-1.7	13.5	0.22 \pm 0.02 ^(b)
NGC 6681	MW	280.80317	-32.29211	-1.62	13	
NGC 6715	MW	283.76388	-30.47986	-1.49	13.25	
NGC 6717	MW	283.77517	-22.70147	-1.26	13	
NGC 6723	MW	284.88813	-36.63225	-1.1	12.75	
NGC 6752	MW	287.71713	-59.98456	-1.54	12.5	0.22 \pm 0.05 ^(b)
NGC 6809	MW	294.99879	-30.96475	-1.94	13.5	

Table A.1 Continued						
Name	Galaxy	Ra	Dec	[Fe/H] ^(w)	Age ^(w)	[α /Fe]
			D	(dex)	(Gyr)	(dex)
NGC 6838	MW	298.44371	18.77919	-0.78	12.5	0.29 \pm 0.03 ^(b)
NGC 6864	MW	301.52017	-21.92226	-1.29	11.25	0.22 \pm 0.03 ^(b)
NGC 6934	MW	308.54738	7.40447	-1.47	12	
NGC 7006	MW	315.37275	16.18791	-1.52	12.25	0.25 \pm 0.05 ^(b)
NGC 7078	MW	322.49304	12.16700	-2.37	13.25	0.24 \pm 0.03 ^(b)
NGC 7089	MW	323.36258	-0.82325	-1.65	12.5	
NGC 7099	MW	325.09217	-23.17986	-2.27	13.25	
End of Table						

Table A.2: Part 2 of the table of WAGGS globular cluster data used in this project.

Name	$V^{(w)}$	$r_h^{(w)}$	A_V	E(B-V) ^(g)	$M_\odot^{(w)}$	$M_{\odot F}^{(w)}$	$\sigma^{(a)}$
	(km/s)	(pc)			(Total)	(FoV)	(km/s)
Fornax 3	54.958	6.41	0.11	0.0211 \pm 0.0009	5.42	5.29	
Fornax 4	39.937	4.68	0.43	0.0198 \pm 0.0014	5.23	5.13	
Fornax 5	54.894	6.99	0.1	0.0186 \pm 0.0003	5.11	4.94	
NGC 0104	-21.357	190.2	0.12	0.0275 \pm 0.0003	6	4.68	12.2000
NGC 0121	139.436	19.02	0.45	0.0282 \pm 0.0004	5.61	5.2	
NGC 0330	157.619	21	0.2	0.3442 \pm 0.0255	4.57	4.14	
NGC 0361	164.648	39.2	0.21	0.1217 \pm 0.0270	5.29	4.44	
NGC 0362	221.04	49.2	0.15	0.0276 \pm 0.0005	5.6	4.82	8.8000
NGC 0416	155.958	15.43	0.39	0.1042 \pm 0.0078	5.22	4.85	
NGC 0419	189.856	27.78	0.31	0.0887 \pm 0.0088	5.17	4.85	
NGC 1261	68.1	40.8	0.03	0.0118 \pm 0.0009	5.35	4.41	5.6000
NGC 1783	253.506	60.6	0.02	0.1559 \pm 0.0468	4.95	3.84	
NGC 1786	279.506	13.95	0.39	0.1914 \pm 0.0098	5.58	5.3	
NGC 1846	242.512	34.5	0.08	0.1700 \pm 0.0095	4.86	4.08	
NGC 1850	261.87	46.3	0.32	1.1230 \pm 0.3685	5.1	4.39	
NGC 1851	270.853	30.6	0.06	0.0319 \pm 0.0015	5.56	5.02	10.2000
NGC 1856	304.807	31.96	0.71	0.6905 \pm 0.1665	5.17	4.63	
NGC 1866	319.714	42.91	0.4	0.0495 \pm 0.0009	5.07	4.39	
NGC 1868	287.031	13.66	0.41	0.0309 \pm 0.0006	4.58	4.28	
NGC 1898	208.961	25.74	0.26	0.5739 \pm 0.1603	5.36	4.83	
NGC 1904	271.511	39	0.03	0.0270 \pm 0.0006	5.37	4.63	6.5000
NGC 1916	197.402	8.06	0.58	1.4179 \pm 0.1552	5.78	5.59	
NGC 1978	295.193	39.53	0.21	0.1313 \pm 0.0470	5.12	4.62	

Table A.2 Continued							
Name	$V^{(w)}$ (km/s)	$r_h^{(w)}$ (pc)	$A_V^{(w)}$	E(B-V) ^(g)	$M_\odot^{(w)}$ (Total)	$M_{\odot F}^{(w)}$ (FoV)	$\sigma^{(a)}$ (km/s)
NGC 2004	305.776	21.71	0.36	0.2503 ±0.0340	4.32	3.83	
NGC 2019	275.073	9.72	0.43	0.3794 ±0.0698	5.49	5.29	
NGC 2100	258.178	18.14	0.65	1.7385 ±0.3897	4.4	4.03	
NGC 2136	270.856	14.08	0.59	0.1475 ±0.0167	4.36	4.04	
NGC 2808	103.316	48	0.67	0.1954 ±0.0058	5.99	5.18	14.4000
NGC 3201	493.324	186	0.73	0.2190 ±0.0149	5.21	3.6	4.5000
NGC 4147	174.534	28.8	0.06	0.0225 ±0.0004	4.7	4.16	3.1000
NGC 4590	-98.566	90.6	0.15	0.0526 ±0.0006	5.18	3.69	3.7000
NGC 4833	197.17	144.6	0.98	0.2822 ±0.0141	5.5	3.82	4.8000
NGC 5024	-70.233	78.6	0.06	0.0179 ±0.0003	5.71	4.65	5.9000
NGC 5139	228.085	300	0.37	0.1212 ±0.0021	6.33	4.05	17.6000
NGC 5272	-147.122	138.6	0.03	0.0115 ±0.0006	5.78	4.45	8.1000
NGC 5286	58.447	43.8	0.73	0.2610 ±0.0127	5.73	4.93	9.3000
NGC 5634	-13.999	51.6	0.15	0.0477 ±0.0033	5.31	4.52	5.3000
NGC 5694	-140.469	24	0.27	0.0857 ±0.0010	5.36	4.92	8.9000
NGC 5824	-26.841	27	0.4	0.1482 ±0.0028	5.77	5.42	11.9000
NGC 5904	54.429	106.2	0.09	0.0319 ±0.0008	5.75	4.42	7.7000
NGC 5927	-106.107	66	1.37	0.4480 ±0.0173	5.35	4.66	6.5000
NGC 5986	96.375	58.8	0.86	0.2892 ±0.0097	5.61	4.42	8.3000
NGC 6093	8.591	36.6	0.55	0.1836 ±0.0058	5.52	4.9	9.5000
NGC 6121	65.416	259.8	1.07	0.4278 ±0.0052	5.11	3.63	4.6000
NGC 6139	20.924	51	2.29	0.7855 ±0.0165	5.57	4.84	9.2000
NGC 6171	-35.938	103.8	1.01	0.3952 ±0.0076	5.08	3.57	4.3000
NGC 6218	-41.657	106.2	0.58	0.1524 ±0.0014	5.15	3.48	4.5000
NGC 6254	73.086	117	0.86	0.2479 ±0.0063	5.22	3.71	6.2000
NGC 6266	-75.933	55.2	1.44	0.3916 ±0.0195	5.9	5.12	15.2000
NGC 6273	141.373	79.2	1.16	0.2672 ±0.0106	5.88	4.75	11.0000
NGC 6284	28.916	39.6	0.86	0.2611 ±0.0102	5.41	4.6	8.9000
NGC 6293	-143.35	53.4	1.1	0.5241 ±0.0259	5.34	4.38	7.5000
NGC 6304	-104.084	85.2	1.65	0.4538 ±0.0076	5.15	4.15	5.7000
NGC 6316	95.118	39	1.65	0.6531 ±0.0313	5.57	4.55	9.0000
NGC 6333	311.804	57.6	1.16	0.3746 ±0.0216	5.41	4.41	
NGC 6342	120.557	43.8	1.4	0.4710 ±0.0360	4.8	3.9	4.5000
NGC 6352	45.405	123	0.67	0.3060 ±0.0203	4.82	3.64	4.4000
NGC 6356	-129.662	48.6	0.86	0.2690 ±0.0040	5.63	4.86	7.8000
NGC 6362	-3.026	123	0.27	0.0642 ±0.0010	5.01	3.32	3.9000
NGC 6388	81.108	31.2	1.13	0.3435 ±0.0177	5.99	5.34	18.2000

Table A.2 Continued							
Name	$V^{(w)}$ (km/s)	$r_h^{(w)}$ (pc)	$A_V^{(w)}$	E(B-V) ^(g)	$M_\odot^{(w)}$ (Total)	$M_{\odot F}^{(w)}$ (FoV)	$\sigma^{(a)}$ (km/s)
NGC 6397	22.153	174	0.55	0.1618 ±0.0027	4.89	3.12	5.2000
NGC 6440	-71.248	28.8	3.27	0.9851 ±0.0413	5.73	5.09	15.8000
NGC 6441	21.09	34.2	1.44	0.5373 ±0.0215	6.08	5.46	18.8000
NGC 6522	-9.372	60	1.47	0.5033 ±0.0220	5.29	4.2	8.2000
NGC 6528	210.905	22.8	1.65	0.6233 ±0.0419	4.86	4.44	6.4000
NGC 6541	-167.482	63.6	0.43	0.1338 ±0.0105	5.64	4.56	8.7000
NGC 6553	-2.003	61.8	1.92	1.1817 ±0.0470	5.34	4.18	8.5000
NGC 6569	-57.634	48	1.62	0.3692 ±0.0085	5.54	4.49	7.5000
NGC 6584	260.268	43.8	0.31	0.0914 ±0.0056	5.31	4.31	4.2000
NGC 6624	58.607	49.2	0.86	0.2283 ±0.0112	5.23	4.38	6.1000
NGC 6637	44.762	50.4	0.55	0.1422 ±0.0020	5.29	4.43	
NGC 6652	-99.813	28.8	0.27	0.0970 ±0.0023	4.89	4.26	
NGC 6656	-143.979	201.6	1.04	0.2797 ±0.0036	5.63	3.64	8.4000
NGC 6681	220.035	42.6	0.21	0.0921 ±0.0048	5.08	4.29	7.1000
NGC 6715	142.314	49.2	0.46	0.1318 ±0.0010	6.22	5.67	16.2000
NGC 6717	26.388	40.8	0.67	0.2188 ±0.0066	4.49	3.76	
NGC 6723	-94.861	91.8	0.15	0.1424 ±0.0251	5.36	3.86	5.3000
NGC 6752	-29.817	114.6	0.12	0.0485 ±0.0010	5.32	4.11	8.3000
NGC 6809	172.218	169.8	0.24	0.1170 ±0.0008	5.26	3.02	4.8000
NGC 6838	-27.94	100.2	0.76	0.2781 ±0.0151	4.47	2.69	3.3000
NGC 6864	-189.743	27.6	0.49	0.1296 ±0.0040	5.66	5.16	11.8000
NGC 6934	-412.888	41.4	0.31	0.0903 ±0.0024	5.21	4.5	4.7000
NGC 7006	-379.979	26.4	0.15	0.0703 ±0.0034	5.3	4.67	4.4000
NGC 7078	-108.111	60	0.31	0.0934 ±0.0028	5.91	5.24	12.9000
NGC 7089	-5.953	63.6	0.18	0.0386 ±0.0008	5.84	4.91	10.6000
NGC 7099	-185.956	61.8	0.09	0.0439 ±0.0017	5.21	4.05	5.5000

End of Table

The sources of the information presented in the previous tables are: *w*: the supplementary files of Usher et al. (2019a) (the second paper on the WAGGS data release), *a*: Baumgardt & Hilker (2018), *b*: Dias et al. (2016), *c*: Colucci et al. (2012), *d*: Anguiano et al. (2015), *e*: Pallanca et al. (2021), *f*: Saracino et al. (2019), *g*: This was calculated using the NASA/IPAC Infrared Science Archive Galactic Dust Reddening and Extinction tool (NASA/IPAC, 2013) which is based on dust reddening measurements from Schlafly & Finkbeiner (2011).

A.2 Other Compact Stellar systems

Next we will introduce the other CSSs we use in this project. This data (except for the M87 objects) was provided as raw unreduced spectra. In Chapter 2 we go through the steps taken for the reduction of each source of data. The objects with “instr” labelled as “GHTS” were observed specifically for this project.

Table A.3: The CSSs from MODS, GHTS, XShooter and Keck used in this thesis.

Class	Name	Ra	Dec	Instr	Obsv date	SNR (5000Å)	M_{\odot}	r_h pc	Σ ($M_{\odot} \text{pc}^{-3}$)	Age (Gyr)	[Fe/H] (dex)	$[\alpha/\text{Fe}]$ (dex)
UCD	M59cO	12:41:55.33	11:40:03.79	Xshooter	10/05/2011	38	6.9×10^7	32 ± 5	10724	14.5	-0.23 ± 0.04	0.21 ± 0.2
				MODS	11/03/2015							
UCD	NGC4546-UCD1	12:35:28.7	-03:47:21	Xshooter	09/05/2011	48	$3.59 \pm 0.99 \times 10^7$	25.54 ± 1.3	8759	5.8 ± 0.1	-1.26 ± 0.05	-0.04 ± 0.02
UCD	VUCD1	12:30:07.57	12:36:31	Xshooter	10/05/2011	42	1.55×10^7	12.1	16849	11.9 ± 2	-1.26 ± 0.05	0.38 ± 0.09
UCD	VUCD3	12:30:57.38	12:25:44.5	Xshooter	10/05/2011	38	6.46×10^7	21.6 ± 1.5	22037	15 ± 1.3	-0.23 ± 0.03	0.38 ± 0.03
UCD	VUCD7	12:31:52.9	12:15:59.04	Xshooter	10/05/2011	33	2.34×10^7	19.6	9694	10.7 ± 0.9	-0.66 ± 0.03	0.13 ± 0.04
GC	NGC7252-W3	22:20:43.7	-24:40:38	Xshooter	07/11/2018	56	$8.00 \pm 2.0 \times 10^7$	17.7	40641	0.3 ± 0.2		
GC	CSS-1097	03:38:06.92	-35:24:15.4	Xshooter	06/11/2018	19						
UCD	CSS-1145	03:38:06.50	-35:23:03.71	Xshooter	05/11/2018	23	2.04×10^6	14.5	1544	12.9 ± 5.4	-0.73 ± 0.09	
UCD	CSS-1555	03:39:52.55	-35:04:24.00	Xshooter	06/11/2018	37	9.33×10^6	26.2	2163	12.45 ± 0.28	-1.2	0.3 ± 0.2
UCD	CSS-251	03:37:03.25	-35:38:04.39	Xshooter	05/11/2018	29	2.82×10^7	23.5	8127	9.71 ± 0.26	-0.67	0.5 ± 0.2
UCD	CSS-756	03:39:35.92	-35:28:24.44	Xshooter	05/11/2018	37	2.04×10^7	30.9	3400	15 ± 2	-0.67 ± 0.03	
UCD	CSS-969	03:38:10.74	-35:25:46.02	Xshooter	06/11/2018	29	1.95×10^7	5.24	113030	15 ± 3.2	-0.34 ± 0.03	
cE	AHcE5349	03:21:01.4	41:26:04	MODS	30/11/2016	120	4.521×10^8	389 ± 7	475			
NSC	NGC2344-NSC	07:12:28.56	47:10:00.8	MODS	30/11/2016	265	$1.51 \pm 1.2 \times 10^8$	20.5 ± 20.5	57171			
cE	AHcE9313	14:42:33.83	41:49:44.4	MODS	10/05/2016	216	8.91×10^9	361	10867	4.6 ± 0.2	0.17 ± 0.02	
UCD	NGC4565-UCD1	12:35:28.7	-03:47:21.1	MODS	12/05/2016	118	1.17×10^7	17.4 ± 1.4	6150			
NSC	LEDA4573336-NSC	13:13:47.3	10:03:11	MODS	12/05/2016	110	3.47×10^7	21.75	1166			
UCD	M60-UCD1	12:43:36	11:32:04.6	MODS	07/04/2014	188	$1.80 \pm 0.23 \times 10^8$	27.2 ± 1.0	38722	14.5 ± 3.7		0.33 ± 0.04
					11/03/2015							
					13/05/2016							
cE	AHcE437	10:05:55.33	00:39:7.9	MODS	05/02/2016	48	8.91×10^8	575.705	427.87	7.3 ± 1.0	0.02 ± 0.06	
dE	NGC0052-dE1	00:14:37.28	18:34:22.9	MODS	06/02/1016	125	1.18×10^8	924.62	219.98			
NSC	NGC0628-NSC	01:36:41.7	15:47:01	MODS	06/02/2016	180	$1.13 \pm 0.53 \times 10^7$	3.6	138569			
GC	M31_B023-G078	00:41:01.15	41:13:45.41	MODS	19/09/2015	149	6.7×10^6	3.5	88191			
GC	M31_B017-G070	00:40:48.72	41:12:07.18	MODS	19/09/2015	56	1.3×10^6	3.1	21530			

Table A.3 Continued

Class	Name	Ra	Dec	Instr	Obsv date	SNR (5000Å)	M_{\odot}	r_h pc	Σ ($M_{\odot}\text{pc}^{-3}$)	Age (Gyr)	[Fe/H] (dex)	$[\alpha/\text{Fe}]$ (dex)
cE	AHcE2	23:15:12.62	-01:14:58.3	MODS	14/06/2015	54	5.13×10^9	260	12078	5.4 ± 1.6	-0.01 ± 0.24	0.07 ± 0.22
NSC	UGC12732_NSC	23:40:39.79	26:14:10	MODS	15/06/2015	7	$7.68 \pm 2.82 \times 10^5$	3.2 ± 0.1	11932			
cE	AHcE1674	15:06:34.32	01:33:32.3	MODS	14/03/2015	125	3.2×10^9	240 ± 10	8952	15 ± 4	-0.36 ± 0.05	0.34 ± 0.05
UCD	M60UCDY	12:43:52.41	11:25:34.2	MODS	16/03/2015	29	2.78×10^6	60	123			
cE	NGC4486B	12:30:32	12:29:25	MODS	11/03/2015	335	6.46×10^9	180	31733	11.2 ± 1.8	-0.1 ± 0.05	0.34 ± 0.04
UCD	Sombbrero-UCD1	12:40:03.1	-11:40:04.3	MODS	16/03/2015	54	$1.64 \pm 0.43 \times 10^7$	14.7 ± 1.4	12079	12.6 ± 0.9	-0.08 ± 0.08	0.06 ± 0.07
cE	AHcE6861	13:38:42.45	31:14:57	MODS	31/03/2014	59	1.7×10^9	433 ± 27	1443	4.8 ± 1.5	0.13 ± 0.12	0.08 ± 0.06
cE	AHcE6365	12:26:46.52	07:40:15.8	MODS	07/04/2014	40	4.9×10^7	319 ± 7	77			
cE	AHcE0	09:47:29.24	14:12:45.5	MODS	17/02/2014	57	4.68×10^9	499 ± 10	2991	9.21 ± 3	-0.2 ± 0.2	0.20 ± 0.05
cE	AHcE1	11:04:04.4	45:16:18.9	MODS	17/02/2014	32	7.08×10^9	390 ± 10	7408	5.33 ± 1.52	0.14 ± 0.18	0.12 ± 0.16
cE	AHcE53	10:08:10.32	02:27:48.3	MODS	22/02/2014	132	7.76×10^9	465 ± 13	571	7.2 ± 1.2	-0.37 ± 0.07	0.20 ± 0.05
cE	AHcE732	12:04:28.97	01:53:38.7	MODS	21/02/2014	65	3.24×10^9	616 ± 29	1359	13.8 ± 2.1	-0.32 ± 0.06	0.44 ± 0.04
cE	AHcE1232	07:51:40.4	50:11:02.65	MODS	16/02/2014	24	2.45×10^9	485 ± 34	1658	6.3 ± 1.3	-0.48 ± 0.08	0.50 ± 0.04
cE	NGC2892-cE	09:32:53.9	67:36:54.5	MODS	17/02/2014	38	$1.09 \pm 0.14 \times 10^{10}$	581 ± 85	5141	2.2 ± 0.8	0.35 ± 0.14	0.34 ± 0.06
UCD	NGC4621-UCD3	12:42:11.047	11:38:41.21	MODS	18/02/2014	107	$2.0 \pm 0.1 \times 10^8$	20	79577	8.7 ± 1.3	0.09 ± 0.04	0.28 ± 0.02
cE	NGC0741-cE	01:56:21.3	05:37:46.8	MODS	01/12/2013	191	$5.96 \pm 0.53 \times 10^9$	312 ± 55	9763			
cE	NGC1128-cE	02:57:41.7	06:02:19.1	MODS	06/10/2013	50	$7.50^{+0.15}_{-0.18} \times 10^8$	485 ± 69	509	8.7 ± 3.3	-0.15 ± 0.12	0.26 ± 0.08
cE	NGC2832-cE	09:19:47.9	33:46:04.9	MODS	22/02/2014	60	$2.27 \pm 0.59 \times 10^9$	375 ± 54	2565	12.0 ± 1.8	0.20 ± 0.06	0.42 ± 0.04
cE	cE1	00:50:44.45	-01:12:02.65	GHTS	28/10/2022	58	3.09×10^9	981	511	13.7 ± 1	-0.43 ± 0.04	
cE	cE4	03:25:53.68	-00:35:33.81	GHTS	22/11/2022	52	3.24×10^9	835	740	8.7 ± 0.6	-0.37 ± 0.07	
cE	Galaxy266	04:33:36.12	-13:14:42.82	GHTS	28/10/2022	48	2.57×10^{10}	370	29878			
cE	A496cE	04:33:37.3	-13:15:18.00	GHTS	22/11/2022	28	6.17×10^9	240	17048			
red nugget	MRK1216	08:28:47.11	-06:56:24.42	GHTS	22/11/2022	313	1.6×10^{11}	2800	3248			
cE	cE547	10:19:17.52	00:20:39.93	GHTS	27/03/2023	75	9.25×10^9	710	2919			
cE	LEDA43301	12:48:53.91	-41:19:05.80	GHTS	27/03/2023	49	4.47×10^9	340	6154			
GC	HGHH92-G7	13:26:05.39	-42:56:32.38	GHTS	27/03/2023	25	3.24×10^6	7.4 ± 0.1	9418		-0.9	
GC	HGHH92-G22	13:25:53.3	-42:59:07.6	GHTS	27/03/2023	15	2.3×10^6	3.7 ± 0.1	26739		-1	
GC	HGHH92-G23	13:25:54.3	-42:59:25.4	GHTS	27/03/2023	39	8.51×10^6	3.3 ± 0.1	124372		-0.36	
cE	LEDA1414042	22:03:25.29	+12:40:33.20	GHTS	15/06/2023	64	1.23×10^{10}	673	4318	10.5 ± 0.4	-0.09 ± 0.03	
cE	NGC5846A	15:06:29.20	+01:35:42.0	GHTS	15/06/2023	141	7.41×10^9	520	4361			

Table A.3 Continued

Class	Name	Ra	Dec	Instr	Obsv date	SNR (5000Å)	M_{\odot}	r_h pc	Σ ($M_{\odot}\text{pc}^{-3}$)	Age (Gyr)	[Fe/H] (dex)	$[\alpha/\text{Fe}]$ (dex)
cE	NGC7014-cE	21:07:51.5	-47:11:25.6	GHTS	15/06/2023	15	$2.99 \pm 1.02 \times 10^8$	329.8 ± 23.6	438			
GC	NGC7252-W30	22:20:45.4	-24:40:52.5	GHTS	15/06/2023	24	$2.72 \pm 2.71 \times 10^7$	9.4	49343	0.3 ± 0.2		
cE	rs685	12:04:36.7	+01:53:33.54	GHTS	15/06/2023	41	1.23×10^9	659	451	8.1 ± 0.5	-0.04 ± 0.05	
cE	rs686	12:04:36.76	+01:55:08.50	GHTS	15/06/2023	25	6.9×10^8	579	327			
cE	Chillingarian 117	16:25:14.8	+07:08:44.66	GHTS	15/06/2023	61	4.07×10^9	689	1363	3.0 ± 0.1	-0.07 ± 0.04	
GC	M87-GC2	12:30:48.00	+12:24:32.25	Keck	09/05/2018	18	$4.37 \pm 0.38 \times 10^6$	1.9	192661.2469	11.6 ± 1.4	-0.10 ± 0.09	0.4 ± 0.2
GC	M87-GC5	12:30:46.27	+12:24:20.60	Keck	09/05/2018	15	$1.9 \pm 42 \times 10^6$	6.68	6776.739751	8.2 ± 0.9	-0.61 ± 0.08	-0.1 ± 0.3
GC	M87-GC6	12:30:47.54	+12:24:23.39	Keck	09/05/2018	8	$1.29 \pm 38 \times 10^6$	1.98	52369.62468	10.3 ± 1.3	-0.36 ± 0.08	0.35 ± 0.4
UCD	M87-UCD1	12:30:47.70	+12:24:30.50	Keck	09/05/2018	43	$5.99 \pm 0.49 \times 10^6$	36.3	723.4919512	7.7 ± 0.6	-1.25 ± 0.12	0.40 ± 0.15
UCD	M87-UCD3	12:30:46.65	+12:24:22.12	Keck	09/05/2018	24	$3.19 \pm 0.38 \times 10^6$	31.7	505.2336758	9.2 ± 1.1	-0.86 ± 0.35	0.0 ± 0.3
UCD	M87-UCD4	12:30:46.20	+12:24:23.10	Keck	09/05/2018	26	$3.98 \pm 0.54 \times 10^6$	36.9	465.2115316	9.4 ± 0.6	-0.79 ± 0.38	0.00 ± 0.35

End of Table

All information in this table has been taken from the extended AIMSS catalogue (Norris et al., 2014; Forbes et al., 2014; Janz et al., 2016) and references therein. Information on the M87 objects was taken from Forbes et al. (2020).

Appendix B

CSS Analysis Method Results

In this appendix chapter we present the results of the three methods developed in Chapter 3. We present the results of all of the objects (except for those of the SDSS binned galaxies and the M31 GCs for the reasons mentioned in the last appendix chapter).

B.1 Local Globular Cluster Results

Firstly we will show the results of Chapter 3, where 3 different analysis methods (BpPXF, SpPXF, & LISm χ) were used to measure age, metallicity and $[\alpha/\text{Fe}]$ for the WAGGS GC sample. These methods were used on 3 different wavelength regions/ranges (except LISm χ) and we present the results for each method and wavelength region here.

For BpPXF in Chapter 3 we emphasised the importance of finding the correct regul value. In these results we have published the regul values of the fits for each objects highlighting those which went over the 100 “realistic” limit. In later tables, we do not cover the regul values, this is because due to the increased binning of the SSP models and the reduced signal to noise of the other CSS data (comparatively to WAGGS) meant that the regul value commonly went over 100. In Section 5.3.1 we have explained how this is not drastically detrimental to the results, however, and have explained how an overly large regul value effects the results.

Table B.1: BpPXF Outputs for WAGGS GCs

Name	3800 - 6000 Å			Regions Omitted			4828 - 5363 Å		
	Age (Gyr)	[Fe/H] (dex)	regul	Age (Gyr)	[Fe/H] (dex)	regul	Age (Gyr)	[Fe/H] (dex)	regul
Fornax 4	8.38	-1.2	8.385	8.31	-1.21	7.880	8.83	-1.27	7.808

Table B.1 Continued									
Name	3800 - 6000 Å			Regions Omitted			4828 - 5363 Å		
	Age (Gyr)	[Fe/H] (dex)	regul	Age (Gyr)	[Fe/H] (dex)	regul	Age (Gyr)	[Fe/H] (dex)	regul
Fornax 5	6.72	-1.8	12.224	6.46	-1.8	11.194	7.43	-1.89	8.575
NGC 0104	11	-0.424	7.949	11.2	-0.448	7.652	10.8	-0.463	3.940
NGC 0121	8.77	-1.14	7.780	8.74	-1.15	7.815	9.75	-1.27	3.953
NGC 0362	8.83	-0.932	17.413	8.67	-0.948	17.510	8.93	-0.955	2.547
NGC 0419	5.93	-0.947	74.563	3.83	-0.793	61.122	1.43	-0.716	25.664
NGC 1261	8.58	-1.17	2.809	8.88	-1.17	3.200	8.65	-1.2	6.022
NGC 1783	3.25	-0.693	27.400	2.34	-0.579	22.300	2.31	-0.311	18.400
NGC 1786	6.91	-1.66	20.070	6.57	-1.66	23.950	6.24	-1.63	33.728
NGC 1846	1.97	-0.33	31.205	2.77	-0.3	27.500	4.47	-0.089	147.000
NGC 1850	0.11	-0.486	3.248	0.123	-0.59	4.365	0.254	-1.28	4.160
NGC 1851	8.39	-0.983	9.895	8.4	-0.981	11.146	8.72	-0.974	6.069
NGC 1856	0.22	-0.059	365.000	0.216	-0.0954	151.000	0.338	-0.577	110.500
NGC 1866	0.23	-0.282	295.000	0.381	-0.452	195.000	0.248	-0.472	106.400
NGC 1868	0.88	-0.423	128.000	0.829	-0.392	138.600	4.99	-1.12	370.000
NGC 1898	7.86	-1.19	14.940	7.93	-1.15	14.509	8.51	-1.11	19.700
NGC 1904	8.82	-1.48	16.340	8.18	-1.48	19.200	7.56	-1.5	9.287
NGC 1916	6.95	-1.5	205.000	9.74	-1.25	159.000	2.35	-1.26	91.000
NGC 1978	4.91	-0.662	32.628	4.6	-0.654	33.631	7.02	-0.712	19.792
NGC 2019	7.43	-1.29	102.351	7.37	-1.3	74.050	6.49	-1.32	129.279
NGC 2100	4.31	-0.004	3.165	1.16	-1.98	3.682	7.52	-0.308	3.743
NGC 2136	0.19	-0.379	394.233	0.204	-0.428	366.399	0.607	-1.02	339.235
NGC 2808	9.74	-0.801	5.396	9.57	-0.84	5.253	8.69	-0.943	2.921
NGC 3201	9.96	-1.14	12.384	10	-1.16	12.368	7.21	-1.14	14.822
NGC 4147	6.25	-1.59	27.946	5.5	-1.59	26.351	4.56	-1.69	154.536
NGC 4590	8.64	-1.96	2.054	7.2	-2.089	2.089	7.46	-1.99	9.045
NGC 4833	7.2	-1.64	59.442	4.36	-1.69	47.713	3.95	-1.94	31.688
NGC 5024	8.72	-1.72	14.462	8.05	-1.72	17.645	7.43	-1.76	33.233
NGC 5139	11.4	-1.37	14.315	9.82	-1.41	6.504	8.4	-1.43	4.663
NGC 5272	8.79	-1.34	4.759	9.02	-1.33	4.089	8.28	-1.34	2.795
NGC 5286	13.1	-1.02	8.184	10.5	-1.43	18.472	7.47	-1.45	13.105
NGC 5634	6.17	-1.57	40.939	6.33	-1.58	15.579	6.63	-1.61	12.986
NGC 5694	6.44	-1.73	16.014	6.48	-1.71	16.000	7.59	-1.85	10.486
NGC 5824	7.42	-1.72	13.737	7.2	-1.74	13.182	7.38	-1.77	5.816
NGC 5904	11.1	-1.12	4.809	9.99	-1.12	9.705	7.75	-1.11	16.582
NGC 5927	13.4	0.309	4.378	11.8	-0.107	5.170	11.6	-0.122	11.559
NGC 5986	12.2	-1.05	40.856	6.67	-1.33	78.132	7.88	-1.35	26.047

Table B.1 Continued									
Name	3800 - 6000 Å			Regions Omitted			4828 - 5363 Å		
	Age (Gyr)	[Fe/H] (dex)	regul	Age (Gyr)	[Fe/H] (dex)	regul	Age (Gyr)	[Fe/H] (dex)	regul
NGC 6093	11.2	-1.29	6.909	8.39	-1.43	40.461	7.34	-1.57	80.919
NGC 6121	12.2	-1.02	5.557	9.22	-1.13	15.095	8.88	-1.09	21.934
NGC 6139	12.2	-0.178	28.110	7.65	-1.27	15.945	8.09	-1.28	120.163
NGC 6171	10.5	-0.595	12.500	10.2	-0.635	11.733	9.57	-0.638	34.538
NGC 6218	7.79	-1.03	12.787	7.61	-1.08	12.056	10.5	-1.08	16.733
NGC 6254	11.2	-1.27	9.063	10.2	-1.34	4.647	8.12	-1.36	4.432
NGC 6266	11.7	-0.412	18.444	7.72	-0.866	16.380	8.93	-0.859	6.327
NGC 6273	11	-1.25	12.381	8.84	-1.36	5.098	8.94	-1.45	4.761
NGC 6284	10.4	-0.588	12.622	7.55	-0.952	22.421	7.92	-0.953	76.393
NGC 6293	9.54	-1.49	53.571	5.4	-1.74	19.137	6.03	-1.95	17.320
NGC 6304	13.3	0.236	2.319	9.52	-0.191	25.749	10.4	-0.242	9.250
NGC 6316	13.3	-0.085	7.172	10.7	-0.425	15.556	11.2	-0.424	6.917
NGC 6333	10.6	-1.48	27.500	9.52	-1.54	20.973	7.65	-1.56	11.191
NGC 6342	10.7	-0.013	8.161	4.88	-0.675	17.210	9.9	-0.465	6.648
NGC 6352	13.2	-0.05	3.322	12.3	-0.301	3.844	12.1	-0.248	2.473
NGC 6356	12.7	-0.11	5.561	11.5	-0.374	5.095	11.7	-0.366	3.081
NGC 6362	13.4	-0.352	2.510	13.7	-0.359	2.354	13.4	-0.465	1.525
NGC 6388	12.7	-0.141	6.345	9.89	-0.383	13.817	9.06	-0.371	5.168
NGC 6397	10	-1.89	63.144	4.25	-1.84	40.887	3.18	-2.13	32.439
NGC 6440	13.3	0.375	3.684	8.71	-0.0769	760.000	12.1	-0.168	17.359
NGC 6441	13.3	0.073	4.654	10.5	-0.272	25.808	9.76	-0.271	23.056
NGC 6522	12.8	-0.508	6.744	8.38	-1.02	12.680	9.65	-1.03	15.197
NGC 6528	13.5	0.226	4.628	12.4	0.104	111.570	11.3	0.139	50.968
NGC 6541	11.8	-1.43	8.950	9.06	-1.56	7.056	7.89	-1.63	4.447
NGC 6553	13.3	0.288	1.703	13.1	0.116	4.620	11	0.0939	28.107
NGC 6569	11.7	-0.249	10.237	8.49	-0.514	18.569	10.6	-0.635	7.736
NGC 6584	9.15	-1.18	12.279	7.97	-1.19	5.539	8.3	-1.19	8.035
NGC 6624	12.6	-0.264	5.869	10	-0.363	10.260	10.3	-0.346	6.886
NGC 6637	12.7	-0.403	6.718	9.62	-0.368	6.085	9.68	-0.321	4.362
NGC 6652	7.68	-0.588	32.822	7.57	-0.651	11.497	8.88	-0.625	5.631
NGC 6656	11.7	-1.17	65.035	7.04	-1.46	56.514	6.81	-1.49	51.450
NGC 6681	9.05	-1.41	20.334	7.83	-1.41	19.168	6.77	-1.42	10.400
NGC 6715	9.13	-0.876	8.769	7.22	-1.04	5.450	7.43	-0.993	7.538
NGC 6717	13.4	-0.43	4.065	12.4	-0.602	11.192	12.8	-0.631	31.419
NGC 6723	8.82	-0.753	24.692	9.48	-0.761	13.663	10.7	-0.779	5.662
NGC 6752	10.1	-1.4	5.787	9.77	-1.41	5.340	7.96	-1.46	6.216

Table B.1 Continued									
Name	3800 - 6000 Å			Regions Omitted			4828 - 5363 Å		
	Age (Gyr)	[Fe/H] (dex)	regul	Age (Gyr)	[Fe/H] (dex)	regul	Age (Gyr)	[Fe/H] (dex)	regul
NGC 6809	7.67	-1.74	9.836	6.64	-1.79	11.663	6.17	-1.87	13.747
NGC 6838	7.24	-0.267	13.405	5.27	-0.626	30.457	9.61	-0.599	7.185
NGC 6864	7.14	-0.982	22.708	7.05	-0.977	9.191	7.98	-0.903	5.812
NGC 6934	8.38	-1.41	51.284	7.39	-1.42	11.213	7.02	-1.33	9.548
NGC 7006	7.92	-1.33	11.006	7.73	-1.44	9.639	7.85	-1.42	8.313
NGC 7078	8.52	-1.68	13.300	5.52	-1.81	16.964	6.89	-2.04	12.894
NGC 7089	8.02	-1.43	7.777	7.94	-1.49	14.927	7.77	-1.49	7.113
NGC 7099	3.95	-1.83	14.484	4.08	-1.81	14.039	4.32	-1.96	106.189
End of Table									

We next show the results of the SpPXF method used on the same WAGGS GC sample as BpPXF, we now see how we can estimate $[\alpha/\text{Fe}]$ when SSP models with a range of $[\alpha/\text{Fe}]$ values.

Table B.2: SpPXF outputs using $[\alpha/\text{Fe}] = 0.3$ and all $[\alpha/\text{Fe}]$ value models.

Name	Full		Omitted		Narrow		Full $[\alpha/\text{Fe}]=0.3$		Omitted $[\alpha/\text{Fe}]=0.3$		Narrow $[\alpha/\text{Fe}]=0.3$	
	Age	$[\text{Fe}/\text{H}]$	Age	$[\text{Fe}/\text{H}]$	Age	$[\text{Fe}/\text{H}]$	Age	$[\text{Fe}/\text{H}]$	Age	$[\text{Fe}/\text{H}]$	Age	$[\text{Fe}/\text{H}]$
Fornax4	8.5	-1.43	9	-1.43	8.5	-1.35	8.5	-1.46	9	-1.52	8.5	-1.52
Fornax5	5.5	-2.14	5.5	-2.14	14	-2.44	5.7	-2.06	5	-2.05	14	-2.53
NGC0104	6	-0.44	13.5	-0.83	6.5	-0.61	10.5	-0.76	8	-0.61	6.5	-0.61
NGC0121	8	-1.31	8	-1.31	8	-1.26	8.9	-1.36	6.5	-1.22	8.5	-1.52
NGC0362	9	-1.22	9	-1.22	9	-1.22	9	-1.26	9	-1.22	9	-1.22
NGC0419	1	-0.42	1.25	-0.92	1.25	-0.83	1.1	-0.66	1.25	-0.92	1.25	-0.92
NGC1261	6.5	-1.31	9	-1.43	9	-1.52	8.5	-1.46	9	-1.52	9	-1.52
NGC1783	1.25	-0.51	1.25	-0.61	1.25	-0.61	1.2	-0.56	1.25	-0.61	1.25	-0.61
NGC1786	7	-1.96	6	-1.96	6	-1.96	7.5	-1.96	7	-2.05	7.5	-2.05
NGC1846	1.5	-0.61	1.5	-0.35	1.25	-0.34	1.5	-0.66	1.5	-0.61	1.25	-0.51
NGC1850	0.06	-0.68	0.06	-0.77	0.06	-1.13	0.1	-0.56	0.1	-0.61	0.06	-1.22
NGC1851	9	-1.31	9	-1.31	9	-1.22	9	-1.26	8	-1.22	9	-1.22
NGC1856	0.25	-0.42	0.25	-0.42	0.3	-0.52	0.2	-0.36	0.25	-0.51	0.25	-0.51
NGC1866	0.15	-0.42	0.15	-0.42	0.2	-0.61	0.2	-0.66	0.15	-0.51	0.2	-0.61
NGC1868	0.8	-0.42	0.8	-0.42	0.9	-0.52	0.8	-0.56	0.8	-0.61	0.8	-0.61
NGC1898	6.5	-1.31	6	-1.31	8	-1.26	7	-1.36	8.5	-1.52	6.5	-1.22
NGC1904	8.5	-1.75	8.5	-1.84	8	-1.75	8.5	-1.76	8.5	-1.75	8	-1.75
NGC1916	1.75	-1.31	2.5	-1.61	2.75	-1.43	2.1	-1.36	2.5	-1.52	2.5	-1.52
NGC1978	2.5	-0.83	2.5	-0.75	2.25	-0.66	2.4	-0.86	2.75	-0.92	2.5	-0.92
NGC2019	7	-1.43	7.5	-1.52	5.5	-1.43	9.1	-1.56	7.5	-1.52	6	-1.52

Table B.2 Continued

Name	Full		Omitted		Narrow		Full $[\alpha/Fe]=0.3$		Omitted $[\alpha/Fe]=0.3$		Narrow $[\alpha/Fe]=0.3$		
	Age	$[Fe/H]$	Age	$[Fe/H]$	Age	$[Fe/H]$	Age	$[Fe/H]$	Age	$[Fe/H]$	Age	$[Fe/H]$	
NGC2136	0.15	-0.44	0.1	-0.52	0.2	-0.57	-0.1	0.1	-0.36	0.15	-0.51	0.09	-0.61
NGC2808	10	-1.22	0.3	-1.22	0.3	-1.22	0.3	10.3	-1.16	9	-1.22	9	-1.22
NGC3201	10.5	-1.31	0.4	-1.35	0.1	-1.31	0.4	10	-1.36	14	-1.52	4.5	-1.22
NGC4147	3.75	-1.84	0.4	-1.84	0.4	-2.05	0.3	3.8	-1.86	3.5	-1.75	3.75	-2.05
NGC4590	6	-2.14	0.4	-2.14	0.4	-2.44	0.2	6	-2.06	4.5	-2.05	14	-2.53
NGC4833	2.5	-2.05	0.3	-2.14	0.4	-2.22	0.5	2.5	-1.96	2.5	-2.05	2.5	-2.05
NGC5024	13.5	-2.14	0.4	-2.14	0.4	-2.05	0.3	8.9	-1.96	13	-2.05	8.5	-2.05
NGC5139	9	-1.52	0.3	-1.52	0.3	-1.75	0.3	9	-1.46	9	-1.52	8.5	-1.75
NGC5272	8.5	-1.52	0.3	-1.43	0.2	-1.52	0.3	8.5	-1.56	9	-1.52	8	-1.52
NGC5286	14	-1.43	0.2	-1.75	0.3	-1.75	0.3	10.5	-1.36	14	-1.75	8.5	-1.75
NGC5634	5	-1.84	0.4	-1.84	0.4	-1.92	0.5	6.1	-1.86	5	-1.75	13.5	-2.05
NGC5694	6	-1.96	0.2	-1.96	0.2	-2.05	0.3	6	-2.06	6	-2.05	6.5	-2.05
NGC5824	8	-2.05	0.3	-2.05	0.3	-2.05	0.3	8	-1.96	7.5	-2.05	8	-2.05
NGC5904	11	-1.31	0.4	-1.31	0.4	-1.31	0.4	10.5	-1.36	14	-1.52	4.5	-1.22
NGC5927	6	0.26	0	-0.42	0.2	-0.42	0.2	13.9	-0.16	13.5	-0.51	13.5	-0.51
NGC5986	14	-1.43	0.2	-1.52	0.3	-1.52	0.3	11.4	-1.36	6	-1.52	7	-1.52
NGC6093	14	-1.52	0.3	-1.75	0.3	-1.92	0.5	10.5	-1.46	14	-1.75	8	-1.75
NGC6121	10.5	-1.22	0.3	-1.31	0.4	-1.39	0.5	10.5	-1.26	5.5	-1.22	5	-1.22
NGC6139	13	-0.79	-0.2	-1.43	0.2	-1.61	0.4	10.5	-1.26	7.5	-1.52	9	-1.52
NGC6171	6.5	-0.83	0.2	-0.92	0.3	-1.01	0.4	11.5	-0.96	7	-0.92	8.5	-0.92
NGC6218	5	-1.22	0.3	-1.22	0.3	-1.31	0.4	4	-1.16	5	-1.22	5.5	-1.22
NGC6254	9	-1.43	0.2	-1.43	0.2	-1.52	0.3	9	-1.46	9	-1.52	8	-1.52
NGC6266	11.5	-0.79	-0.2	-1.22	0.3	-1.22	0.3	13.9	-1.06	8	-1.22	9.5	-1.22

Table B.2 Continued

Name	Full		Omitted		Narrow		Full $[\alpha/Fe]=0.3$		Omitted $[\alpha/Fe]=0.3$		Narrow $[\alpha/Fe]=0.3$		
	Age	$[Fe/H]$	Age	$[Fe/H]$	Age	$[Fe/H]$	Age	$[Fe/H]$	Age	$[Fe/H]$	Age	$[Fe/H]$	
NGC6273	9	-1.43	8.5	-1.43	8.5	-1.66	0.2	9	-1.46	9	-1.52	8.5	-1.75
NGC6284	11	-1.05	5.5	-1.22	9	-1.31	0.4	10.5	-1.16	5.5	-1.22	8	-1.22
NGC6293	10	-1.79	4.5	-2.05	14	-2.44	0.2	9.8	-1.96	4.5	-2.05	5	-2.05
NGC6304	14	-0.16	8.5	-0.34	9.5	-0.51	0.3	13.7	-0.06	9.5	-0.51	9.5	-0.51
NGC6316	13	-0.26	13.5	-0.75	8	-0.61	0.3	13.9	-0.66	6.5	-0.61	8	-0.61
NGC6333	14	-1.75	8.5	-1.75	8.5	-1.84	0.4	13.9	-1.86	8.5	-1.75	8	-1.75
NGC6342	1.75	0.32	4.5	-0.57	13.5	-0.83	0.2	1.3	0.14	1.25	-0.51	6.5	-0.61
NGC6352	13	-0.25	11	-0.44	13	-0.52	0.2	13.9	-0.46	11.5	-0.51	12.5	-0.61
NGC6356	10.5	-0.35	8	-0.52	9	-0.52	0.2	13.9	-0.56	9.5	-0.61	11	-0.61
NGC6362	9	-0.78	14	-0.87	4.5	-0.60	0.4	13.9	-0.76	7	-0.61	5.5	-0.61
NGC6388	7.5	-0.26	5	-0.44	5	-0.44	0.1	13.9	-0.66	6.5	-0.61	6.5	-0.61
NGC6397	2.25	-2.14	2.75	-2.10	2.75	-2.36	0.1	2.5	-2.16	2.25	-2.05	2.5	-2.53
NGC6440	5	0.49	8.5	-0.25	0	-0.51	0.3	10.5	0.14	9.5	-0.51	13	-0.51
NGC6441	11.5	-0.16	7	-0.44	8	-0.44	0.1	13.9	-0.46	6.5	-0.51	6.5	-0.51
NGC6522	13.5	-0.79	10	-1.31	8.5	-1.31	0.4	13.9	-1.06	6	-1.22	7	-1.22
NGC6528	9.5	0.35	9	-0.03	9	-0.03	0.1	13.9	0.04	12.5	-0.20	8	-0.11
NGC6541	14	-1.84	8	-1.92	8	-1.92	0.5	13.9	-1.66	14	-2.05	14	-2.05
NGC6553	5	0.40	8	-0.11	10	-0.20	0.3	13.9	-0.06	11	-0.20	10	-0.20
NGC6569	14	-0.75	7	-0.83	10.5	-0.92	0.3	13.9	-0.86	7.5	-0.92	10.5	-0.92
NGC6584	9	-1.43	9	-1.43	9	-1.43	0.2	9	-1.46	9	-1.52	9	-1.52
NGC6624	9	-0.52	9	-0.61	12.5	-0.70	0.4	13.9	-0.66	9	-0.61	9.5	-0.61
NGC6637	14	-0.78	10	-0.78	12	-0.87	0.6	12.5	-0.66	8.5	-0.61	8.5	-0.61
NGC6652	7.5	-0.75	5.5	-0.75	8.5	-0.92	0.3	7	-0.86	7	-0.92	8.5	-0.92

Table B.2 Continued

Name	Full		Omitted		Narrow		Full $[\alpha/Fe]=0.3$		Omitted $[\alpha/Fe]=0.3$		Narrow $[\alpha/Fe]=0.3$	
	Age	[Fe/H] $[\alpha/Fe]$	Age	[Fe/H] $[\alpha/Fe]$	Age	[Fe/H] $[\alpha/Fe]$	Age	[Fe/H]	Age	[Fe/H]	Age	[Fe/H]
NGC6656	12.5	-1.43 0.2	9.5	-1.75 0.3	7.5	-1.75 0.3	12	-1.46	9.5	-1.75	7.5	-1.75
NGC6681	14	-1.75 0.3	9	-1.75 0.3	8	-1.75 0.3	9	-1.66	9	-1.75	8	-1.75
NGC6715	10.5	-1.22 0.3	6	-1.22 0.3	6.5	-1.22 0.3	10.2	-1.26	6	-1.22	6.5	-1.22
NGC6717	14	-0.92 0.3	4.5	-0.83 0.2	14	-0.92 0.3	13.9	-0.96	14	-0.92	14	-0.92
NGC6723	5.5	-0.92 0.3	5.5	-0.92 0.3	7	-1.01 0.4	8.5	-1.06	5.5	-0.92	7	-0.92
NGC6752	9	-1.52 0.3	9	-1.52 0.3	8.5	-1.75 0.3	8.5	-1.56	9	-1.52	8.5	-1.75
NGC6809	8	-2.14 0.4	8.5	-2.14 0.4	6.5	-2.22 0.5	8	-2.06	6.5	-2.05	5	-2.05
NGC6838	4	-0.49 -0.2	3.5	-0.57 -0.1	9	-0.83 0.2	1.2	-0.26	1.25	-0.51	10.5	-0.92
NGC6864	7.5	-1.22 0.3	6.5	-1.22 0.3	8	-1.13 0.2	6.3	-1.16	6.5	-1.22	9	-1.22
NGC6934	14	-1.66 0.2	9	-1.66 0.2	6	-1.52 0.3	9	-1.66	9	-1.75	6	-1.52
NGC7006	8.5	-1.61 0.4	8.5	-1.75 0.3	8.5	-1.75 0.3	8.5	-1.66	8.5	-1.75	8.5	-1.75
NGC7078	8	-2.05 0.3	4.5	-2.14 0.4	14	-2.44 0.2	8	-2.06	4.5	-2.05	14	-2.53
NGC7089	8.5	-1.75 0.3	8.5	-1.75 0.3	8	-1.75 0.3	8.3	-1.66	8.5	-1.75	8	-1.75
NGC7099	3.25	-2.05 0.3	3.25	-2.05 0.3	3.25	-2.31 0.6	3.3	-2.06	3.25	-2.05	4	-2.05

End of Table

The output values for SpPXF in Chapter 3 used on the WAGGS GC sample. the first column designates the cluster, while the next 9 columns show the results of SpPXF when they are compared to sMILES models (Knowles et al., 2023) with alpha values ranging from $[\alpha/Fe] = -0.2$ to 0.6 at an interval of 0.1 dex. the last 6 columns show the outputs when SpPXF is used with sMILES models with $[\alpha/Fe] = 0.3$.

Finally for the results of Chapter 3, we show the results of the LISm χ method. Since this method relied on specific LIS indices instead of wavelength regions like the previous two methods, we do not show multiple wavelength ranges in the table. Like SpPXF we show how $[\alpha/\text{Fe}]$ can be measured with this method and we split the table in two. one side used SSP models with all available values of $[\alpha/\text{Fe}]$, the other used a fixed values of $[\alpha/\text{Fe}] = 0.3$.

Table B.3: LISm χ outputs using $[\alpha/\text{Fe}] = 0.3$ and all $[\alpha/\text{Fe}]$ value models.

Name	All $[\alpha/\text{Fe}]$			$[\alpha/\text{Fe}] = 0.3$	
	Age (Gyr)	[Fe/H] (dex)	$[\alpha/\text{Fe}]$ (dex)	Age (Gyr)	[Fe/H] (dex)
Fornax4	8.50 ^{+0.12} _{-0.05}	-1.23 ^{+0.05} _{-0.06}	-0.10 ^{+0.05} _{-0.05}	8.50 ^{+0.12} _{-0.05}	-1.23 ^{+0.05} _{-0.06}
NGC0104	11.00 ^{+0.05} _{-0.05}	-0.64 ^{+0.05} _{-0.05}	0.20 ^{+0.05} _{-0.05}	11.00 ^{+0.05} _{-0.05}	-0.64 ^{+0.05} _{-0.05}
NGC0121	9.00 ^{+0.05} _{-0.05}	-1.13 ^{+0.05} _{-0.05}	-0.10 ^{+0.05} _{-0.05}	9.00 ^{+0.05} _{-0.05}	-1.13 ^{+0.05} _{-0.05}
NGC0362	9.50 ^{+0.05} _{-0.05}	-1.07 ^{+0.05} _{-0.05}	0.10 ^{+0.05} _{-0.05}	9.50 ^{+0.05} _{-0.05}	-1.07 ^{+0.05} _{-0.05}
NGC0419	1.20 ^{+0.05} _{-0.05}	-0.63 ^{+0.05} _{-0.05}	-0.10 ^{+0.05} _{-0.05}	1.20 ^{+0.05} _{-0.05}	-0.63 ^{+0.05} _{-0.05}
NGC1261	9.00 ^{+0.05} _{-0.12}	-1.34 ^{+0.05} _{-0.05}	0.20 ^{+0.06} _{-0.05}	9.00 ^{+0.05} _{-0.12}	-1.34 ^{+0.05} _{-0.05}
NGC1783	1.40 ^{+0.05} _{-0.06}	-0.64 ^{+0.05} _{-0.06}	0.20 ^{+0.06} _{-0.05}	1.40 ^{+0.05} _{-0.06}	-0.64 ^{+0.05} _{-0.06}
NGC1786	5.70 ^{+1.67} _{-0.05}	-1.80 ^{+0.05} _{-0.15}	0.30 ^{+0.12} _{-0.05}	5.70 ^{+1.67} _{-0.05}	-1.80 ^{+0.05} _{-0.15}
NGC1846	1.20 ^{+0.21} _{-0.11}	-0.06 ^{+0.16} _{-0.16}	-0.20 ^{+0.14} _{-0.05}	1.20 ^{+0.21} _{-0.11}	-0.06 ^{+0.16} _{-0.16}
NGC1851	9.00 ^{+0.09} _{-0.05}	-1.20 ^{+0.05} _{-0.05}	0.30 ^{+0.05} _{-0.05}	9.00 ^{+0.09} _{-0.05}	-1.20 ^{+0.05} _{-0.05}
NGC1856	0.40 ^{+0.05} _{-0.05}	-0.30 ^{+0.06} _{-0.09}	0.00 ^{+0.08} _{-0.05}	0.40 ^{+0.05} _{-0.05}	-0.30 ^{+0.06} _{-0.09}
NGC1866	0.70 ^{+0.05} _{-0.12}	-0.46 ^{+0.13} _{-0.07}	-0.20 ^{+0.10} _{-0.05}	0.70 ^{+0.05} _{-0.12}	-0.46 ^{+0.13} _{-0.07}
NGC1868	0.80 ^{+0.09} _{-0.11}	-0.44 ^{+0.10} _{-0.05}	0.20 ^{+0.11} _{-0.05}	0.80 ^{+0.09} _{-0.11}	-0.44 ^{+0.10} _{-0.05}
NGC1898	9.00 ^{+0.60} _{-0.85}	-1.17 ^{+0.07} _{-0.14}	0.10 ^{+0.13} _{-0.05}	9.00 ^{+0.60} _{-0.85}	-1.17 ^{+0.07} _{-0.14}
NGC1904	8.10 ^{+1.06} _{-0.05}	-1.74 ^{+0.05} _{-0.05}	0.20 ^{+0.05} _{-0.05}	8.10 ^{+1.06} _{-0.05}	-1.74 ^{+0.05} _{-0.05}
NGC1916	2.20 ^{+0.06} _{-0.28}	-1.40 ^{+0.06} _{-0.05}	0.30 ^{+0.07} _{-0.05}	2.20 ^{+0.06} _{-0.28}	-1.40 ^{+0.06} _{-0.05}
NGC1978	2.20 ^{+0.17} _{-0.21}	-0.60 ^{+0.05} _{-0.05}	0.00 ^{+0.05} _{-0.05}	2.20 ^{+0.17} _{-0.21}	-0.60 ^{+0.05} _{-0.05}
NGC2019	13.50 ^{+0.05} _{-1.95}	-1.37 ^{+0.05} _{-0.14}	0.10 ^{+0.11} _{-0.05}	13.50 ^{+0.05} _{-1.95}	-1.37 ^{+0.05} _{-0.14}
NGC2136	0.10 ^{+0.39} _{-0.05}	-0.37 ^{+0.05} _{-0.17}	0.10 ^{+0.05} _{-0.06}	0.10 ^{+0.39} _{-0.05}	-0.37 ^{+0.05} _{-0.17}
NGC2808	9.50 ^{+0.05} _{-0.05}	-1.14 ^{+0.05} _{-0.05}	0.20 ^{+0.05} _{-0.05}	9.50 ^{+0.05} _{-0.05}	-1.14 ^{+0.05} _{-0.05}
NGC3201	7.90 ^{+0.36} _{-0.05}	-1.27 ^{+0.05} _{-0.05}	0.10 ^{+0.05} _{-0.05}	7.90 ^{+0.36} _{-0.05}	-1.27 ^{+0.05} _{-0.05}
NGC4147	3.40 ^{+2.20} _{-0.67}	-1.80 ^{+0.21} _{-0.08}	0.30 ^{+0.15} _{-0.05}	3.40 ^{+2.20} _{-0.67}	-1.80 ^{+0.21} _{-0.08}
NGC4590	13.90 ^{+0.05} _{-2.86}	-2.34 ^{+0.05} _{-0.05}	0.20 ^{+0.10} _{-0.05}	13.90 ^{+0.05} _{-2.86}	-2.34 ^{+0.05} _{-0.05}
NGC4833	2.60 ^{+0.07} _{-0.05}	-2.41 ^{+0.05} _{-0.05}	0.60 ^{+0.05} _{-0.11}	2.60 ^{+0.07} _{-0.05}	-2.41 ^{+0.05} _{-0.05}
NGC5024	13.90 ^{+0.05} _{-2.82}	-2.27 ^{+0.05} _{-0.07}	0.40 ^{+0.05} _{-0.06}	13.90 ^{+0.00} _{-2.82}	-2.27 ^{+0.05} _{-0.07}
NGC5139	8.00 ^{+0.05} _{-0.05}	-1.81 ^{+0.05} _{-0.05}	0.60 ^{+0.05} _{-0.06}	8.00 ^{+0.05} _{-0.05}	-1.81 ^{+0.05} _{-0.05}
NGC5272	8.50 ^{+0.05} _{-0.05}	-1.37 ^{+0.05} _{-0.05}	0.10 ^{+0.05} _{-0.05}	8.50 ^{+0.05} _{-0.05}	-1.37 ^{+0.05} _{-0.05}
NGC5286	8.50 ^{+0.52} _{-0.45}	-1.74 ^{+0.05} _{-0.05}	0.20 ^{+0.08} _{-0.05}	8.50 ^{+0.52} _{-0.45}	-1.74 ^{+0.05} _{-0.05}

Table B.3 Continued					
Name	All $[\alpha/Fe]$			$[\alpha/Fe] = 0.3$	
	Age (Gyr)	[Fe/H] (dex)	$[\alpha/Fe]$ (dex)	Age (Gyr)	[Fe/H] (dex)
NGC5634	13.60 ^{+0.05} _{-1.26}	-2.07 ^{+0.05} _{-0.05}	0.40 ^{+0.05} _{-0.05}	13.60 ^{+0.05} _{-1.26}	-2.07 ^{+0.05} _{-0.05}
NGC5694	8.50 ^{+2.25} _{-0.13}	-2.04 ^{+0.06} _{-0.05}	0.20 ^{+0.05} _{-0.05}	8.50 ^{+2.25} _{-0.13}	-2.04 ^{+0.06} _{-0.05}
NGC5824	8.50 ^{+0.52} _{-0.44}	-1.84 ^{+0.12} _{-0.06}	0.20 ^{+0.08} _{-0.05}	8.50 ^{+0.52} _{-0.44}	-1.84 ^{+0.12} _{-0.06}
NGC5904	5.90 ^{+1.29} _{-0.24}	-1.24 ^{+0.05} _{-0.05}	0.20 ^{+0.05} _{-0.05}	5.90 ^{+1.29} _{-0.24}	-1.24 ^{+0.05} _{-0.05}
NGC5927	13.00 ^{+0.45} _{-0.13}	-0.34 ^{+0.05} _{-0.05}	0.20 ^{+0.05} _{-0.05}	13.00 ^{+0.45} _{-0.13}	-0.34 ^{+0.05} _{-0.05}
NGC5986	8.50 ^{+0.50} _{-0.56}	-1.64 ^{+0.05} _{-0.05}	0.20 ^{+0.06} _{-0.05}	8.50 ^{+0.50} _{-0.56}	-1.64 ^{+0.05} _{-0.05}
NGC6093	8.50 ^{+1.35} _{-0.05}	-1.94 ^{+0.16} _{-0.14}	0.20 ^{+0.15} _{-0.05}	8.50 ^{+1.35} _{-0.05}	-1.94 ^{+0.16} _{-0.14}
NGC6121	10.60 ^{+0.11} _{-1.91}	-1.41 ^{+0.05} _{-0.05}	0.60 ^{+0.05} _{-0.02}	10.60 ^{+0.11} _{-1.91}	-1.41 ^{+0.05} _{-0.05}
NGC6139	8.50 ^{+0.05} _{-0.21}	-1.74 ^{+0.05} _{-0.07}	0.50 ^{+0.05} _{-0.08}	8.50 ^{+0.05} _{-0.21}	-1.74 ^{+0.05} _{-0.07}
NGC6171	10.00 ^{+0.05} _{-0.11}	-0.97 ^{+0.05} _{-0.05}	0.40 ^{+0.05} _{-0.05}	10.00 ^{+0.05} _{-0.11}	-0.97 ^{+0.05} _{-0.05}
NGC6218	5.50 ^{+1.54} _{-0.05}	-1.20 ^{+0.05} _{-0.05}	0.30 ^{+0.05} _{-0.05}	5.50 ^{+1.54} _{-0.05}	-1.20 ^{+0.05} _{-0.05}
NGC6254	8.00 ^{+0.11} _{-0.05}	-1.81 ^{+0.07} _{-0.06}	0.60 ^{+0.05} _{-0.18}	8.00 ^{+0.11} _{-0.05}	-1.81 ^{+0.07} _{-0.06}
NGC6266	9.50 ^{+0.05} _{-0.05}	-1.10 ^{+0.05} _{-0.05}	0.30 ^{+0.05} _{-0.05}	9.50 ^{+0.05} _{-0.05}	-1.10 ^{+0.05} _{-0.05}
NGC6273	8.00 ^{+0.11} _{-0.05}	-1.30 ^{+0.05} _{-0.05}	0.00 ^{+0.05} _{-0.05}	8.00 ^{+0.11} _{-0.05}	-1.30 ^{+0.05} _{-0.05}
NGC6284	9.00 ^{+0.27} _{-1.14}	-1.14 ^{+0.05} _{-0.05}	0.20 ^{+0.05} _{-0.06}	9.00 ^{+0.27} _{-1.14}	-1.14 ^{+0.05} _{-0.05}
NGC6293	13.90 ^{+0.05} _{-2.36}	-2.40 ^{+0.05} _{-0.05}	0.30 ^{+0.09} _{-0.05}	13.90 ^{+0.05} _{-2.36}	-2.40 ^{+0.05} _{-0.05}
NGC6304	12.50 ^{+0.49} _{-1.72}	-0.50 ^{+0.05} _{-0.05}	0.30 ^{+0.06} _{-0.05}	12.50 ^{+0.49} _{-1.72}	-0.50 ^{+0.05} _{-0.05}
NGC6316	10.50 ^{+0.46} _{-0.08}	-0.70 ^{+0.05} _{-0.05}	0.30 ^{+0.05} _{-0.05}	10.50 ^{+0.46} _{-0.08}	-0.70 ^{+0.05} _{-0.05}
NGC6333	8.50 ^{+1.60} _{-0.21}	-1.84 ^{+0.05} _{-0.06}	0.20 ^{+0.05} _{-0.05}	8.50 ^{+1.60} _{-0.21}	-1.84 ^{+0.05} _{-0.06}
NGC6342	10.50 ^{+0.77} _{-0.98}	-0.77 ^{+0.05} _{-0.05}	0.40 ^{+0.05} _{-0.06}	10.50 ^{+0.77} _{-0.98}	-0.77 ^{+0.05} _{-0.05}
NGC6356	11.00 ^{+0.46} _{-0.05}	-0.54 ^{+0.05} _{-0.05}	0.20 ^{+0.05} _{-0.05}	11.00 ^{+0.46} _{-0.05}	-0.54 ^{+0.05} _{-0.05}
NGC6362	10.50 ^{+0.05} _{-0.21}	-0.77 ^{+0.05} _{-0.05}	0.40 ^{+0.05} _{-0.05}	10.50 ^{+0.05} _{-0.21}	-0.77 ^{+0.05} _{-0.05}
NGC6388	8.40 ^{+0.44} _{-0.33}	-0.50 ^{+0.05} _{-0.05}	0.00 ^{+0.05} _{-0.05}	8.40 ^{+0.44} _{-0.33}	-0.50 ^{+0.05} _{-0.05}
NGC6397	2.50 ^{+0.05} _{-0.05}	-2.34 ^{+0.05} _{-0.05}	0.20 ^{+0.05} _{-0.05}	2.50 ^{+0.05} _{-0.05}	-2.34 ^{+0.05} _{-0.05}
NGC6440	13.50 ^{+0.05} _{-1.24}	-0.44 ^{+0.05} _{-0.05}	0.20 ^{+0.05} _{-0.05}	13.50 ^{+0.05} _{-1.24}	-0.44 ^{+0.05} _{-0.05}
NGC6441	9.50 ^{+0.27} _{-0.08}	-0.47 ^{+0.05} _{-0.05}	0.10 ^{+0.05} _{-0.05}	9.50 ^{+0.27} _{-0.08}	-0.47 ^{+0.05} _{-0.05}
NGC6522	8.80 ^{+0.18} _{-0.22}	-1.27 ^{+0.05} _{-0.05}	0.40 ^{+0.05} _{-0.05}	8.80 ^{+0.18} _{-0.22}	-1.27 ^{+0.05} _{-0.05}
NGC6528	13.90 ^{+0.05} _{-3.02}	-0.17 ^{+0.05} _{-0.05}	0.10 ^{+0.05} _{-0.05}	13.90 ^{+0.05} _{-3.02}	-0.17 ^{+0.05} _{-0.05}
NGC6541	8.50 ^{+0.05} _{-0.05}	-1.84 ^{+0.05} _{-0.05}	0.20 ^{+0.05} _{-0.05}	8.50 ^{+0.05} _{-0.05}	-1.84 ^{+0.05} _{-0.05}
NGC6553	9.80 ^{+2.30} _{-0.8}	-0.14 ^{+0.05} _{-0.05}	0.20 ^{+0.05} _{-0.05}	9.80 ^{+2.30} _{-0.8}	-0.14 ^{+0.05} _{-0.05}
NGC6569	10.50 ^{+0.05} _{-0.23}	-0.90 ^{+0.05} _{-0.05}	0.30 ^{+0.05} _{-0.05}	10.50 ^{+0.05} _{-0.23}	-0.90 ^{+0.05} _{-0.05}
NGC6584	9.00 ^{+0.09} _{-1.08}	-1.40 ^{+0.07} _{-0.08}	0.30 ^{+0.09} _{-0.05}	9.00 ^{+0.09} _{-1.08}	-1.40 ^{+0.07} _{-0.08}
NGC6624	11.50 ^{+0.05} _{-0.43}	-0.60 ^{+0.05} _{-0.05}	0.30 ^{+0.05} _{-0.05}	11.50 ^{+0.05} _{-0.43}	-0.60 ^{+0.05} _{-0.05}
NGC6652	10.00 ^{+0.45} _{-0.15}	-0.87 ^{+0.05} _{-0.05}	0.40 ^{+0.05} _{-0.05}	10.00 ^{+0.45} _{-0.15}	-0.87 ^{+0.05} _{-0.05}
NGC6656	13.90 ^{+0.05} _{-2.52}	-1.84 ^{+0.05} _{-0.05}	0.20 ^{+0.05} _{-0.05}	13.90 ^{+0.05} _{-2.52}	-1.84 ^{+0.05} _{-0.05}
NGC6681	7.40 ^{+1.26} _{-0.05}	-1.74 ^{+0.05} _{-0.05}	0.50 ^{+0.05} _{-0.05}	7.40 ^{+1.26} _{-0.05}	-1.74 ^{+0.05} _{-0.05}

Table B.3 Continued					
Name	All $[\alpha/Fe]$			$[\alpha/Fe] = 0.3$	
	Age (Gyr)	[Fe/H] (dex)	$[\alpha/Fe]$ (dex)	Age (Gyr)	[Fe/H] (dex)
NGC6715	$6.10^{+1.00}_{-0.05}$	$-1.07^{+0.05}_{-0.05}$	$0.10^{+0.05}_{-0.05}$	$6.10^{+1.00}_{-0.05}$	$-1.07^{+0.05}_{-0.05}$
NGC6717	$4.90^{+1.64}_{-0.05}$	$-0.74^{+0.05}_{-0.05}$	$0.20^{+0.05}_{-0.05}$	$4.90^{+1.64}_{-0.05}$	$-0.74^{+0.05}_{-0.05}$
NGC6723	$9.50^{+0.08}_{-0.35}$	$-1.00^{+0.05}_{-0.05}$	$0.30^{+0.05}_{-0.05}$	$9.50^{+0.08}_{-0.35}$	$-1.00^{+0.05}_{-0.05}$
NGC6752	$8.00^{+0.12}_{-0.05}$	$-1.91^{+0.05}_{-0.09}$	$0.60^{+0.05}_{-0.21}$	$8.00^{+0.12}_{-0.05}$	$-1.91^{+0.05}_{-0.09}$
NGC6809	$8.00^{+1.13}_{-0.05}$	$-2.21^{+0.05}_{-0.05}$	$0.60^{+0.05}_{0.05}$	$8.00^{+1.13}_{-0.05}$	$-2.21^{+0.05}_{-0.05}$
NGC6838	$10.50^{+0.12}_{-0.25}$	$-0.87^{+0.05}_{-0.05}$	$0.40^{+0.05}_{-0.05}$	$10.50^{+0.12}_{-0.25}$	$-0.87^{+0.05}_{-0.05}$
NGC6864	$9.50^{+0.13}_{-0.53}$	$-1.14^{+0.05}_{-0.05}$	$0.20^{+0.05}_{-0.05}$	$9.50^{+0.13}_{-0.53}$	$-1.14^{+0.05}_{-0.05}$
NGC6934	$7.60^{+1.59}_{-0.98}$	$-1.50^{+0.10}_{-0.06}$	$0.30^{+0.10}_{-0.05}$	$7.60^{+1.59}_{-0.98}$	$-1.50^{+0.10}_{-0.06}$
NGC7006	$8.50^{+0.43}_{-0.56}$	$-1.74^{+0.05}_{-0.05}$	$0.50^{+0.05}_{-0.07}$	$8.50^{+0.43}_{-0.56}$	$-1.74^{+0.05}_{-0.05}$
NGC7078	$8.00^{+1.17}_{-0.34}$	$-2.51^{+0.05}_{-0.05}$	$0.60^{+0.05}_{-0.07}$	$8.00^{+1.17}_{-0.34}$	$-2.51^{+0.05}_{-0.05}$
NGC7089	$8.00^{+0.15}_{-0.05}$	$-1.91^{+0.05}_{-0.05}$	$0.60^{+0.05}_{-0.17}$	$8.00^{+0.15}_{-0.05}$	$-1.91^{+0.05}_{-0.05}$
NGC7099	$3.30^{+2.35}_{-0.19}$	$-2.21^{+0.09}_{-0.05}$	$0.60^{+0.05}_{-0.18}$	$3.30^{+2.35}_{-0.19}$	$-2.21^{+0.09}_{-0.05}$
End of Table					

The output values for LISM χ in Chapter 3 used on the WAGGS GC sample using the indices, H β Fe5270, Fe5335, & Mg $_b$. The first column designates the cluster, while the next 3 columns show the results of LISM χ when they are compared to sMILES models (Knowles et al., 2023) with alpha values ranging from $[\alpha/Fe] = -0.2$ to 0.6 at an interval of 0.1 dex. The last 2 columns show the outputs when LISM χ is used with sMILES models with $[\alpha/Fe] = 0.3$.

B.1.1 Local GC Results with BSsMILES Models

In Chapter 4 we introduced SSP models which take into account the BSS populations present in GCs. Due to time constraints we only used LISM χ with these models in that chapter while using BpPXF on only a small sample of GCs.

In this section we show the results of LISM χ used with the BSsMILES models on the WAGGS GC sample.

Table B.4: LISM χ Outputs with BSsMILES models

Name	1% BSS		5% BSS		10% BSS	
	Age (Gyr)	[Fe/H] (dex)	Age (Gyr)	[Fe/H] (dex)	Age (Gyr)	[Fe/H] (dex)
Fornax4	$8.50^{+0.09}_{-0.09}$	$-1.52^{+0.05}_{-0.06}$	$8.50^{+0.10}_{-0.10}$	$-1.42^{+0.05}_{-0.06}$	$8.50^{+0.16}_{-0.05}$	$-1.32^{+0.05}_{-0.05}$
NGC0104	$10.50^{+0.05}_{-0.05}$	$-0.72^{+0.05}_{-0.05}$	$10.50^{+0.05}_{-0.05}$	$-0.62^{+0.05}_{-0.05}$	$10.70^{+0.05}_{-0.05}$	$-0.62^{+0.05}_{-0.05}$
NGC0121	$9.00^{+0.09}_{-0.09}$	$-1.32^{+0.05}_{-0.05}$	$9.00^{+0.06}_{-0.06}$	$-1.22^{+0.05}_{-0.05}$	$9.40^{+0.08}_{-0.08}$	$-1.12^{+0.05}_{-0.05}$

Table B.4 Continued

Name	1% BSS		5% BSS		10% BSS	
	Age (Gyr)	[Fe/H] (dex)	Age (Gyr)	[Fe/H] (dex)	Age (Gyr)	[Fe/H] (dex)
NGC0362	9.40 ^{+0.05} _{-0.05}	-1.12 ^{+0.05} _{-0.05}	9.40 ^{+0.05} _{-0.05}	-1.12 ^{+0.05} _{-0.05}	9.40 ^{+0.05} _{-0.05}	-1.02 ^{+0.05} _{-0.05}
NGC1261	9.00 ^{+0.12} _{-0.12}	-1.32 ^{+0.05} _{-0.05}	9.00 ^{+0.05} _{-0.05}	-1.22 ^{+0.05} _{-0.05}	9.40 ^{+0.05} _{-0.05}	-1.12 ^{+0.05} _{-0.05}
NGC1786	9.00 ^{+1.02} _{-2.02}	-1.92 ^{+0.05} _{-0.07}	8.50 ^{+0.80} _{-0.80}	-1.82 ^{+0.05} _{-0.08}	8.50 ^{+0.05} _{-0.05}	-1.62 ^{+0.05} _{-0.08}
NGC1851	9.00 ^{+0.05} _{-0.05}	-1.22 ^{+0.05} _{-0.05}	9.40 ^{+0.05} _{-0.05}	-1.12 ^{+0.05} _{-0.05}	9.40 ^{+0.05} _{-0.05}	-1.02 ^{+0.05} _{-0.05}
NGC1898	9.00 ^{+0.42} _{-0.42}	-1.32 ^{+0.05} _{-0.09}	9.00 ^{+0.32} _{-0.32}	-1.22 ^{+0.05} _{-0.08}	9.40 ^{+0.19} _{-0.19}	-1.12 ^{+0.05} _{-0.07}
NGC1904	8.50 ^{+0.85} _{-0.85}	-1.82 ^{+0.05} _{-0.05}	8.50 ^{+0.05} _{-0.05}	-1.82 ^{+0.05} _{-0.05}	8.50 ^{+0.05} _{-0.05}	-1.52 ^{+0.05} _{-0.05}
NGC1916	3.00 ^{+0.05} _{-0.05}	-1.52 ^{+0.05} _{-0.05}	3.60 ^{+0.95} _{-0.95}	-1.52 ^{+0.05} _{-0.05}	9.40 ^{+0.05} _{-1.06}	-1.62 ^{+0.05} _{-0.05}
NGC2019	7.00 ^{+3.20} _{-0.4}	-1.52 ^{+0.05} _{-0.10}	8.50 ^{+0.39} _{-0.39}	-1.42 ^{+0.05} _{-0.08}	8.50 ^{+0.18} _{-0.18}	-1.32 ^{+0.05} _{-0.06}
NGC2808	9.00 ^{+0.05} _{-0.05}	-1.22 ^{+0.05} _{-0.05}	9.40 ^{+0.05} _{-0.05}	-1.12 ^{+0.05} _{-0.05}	9.40 ^{+0.05} _{-0.05}	-1.02 ^{+0.05} _{-0.05}
NGC3201	8.50 ^{+0.05} _{-0.05}	-1.42 ^{+0.05} _{-0.05}	8.50 ^{+0.08} _{-0.08}	-1.32 ^{+0.05} _{-0.05}	9.00 ^{+0.05} _{-0.05}	-1.22 ^{+0.05} _{-0.05}
NGC4147	3.60 ^{+1.70} _{-1.70}	-1.82 ^{+0.05} _{-0.10}	9.70 ^{+1.21} _{-2.21}	-1.92 ^{+0.05} _{-0.09}	8.50 ^{+0.92} _{-0.92}	-1.82 ^{+0.05} _{-0.10}
NGC4590	13.90 ^{+0.05} _{-0.05}	-2.42 ^{+0.05} _{-0.05}	13.90 ^{+0.00} _{-2.40}	-2.42 ^{+0.16} _{-0.05}	7.60 ^{+0.62} _{-0.62}	-2.02 ^{+0.05} _{-0.05}
NGC4833	3.00 ^{+0.05} _{-0.05}	-2.32 ^{+0.05} _{-0.05}	3.40 ^{+0.05} _{-0.05}	-2.32 ^{+0.05} _{-0.05}	4.90 ^{+0.70} _{-0.70}	-2.22 ^{+0.05} _{-0.05}
NGC5024	13.90 ^{+0.05} _{-2.97}	-2.22 ^{+0.05} _{-0.05}	8.00 ^{+0.42} _{-0.42}	-2.02 ^{+0.05} _{-0.05}	8.50 ^{+0.12} _{-0.12}	-1.92 ^{+0.05} _{-0.05}
NGC5139	8.50 ^{+0.05} _{-0.05}	-1.62 ^{+0.05} _{-0.05}	8.50 ^{+0.05} _{-0.05}	-1.52 ^{+0.05} _{-0.05}	8.50 ^{+0.06} _{-0.06}	-1.32 ^{+0.05} _{-0.05}
NGC5272	8.50 ^{+0.05} _{-0.05}	-1.52 ^{+0.05} _{-0.05}	8.50 ^{+0.05} _{-0.05}	-1.42 ^{+0.05} _{-0.05}	9.00 ^{+0.12} _{-0.12}	-1.22 ^{+0.05} _{-0.05}
NGC5286	8.50 ^{+0.05} _{-0.05}	-1.82 ^{+0.05} _{-0.05}	8.50 ^{+0.05} _{-0.05}	-1.62 ^{+0.05} _{-0.05}	8.50 ^{+0.05} _{-0.05}	-1.52 ^{+0.05} _{-0.05}
NGC5634	7.90 ^{+0.93} _{-0.73}	-1.92 ^{+0.05} _{-0.05}	8.50 ^{+0.05} _{-0.05}	-1.82 ^{+0.05} _{-0.05}	8.50 ^{+0.05} _{-0.05}	-1.82 ^{+0.05} _{-0.05}
NGC5694	13.90 ^{+0.05} _{-2.59}	-2.22 ^{+0.05} _{-0.05}	8.00 ^{+0.29} _{-0.29}	-2.02 ^{+0.05} _{-0.05}	8.00 ^{+0.12} _{-0.12}	-2.02 ^{+0.05} _{-0.05}
NGC5824	8.00 ^{+0.69} _{-0.69}	-1.92 ^{+0.05} _{-0.05}	8.50 ^{+0.11} _{-0.11}	-1.82 ^{+0.05} _{-0.10}	8.50 ^{+0.05} _{-0.05}	-1.42 ^{+0.05} _{-0.07}
NGC5904	6.90 ^{+0.42} _{-0.42}	-1.32 ^{+0.05} _{-0.05}	9.00 ^{+0.05} _{-0.05}	-1.32 ^{+0.05} _{-0.05}	9.00 ^{+0.09} _{-0.09}	-1.22 ^{+0.05} _{-0.05}
NGC5927	13.50 ^{+0.19} _{-0.19}	-0.42 ^{+0.05} _{-0.05}	13.50 ^{+0.05} _{-0.05}	-0.32 ^{+0.05} _{-0.05}	9.70 ^{+0.96} _{-0.96}	-0.22 ^{+0.05} _{-0.05}
NGC5986	8.50 ^{+0.05} _{-0.05}	-1.62 ^{+0.05} _{-0.05}	8.50 ^{+0.05} _{-0.05}	-1.52 ^{+0.05} _{-0.05}	8.50 ^{+0.05} _{-0.05}	-1.42 ^{+0.05} _{-0.05}
NGC6093	8.00 ^{+1.30} _{-1.00}	-2.02 ^{+0.05} _{-0.11}	8.50 ^{+0.92} _{-0.92}	-1.92 ^{+0.05} _{-0.12}	8.50 ^{+0.62} _{-0.62}	-1.82 ^{+0.05} _{-0.13}
NGC6121	10.50 ^{+1.12} _{-0.52}	-1.32 ^{+0.05} _{-0.05}	9.60 ^{+0.12} _{-0.32}	-1.22 ^{+0.05} _{-0.05}	9.40 ^{+0.05} _{-0.05}	-1.12 ^{+0.05} _{-0.05}
NGC6139	8.50 ^{+0.08} _{-0.08}	-1.62 ^{+0.05} _{-0.05}	8.50 ^{+0.05} _{-0.05}	-1.52 ^{+0.05} _{-0.05}	8.50 ^{+0.06} _{-0.06}	-1.42 ^{+0.05} _{-0.05}
NGC6171	9.90 ^{+0.21} _{-0.11}	-0.92 ^{+0.05} _{-0.05}	10.50 ^{+0.05} _{-0.05}	-0.92 ^{+0.05} _{-0.05}	10.50 ^{+0.05} _{-0.05}	-0.82 ^{+0.05} _{-0.05}
NGC6218	6.00 ^{+1.11} _{-0.05}	-1.22 ^{+0.05} _{-0.05}	9.00 ^{+0.18} _{-0.18}	-1.22 ^{+0.05} _{-0.05}	9.40 ^{+0.05} _{-0.05}	-1.12 ^{+0.05} _{-0.05}
NGC6254	8.50 ^{+0.05} _{-0.05}	-1.62 ^{+0.05} _{-0.05}	8.50 ^{+0.05} _{-0.05}	-1.52 ^{+0.05} _{-0.05}	8.50 ^{+0.05} _{-0.05}	-1.42 ^{+0.05} _{-0.05}
NGC6266	9.40 ^{+0.05} _{-0.05}	-1.12 ^{+0.05} _{-0.05}	9.40 ^{+0.05} _{-0.05}	-1.02 ^{+0.05} _{-0.05}	9.40 ^{+0.05} _{-0.05}	-0.92 ^{+0.05} _{-0.05}
NGC6273	8.50 ^{+0.05} _{-0.05}	-1.62 ^{+0.05} _{-0.05}	8.50 ^{+0.05} _{-0.05}	-1.52 ^{+0.05} _{-0.05}	8.50 ^{+0.05} _{-0.05}	-1.42 ^{+0.05} _{-0.05}
NGC6284	9.00 ^{+0.31} _{-0.31}	-1.22 ^{+0.05} _{-0.05}	9.40 ^{+0.08} _{-0.08}	-1.12 ^{+0.05} _{-0.05}	9.40 ^{+0.05} _{-0.05}	-1.02 ^{+0.05} _{-0.05}
NGC6293	13.90 ^{+0.05} _{-0.05}	-2.42 ^{+0.05} _{-0.05}	13.90 ^{+0.05} _{-1.77}	-2.42 ^{+0.11} _{-0.05}	7.60 ^{+0.69} _{-0.69}	-2.02 ^{+0.05} _{-0.05}
NGC6304	12.50 ^{+0.61} _{-0.61}	-0.52 ^{+0.05} _{-0.05}	13.50 ^{+0.05} _{-0.42}	-0.52 ^{+0.05} _{-0.05}	13.50 ^{+0.12} _{-0.12}	-0.42 ^{+0.05} _{-0.05}
NGC6316	10.50 ^{+0.05} _{-0.05}	-0.72 ^{+0.05} _{-0.05}	10.50 ^{+0.05} _{-0.05}	-0.62 ^{+0.05} _{-0.05}	10.70 ^{+0.27} _{-0.27}	-0.62 ^{+0.05} _{-0.05}
NGC6333	13.90 ^{+0.05} _{-2.32}	-2.02 ^{+0.05} _{-0.05}	8.50 ^{+0.05} _{-0.05}	-1.82 ^{+0.05} _{-0.05}	8.50 ^{+0.05} _{-0.05}	-1.52 ^{+0.05} _{-0.05}

Table B.4 Continued						
Name	1% BSS		5% BSS		10% BSS	
	Age (Gyr)	[Fe/H] (dex)	Age (Gyr)	[Fe/H] (dex)	Age (Gyr)	[Fe/H] (dex)
NGC6342	10.50 ^{+0.70} _{-0.70}	-0.72 ^{+0.05} _{-0.05}	10.50 ^{+0.22} _{-0.22}	-0.72 ^{+0.05} _{-0.05}	10.70 ^{+0.39} _{-0.39}	-0.62 ^{+0.05} _{-0.05}
NGC6356	11.50 ^{+0.28} _{-0.28}	-0.62 ^{+0.05} _{-0.05}	12.50 ^{+0.26} _{-0.26}	-0.52 ^{+0.05} _{-0.05}	12.50 ^{+0.19} _{-0.19}	-0.52 ^{+0.05} _{-0.05}
NGC6362	9.80 ^{+0.29} _{-0.29}	-0.72 ^{+0.05} _{-0.05}	10.50 ^{+0.05} _{-0.05}	-0.72 ^{+0.05} _{-0.05}	10.70 ^{+0.05} _{-0.05}	-0.62 ^{+0.05} _{-0.05}
NGC6388	10.50 ^{+0.20} _{-0.20}	-0.82 ^{+0.05} _{-0.05}	10.50 ^{+0.05} _{-0.05}	-0.72 ^{+0.05} _{-0.05}	10.50 ^{+0.05} _{-0.05}	-0.62 ^{+0.05} _{-0.05}
NGC6397	3.00 ^{+0.05} _{-0.05}	-2.42 ^{+0.05} _{-0.05}	3.00 ^{+0.05} _{-0.05}	-2.42 ^{+0.05} _{-0.05}	3.30 ^{+0.05} _{-0.05}	-2.42 ^{+0.05} _{-0.05}
NGC6440	11.00 ^{+1.34} _{-0.05}	-0.42 ^{+0.05} _{-0.05}	13.50 ^{+0.36} _{-0.36}	-0.42 ^{+0.05} _{-0.05}	13.50 ^{+0.40} _{-2.30}	-0.32 ^{+0.05} _{-0.05}
NGC6441	10.50 ^{+0.11} _{-0.11}	-0.62 ^{+0.05} _{-0.05}	10.70 ^{+0.41} _{-0.41}	-0.52 ^{+0.05} _{-0.05}	12.50 ^{+0.18} _{-0.18}	-0.52 ^{+0.05} _{-0.05}
NGC6522	8.90 ^{+0.11} _{-0.05}	-1.22 ^{+0.05} _{-0.05}	9.00 ^{+0.10} _{-0.10}	-1.22 ^{+0.05} _{-0.05}	9.40 ^{+0.05} _{-0.05}	-1.12 ^{+0.05} _{-0.05}
NGC6528	10.50 ^{+1.92} _{-0.05}	-0.22 ^{+0.05} _{-0.06}	13.90 ^{+0.05} _{-2.71}	-0.22 ^{+0.05} _{-0.05}	13.90 ^{+0.05} _{-1.47}	-0.12 ^{+0.05} _{-0.05}
NGC6541	8.00 ^{+0.05} _{-0.05}	-1.92 ^{+0.05} _{-0.05}	8.50 ^{+0.05} _{-0.05}	-1.82 ^{+0.05} _{-0.05}	8.50 ^{+0.05} _{-0.05}	-1.52 ^{+0.05} _{-0.05}
NGC6553	10.50 ^{+1.79} _{-1.79}	-0.22 ^{+0.05} _{-0.05}	13.90 ^{+0.05} _{-2.28}	-0.22 ^{+0.05} _{-0.05}	13.90 ^{+0.05} _{-0.42}	-0.12 ^{+0.05} _{-0.05}
NGC6569	10.50 ^{+0.14} _{-0.14}	-0.92 ^{+0.05} _{-0.05}	10.50 ^{+0.05} _{-0.05}	-0.82 ^{+0.05} _{-0.05}	10.50 ^{+0.05} _{-0.05}	-0.82 ^{+0.05} _{-0.05}
NGC6584	9.00 ^{+0.05} _{-0.20}	-1.42 ^{+0.05} _{-0.05}	9.00 ^{+0.14} _{-0.14}	-1.32 ^{+0.05} _{-0.05}	9.00 ^{+0.16} _{-0.16}	-1.22 ^{+0.05} _{-0.05}
NGC6624	11.50 ^{+0.21} _{-0.21}	-0.62 ^{+0.05} _{-0.05}	11.90 ^{+0.16} _{-0.05}	-0.52 ^{+0.05} _{-0.05}	12.50 ^{+0.05} _{-0.05}	-0.52 ^{+0.05} _{-0.05}
NGC6652	9.50 ^{+0.32} _{-0.05}	-0.82 ^{+0.05} _{-0.05}	10.50 ^{+0.05} _{-0.05}	-0.82 ^{+0.05} _{-0.05}	10.50 ^{+0.05} _{-0.05}	-0.72 ^{+0.05} _{-0.05}
NGC6656	8.50 ^{+0.88} _{-0.88}	-1.82 ^{+0.05} _{-0.05}	8.50 ^{+0.05} _{-0.05}	-1.72 ^{+0.05} _{-0.05}	8.50 ^{+0.05} _{-0.05}	-1.52 ^{+0.05} _{-0.05}
NGC6681	8.50 ^{+0.11} _{-0.11}	-1.72 ^{+0.05} _{-0.05}	8.50 ^{+0.05} _{-0.05}	-1.52 ^{+0.05} _{-0.05}	8.50 ^{+0.05} _{-0.05}	-1.42 ^{+0.05} _{-0.05}
NGC6715	8.00 ^{+0.34} _{-0.34}	-1.22 ^{+0.05} _{-0.05}	9.00 ^{+0.05} _{-0.05}	-1.22 ^{+0.05} _{-0.05}	9.40 ^{+0.05} _{-0.05}	-1.12 ^{+0.05} _{-0.05}
NGC6717	7.40 ^{+0.82} _{-0.72}	-0.92 ^{+0.05} _{-0.05}	9.90 ^{+0.05} _{-0.32}	-0.92 ^{+0.05} _{-0.05}	10.50 ^{+0.11} _{-0.11}	-0.82 ^{+0.05} _{-0.05}
NGC6723	9.40 ^{+0.13} _{-0.05}	-0.92 ^{+0.05} _{-0.05}	9.40 ^{+0.26} _{-0.26}	-0.92 ^{+0.05} _{-0.05}	10.50 ^{+0.20} _{-0.20}	-0.82 ^{+0.05} _{-0.05}
NGC6752	8.50 ^{+0.05} _{-0.05}	-1.62 ^{+0.05} _{-0.05}	8.50 ^{+0.05} _{-0.05}	-1.52 ^{+0.05} _{-0.05}	8.50 ^{+0.05} _{-0.05}	-1.32 ^{+0.05} _{-0.05}
NGC6809	7.00 ^{+0.3} _{-0.05}	-2.02 ^{+0.05} _{-0.05}	8.00 ^{+0.05} _{-0.05}	-2.02 ^{+0.05} _{-0.05}	8.00 ^{+0.05} _{-0.05}	-2.02 ^{+0.05} _{-0.05}
NGC6838	10.00 ^{+0.37} _{-0.05}	-0.82 ^{+0.05} _{-0.05}	10.50 ^{+0.11} _{-0.11}	-0.82 ^{+0.05} _{-0.05}	10.50 ^{+0.05} _{-0.05}	-0.72 ^{+0.05} _{-0.05}
NGC6864	8.90 ^{+0.11} _{-0.05}	-1.12 ^{+0.05} _{-0.05}	9.40 ^{+0.05} _{-0.05}	-1.12 ^{+0.05} _{-0.05}	9.40 ^{+0.05} _{-0.05}	-1.02 ^{+0.05} _{-0.05}
NGC6934	8.10 ^{+1.26} _{-0.46}	-1.52 ^{+0.05} _{-0.06}	8.50 ^{+0.25} _{-0.25}	-1.52 ^{+0.05} _{-0.05}	8.50 ^{+0.08} _{-0.08}	-1.42 ^{+0.05} _{-0.05}
NGC7006	8.50 ^{+0.28} _{-0.28}	-1.62 ^{+0.05} _{-0.05}	8.50 ^{+0.05} _{-0.05}	-1.62 ^{+0.05} _{-0.05}	8.50 ^{+0.05} _{-0.05}	-1.52 ^{+0.05} _{-0.05}
NGC7078	13.90 ^{+0.05} _{-0.05}	-2.42 ^{+0.05} _{-0.05}	13.90 ^{+0.05} _{-0.05}	-2.42 ^{+0.05} _{-0.05}	13.90 ^{+0.05} _{-3.04}	-2.42 ^{+0.19} _{-0.05}
NGC7089	8.50 ^{+0.05} _{-0.05}	-1.82 ^{+0.05} _{-0.05}	8.50 ^{+0.05} _{-0.05}	-1.62 ^{+0.05} _{-0.05}	8.50 ^{+0.05} _{-0.05}	-1.42 ^{+0.05} _{-0.05}
NGC7099	3.70 ^{+0.77} _{-0.97}	-2.12 ^{+0.05} _{-0.09}	4.90 ^{+1.58} _{-1.58}	-2.12 ^{+0.05} _{-0.09}	7.60 ^{+1.33} _{-1.33}	-2.02 ^{+0.05} _{-0.10}

End of Table

The output values for LISM χ in Chapter 4 used on the WAGGS GC sample using the indices, H β Fe5270, Fe5335, & Mg $_b$ and the BSsmILES models at different BSS percentages with $[\alpha/Fe] = 0.3$.

B.2 Results for the Other CSSs

In Chapter 5 we use BpPXF and LISm χ to measure the ages and metallicities of the non-WAGGS CSSs using both sMILES and BSsMILES models for comparison between the two methods and two sets of models. We do not attempt to measure alpha. Although, as discussed in that chapter, we should have.

Bellow we present the results of the age and metallicity measurements.

Table B.5: CSS BpPXF & LISm χ Outputs with sMILES & BSsMILES models

Name	BpPXF				LISm χ			
	sMILES		BSsMILES		sMILES		BSsMILES	
	Age (Gyr)	[Fe/H] (dex)	Age (Gyr)	[Fe/H] (dex)	Age (Gyr)	[Fe/H] (dex)	Age (Gyr)	[Fe/H] (dex)
A496-cE	12.00	-0.11	13.10	-0.01	13.90 ^{+0.05} _{-1.08}	-0.02 ^{+0.05} _{-0.05}	12.70 ^{+0.72} _{-0.07}	0.08 ^{+0.05} _{-0.05}
AHcE0	12.20	-0.42	12.50	-0.35	13.50 ^{+0.05} _{-0.05}	-0.52 ^{+0.05} _{-0.05}	13.50 ^{+0.45} _{-2.43}	-0.32 ^{+0.06} _{-0.07}
AHcE1	13.10	-0.33	12.70	-0.41	8.10 ^{+0.05} _{-0.23}	-0.22 ^{+0.05} _{-0.05}	13.90 ^{+0.05} _{-1.39}	-0.22 ^{+0.05} _{-0.05}
AHcE1232	12.20	-0.49	11.50	-0.48	13.90 ^{+0.05} _{-0.53}	-0.52 ^{+0.05} _{-0.05}	13.30 ^{+0.33} _{-0.12}	-0.42 ^{+0.05} _{-0.05}
AHcE1674	13.50	-0.05	13.60	0.05	11.10 ^{+2.90} _{-1.19}	0.18 ^{+0.05} _{-0.08}	13.90 ^{+0.05} _{-0.05}	0.18 ^{+0.05} _{-0.05}
AHcE2	12.10	-0.12	12.00	-0.14	5.80 ^{+0.99} _{-0.73}	-0.02 ^{+0.06} _{-0.06}	13.40 ^{+0.41} _{-0.55}	-0.12 ^{+0.05} _{-0.05}
AHcE437	12.70	-0.29	13.40	-0.31	10.50 ^{+0.89} _{-0.54}	-0.22 ^{+0.05} _{-0.05}	13.90 ^{+0.05} _{-0.77}	-0.12 ^{+0.05} _{-0.05}
AHcE53	13.20	-0.44	13.30	-0.34	13.90 ^{+0.05} _{-0.05}	-0.42 ^{+0.05} _{-0.05}	9.70 ^{+0.67} _{-0.50}	-0.22 ^{+0.05} _{-0.05}
AHcE5349	13.50	-0.27	13.60	-0.19	13.90 ^{+0.05} _{-0.05}	0.18 ^{+0.05} _{-0.05}	13.90 ^{+0.05} _{-0.05}	0.18 ^{+0.05} _{-0.05}
AHcE6365	12.40	-0.55	12.40	-0.58	13.90 ^{+0.05} _{-7.09}	-0.72 ^{+0.16} _{-0.09}	9.10 ^{+1.58} _{-0.08}	-0.52 ^{+0.05} _{-0.05}
AHcE6861	10.80	-0.24	13.30	-0.21	13.50 ^{+0.07} _{-0.33}	-0.32 ^{+0.05} _{-0.05}	13.90 ^{+0.05} _{-0.05}	-0.12 ^{+0.05} _{-0.05}
AHcE732	13.60	-0.27	13.50	-0.19	13.90 ^{+0.05} _{-0.05}	-0.22 ^{+0.05} _{-0.05}	13.90 ^{+0.05} _{-0.05}	-0.02 ^{+0.05} _{-0.05}
AHcE9313	11.10	-0.09	13.40	-0.04	8.70 ^{+1.66} _{-0.44}	-0.02 ^{+0.05} _{-0.05}	13.90 ^{+0.05} _{-0.05}	-0.02 ^{+0.05} _{-0.05}
cE1	13.00	-0.49	13.00	-0.38	10.80 ^{+0.45} _{-0.30}	-0.52 ^{+0.05} _{-0.05}	13.30 ^{+0.05} _{-0.05}	-0.42 ^{+0.05} _{-0.05}
cE4	13.00	-0.40	13.30	-0.31	13.90 ^{+0.05} _{-0.26}	-0.42 ^{+0.05} _{-0.05}	9.70 ^{+0.90} _{-0.60}	-0.22 ^{+0.05} _{-0.05}
cE547	13.10	-0.37	13.50	-0.30	13.90 ^{+0.05} _{-0.05}	-0.32 ^{+0.05} _{-0.05}	13.90 ^{+0.05} _{-0.05}	-0.22 ^{+0.05} _{-0.05}
chillingarian 117	7.39	-0.26	8.04	-0.27	3.70 ^{+0.91} _{-0.25}	-0.22 ^{+0.05} _{-0.05}	13.30 ^{+0.05} _{-0.08}	-0.42 ^{+0.05} _{-0.05}
CSS-1097	12.90	-0.29	12.50	-0.32	11.30 ^{+2.65} _{-1.57}	-0.52 ^{+0.07} _{-0.06}	13.30 ^{+0.17} _{-0.08}	-0.42 ^{+0.05} _{-0.05}
CSS-1145	13.10	-0.85	12.20	-0.80	11.80 ^{+0.30} _{-0.51}	-0.82 ^{+0.05} _{-0.05}	10.70 ^{+0.05} _{-0.20}	-0.62 ^{+0.05} _{-0.05}
CSS-1555	10.90	-0.89	9.16	-0.83	9.50 ^{+0.08} _{-0.39}	-1.02 ^{+0.05} _{-0.05}	10.50 ^{+0.20} _{-0.36}	-0.82 ^{+0.05} _{-0.05}
CSS-251	13.40	-0.35	13.70	-0.25	13.90 ^{+0.05} _{-0.21}	-0.32 ^{+0.05} _{-0.05}	13.90 ^{+0.05} _{-0.05}	-0.22 ^{+0.05} _{-0.05}
CSS-756	13.00	-0.57	12.00	-0.48	13.90 ^{+0.05} _{-4.22}	-0.62 ^{+0.05} _{-0.05}	13.20 ^{+0.29} _{-0.10}	-0.52 ^{+0.05} _{-0.05}
CSS-969	13.30	0.13	13.50	0.16	13.90 ^{+0.05} _{-0.05}	0.18 ^{+0.05} _{-0.05}	13.90 ^{+0.05} _{-0.05}	0.18 ^{+0.05} _{-0.05}
Galaxy266	11.60	0.07	12.70	0.11	13.90 ^{+0.05} _{-5.05}	-0.12 ^{+0.33} _{-0.05}	13.50 ^{+0.18} _{-0.18}	0.18 ^{+0.05} _{-0.05}
HGHH92-G22	10.40	-1.19	9.14	-1.10	13.00 ^{+0.95} _{-7.41}	-1.02 ^{+0.12} _{-0.11}	9.70 ^{+1.49} _{-2.16}	-1.02 ^{+0.13} _{-0.05}
HGHH92-G23	9.76	-0.24	9.64	-0.36	7.30 ^{+3.89} _{-1.54}	-0.42 ^{+0.05} _{-0.13}	13.30 ^{+0.05} _{-0.05}	-0.42 ^{+0.05} _{-0.05}
HGHH92-G7	1.75	-0.08	3.63	-0.57	1.70 ^{+4.19} _{-1.65}	-0.32 ^{+0.19} _{-0.24}	3.70 ^{+3.84} _{-0.70}	-0.62 ^{+0.11} _{-0.05}
LEDA1414042	12.60	-0.15	13.40	-0.09	13.90 ^{+0.05} _{-0.05}	-0.22 ^{+0.05} _{-0.05}	13.90 ^{+0.05} _{-0.05}	-0.02 ^{+0.05} _{-0.05}
LEDA43301	13.30	-0.04	13.60	0.05	13.60 ^{+0.35} _{-2.87}	-0.02 ^{+0.09} _{-0.05}	13.50 ^{+0.16} _{-0.52}	0.18 ^{+0.05} _{-0.05}
LEDA4573336-NSC	8.03	-1.75	8.45	-1.60	8.50 ^{+0.07} _{-0.10}	-1.82 ^{+0.05} _{-0.05}	8.50 ^{+0.05} _{-0.05}	-1.42 ^{+0.05} _{-0.05}
M31_B017-G070	10.80	-0.63	10.50	-0.63	11.20 ^{+0.59} _{-2.52}	-0.82 ^{+0.05} _{-0.05}	10.70 ^{+0.05} _{-0.05}	-0.62 ^{+0.05} _{-0.05}
M31_B023-G078	10.10	-0.56	11.20	-0.61	12.60 ^{+0.61} _{-0.76}	-0.72 ^{+0.05} _{-0.05}	13.10 ^{+0.05} _{-0.05}	-0.52 ^{+0.05} _{-0.05}
M59cO	13.40	-0.13	13.60	-0.05	13.90 ^{+0.05} _{-0.08}	-0.12 ^{+0.05} _{-0.05}	13.90 ^{+0.05} _{-0.05}	-0.02 ^{+0.05} _{-0.05}

Table B.5 Continued								
Name	BpPXF				LISm χ			
	sMILES		BSsMILES		sMILES		BSsMILES	
	Age (Gyr)	[Fe/H] (dex)	Age (Gyr)	[Fe/H] (dex)	Age (Gyr)	[Fe/H] (dex)	Age (Gyr)	[Fe/H] (dex)
M60-UCD1	13.10	0.07	13.50	0.12	10.60 ^{+0.09} _{-0.08}	0.18 ^{+0.05} _{-0.05}	13.90 ^{+0.05} _{-0.05}	0.18 ^{+0.05} _{-0.05}
M60UCDY	11.40	-0.53	12.10	-0.46	10.10 ^{+3.53} _{-0.05}	-0.52 ^{+0.05} _{-0.05}	13.50 ^{+0.04} _{-0.26}	-0.52 ^{+0.05} _{-0.05}
M87_GC2	12.60	0.07	13.30	0.11	13.90 ^{+0.05} _{-1.43}	0.18 ^{+0.05} _{-0.05}	13.90 ^{+0.05} _{-0.05}	0.18 ^{+0.05} _{-0.05}
M87_GC5	7.11	-0.93	7.82	-8.04	8.30 ^{+3.47} _{-3.63}	-1.12 ^{+0.67} _{-0.45}	9.40 ^{+2.14} _{-3.45}	-0.92 ^{+0.38} _{-0.35}
M87_GC6	11.80	-0.06	11.50	-0.10	13.50 ^{+0.10} _{-0.13}	-0.42 ^{+0.11} _{-0.05}	9.70 ^{+4.06} _{-0.05}	-0.22 ^{+0.25} _{-0.05}
M87-UCD1	9.22	-1.50	7.46	-1.21	9.00 ^{+0.06} _{-0.11}	-1.32 ^{+0.05} _{-0.05}	9.40 ^{+0.05} _{-0.05}	-1.12 ^{+0.05} _{-0.05}
M87-UCD3	8.97	-1.06	9.28	-1.13	9.00 ^{+0.43} _{-1.31}	-1.32 ^{+0.13} _{-0.05}	9.40 ^{+0.15} _{-0.45}	-1.12 ^{+0.11} _{-0.05}
M87-UCD4	8.43	-0.81	9.07	-1.03	6.60 ^{+3.22} _{-2.30}	-1.02 ^{+0.25} _{-0.14}	9.40 ^{+0.55} _{-1.35}	-0.92 ^{+0.11} _{-0.05}
MRK1216	12.50	0.04	13.70	0.11	13.90 ^{+0.05} _{-0.05}	0.18 ^{+0.05} _{-0.05}	13.90 ^{+0.05} _{-0.05}	0.18 ^{+0.05} _{-0.05}
NGC0052-dE1	11.50	-0.44	10.60	-0.42	4.20 ^{+0.05} _{-0.10}	-0.32 ^{+0.05} _{-0.05}	13.20 ^{+0.22} _{-0.12}	-0.52 ^{+0.05} _{-0.05}
NGC0628-NSC	10.10	-0.53	9.43	-0.53	3.70 ^{+0.54} _{-0.21}	-0.52 ^{+0.05} _{-0.05}	9.10 ^{+0.05} _{-0.05}	-0.62 ^{+0.05} _{-0.05}
NGC1128-cE	12.70	-0.34	12.30	-0.31	11.60 ^{+1.67} _{-0.68}	-0.42 ^{+0.05} _{-0.05}	13.50 ^{+0.45} _{-2.84}	-0.32 ^{+0.05} _{-0.05}
NGC2344-NSC	11.20	-0.28	13.40	-0.25	7.60 ^{+0.05} _{-0.05}	-0.22 ^{+0.05} _{-0.05}	13.90 ^{+0.05} _{-0.05}	-0.22 ^{+0.05} _{-0.05}
NGC2832-cE	13.50	-0.40	13.40	-0.31	13.90 ^{+0.05} _{-0.05}	-0.42 ^{+0.05} _{-0.05}	13.90 ^{+0.05} _{-2.86}	-0.22 ^{+0.05} _{-0.05}
NGC2892-cE	12.70	-0.12	12.80	-0.08	5.00 ^{+0.30} _{-0.22}	0.18 ^{+0.05} _{-0.05}	13.90 ^{+0.05} _{-0.84}	-0.02 ^{+0.05} _{-0.05}
NGC4486B	13.60	-0.09	13.70	0.03	11.00 ^{+0.05} _{-0.05}	0.18 ^{+0.05} _{-0.05}	13.90 ^{+0.05} _{-0.05}	0.18 ^{+0.05} _{-0.05}
NGC4546-UCD1	11.60	-0.16	13.50	-0.08	13.50 ^{+0.32} _{-0.20}	-0.22 ^{+0.05} _{-0.05}	13.90 ^{+0.05} _{-0.05}	-0.02 ^{+0.05} _{-0.05}
NGC4565-UCD1	8.51	-1.04	9.19	-1.02	10.70 ^{+0.05} _{-0.05}	-1.12 ^{+0.05} _{-0.05}	8.90 ^{+0.45} _{-0.05}	-0.92 ^{+0.05} _{-0.05}
NGC4621-UCD3	13.40	-0.13	13.60	-0.05	13.90 ^{+0.05} _{-0.05}	-0.12 ^{+0.05} _{-0.05}	13.90 ^{+0.05} _{-1.16}	-0.02 ^{+0.05} _{-0.05}
NGC5846A	13.20	-0.03	13.50	0.06	13.90 ^{+0.05} _{-0.05}	-0.02 ^{+0.05} _{-0.05}	13.80 ^{+0.10} _{-0.20}	0.18 ^{+0.05} _{-0.05}
NGC7014-cE	11.70	-0.19	12.90	-0.25	6.30 ^{+3.31} _{-2.21}	-0.22 ^{+0.14} _{-0.15}	9.70 ^{+1.39} _{-0.96}	-0.22 ^{+0.05} _{-0.08}
NGC7252-W30	1.18	-0.31	3.13	-1.58	0.90 ^{+0.05} _{-0.05}	-0.62 ^{+0.18} _{-0.05}	3.00 ^{+0.05} _{-0.05}	-1.52 ^{+0.05} _{-0.05}
NGC741-cE	13.40	-0.09	13.60	0.00	10.70 ^{+0.07} _{-0.11}	0.18 ^{+0.05} _{-0.05}	13.90 ^{+0.05} _{-0.05}	0.18 ^{+0.05} _{-0.05}
rs0685	10.60	-0.11	12.70	-0.09	11.90 ^{+1.50} _{-0.33}	-0.22 ^{+0.05} _{-0.05}	13.90 ^{+0.05} _{-0.43}	-0.02 ^{+0.05} _{-0.05}
rs0686	11.00	-0.36	12.80	-0.32	8.90 ^{+1.56} _{-1.21}	-0.32 ^{+0.07} _{-0.06}	9.70 ^{+2.41} _{-0.84}	-0.22 ^{+0.05} _{-0.05}
Sombrero-UCD1	13.20	-0.27	13.40	-0.23	13.90 ^{+0.05} _{-0.45}	-0.32 ^{+0.05} _{-0.05}	13.90 ^{+0.05} _{-0.05}	-0.22 ^{+0.05} _{-0.05}
UGC12732-NSC	7.83	-1.24	8.49	-1.13	8.50 ^{+1.65} _{-1.09}	-1.72 ^{+0.16} _{-0.13}	8.50 ^{+0.81} _{-0.38}	-1.52 ^{+0.17} _{-0.16}
VUCD1	11.90	-0.72	9.48	-0.65	10.50 ^{+0.09} _{-0.14}	-0.82 ^{+0.05} _{-0.05}	10.50 ^{+0.08} _{-0.05}	-0.62 ^{+0.05} _{-0.05}
VUCD3	13.60	-0.08	13.70	0.03	13.90 ^{+0.05} _{-0.05}	-0.02 ^{+0.05} _{-0.05}	13.90 ^{+0.05} _{-0.05}	0.18 ^{+0.05} _{-0.05}
VUCD7	11.90	-0.60	9.60	-0.59	10.50 ^{+0.23} _{-0.26}	-0.72 ^{+0.05} _{-0.05}	13.10 ^{+0.13} _{-1.66}	-0.52 ^{+0.05} _{-0.05}
NGC7252-W3	0.46	-0.06	3.08	-1.59	0.40 ^{+0.05} _{-0.05}	0.08 ^{+0.05} _{-0.05}	3.00 ^{+0.05} _{-0.05}	-2.42 ^{+0.05} _{-0.05}

End of Table

The output results of BpPXF and LISm χ for the non-WAGGS CSSs in the sample from Chapter 5. We use both sMILES and BSsMILES SSP models for comparison.

Appendix C

Results Analysis Plots

In this Appendix chapter we will show the plots from Chapter 5 which did not fit into the chapter without disrupting narrative of the chapter (or making it far too long). They cover a range of topics from further analysis of the age and metallicity outputs of the CSSs to BpPXF mass-fraction plots for many objects and a comparison of C and N enriched SSP models

C.1 Age and Metallicity Residual Comparison.

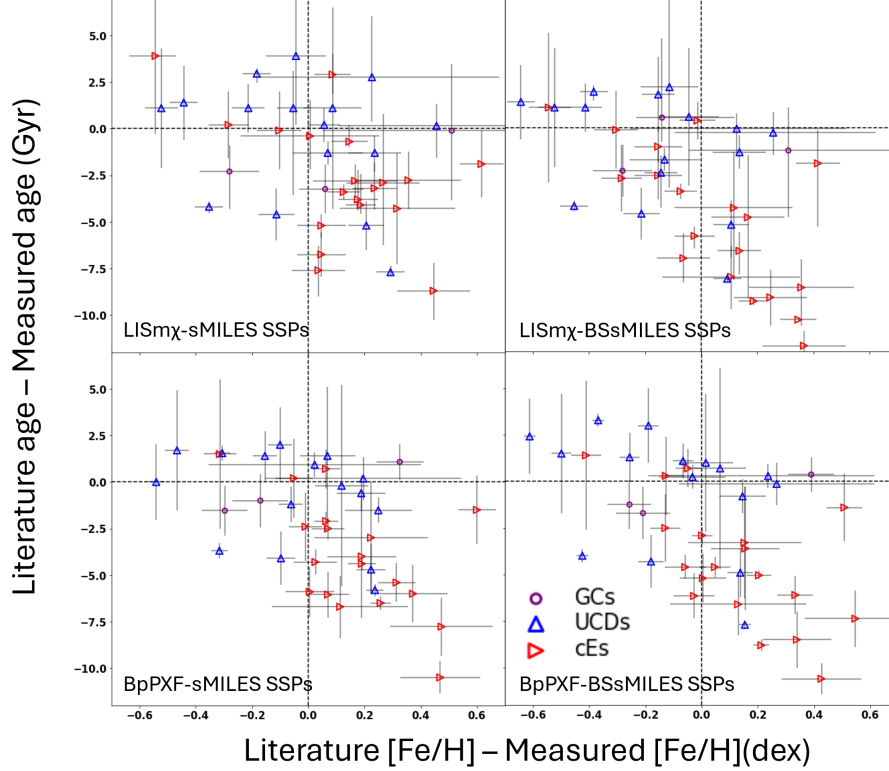


Figure C.1: Residual age (literature minus measured) against Residual metallicity (literature $[\text{Fe}/\text{H}]$ minus Measured $[\text{Fe}/\text{H}]$) for GCs, UCDs, & cEs. The top left shows the output results from the LISm χ method using interpolated sMILES SSP models, and the top right shows the same method using the interpolated BSsMILES SSP models. The bottom left panel shows the results from BpPXF using sMILES SSP models and the bottom right panel shows the BpPXF results with BSsMILES SSPs.

C.2 BpPXF NSCs

The following plots are used to show the BpPXF fits of the four NSCs in the sample. They are supporting evidence for the speculative classifications made for the formation of these objects made in Section 5.6.

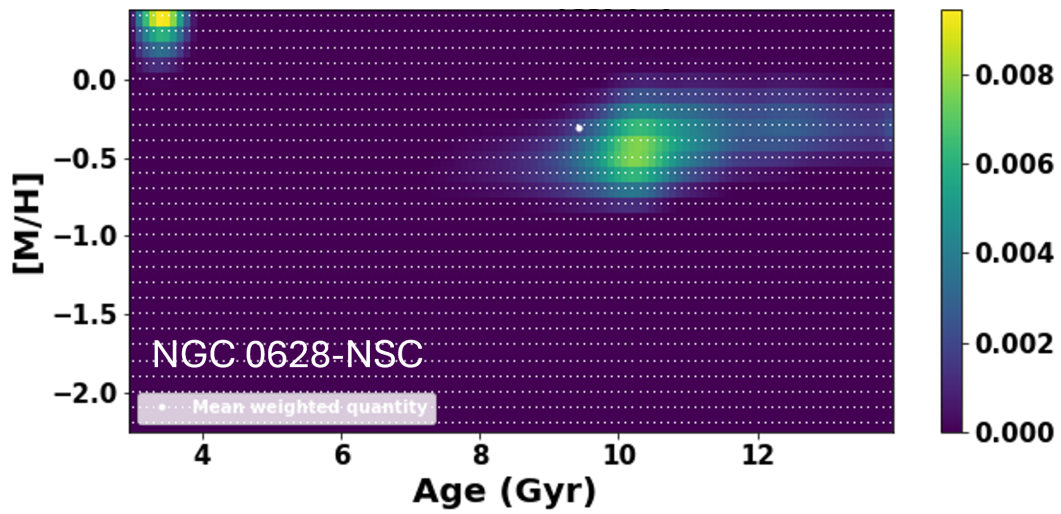


Figure C.2: The BpPXF output mass-fraction weights plots for the CSSs NGC 628-NSC.

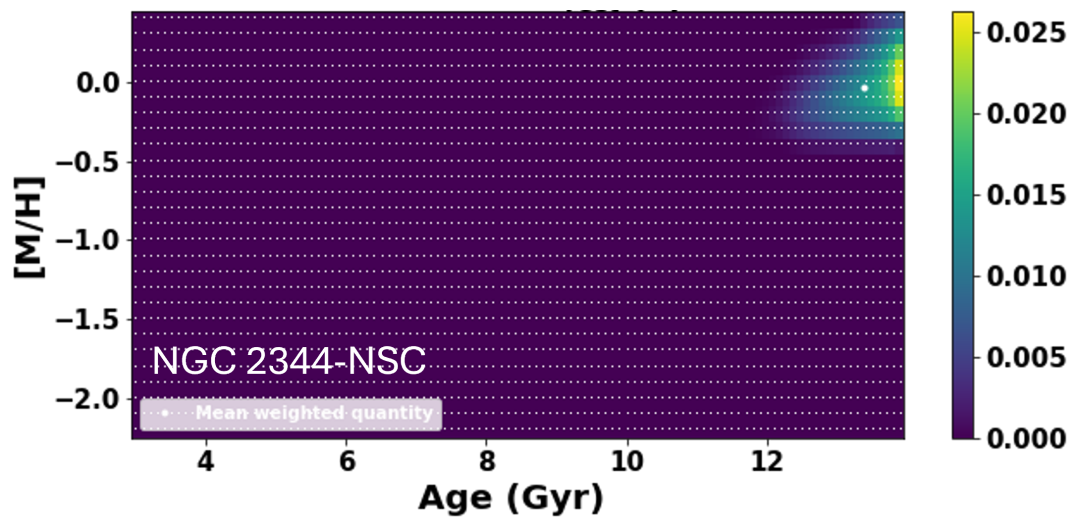


Figure C.3: The BpPXF output mass-fraction weights plots for the CSSs NGC 2344-NSC.

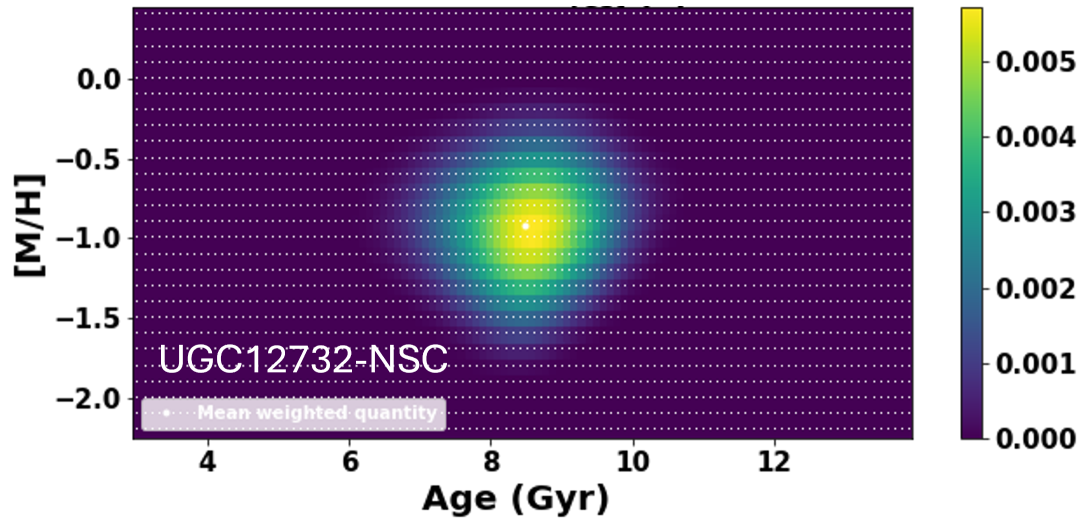


Figure C.4: The BpPXF output mass-fraction weights plots for the CSSs UGC12732-NSC.

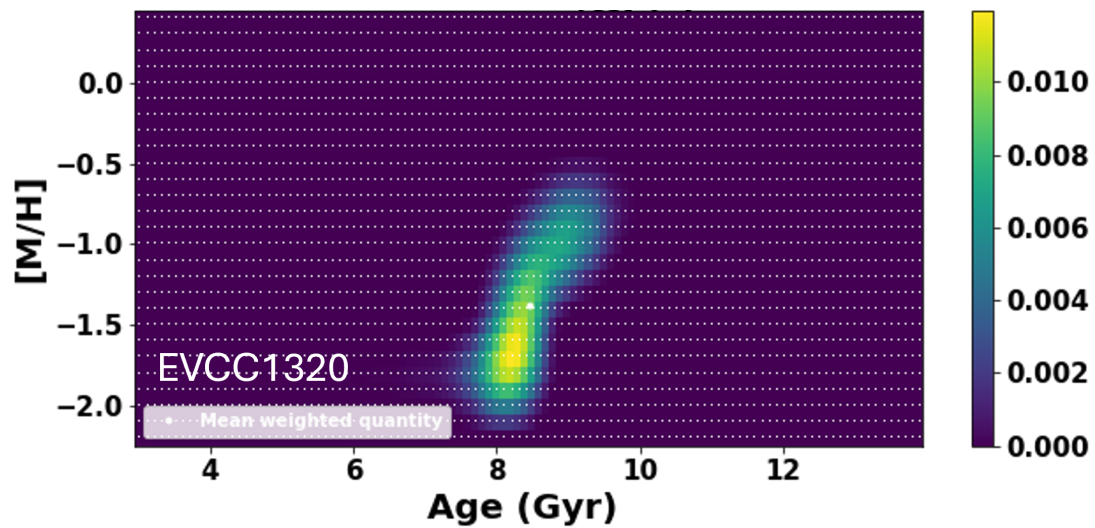


Figure C.5: The BpPXF output mass-fraction weights plots for the CSSs EVCC1320.

C.3 CN enhancements

In Section 5.7.4 we state that the CN LIS index is more sensitive to nitrogen than it is for carbon. We reference the plot below stating that because the carbon region to the right of our extended CN region doesn't show enhanced absorption and because there is a C-N anti correlation that carbon will be depleted, which would reduce the absorption of that region if it were dominant the CN region is dominated by

nitrogen abundance. This is in agreement with the literature

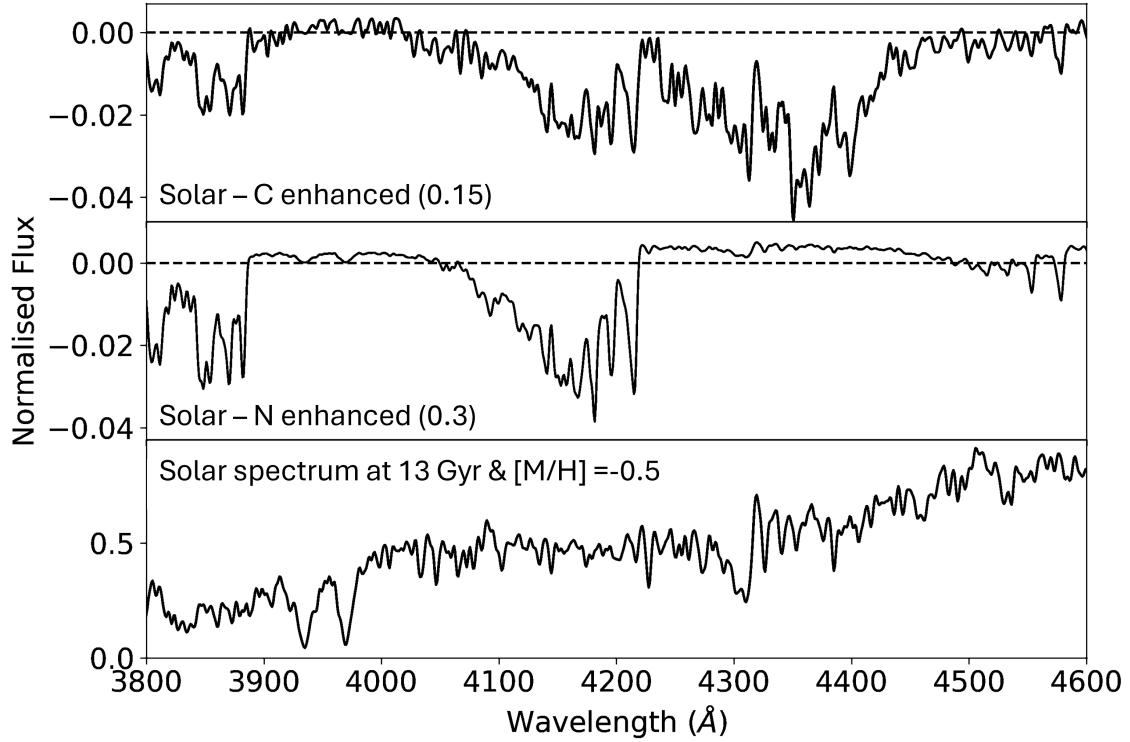


Figure C.6: Comparison plot showing the residuals for the Conroy et al. (2018) C and N enhanced spectra to a Solar abundance spectrum. The N spectrum is enhanced by 0.3 dex while the C spectrum is enhanced by 0.15 dex to avoid the formation of carbon stars. This plot is taken from Banister (2020) where it was used to define the extended CN region and to show how N is the dominant element in that region for GCs showing signatures of MPs.

Appendix D

Further Information

The following tables are just supplementary information which may be useful to help explain certain points in this thesis.

The first table shows the specific wavelength regions of the LICK/IDS (LIS) indices, and shows what units they are measured in.

Table D.1: Table of LICK/IDS Indices.

Name	Index units	Min \AA	Max \AA	Min blue \AA	Max blue \AA	Min red \AA	Max red \AA
CN ₁	Mag	4142.125	4177.125	4080.125	4117.625	4244.125	4284.125
CN ₂	Mag	4142.125	4177.125	4083.875	4096.375	4244.125	4284.125
Ca1 _{LB13}	EW	8484.000	8513.000	8474.000	8484.000	8563.000	8577.000
Ca2 _{LB13}	EW	8522.000	8562.000	8474.000	8484.000	8563.000	8577.000
Ca3 _{LB13}	EW	8642.000	8682.000	8619.000	8642.000	8700.000	8725.000
Ca4227	EW	4222.250	4234.750	4211.000	4219.750	4241.000	4251.000
Ca4455	EW	4452.125	4474.625	4445.875	4454.625	4477.125	4492.125
CaH	EW	6775.000	6817.000	6520.000	6545.000	7035.000	7050.000
CaHK _{LB13}	EW	3899.470	4003.470	3806.500	3833.820	4020.690	4052.360
CaH ₁	Mag	6357.500	6401.750	6342.125	6356.500	6408.500	6429.750
CaH ₂	Mag	6775.000	6900.000	6510.000	6539.250	7017.000	7064.000
Fe4383	EW	4369.125	4420.375	4359.125	4370.375	4442.875	4455.375
Fe4531	EW	4514.250	4559.250	4504.250	4514.250	4560.500	4579.250
Fe4668	EW	4634.000	4720.250	4611.500	4630.250	4742.750	4756.500
Fe5015	EW	4977.750	5054.000	4946.500	4977.750	5054.000	5065.250
Fe5270	EW	5245.650	5285.650	5233.150	5248.150	5285.650	5318.150
Fe5335	EW	5312.125	5352.125	5304.625	5315.875	5353.375	5363.375

Table D.1 Continued							
Name	Index units	Min Å	Max Å	Min blue Å	Max blue Å	Min red Å	Max red Å
Fe5406	EW	5387.500	5415.000	5376.250	5387.500	5415.000	5425.000
Fe5709	EW	5696.625	5720.375	5672.875	5696.625	5722.875	5736.625
Fe5782	EW	5776.625	5796.625	5765.375	5775.375	5797.875	5811.625
G4300	EW	4281.375	4316.375	4266.375	4282.625	4318.875	4335.125
H β	EW	4847.875	4876.625	4827.875	4847.875	4876.625	4891.625
H β 0	EW	4839.275	4877.097	4821.175	4838.404	4897.445	4915.845
H β EW	EW	4847.875	4876.625	4799.000	4839.000	4886.000	4926.000
H δ EW	EW	4083.500	4122.250	4017.000	4057.000	4153.000	4193.000
H δ _A	EW	4083.500	4122.250	4041.600	4079.750	4128.500	4161.000
H δ _F	EW	4091.000	4112.250	4057.250	4088.500	4114.750	4137.250
H γ EW	EW	4319.750	4363.500	4242.000	4282.000	4404.000	4444.000
H γ _A	EW	4319.750	4363.500	4283.500	4319.750	4367.250	4419.750
H γ _F	EW	4331.250	4352.250	4283.500	4319.750	4354.750	4384.750
Mg4780	EW	4760.780	4798.800	4738.910	4757.310	4819.780	4835.510
Mg ₁	Mag	5069.125	5134.125	4895.125	4957.625	5301.125	5366.125
Mg ₂	Mag	5154.125	5196.625	4895.125	4957.625	5301.125	5366.125
Mg _b	EW	5160.125	5192.625	5142.625	5161.375	5191.375	5206.375
NaI	EW	8163.500	8229.125	8140.000	8163.500	8230.250	8250.000
NaI _{F13}	EW	8180.000	8200.000	8137.000	8147.000	8233.000	8244.000
NaI _{LB13}	EW	8180.000	8200.000	8143.000	8153.000	8233.000	8244.000
NaI _{V12}	EW	8180.000	8200.000	8164.000	8173.000	8233.000	8244.000
NaD	EW	5876.875	5909.375	5860.625	5875.625	5922.125	5948.125
OIIEW	EW	3716.300	3738.300	3696.300	3716.300	3738.300	3758.300
TiO2SDSS _{LB13}	Mag	6189.625	6272.125	6066.625	6141.625	6442.000	6455.000
TiO3	EW	6600.000	6723.000	6520.000	6545.000	7035.000	7050.000
TiOCaH	EW	6600.000	6817.000	6520.000	6545.000	7035.000	7050.000
TiO ₁	Mag	5936.625	5994.125	5816.625	5849.125	6038.625	6103.625
TiO ₂	Mag	6189.625	6272.125	6066.625	6141.625	6372.625	6415.125
TiO ₃	Mag	7123.750	7162.500	7017.000	7064.000	7234.000	7269.000
TiO ₄	Mag	7643.250	7717.250	7527.000	7577.750	7735.500	7782.750
aTiO	Mag	5445.000	5600.000	5420.000	5442.000	5630.000	5655.000
bTiO	EW	4758.500	4800.000	4742.750	4756.500	4827.875	4847.875
End of Table							

The second set of tables in this appendix chapter shows the conversion values for Equation 3.3, which is used to convert LICK/IDS indices onto the newer LIS index system.

Table D.2: Table 1 of LICK/IDS - LIS Index conversion values for Equation 3.3

	LIS-5.0Å				LIS-8.4Å			
	a0	a1	a2	a3	a0	a1	a2	a3
CN1	0.018	0.941	-0.137	0.352	0.011	0.913	-0.119	0.400
CN2	0.027	0.955	-0.059	0.106	0.016	0.911	0.025	0.076
Ca4227	0.253	0.738	0.177	-0.018	0.217	0.668	0.140	-0.014
G4300	0.709	0.944	0.029	-0.006	0.541	0.540	0.015	-0.004
Fe4383	0.211	0.923	-0.005	0.001	0.106	0.796	0.015	—
Ca4455	0.035	0.602	0.250	-0.032	0.021	0.466	0.187	-0.016
Fe4531	0.304	1.092	-0.046	0.002	0.267	0.972	-0.032	0.003
C4668	0.642	0.831	0.017	—	0.616	0.819	0.017	—
H β	0.116	1.001	-0.003	0.001	0.159	0.953	-0.002	0.001
Fe5015	-0.154	1.162	-0.025	—	-0.037	0.994	-0.018	—
Mg1	-0.001	0.886	0.146	0.140	-0.001	0.884	0.056	0.358
Mg2	-0.004	0.924	0.013	-0.028	-0.004	0.906	0.054	-0.051
Mgb	0.116	0.950	0.009	-0.001	0.116	0.912	0.009	-0.001
Fe5270	0.256	0.705	0.122	-0.013	0.253	0.649	0.104	-0.010
Fe5335	0.259	0.805	0.141	-0.019	0.214	0.708	0.120	-0.015
Fe5406	0.289	0.629	0.266	-0.047	0.257	0.587	0.225	-0.040
Fe5709	0.006	1.045	-0.052	0.016	-0.005	1.024	-0.108	0.030
Fe5782	0.119	0.467	0.693	-0.213	0.055	0.707	0.182	—
Na5895	-0.074	0.921	0.023	-0.001	-0.057	0.887	0.025	-0.001
TiO1	-0.004	0.773	0.723	-0.826	-0.004	0.766	0.736	-0.841
TiO2	0.001	0.924	0.116	-0.132	0.001	0.919	0.128	-0.142
H δ A	-0.369	1.012	1.012	—	-0.246	0.977	0.006	—
H γ A	-0.151	0.974	0.001	—	-0.175	0.986	—	—
H δ F	0.028	0.970	0.037	-0.003	0.027	0.973	0.016	-0.001
H γ F	-0.174	1.050	0.013	-0.002	-0.149	1.010	0.015	-0.002

Table D.3: Table 2 of LICK/IDS - LIS Index conversion values for Equation 3.3

	LIS-14.0Å			
	a0	a1	a2	a3
CN1	0.005	0.875	-0.091	0.402
CN2	-0.002	0.863	-0.110	0.477
Ca4227	0.134	0.380	0.113	-0.008
G4300	0.251	0.910	0.019	-0.004
Fe4383	-0.203	0.749	-0.004	0.001
Ca4455	0.031	0.331	0.073	0.005
Fe4531	0.211	0.814	-0.025	0.004
C4668	0.500	0.779	0.006	—
H β	0.257	0.861	-0.003	0.001
Fe5015	0.123	0.738	-0.004	—
Mg1	-0.003	0.885	-0.164	0.856
Mg2	-0.003	0.874	0.154	-0.134
Mgb	0.112	0.738	0.022	-0.001
Fe5270	0.224	0.565	0.076	-0.007
Fe5335	0.178	0.496	0.090	-0.010
Fe5406	0.160	0.547	0.084	-0.015
Fe5709	-0.018	0.929	-0.064	-0.013
Fe5782	0.038	0.490	0.254	-0.056
Na5895	-0.022	0.801	0.034	-0.002
TiO1	-0.004	0.749	0.798	-0.902
TiO2	0.000	0.909	0.144	-0.155
H δ A	-0.017	0.914	0.008	—
H γ A	-0.126	0.971	—	—
H δ F	-0.074	0.909	0.013	-0.001
H γ F	-0.199	0.925	0.014	-0.002

The tables of values for LICK/IDS to LIS conversion provided in Vazdekis et al. (2010).